

Characterization and Modeling of Hydrozincite Precipitation in Continuous Tubular Reactor. A Study on Nucleation and Aggregation



Pablo Miguel Martin Soladana

University of Leeds

School of Chemical and Process Engineering

Submitted in accordance with the requirements for the degree of

Doctor of Philosophy

September 2017

The candidate confirms that the work submitted is his/her/their own, except where work which has formed part of jointly authored publications has been included. The contribution of the candidate and the other authors to this work has been explicitly indicated below. The candidate confirms that appropriate credit has been given within the thesis where reference has been made to the work of others.

This copy has been supplied on the understanding that it is copyright material and that no quotation from the thesis may be published without proper acknowledgement

The right of Pablo M Martin Soladana to be identified as Author of this work has been asserted by Pablo M Martin Soladana in accordance with the Copyright, Designs and Patents Act 1988.

©2017 University of Leeds and Pablo M Martin Soladana

This thesis is dedicated to my family whose love of support made this possible.

Acknowledgements

I would firstly like to thanks my supervisors Dr. Xiaojun Lai and Prof. David York for their constant tutorship, both academic and professional, their enthusiastic support and the guidance received in this work. I would like to also acknowledge the support provided by Dr. Jeoff Wise, Dr. Simon Greener, Dr Luis Martin de Juan and Dr. Anne Buchkremer, my industrial supervisors, whose discussions enlightened this work.

I would like to extend my thanks to the many colleges and friends I have met along my graduate studies at the university of Leeds. To Simon Lloyd, for his training in AAS and innumerable other techniques, to Dr. Diana Camacho for her constant life advice and support, to Mr. John Harrington and Mr Stuart Micklethwaite for his patient training on SEM. My special thanks to my collages and friends, Boyang Zou, Xue Tang and David Booth for sharing his knowledge in discussions, and space in the office. Also thanks to Tom, Ian, Jabbar, Guilherme, Paul, Mohammed, Fatima for being a great support within IPSE.

I would also thanks to the people who supported me on my professional development in Procter & Gamble, The ADdOPT Project and AbbVie. The experience gained showed me the big picture of what we do.

I gratitude is extended to my sincere friends, Cecilia Pilia, Andrea Rodriguez, Lucia Gomez, Arturo Andersen for the support in the good and the bad moments. Special thanks to Alejandra Figueroa whom I am forever grateful.

Finally, this thesis would not be possible without the continuous love and encouragement from my parents and sister, always close to me although far way.

Abstract

Control of particle size in rapid crystallizing processes, also called precipitation processes, present a challenge for a number of industries such as pharmaceutical, food or water treatment. It is commonly found that milling and agglomeration processes are needed in the latest stages of the synthesis to achieve the desired particle size. These processes are costly and may alter the polymorphic form. It is believed that a better fundamental understanding of the synthesis would allow better control over the process parameter in order to yield the desired product

In the present study the hydrozincite will be firstly characterized in terms of its crystal structure, solubility, induction time and morphology. Then, a continuous precipitation process was chosen to study its synthesis, as it allows fine control of process parameters such flow rate, geometry and residence time which are known to control the final particle size. The methodologies used in this study aim to elucidate the kinetics of the process of mixing, nucleation, aggregation and breakage. Turbidity measurements in batch reactor allows the determination of the nucleation kinetics as function of reactant concentration. CFD was used to the determination of mixing kinetics well as supersaturation profiles inside the Y-junction as well as within the tubular section. Finally, the the particle size distribution as function of the residence time was determined by in-line static light scattering. It is been observed that the small surface energy ($0.051 J/m^2$) of hydrozincite allows nucleation to occur rapidly. However, the rate of crystal generation decrease with decreasing pH as the reactant CO_3 decreases. The study of the relative importance of reaction over mixing (Damkholer number) reveals a general dominance of mixing. We can conclude that pH is the single most important process parameter for controlling the particle size, followed by residence time.

Contents

1	Introduction	1
1.1	Research Motivation	1
1.2	Research aims and Objectives	4
1.3	Research Background	5
1.4	Project Management	8
1.5	Scope of the Thesis	10
2	Crystallization, Mixing and Aggregation Theory	12
2.1	Introduction	12
2.2	Crystallization Theory	13
2.2.1	Introduction	13
2.2.2	Crystallization driving force, the supersaturation	13
2.2.3	Nucleation	16
2.2.4	Crystallography	23
2.2.5	Growth	26
2.2.6	Reactive crystallization	30
2.2.7	Ostwald Ripening	34
2.3	Turbulent Flow and Mixing Kinetics	37
2.3.1	Introduction	37
2.3.2	Laminar and turbulent flows	37
2.3.3	Turbulent scales	38
2.3.4	Mixing kinetics in reactive flows	40
2.3.5	Mixing models	42
2.4	Colloid Stability, Aggregation and Breakage Phenomena	44
2.4.1	Introduction	44

2.4.2	Colloidal stability	45
2.4.3	Aggregation phenomena	49
2.5	Aggregation in Turbulent Flows	56
2.6	Literature Review of Zinc Carbonate Hydroxide.	59
2.6.1	Introduction, properties and applications	59
2.6.2	Synthesis methods for the production of hydrozincite	60
2.6.3	Speciation of zinc in solution	61
2.6.4	Solid phases and hydrozincite crystal structure	65
2.6.5	Surface chemistry of carbonates	69
2.7	Scattering Theory	71
2.7.1	Light scattering theory	71
2.7.2	X-Ray Diffraction	74
2.7.3	Sources, filters and monochromator	75
2.7.4	Powder X-ray diffraction	77
3	Materials and Methodologies	80
3.1	Introduction	80
3.2	Materials	80
3.3	Light scattering	81
3.3.1	Inline Light scattering	81
3.4	X-ray diffraction	83
3.4.1	Equipment	83
3.4.2	Sample preparation	83
3.4.3	Analysis	84
3.5	Electron Microscopy	85
3.6	High Shear Mixer	85
3.7	Zinc solubility and adsorbed magnesium determination	87
3.7.1	Atomic Absorption Spectroscopy	87
3.8	Induction time determination	91
3.8.1	Measurement	92
3.9	Electroacoustic spectroscopy	93
3.10	Population balance model and gPROMS methodology	94
3.11	CFD methodology	98

3.12 Tracer experiments	101
4 Zinc Carbonate Properties: Induction time, solubility and distortion of crystal structures	107
4.1 Introduction	107
4.2 Hydrozincite equilibrium properties. Crystal structure, solubility and induction time	108
4.2.1 Experimental conditions	108
4.2.2 XRD and crystal structure characterization	108
4.2.3 Solubility	110
4.2.4 Induction time	115
4.3 Phase and Morphology of the Hydrozincite Product.	122
4.3.1 Structure change of hydrozincite as function of pH	122
4.3.2 Hydrozincite ripening	126
4.3.3 Morphology changes as a function of ripening time	127
4.4 Conclusions	127
5 Influence of Synthesis Conditions on the Hydrozincite Properties	131
5.1 Introduction	131
5.2 Results and Discussion	132
5.2.1 Product characterization.	132
5.2.2 Physical factors influencing size	132
5.2.3 Chemical factors influencing size and colloidal stability	143
5.3 Conclusions	154
6 Aggregation Kinetics of Sparingly Soluble Compounds in Turbulent Tubular Reactor	156
6.1 Introduction	156
6.2 Results and Discussion	157
6.2.1 Size analysis	157
6.2.2 Fractal dimension analysis	163
6.2.3 Concentration analysis	165
6.2.4 pH influence on the aggregation kinetics	167
6.2.5 Aggregates restructuring	169

6.3	Conclusions	171
7	Aggregation Kinetic Modelling: Population balance model in a tubular reactor	173
7.1	Introduction	173
7.2	Qualitative Hydrozincite Precipitation Model	174
7.3	Micromixing Time Characterization and Damkohler Number by means of CFD Simulations	178
7.4	Population balance model	187
7.5	Population Balance formulation and Solution	187
7.6	Data collection and optimization procedure.	192
7.7	Results and Discussion	193
7.7.1	Sensitivity analysis	201
7.8	Limitations of the Model	202
7.9	Conclusions	204
8	Magnesium Doped Hydrozincite Precipitation: Segregation Coefficient and XRD Study	206
8.1	Introduction	206
8.2	Results and discussion	208
8.2.1	SEM	208
8.2.2	Dopant adsorption	210
8.2.3	XRD analysis	214
8.3	Conclusions	221
9	Conclusions and Future Work	223
9.1	Introduction	223
9.2	Conclusions	223
9.2.1	Characterization of hydrozincite produced by continuous precipitation	223
9.2.2	Model development for the precipitation of hydrozincite in tubular reactors	224
9.2.3	Magnesium incorporation on hydrozincite crystal structure	224
9.3	Review of Aims and Objectives	225

CONTENTS

9.3.1	Study of individual phenomena involved in the precipitation phenomena	226
9.3.2	Holistic view of the precipitation phenomena.	227
9.3.3	Particle size and morphology control in a precipitation process .	228
9.3.4	Scale-up potential	228
9.4	Suggestions for Future Work	230
A	Code samples	233
A.1	PHREEQC	233
B	Code samples	245
B.1	Topas Pawley Refinement	245
C	Code samples	249
C.1	gPROMS code	249
	References	274

List of Figures

1.1	Commercially available zinc carbonate products as listed in patent submitted by Schwartz & Johnson (2004) with its crystalline size. The patent shows increased zinc availability with decreasing crystalline size.	6
1.2	XRD patent and SEM image of hydrozincite as previously reported in the literature	7
1.3	Gantt chart showing the time scales of the activities performed along this PhD. Including collaborations teaching and conferences.	9
1.4	Flow diagram showing the lay out of the thesis and the link between chapters and contents.	11
2.1	Phase diagram showing the crystallization process induced by reactive crystallization. Point A shows an undersaturated solution with not precipitant present. Point B shows a solution with sufficient precipitant for saturating the solution. Point C indicates the amount of precipitant needed for nucleation to commence, when the metastable limit is reached.	18
2.2	Evolution of free energy with nuclei radius. A free energy barrier needs to be overcome for the nucleation to proceed. Before the nuclei reach a critical radius, it cannot grow bigger. Mullin (2001)	19
2.3	Diagram showing the various nucleation mechanisms. Nucleation can commence as progressive or instantaneous, then depending on the availability of crystal surfaces, the nucleation can undergo, primary or secondary mechanism. Under primary mechanism homogeneous nucleation occurs when no foreign surfaces are present, and heterogeneous nucleation in the presence of active sites. (Camacho Corzo <i>et al.</i> , 2014) . . .	20

LIST OF FIGURES

2.4	The 14 Bravais lattice. Possible structures of the crystal unit cell as function of the combination of the unit cell parameters (Hargittai, 2009)	25
2.5	Illustration of the use of Miller indexes for the definition of planes and crystal surfaces.	26
2.6	Types of crystal defects on a 2D lattice. a) Interstitial impurity atom, b) Edge dislocation, c) Self interstitial atom, d) Vacancy, e) Precipitate of impurity atoms, f) Vacancy type dislocation loop, g) Interstitial type dislocation loop, h) Substitutional impurity atom.	27
2.7	(Cubillas & Anderson, 2010) Representation of the different energy levels on crystal surface.(1) Bulk diffusion (2) Diffusion to crystal surface, (3) Molecular attachment, (4) Surface diffusion, (4)* Surface detachment, (5) Step attachment, (6) Step diffusion, (7) Kink attachment.	28
2.8	Spiral growth from a dislocation in a C36 alkane (Mullin, 2001) as predicted by the BFC theory	29
2.9	Representation of the birth of a new layer on the crystal surface.	30
2.10	Growth rates as a function of supersaturation. Three trends can be identified depending on the growth mechanism, spiral growth from the BFC theory, birth and spread model and adhesive growth or surface roughening.	31
2.11	Supersaturation vs. time during a precipitation (Myerson, 2002). Supersaturation initially builds as the concentration of precipitant increases. After the first nuclei is formed nucleation occurs and supersaturation decreases as solute precipitates.	32
2.12	Boundaries separating the different precipitation regions as function of the reactant concentration , metal salt [M] and precipitant [X].(1) Under-saturated solution(2)Metastable supersaturated solution,(3) (4) heterogeneous nucleation (5) homogeneous nucleation., (6) positively charged colloids, (7) negatively charge colloids. (Myerson (2002))	33

LIST OF FIGURES

2.13	Diagram of a precipitation process ((Brecevic & Kralj, 2007)). Reactive crystallization commences with mixing of reactants, supersaturation builds and nucleation commences followed by growth. This may occur by a number of paths such as primary nucleation (homogeneous-heterogeneous) or secondary nucleation. Crystal matter can then undergo aggregation sedimentation or Ostwald ripening. If given enough time one single crystal will be formed.	35
2.14	Evolution of the crystal sizes as a function of time. Initially, all crystal increases in size under the effect of supersaturation. As it is consumed, smaller particles decrease their growth rate, until they reach the critical size, r_c where they re-dissolve. The largest crystals dissolve last. Only the largest crystals or radius r^* remain at infinite time (Kahlweit, 1975).	36
2.15	Mixing scales in vessels and impinging jets. Macro-scale is of the size of the vessel. Impinging reactors decrease or abolish this scale. Mesomixing occurs at the size of the turbulent eddies and micro-mixing at the smallest scales, where momentum and molecular diffusion are present (Johnson & Prud'homme, 2003).	38
2.16	Turbulent kinetic energy, $E(k)$, and concentration of fluctuations, $G(k)$ as function of the eddy wavenumber (Badyga & Pohorecki, 1995). Turbulent kinetic energy dissipation can occur in three subranges, inertial-convective, viscous-convective and viscous-diffusive corresponding to the mesoscale, Kolmogorov and Batchelor scale respectively	41
2.17	Complete segregation model, Fogler (2006b). In this model elements remain unmixed for certain residence time until they leave the reactor.	43
2.18	Maximum mixedness Fogler (2006b). Elements immediately mix as they enter the reactor to later expend certain residence time	44
2.19	Stern model for a charged surface in solution. 1: Charged surface (black circles); 2: Diffuse layer with counter-ions (white circles); 3: Bulk solution; 4: Stern layer.	46
2.20	Representation of the repulsive and attractive forces between colloidal particles as a function of distance. This is the classical DLVO representation	48

LIST OF FIGURES

2.21	Schematic of Orthokinetic aggregation. Velocity gradients enhances changes in particle collision	51
2.22	Representation of a high strain and low vorticity zone where particles accumulate and a low strain and high vorticity zone is depleted of particles. Eaton & Fessler (1994)	57
2.23	Evolution of dimensionless particle size with the dimensionless number of collisions in the system ($t^* = t\dot{\gamma}\phi$) polystyrene latex-water. Smaller equilibrium size was found with increasing shear (Oles, 1992).	58
2.24	Dependence of supersaturation from the variables pH and Carbonate concentration.	65
2.25	Predominance diagram of the system $Zn-CO_3-H_2O$ for zinc concentration $[Zn^{+2}] = 10^{-4}$	66
2.26	67
2.27	Zinc carbonate hydroxide structure, as extracted from mercury and modelled using blocks. The double layer structure is represented in as blue blocks. It is linked by carbonate and tetrahedral zinc.	68
2.28	Hydrozincite $Zn_5(CO_3)_2(OH)_2$ simulated spectrum and its corresponding planes against synthesized hydrozincite.	69
2.29	Guinier plot showing the three light scattering regions. Rayleigh, Guinier and power low regime.	73
2.30	Array of atoms scattering electromagnetic radiation. Only constructive interferences (orders from 0 to 3) are allowed (Dinnebier & Billinge, 2008)	75
2.31	Single crystal X-ray diffraction for a single crystal of NaCl	76
2.32	Construction of powder XRD pattern from single crystal XRD.	77
2.33	Crystal structure defects and their effect on the powder diffraction pattern. (Dinnebier & Billinge, 2008)	78
2.34	Typical amorphous pattern	79
3.1	Flow diagram of the inline light scattering system showing the equipment set-up for the continuous synthesis and analysis of the PSD. (1) Reactant reservoir, (2) Peristaltic heads, (3) Y-Mixer, (4) Light scattering equipment, (5) Product recovery.	82

LIST OF FIGURES

3.2	Guinier plot showing the three light scattering regions. The Rayleigh regime provides information on the particle size, the Guinier regime is a transition regime, whereas power law contains information of the particle shape.	83
3.3	Bruker D8 power X-ray diffraction equipment used for hydrozincite characterization	84
3.4	Wet mill diagram	86
3.5	Flow diagram showing the experimental set-up for the continuous synthesis and milling of hydrozincite under high shear conditions. (1) Reactant reservoir, (2) Peristaltic heads, (3) Y-Mixer, (4) High shear mixer, (5) Light scattering equipment, (6) Product recovery.	87
3.6	Flow diagram of an atomic absorption spectroscopy system. The sample is neutralized and ionized with an acetylene flame. A light source interacts with the flame and absorbance is recorded, cleaned and transformed to concentration by a calibration model.	88
3.7	Example of a calibration curve for AAS. Reference sample was automatically diluted by the AAS sampler in ranges from 0 to 1 ml/L. Absorbance correlates adequately with zinc ion concentration.	89
3.8	Automate equipment for recording turbidity as function of time.	92
3.9	Turbidity vs time. Mixing occurs at time τ_0 . Turbidity increases after induction time τ_i	93
3.10	Electroacoustic spectroscopy equipment (Zeta Probe) used for measuring the ζ -potential as function of pH	94
3.11	Flow diagram for the preparation of a CFD simulation. Feedback loops represent common problems found in simulation set-up Eesa (2009).	104
3.12	Y-Junction dimension utilized in the definition of the geometry for CFD study.	105
3.13	Details of the refined mesh used in this work after the mesh independence test.	105
3.14	Experimental set-up for tracer experiments. A tracer was injected into one of the inlets and pumped through the system and its concentration recorded by a pH probe at the end of the reactor	106

LIST OF FIGURES

4.1	Hydrozincite $Zn_5(CO_3)_2(OH)_2$ reference spectrum and its corresponding planes against synthesized hydrozincite. Preferential plane 100 is found at $13\ 2\theta$	109
4.2	Molecular structure of hydrozincite showing the 100 plane. Interplanar distance of this plane widens or shortens as a function of the $ZnCO_3$ ratio	110
4.3	Hydrozincite spectrums synthesized at various Zn/CO_3 ratios showing widening of peaks. Peak at $12\ 2\theta$ seems to widen as ratio increases. . .	111
4.4	Unit cell parameter a as function of the ratio between reactants. Close to stoichiometric ratio, the unit cell parameters resemble those of the perfect crystalline structure. After an initial increase, the value of a suddenly decreases.	113
4.5	Speciation diagram in the system zinc-carbonate-water as function of pH calculated from the species ideal equilibrium (ISC). It includes the species, Zn^{+2} , $Zn(OH)_2^0$, $Zn(OH)_3^-$, $Zn(OH)_4^{2-}$ and CO_2^{-2}	114
4.6	Comparison of zinc ion concentration obtained by AAS, simulated with PHREEQ and computed from the ideal species contribution (ISC). A common minimum is found in all the results. Displacement among them may be a consequence of the method used.	116
4.7	Turbidity vs. time. Mixing occurs at time τ_0 . Turbidity increases after induction time τ_i	117
4.8	Nucleation rate ($\ln(J)$) vs. $\ln(SS)^{-2}$ obtained from induction time experiments. Large error bars are inherently linked with stochastic process such as nucleation. The linear trend indicates a good agreement with classical nucleation theory	119
4.9	Nuclei radius vs. supersaturation based on Equation 4.4 for interfacial energy = $0.051(J/m^2)$. It shows small nuclei radius.	122
4.10	XRD of spectrum of hydrozincite synthesized at various pH compared to a reference sample. Experiment 54 was prepared with sodium carbonate at 7.2 pH. A higher number of counts were found at lower pH indicating a better crystalline structure.	123

LIST OF FIGURES

4.11	SEM images of hydrozincite product synthesized at low and high pH conditions. Low pH shows aggregates of flake like particles, whereas high pH present rounded primary particles. The morphology changes found in both samples are a consequence of differences in supersaturation as well as the difference in surface chemistry	125
4.12	XRD spectrum obtained for products ripped for 1 2 3 and 4 days after synthesis. Crystallinity increases greatly after one day as a consequence of Ostwald ripening and particle rearrangement	126
4.13	SEM images of samples after 2 and 3 days synthesizes at low pH. Plates like structures are found.	128
4.14	SEM images of samples after 2 and 3 days synthesizes at high pH. Larger single particles with flat surfaces were found. Particle rearrangement into ordered structures is believed to be the cause of these features. . .	129
5.1	Particle size distribution of hydrozincite synthesized in the plug flow reactor and its variability with flow velocity. Reactor length was set to 4.22m	134
5.2	Phase and morphology of hydrozincite precipitated in the tubular reactor.	135
5.3	Evolution of $D[4,3]$ and particle size distribution (PSD) at two concentrations 0.01M and 0.1M. Lower concentrations shown particle aggregation whereas breakage is observer at higher concentrations. The relative importance of shear forces against particle-particle collision produces the change in behaviour.	137
5.4	Studies of freshly synthesized particles under shear for low (0.01M) and high (0.1M) concentration of Zinc. 5.3(d) and 5.3(c) shown particle size $D[4,3]$ against Mixer rpm. 5.4(a) and 5.4(b) shows SEM images of the synthesized particles.	138
5.5	Evolution of $D[4,3]$ and particle size distribution (PSD) of 3 days ripened product at two concentrations 0.01 and 0.1M. Larger concentrations are shown to be more sensitive to shear due to the larger particle-particle collision rate.	140

LIST OF FIGURES

5.6	Studies of ripened particles under shear for low (0.01M) and high (0.1M) concentration of zinc. 5.6(a) and 5.6(b) shows SEM images of the synthesized particles at 0.01 and 0.1M respectively.	141
5.7	Suspensions prepared from different ratios of surfactant and solid. Suspension were kept at room temperatures. Values of turbidity across a horizontal line are shown by blue lines.	143
5.8	Turbidity map extracted from image analysis. Solution concentration was computed from the volume of hydrozincite suspension and its concentration (both shown in Figure 5.7) . Red indicates high turbidity. A localized area of stability was found.	144
5.9	D[0.9] of particles synthesized at various pH by changing CO_3^{2-}/HCO_3^- and two different concentrations.	146
5.10	Particle size distribution of the hydrozincite product precipitated under the conditions summarized in Table 5.5. Distributions towards the smaller particle sizes are found at low pH and low concentrations. . . .	147
5.11	Theoretical evolution of final particle size with volume fraction of solids in suspension. Computed using the population balance equation shown in Equation ?? in gPROMS.	149
5.12	ζ -potential and fractal dimension as function of pH. We observe that as the ζ -potential becomes close to 0, the fractal aggregates becomes tighter	151
5.13	XRD of spectrum of hydrozincite synthesized at various pH compared to a reference sample. Experiment 54 yielded 7.2 pH. A higher number of counts was found at lower pH indicating better crystalline structure.	152
5.14	Planes 200, 001 and 20-1 showed in the hydrozincite structure.	153
6.1	Evolution of D[0.9] with dimensionless number of collisions $t^*(= \dot{\gamma}\phi\tau)$. (*) 442.92ml/min, (×) 373.97ml/min, (Δ) 305.02ml/min, (\diamond) 236.07ml/min, (−) 167.12ml/min. Three regimes were found: Stable Brownian, exponential growth and steady state.	158

LIST OF FIGURES

6.2	Study of dimensionless numbers, Peclet and Stokes, with dimensionless residence time and size. (*) $0.38m/s$, (\times) $0.35m/s$, (Δ) $0.26m/s$, (\diamond) $0.208m/s$, ($-$) $0.140m/s$. Peclet number increases with larger residence time, Suggesting greater importance of flow forces against thermal forces. Stokes number also increases which indicates ghost like particles gain inertia becoming less flow driven.	160
6.3	Dimensionless number of particles vs. dimensional length for exponential growth regime for three shear rates: (\bullet) $376.96s^{-1}$, ($-$) $298.7s^{-1}$, (\times) $225.7s^{-1}$. Exponential growth kinetics were found to increase with decreasing flow rate.	161
6.4	Study of fractal dimension with dimensionless residence time and size. (*) $442.9ml/min$, (\times) $374.0mL/min$, (Δ) $305.0mL/min$, (\diamond) $236.1mL/min$, ($-$) $167.1mL/min$. Under the present experimental conditions, fractal dimension seems to correlate with particle size better than with dimensionless residence time.	164
6.5	Particle size as a function of reactor length for two flow rates (140 and 200ml/min) and three solid concentrations 0.54%, 0.44% and 0.33% corresponding to 0.01M 0.008M and 0.006M of zinc salt. Similar to previous results, aggregation progressed in the three regimes towards a stable final particle size.	166
6.6	Evolution of $D[4,e]$ with reactor length for low pH and three flow rates (63ml/min, 98ml/min and 167ml/min). The particle size is 10 times lower than at high pH. The reading seems to be less consistent. However, particle size increases with reactor length.	168
6.7	Fractal dimension as a function of reactor length and particle size. d_f correlates adequately with particle size at high pH but it does not for low pH ones. At low pH the particles initially decrease d_f for latter increase possibly due to growth and list of the exposed branches.	170
7.1	Representation of the descriptive model for the reaction, aggregation and ripening of hydrozincite in turbulent flows. High and low pH conditions are contemplated as well as high and low flow rates.	175

LIST OF FIGURES

7.2	Kolmogorov time scales at various flow rates. A decrease in the Kolmogorov time scale is found as flow rate increases. A zone of decrease Kolmogorov time scale is found between the two jets which is probably going to have a great impact in mixing since where both species coincide.	181
7.3	Kolmogorov time scale as a function of reactor length for flow velocities 0.075, 0.115, 0.16 and 0.32m/s. The initial low value around 0.05m indicates a high energy collision between streams. The maximum mixing time is found after the streams collide and create a mixing front. Finally, the time scales homogenizes across the reactor section. As expected, the largest values of Kolmogorov time scales correspond to the lowest flow rates as a consequence of the less energy being dissipated.	182
7.4	Length average supersaturation across the reaction section as a function of the reactor length. Three section can be identified as functions of the trend. (1) supersaturation buildup independent of flow rate. (2) mixing driven supersaturation build-up. (3) Reactant exhaustion and consequent supersaturation decrease.	184
7.5	Contour plot of supersaturation at 0.075m/s. A localized mixing front is found at the reactor entrance. Supersaturation then spreads homogeneously across the reactor section driven by mixing. Finally, supersaturation is consumed around the reactor outlet.	185
7.6	Damkohler number across the reactor central line for flow velocities of 0.075, 0.115, 0.16 and 0.32m/s. Low Da number near the junction indicates a reaction limiting process due to the low supersaturation. After the junction (0.2m) mixing controls as indicated by large Da numbers. Finally, reaction limits the process consequence of the reactant exhaustion.	186
7.7	Damkohler number at various velocities. Warmer colours shows where reaction is limited by mixing. Reaction occurs mainly in the central section of the pipe for around 5 to 20 cm. The largest flow rates show the less mixing limiting reaction.	188
7.8	Descriptive model of the aggregation phenomena contemplated for the formulation of the population balance model. Contains reaction, nucleation, aggregation and breakage.	189

LIST OF FIGURES

7.9	Experimental particle size distribution vs. model prediction for various reactor positions 0.17, 0.29, 0.64, 0.76 and 0.88m from the Y-junction for 0.147m/s.	193
7.10	Experimental particle size distribution vs. model prediction for various reactor positions 0.29, 0.41, 0.64 and 1m from the Y-junction for 0.206m/s.	194
7.11	Experimental particle size distribution vs. model prediction for various reactor positions 0.05, 0.17, 0.29, 0.64, 0.76 and 1m from the Y-junction for 0.296m/s.	195
7.12	Experimental particle size distribution vs. model prediction for various reactor positions 0.05, 0.17, 0.29, 0.64, 0.76 and 1m from the Y-junction for 0.331m/s.	196
7.13	Experimental particle size distribution vs. model prediction for various reactor position 0.05, 0.17, 0.29, 0.64, 0.76 and 1m from the Y-junction for 0.392m/s.	197
7.14	Simulated and experimental D[4,3]. Discrepancy between simulated and experiment is appreciated. This different is believed to be caused by the larger weight that large particles has in the D[4,3]. A steady state is found for high flow rates, whereas unfeasible increasing particle size is found at low flow rates.	198
7.15	Graph showing the optimized parameters from the population balance model. 7.2The parameter k_α was chosen to be constant in the optimization due to indetermination in the parameter estimation. The rest of parameters correlate quite well.	200
7.16	Sensitivity analysis for variables reactor length (X) and velocity (u). The minimum particle size can be found at largest flow rate and the shortest residence time. Whereas lower flow rates promote larges particle sizes	203
7.17	Fitting of CSTR and PF models to the experimental tracer experiment. The number of 125 reactor was approximated and a Peclet number of 0.004. Both models support the assumption of plug flow like behaviour	204
8.1	SEM images of hydrozincite synthesized at various concentrations and various impurity ratios. The morphology is not altered by the amount of impurity ratio.	209

LIST OF FIGURES

8.2	Mass percentage of Mg^{2+} in the sample as a function of the percentage of Mg^{2+} over Zn^{2+} in solution at three different zinc concentrations (0.002, 0.1 and 0.5M). Increasing Mg^{2+} is found in the solid sample as the amount of Mg^{2+} increases in the solution. The relationship is almost linear with increasing slope as the supersaturation decreases.	210
8.3	Mass fraction of Mg^{2+} over Zn^{2+} in solid against Mg concentration in solution at three zinc concentrations (0.002, 0.1 and 0.5M). Dashed lines represent the Langmuir fitting using Equation 8.1. A Langmuir like model is valid for model the absorption of Mg^{2+} in hydrozincite . .	212
8.4	Segregation coefficient vs. percentage of magnesium over zinc in solution at three zinc concentrations (0.02M 0.1M and 0.5M). Larger segregation was found at the lowest concentration of zinc indicating better absorption as supersaturation decreases.	214
8.5	XRD spectrum of doped hydrozincite synthesise at 0.02M at various Mg^{2+} concentrations in solution (3, 6, 10, 15% of Mg^{2+} over Zn^{2+} in solution).	215
8.6	XRD spectrum of doped hydrozincite synthesise at 0.1M at various Mg^{2+} concentrations in solution (0, 3, 6, 10, 15% of Mg^{2+} over Zn^{2+} in solution).	216
8.7	XRD spectrum of doped hydrozincite synthesise at 0.5M at various Mg^{2+} concentrations in solution. (0, 3, 6, 10, 15% of Mg^{2+} over Zn^{2+} in solution)	218
8.8	Unit cell volume as a function of Mg^{2+} mass fraction in sample for three concentrations. Dashed line corresponds to reference unit cell volume (Ghose, 1964). There was no significant relation between the unit cell volume and the mass fraction of Mg^{2+} in the sample.	220
8.9	Geometry of Metal ions Zn^{2+} and Mg^{2+} in the crystal structure of hydrozincite and Magnesite respectively. Similarities between the two structures allow substitution without disruption of crystal structure. . .	221

- 9.1 Diagram showing the process parameters (blue), the process variables (beige), the process phenomena (grey), and the features of the final product (white). The arrows show the influences between the parameter variable phenomena and the product features observed in this work. . . 227

List of Tables

2.1	Summary of Debye and Huckel theory based models	16
2.2	Mathematical formulations of the time and spatial scales in a turbulent flow shown in Figure 2.15	40
2.3	Literature review of the synthesis method of hydrozincite classified by their operation modes and reactants used.	62
2.4	Summary of alternative expressions for the definition of supersaturation. They are based on the work of Schindler <i>et al.</i> (1969)	63
2.5	Equilibrium equation of the species involved in the equilibrium of hydrozincite with water	64
2.6	Surface chemistry of carbonated atom base on Van Cappellen <i>et al.</i> (1993)	70
2.7	Light scattering regimes found in a typical Guinier plot.	72
3.1	Experimental conditions for the quantification of Mg^{+2} in precipitated hydrozincite. The table shows the concentration of zinc salt and the mass percentage of magnesium in relation with the amount of zinc salt.	90
4.1	Experimental conditions used for the assessment of crystal structure changes in hydrozincite synthesized in a Y-junction reactor	110
4.2	Crystallinity (%), Scherrer radius (\AA) and unit cell parameters (\AA) obtained from the XRD spectrum refinement of hydrozincite powder synthesized at various ratios of Zn^{+2}/CO_3^{-2}	112
4.3	Set of conditions used for the simulation performed in PHREEQS.	113
4.4	pH, zinc ion concentration and carbonate ion concentration used for computing the solubility product, K_{sp} , of hydrozincite. Temperature was set to 20C using a heating block and a chiller.	115

LIST OF TABLES

4.5	Results of the induction time of hydrozincite with a variety Zinc and coprecipitants (carbonate or bicarbonate) concentration. The use of carbonate or bicarbonate defined the pH. Supersaturation was defined based on expression 3.8. t_{ind} is the induction time in minutes and $t_{ind}\sigma$ is the standard deviation of the induction time measurements.	118
4.6	Slopes of classical nucleation theory fittings from various references compared with this work. Hydrozincite shows the highest of the slopes which coincides with the largest pk_{sp}	120
4.7	Nuclei size computed from Equation 4.4. The nuclei size decreases with increasing supersaturation. However, due to the small interfacial tension the variation in size with supersaturation is not extremely acute.	121
5.1	Experimental conditions for the characterization of the particle size distribution of hydrozincite synthesized in tubular reactor. A range of flow rates as well as reactor lengths were tested.	133
5.2	Experimental conditions for the characterization of hydrozincite synthesized in at tubular reactor. Maximum and minimum flow rates were tested for phase changes and morphology.	135
5.3	Experimental conditions for the study on the influence of shear over freshly synthesized product in a wet mill. The variables concentration and wet mill rpm were studied at a flow velocity of 0.04m/s were studied	136
5.4	Experimental conditions for the study of shear on the 3 days ripened product. Concentration of reactants, rpm of the wet mill head and flow rates through the wet mill volume.	139
5.5	Experimental conditions and d(90) Results obtained from the study of the influence of solution pH and concentration on particle size.	145
6.1	Experimental conditions for the characterization of the particle size distribution of hydrozincite synthesized in tubular reactor. A range of flow rates as well as reactor lengths were tested.	157
6.2	Values of the exponential factor of the Gregory model. Aggregation efficiency decreases as shear rate increases.	162

LIST OF TABLES

6.3	Experimental conditions for the characterization of hydrozincite synthesized in at tubular reactor. Maximum and minimum flow rates were tested for phase changes and morphology.	167
7.1	Boundary conditions, variable value and Reynolds number of the CFD simulations.	180
7.2	Results for parameter estimation for particle size distribution to the PBM (Parameters: $AggFac$, k_α , P_1 and P_2) and its 95% confidence interval.	201
7.3	Matrix of variables for the sensitivity analysis of velocity, u , and reactor length, X	202
8.1	Langmuir model fitting parameters. K_{eq} equilibrium constant and K_1 extension of the adsorption. Fitting for the three Zn^{2+} concentrations.	213
8.2	Results from Pawley refinement (unit cell parameters $a, b, c, \alpha, \beta, \gamma$ and cell volume) for samples synthesized at 0.02M Zn^{2+} concentration at various Mg^{2+} concentrations. (0, 3, 6, 10, 15% of Mg^{2+} over Zn^{2+} in solution).	217
8.3	Results from Pawley refinement (unit cell parameters $a, b, c, \alpha, \beta, \gamma$ and cell volume) for samples synthesised at 0.1M Zn^{2+} concentration at various Mg^{2+} concentrations. (0, 3, 6, 10, 15% of Mg^{2+} over Zn^{2+} in solution).	217
8.4	Results from Pawley refinement (unit cell parameters $a, b, c, \alpha, \beta, \gamma$ and cell volume) for samples synthesized at 0.5M Zn^{2+} concentration at various Mg^{2+} concentrations. (0, 3, 6, 10, 15% of Mg^{2+} over Zn^{2+} in solution).	219
8.5	Sheerer radii calculated from peak 36. For three zinc concentrations and various Mg^{2+} percentages (0, 3, 6, 10, 15% of Mg^{2+} over Zn^{2+} in solution).	219
9.1	Summary of the operating conditions for the operation of the alternative reaction set-ups	230

Abbreviations

A	Concentration of reactant A
A	Pre-exponential factor
A_1	Growth factor
A_2	Growth factor
a	Conant in Gibbs-Thomson equation
Abs	Absorbance
B	Concentration of reactant B
B	Exponential factor
c	Solution concentration (mol/L)
$c_s(r)$	Solubility as function of radius (mol/L)
c_∞	Limit Solubility at infinite radius (mol/L)
\bar{c}_i	Average concentration(mol/L)
c_i	Concentration of specie i (mol/L)
d	Interplanar distance in a lattice (m)
d_f	Fractal dimension
D	Diffusion coefficient (m^2/s)
$D_{i,j}$	Particle-Particle relative diffusion coefficient (m^2/s)
e	Electron charge (C)
e_B	Beer's Law's proportionality constant
E	Engulfment rate
$E(k)$	Turbulent kinetic energy as function of eddy frequency (m^2/s^2)
$E(t)$	Distribution of residence time
F	Faraday constant (C/mol)
g	gravity constant (m/s^2)

LIST OF TABLES

$\Delta_r G$	Gibbs free energy of reaction ($J/K/mol$)
$\Delta_o G$	Standard Gibbs free energy of reaction($J/K/mol$)
ΔG_μ	Surface Gibbs free energy($J/K/mol$)
G	Growth rate (ms^{-1})
ΔH_{fuss}^o	Standard enthalpy of fission($J/K/mol$)
h	Planck's constant (m^2kg/s)
I	Ionic strength
J	Nucleation rate ($s^{-1}m^{-3}$)
k	Eddie frequency (s^{-1})
K_i	Equilibrium constant at temperature i
K_{ideal}	Ideal equilibrium constant
$K_{i,j}^a$	Aggregation collision rate for particles in bins i and j ($1/s^1$)
$K_{i,j,pk}$	Perikinetic Aggregation collision rate ($1/s^1$)
$K_{i,j,ok}$	Ortokinetic Aggregation collision rate ($1/s^1$)
$K_{i,j,sed}$	Sedimentation Aggregation collision rate ($1/s^1$)
K_m^b	Breakage rate for particles in bins m ($1/s^1$)
k_B	Boltzmann's constant($kgm^2s^{-2}K^{-1}$)
$k_B T$	Thermal energy(kgm^2s^{-2})
L	Characteristic length of the equipment (m)
L_p	Length of the light path (m)
m_e	Electron mass (kg)
M	Number of tanks in series
Mm_i	Molecular mass of component i (g/mol)
n	Integer in Bragg's law
$n(i)$	Number of particle in bin i
n_k	Number of particle in bin k
$N(t)$	Total Number of particles as function of time
N_0	Initial Number of particles
$P(t)$	Probability as function of time
P_3	Breakage parameter proportional term
P_2	Breakage parameter shear term
P_1	Breakage parameter size term
Q	Instantaneous reaction contrast
p	Pressure (Pa)
q	Reciprocal space units ($1/m$)

LIST OF TABLES

R	Gas constant ($kgm^2s^{-2}K^1mol^1$)
R_{crys}	Crystal radius (m)
R_g	Growth rate (m/s)
R_{gy}	Radius of gyration (m)
R_i	Generation of specie i ($mol/L/s$)
$R_{c,i}$	Radius of particle in bin i (m)
$R_{c,j}$	Radius of particle in bin j (m)
R_{cp}	Radius of smallest particle bin (m)
R_c	Crystalline size (m)
r_{clu}	Molecule cluster radius (m)
r	Crystal radius(m)
r_i	Radius of particle i (m)
r_j	Radius of particle i (m)
r_p	Radius of particle (m)
ss	Supersaturation
S_i	Scalar generation rate
$S(q)$	Light intensity as function of q
T	Temperature (K)
t	Time (s)
T_c	Transmittance
t_i	Induction time (s)
t_g	Growth time (s)
u_i	Velocity in coordinate i (m/s)
V	Reactor Volume (m^3)
V	Potential gradient (V)
V_m	Mixing zone volume (m^3)
V_A	Volume of Pure reactant A (m^3)
V_B	Volume of Pure reactant A (m^3)
V_{mA}	Volume of zone of enriched reactant A (m^3)
V_{mB}	Volume of zone of enriched reactant B (m^3)
V_{el}	Surface electrical repulsive potential (V)
V_{vdw}	Surface van der Waals attractive potential (V)

LIST OF TABLES

x^{eqsol}	Equilibrium concentration of the solid phase(mol/l)
x^{eqliq}	Equilibrium concentration of the liquid phase(mol/l)
x_i	Molar concentration of specie i (mol/L)
x_i	Spatial coordinate (m)
\bar{X}	Average concentration (mol/L)
X	Average concentration (mol/L)
z_i	Charge of ion i
α	Detectable volume fraction of crystals
α_i	Activity of specie i
γ_i	activity coefficient of specie i
γ	Surface tension (j/m^2)
$\Gamma_{m,k}^b$	Daughter particle size distribution
ϵ	Turbulent Energy dissipation rate ($J/s/kg$)
ϵ_{bi}	Critical turbulent dissipation rate ($J/s/kg$)
ϵ_o	Absolute Vacuum dielectric permeability ($C/mol/m$)
ϵ_r	Relative solvent dielectric permeability ($C/mol/m$)
κ	Debye-Hunkel parameter
λ	wavelength (m)
λ_k	Kolmogorov length scale(m)
μ_{sol}	Solid chemical potential(J/mol)
μ_{liq}	liquid chemical potential(J/mol)
μ	Liquid viscosity ($Pa.s$)
ν	Kinematic viscosity = $\mu/\rho(m^2/s)$
ν	Radiation frequency (s^{-1})
ν_o	Cut-off frequency of a metal (s^{-1})
ν_i	Stoichiometric factor of component i
ν_m	Mean molar ionic volume(m^3/mol)

ϕ	Volume fraction of particles
ϕ_i	Scalar of property i
θ	Angle (<i>rad</i>)
$\psi(x)$	Surface potential as function of distance(V)
ψ_o	Surface potential (V)
ψ_{oi}	Surface potential of particle i (V)
ψ_{ol}	Surface potential of particle l (V)
ρ	Density (kg/m^3)
ρ_{cry}	Density of the crystals (kg/m^3)
ρ_p	Density of particles (kg/m^3)
ρ_l	Density of solids (kg/m^3)
τ_i	Induction time (s)
τ_s	Mesoscale mixing time (s)
τ_k	Kolmogorov scale mixing time (s)
τ_B	Bachelor scale mixing time (s)
τ_c	Reaction time scale (s)
τ_m	Micro mixing time (s)
Θ	Dimensionless time

LIST OF TABLES

AAS	Atomic absorption spectroscopy
CD-MUSIC	Charge distribution multisite ion complexation
CFD	Computational fluid dynamics
CSTR	Continuous stirred tank reactor
DLA	Diffusion limited aggregation
DLVO	Derjaguin, Landau, Verwey and Overbeek theory
FWHM	Full width at half maximum
HSM	High shear mixers
IEM	Interaction by exchange with the mean
ISC	Individual species contribution
KE	Kinetic energy
MSZW	Metastable zone width
NDF	Number density function
NLP	No linear programming
ODE	Ordinary differential equations
PBM	Population balance model
PF	Plug Flow
PSD	Particle size distribution
RAMS	Reynolds averaged Navier Stokes equations
RLA	Reaction limited aggregation
RTD	Residence time distribution
SEM	Scanning electron microscopy
SST	Shear stress transport
SLS	Static light scattering
UDF	User defined function
XRD	X-ray diffraction

Chapter 1

Introduction

1.1 Research Motivation

Precipitation is a rapid crystallization process caused by a large supersaturation normally consequence of either a fast mixing between otherwise high soluble salts that together form a lower solubility one or a mixture of a solvent-antisolvent pair. In the process of precipitation a phase transformation from liquid to solid occurs just as it would happen in any other crystallization process only that the kinetics are much faster. As consequence, of its fast nature, process which were negligible in slow cooling or evaporative crystallization become important in precipitation whereas others may pass unnoticed. For example, mixing and chemical reaction may become limiting steps under fast precipitation kinetics (Pohorecki, 1982). Also primary nucleation dominates under high supersaturation thus yielding a product with small particle size in the range from 0.1 μ m to 10 μ m. It is therefore no rare that the products of precipitation enter the colloidal domain as the large surface area of the systems make the surface forces gain importance. As consequence, aggregation and Ostwald ripening phenomena typically related to colloidal systems are readily encounter under such conditions (Myerson, 2002). On the other hand, crystal growth and secondary nucleation are of secondary importance in precipitation as they require a combination of crystal surfaces and gentle supersaturation not found in precipitation process. In this cases, the supersaturation required for crystal growth has been consumed by an initial large event of primary nucleation and the attrition needed for secondary nucleation is thinned by large number of primary nuclei.

The control of precipitation is of great importance in nature and industries. For example in mollusks, where a biological polymer is capable of controlling the particle size thus avoiding faults on the external shell (Mann *et al.*, 1991). By this means nature controls particle size, shape and layering of the material which is a task that industrial applications are still developing (Dirksen & Ring, 1991). Despite the importance of this process in wastewater treatment, pharmaceuticals, pigments and semiconductors industries, the process remains relatively under-developed and the control of particle size usually requires additional grinding steps to obtain a homogeneous particle distribution. The important of fluid dynamics on the particle size was found by Pohorecki (1982) who developed a precipitation model based on a spectral interpretation of mixing capable of predicting particle size distribution as a function of mixing intensity. Population balance are a common approach for the study of precipitation (Serra & Casamitjana, 1998; Soos *et al.*, 2005). They consist of the formulation of a transport expression for the number of particles which may include generation rates, convective and diffusive transport, growth as well as aggregation or breakage terms. In spite of being a common approach, their formulation is normally specific for a single material and experimental setup (Kostoglou & Karabelas, 1998).

Precipitation systems present strong aggregation behaviour. Finely divided material, as the one produces after a precipitation process, has the tendency to form conglomerates, also called aggregates. Under these circumstances, surfaces forces may control the size and morphology of the final particles. Initially studied by Smoluchowski (1917), aggregation is understood as a the processes of collision of single particles which are later bounded by van der Waals forces. Based on Smoluchowski's theory, particle-particle collision may take place by Brownian motion, hydrodynamic forces or sedimentation which suggests a strong dependence on flow properties as well as from particle properties such as density or particle size. Also the external appearance of the aggregates and their morphology, is found to be dependent on the aggregation mechanism. Klein & Meakin (1989) found that systems with a large number of collisions yielded aggregates which have more open structures whereas products of more inefficient collision were increasingly compact. This is called Universally in Colloidal Aggregation and uses the measure of fractal dimension to characterize the "openness" or the compaction of an aggregate. Analytical techniques such as SEM or static light

scattering can be used to reconstruct the fractal dimension from images or scattered light (Ibaseta & Biscans, 2010).

The incorporation of foreign molecules inside the crystalline structure, known as doping, has been shown to be a useful method for controlling the precipitation process as it inhibits or enhances growth and/or nucleation (Kontrec *et al.*, 2004). It is been shown that foreign ions can alter the unit cell parameters (Qiu *et al.*, 2008; Sarma & Sarma, 2016) or even change the crystal form (Sarma & Sarma, 2016). The use of doping provides an extra process lever to control precipitation however, it hugely enhances the complexity of the problem. A complete understanding requires the definition of the phase diagrams, incorporation mechanism and the process kinetics which, at the moment, represents a large gap in our knowledge.

Mathematical models are usually constructed for the prediction of the system properties. Recent studies have attempted to produce a unified model of the whole precipitation process aiming to include, mixing, reaction, nucleation, growth, aggregation and breakage in a unified model (Cheng *et al.*, 2009). However, the complex interconnection between the individual processes is likely to introduce discrepancies as the contemplation of all inter correlations is challenging. Alternatively, a more common approach utilizes model materials to study each process separately, nucleation and growth, (Hanhoun *et al.*, 2013), or aggregation and breakage (Serra & Casamitjana, 1998; Soos *et al.*, 2007). This approach presents disadvantages such as, they remain specific for the configuration and the materials. In the present work we intend to close the gap between the crystallization and the aggregation which is a step change towards the understanding of the precipitation. This can only be achieved by the combination of a number of diffraction, scattering, spectroscopy and analytical techniques, as well as modelling tools such as CFD and population balance models.

This work will build on previous work on characterization of aggregation kinetics using static light scattering (Ibaseta & Biscans, 2010; Lin *et al.*, 1990; Serra *et al.*, 1997; Yang, 2013b). Hidrozincite ($Zn_5(CO_3)_2(OH)_6$) will be used as study material since is easy to precipitate and its aggregation behaviour is of the interest for industry. Recent methodologies for the development of an equation based modelling will provide the tools to develop the population balance model which will model the particles size distribution. (Serra & Casamitjana, 1998; Smoluchowski, 1917; Soos *et al.*, 2005). Advances in the determination of induction time will provide important information for

defining the crystallization kinetics (Jiang & Ter Horst, 2011; Roelands *et al.*, 2004). CFD simulation will be used to evaluate the time scales of mixing against reaction (Badyga & Bourne, 1999; Johnson & Prud'homme, 2003; Roelands *et al.*, 2003; Tavaré, 1986; Wei & Garside, 1997). The complex problem of doping requires the use of reliable techniques such as atomic absorption spectroscopy and X-ray diffraction (Qiu *et al.*, 2008; Sarma & Sarma, 2016). The combination of these advanced methods will require construction of the current models for precipitation by differentiating the individual contributions of each phenomena and linking them to the individual particle properties as well as the final product properties.

1.2 Research aims and Objectives

Previous studies have aimed to develop integrated models of the overall precipitation process consisting of first principles (Wang *et al.*, 2005b). (Nucleation, growth, aggregation breakage and flow patents). Although this approach is of great interest since it provides an overall description of the process, it loses accuracy as complexity increases. The overall aim of this project is to separate individual processes leading to aggregation which is then studied separately both experimentally and using mathematical models. Once the processes have been studied individually, the influence of each of them will be placed into the global context of the precipitation process. The holistic manner of looking at this phenomena aims to fill the gap that individual examination of the phenomena may leave.

This research also aims to tackle the challenge that process industries face in the production of solid particles of particular characteristics such as, size, shape or polymorphic form. This translates into a number of scientific challenges which include the design of experiments capable of individually capturing the contribution of different phenomena, such as nucleation growth and aggregation, to the overall precipitation process. This approach opposes to integrated studies which aim to account for the precipitation process as a whole. In the particular case of mixing and reaction, however, both processes are deeply tangled and therefore are difficult to separate experimentally. The use of CFD allowed both phenomena to be studied simultaneously. Oppositely, the case of nucleation phenomena has been separated from reaction and aggregation thus allowing its individual study. This is also the case with aggregation and breakage

whose individual study was enabled by means of population balance. Finally, a study of the influence of important process parameters into the overall precipitation process is needed. This allowed the design of an optimized chemical process for the production of material with the desired size properties. A population balance model will allow the contemplation of each parameter individually.

Hydrozincite ($Zn_5(CO_3)_2(OH)_6$) will be used as a model compound as it is a system of interest for the consumer product industry. Its strong aggregating behaviour makes this material inefficient as an active pharmaceutical compound. In order to meet the quality criteria, the following objectives were set by the industrial sponsor:

- Understand and control the hydrozincite crystal size and morphology for its implementation in a scalable industrial application.
- Develop the understanding and propose methodologies for the size control of zinc carbonate around the $1\mu m$ particle size.
 - Particle size tuneable between 0.8 and $1.8\mu m$ via process levers.
 - 90% of the mass in particles less than $3\mu m$.
 - Continuous or batch scalable processes to 1000 to 10000 tonnes per year.
 - Remove the grinding step.
 - 2% of solid material in suspension prior to separation steps.
 - pH in the range 2 to 12 in production and 6 to 9 in the final product.
- Primary particle size control of magnesium doped hydrozincite by varying doping level with process condition.
 - Doping 0.1 to 3%w Mg/Zn.
 - Avoid common dispersant as they interfere with hydrozincite solubility

1.3 Research Background

Initially used as a catalyst and gas adsorbent for its large surface area, zinc carbonate, is used nowadays as a precursor of zinc oxide semiconductors for photocatalyst

1.3 Research Background

applications. In cosmetics zinc carbonate was found to increase the efficiency of zinc pyrithione based anti-dandruff.

Hydrozincite ($Zn_5(CO_3)_2(OH)_6$) is a sparingly soluble compounds which means that its aqueous solubility has very low value around $10^{-7}M$. The slow release of the zinc ions in shampoo formulations increases the anti-dandruff effect of the product. It is been found that the efficiency of hydrozincite as an anti-dandruff booster is related to the availability of zinc in solution as shown in the US patent from Schwartz & Johnson (2004). It is claimed that the increased solubility of the crystalline carbonate material boots the efficiency of zinc pyrithione. Increase zinc availability was found at different solubility levels, which in turn, is related to the particle size and the crystalline size of the sample. Figure 1.1 shows various commercially available zinc carbonate products with various contents of magnesium, introduced to alter crystal size, which has proven to present lower availability for larger crystalline size.

Material	Crystallite Size (XS, Å)
<u>Bruggemann</u>	
Zinc Carbonate 0.0% Mg	175
Zinc Carbonate with 1.1% Mg ¹	105
<u>Elementis²</u>	
Zinc Carbonate 0.0% Mg	181
Zinc Carbonate with 2.5% Mg	122
Zinc Carbonate with 5.0% Mg	107

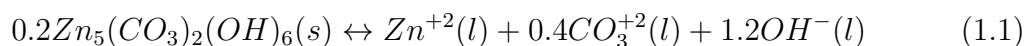
¹Commercially available as Zinc Carbonate AC

²Commerically available as Zinc Carbonate

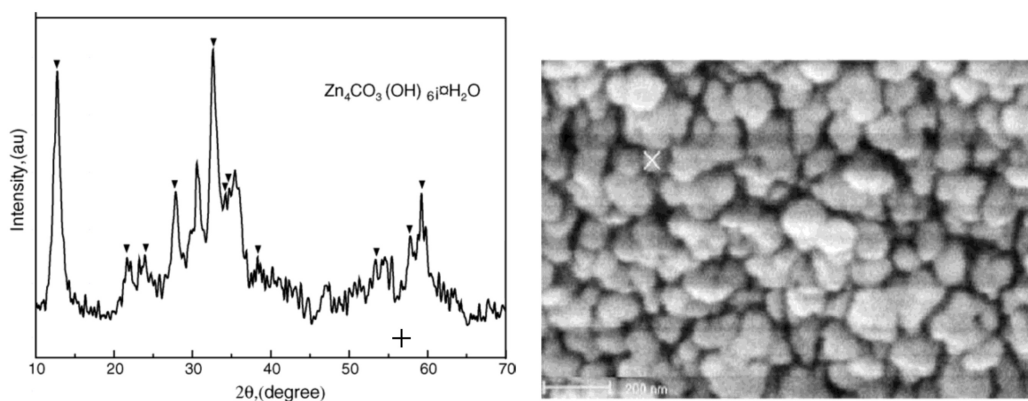
Figure 1.1: Commercially available zinc carbonate products as listed in patent submitted by Schwartz & Johnson (2004) with its crystalline size. The patent shows increased zinc availability with decreasing crystalline size.

However the commercial product is reported to be zinc carbonate, in the present project the final phase of the synthesis is not crucial as far as it is a zinc carbonate product. For the case of hydrozincite the equilibrium reaction can be seen in Equation 1.1

1.3 Research Background



Hydrozincite is reported in the literature as crystalline material with the presence of some amorphous phase as a consequence of rapid crystallization kinetics. However, its morphology can be varied with the addition of surfactants and the presence of other molecules in solution, the hydrozincite is normally reported as an aggregate of spherical particles in the range 10 to 60nm in diameter. Examples of previously synthesized material are shown in Figures 1.2(a) and 1.2(b)



(a) XRD pattern of hydrozincite showing clear peak corresponding to crystalline material as well as large background which is characteristic of amorphous materials. (Shamsipur *et al.*, 2013b)

(b) SEM image showing an aggregate of small round particles. (Li *et al.*, 2005)

Figure 1.2: XRD pattern and SEM image of hydrozincite as previously reported in the literature

The evolution of synthesis methods of hydrozincite has been focused on improving the particle size control. However, the rapid kinetics of the process along with its large surface area cause phenomena such as gradients in supersaturation and aggregation to yield high polydispersity of the product. Current synthesis methods try to minimize the effect of such a phenomena, by a hydrothermal process which reduces the concentration gradient, by carefully controlling the reaction parameters, by continuous technologies or other novel process such as emulsion or bubbles . A number of approaches utilize

direct synthesis from zinc and carbonate salts aiming to optimize the process conditions such as flow rate (Shamsipur *et al.*, 2013b). However, more widely studied area are the hydrothermal methods which use the decomposition of urea as source carbonate (Hu *et al.*, 2010). They are more advantageous in terms of increasing crystallinity although they remain inefficient due to heat transfer limitations. More recently confined crystallization, either in droplets (Alhawi *et al.*, 2015) or in impinging jets (Kickelbick *et al.*, 2012) have been studied reporting smaller aggregates and better control through process parameters such as droplet size or flow rate.

Smoluchowski (1917) introduced a population balance based approach to the aggregation phenomena from which the current more advanced models are based. These models have been applied to systems such as latex for very well-defined geometries such as Taylor-Couette devices (Serra & Casamitjana, 1998; Soos *et al.*, 2007; Wang *et al.*, 2005a). By capturing the particle size distribution as a function of time, they are capable of fitting a general population balance equation, thus obtaining parameters characteristic of the system.

1.4 Project Management

This PhD research has been carried out under an EPSRC grant in the University of Leeds in collaboration with Procter&Gamble. This project has been supported by academic investigators Dr. Xiaojun Lai and Professor David York as well as by industrial scientists, Nathalia Granito, Simon Greener and Geoff Wise.

In covering the previously named objectives a four year plan was designed which set short time deadlines for most of the tasks. It involved pure academic tasks such as a literature search, execution and analysis of experiments, model development, documentation writing, etc. as well as complementary activities to the Ph.D. experience, such as conferences, teaching and industrial collaboration. Figure 1.3 shows the time scales for each activity as they were ultimately performed.

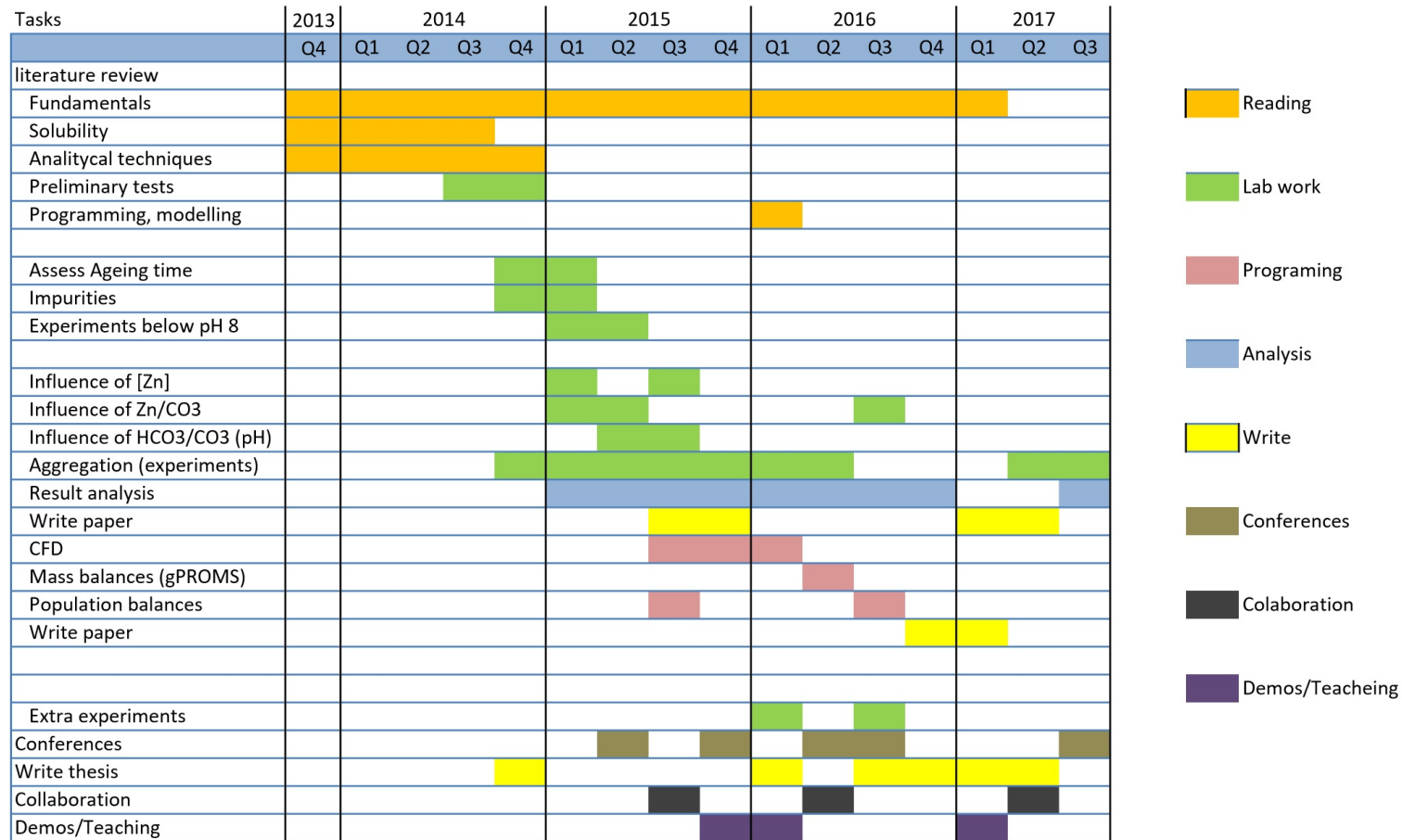


Figure 1.3: Gantt chart showing the time scales of the activities performed along this PhD. Including collaborations teaching and conferences.

1.5 Scope of the Thesis

This thesis contains 9 chapters covering the following topics:

- Chapter 1: contains an introduction to the topic of precipitation and sets the aims and objectives of the thesis, the scope and the research plan
- Chapter 2: presents a literature review of relevant topics of this research. Crystallization, colloidal systems, mixing and light scattering and diffraction.
- Chapter 3: covers the materials and methods used in this research including experimental and computational tools.
- Chapter 4: this section contains characterization of fundamental properties of crystallization such as solubility, crystal form and interfacial energy.
- Chapter 5: characterization of zinc carbonate under various process conditions, flow rate, concentration, pH, shear stress, surfactant concentration, etc. Properties of interest are: primary particle size, aggregate size, etc.
- Chapter 6: this chapter explores the use of in-line light scattering for the evaluation of aggregation kinetics through the measurement of particle size and fractal dimension.
- Chapter 7: develops the model for the precipitation of hydrozincite based on physical properties, experimental results, and in-line light scattering readings. The model consists of a descriptive and a mathematical model.
- Chapter 8: explores the influence of magnesium doping on the morphology and crystal structure of precipitated hydrozincite aiming to observe changes in unit cell parameters.
- Chapter 9: compiles the results of the work and compare them with the initial objectives. It also presents the conclusions and suggests future work which could be conducted in this area.

Figure 1.4 shows the distribution of the previous steps within the overall context of this thesis.

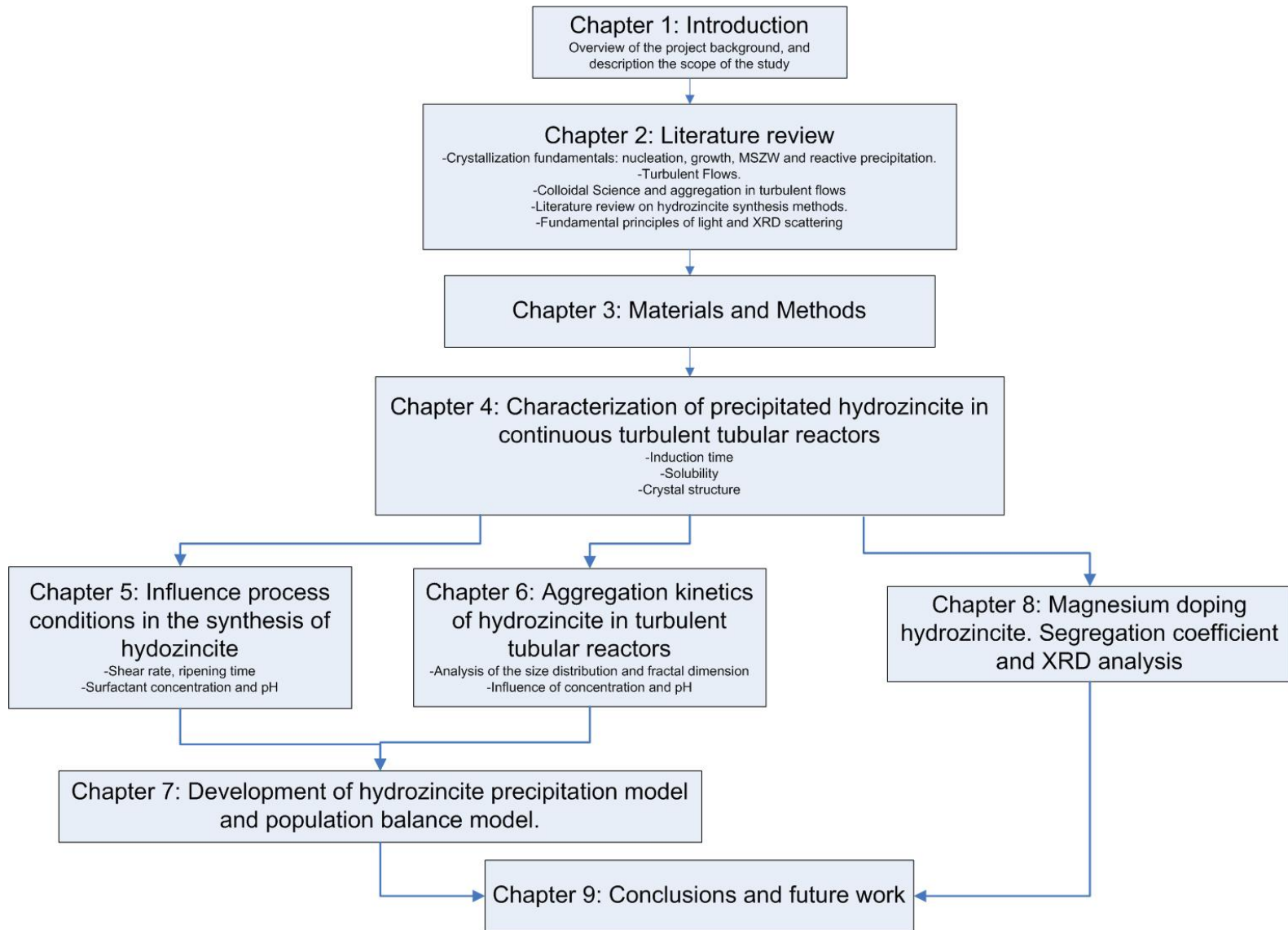


Figure 1.4: Flow diagram showing the lay out of the thesis and the link between chapters and contents.

Chapter 2

Crystallization, Mixing and Aggregation Theory

2.1 Introduction

This study focuses on the development of novel methodology for measuring aggregation kinetics after precipitation by means of readily used analytical techniques and population balance models. Additionally an study on the incorporation of carbonate ions in crystalline structure of hydrozincite will be presented.

The present section aims to review the fundamentals as well as the state of the art knowledge used in this work. In this vein, fields such as crystallization, crystallography turbulent flow, colloidal science, aggregation, zinc carbonate hydroxide synthesis and scattering theory will to be revised.

Concepts of nucleation and growth will be covered in Chapters 4 and 7 to evaluate nucleation and its importance against growth. Chapter 8 will use concepts such as lattice parameter or crystal defect to understand magnesium incorporation in hydrozincite crystal structure. Mass and momentum transport in turbulent flows will be used in Chapter 6 and 7 to explain the mixing and aggregation of precipitating hydrozincite. Chapter 5 and 6 employ colloidal science concepts to explain the changes in particle size under shear, in the presence of surfactants or changes in other process parameters. Concepts such as breakage and aggregation of collision efficiency are used in Chapters 6 and 7 for the study of aggregation kinetics. Finally scattering concepts such as the

Guinier plot, or Bragg's Law will be used in Chapter 4 and 8 aiming to characterize the material in terms of structure.

2.2 Crystallization Theory

2.2.1 Introduction

Crystallization is a change in the physical state of a system from liquid to solid. It consists of molecules, initially in solution which cluster to form a solid arrangement of molecules ordered in a crystal structure. Although the process seems simple it consists of several stages, e.g. nucleation growth and aging which are going to be described later. The aim of this section is to develop the thermodynamics behind the process and defines the driving force of the process.

2.2.2 Crystallization driving force, the supersaturation

In crystallization, as any other chemical transformation, Gibbs free energy controls the direction of the reaction. However, an equivalent variable, known supersaturation is derived from it. This thermodynamic variable is going to be of great importance as is the variable describing the driving force crystallization.

Let us take crystallization phenomena as an example of a chemical transformation controlled by Gibbs free energy. In this case, A is the liquid form of the material in question, whereas B is its solid form. Equation 2.1 shows a simple representation of an equilibrium stage between the forms.



The difference in chemical potential between the liquid and the solid, μ_{liq} and μ_{sol} respectively, defines the Gibbs free energy, $\Delta_c G$, of the crystallization. The complete definition of this variable is described in Equation 2.2. In it, the concentrations of the material in the liquid at equilibrium with the solid is represented by x_{liq}^{eq} for the liquid side and x_{sol}^{eq} for the solid side.

$$\Delta_c G = \mu_{sol} - \mu_{liq} = (\mu_{sol}^o + RT \ln(x_{sol}^{eq})) - (\mu_{liq}^o + RT \ln(x_{liq}^{eq})) = \Delta_c G^o + RT \ln \left(\frac{x_{sol}^{eq}}{x_{liq}^{eq}} \right) \quad (2.2)$$

The process will naturally find an equilibrium point where the concentration of the reactant is in equilibrium with the products. This stage is found to have a $\Delta G = 0$. Equation 2.2 can be cleaned applying this condition to finally read as follows:

$$\Delta G^o + RT \ln \left(\frac{x_{sol}}{x_{liq}} \right) = 0 \quad (2.3)$$

The equilibrium constant K_{ideal} can finally be derived from the previous expressions as shown in Equation 2.4. It is a characteristic value of the crystallization which defines the equilibrium concentration between solid and liquids. In later chapters we will use the term "solubility constant" which is nominally equivalent to "equilibrium constant" which particularly refers to a liquid-solid equilibrium. It is worth noticing the dependence of K_{ideal} on temperature, T , as well as on the standard Gibbs free energy of the material, ΔG^o . An alteration on the material nature or the temperature will therefore change the equilibrium stage. This is the principle of crystallization techniques such as reactive crystallization or cooling crystallization.

$$K_{ideal} = \left(\frac{x_{sol}^{eq}}{x_{liq}^{eq}} \right) = \exp \left(-\frac{\Delta G^o}{RT} \right) \quad (2.4)$$

However, systems are not always in equilibrium. That is to say that $\Delta_c G$ may not be 0. When this is the case, the system experiences a driving force which moves the process towards a stable stage at which Gibbs free energy equals to 0. This driving force is defined as the difference between the Gibbs free energy of the equilibrium state and the one from the initial stage. The mathematical definition of the increment of Gibbs free energy (driving force) at any stage of the crystallization is the difference between the equilibrium stage and the initial stage which can be described by Equation 2.7.

$$\Delta_r G = -RT \ln(K_{ideal}) + RT \ln \left(\frac{x_{sol}}{x_{liq}} \right) \quad (2.5)$$

$$\Delta_r G = RT \ln \left(\frac{Q}{K_{ideal}} \right) \quad (2.6)$$

Where $\frac{Q}{K_{ideal}}$ is the definition of supersaturation and Q is the ratio between the concentration of solid and liquid species in solution. For example, for any arbitrary chemical reaction ($A_{\nu_a} B_{\nu_b} \rightarrow \nu_a A + \nu_b B$) the value of Q is therefore defined as follows:

$$Q = \frac{[A]^{\nu_a} [B]^{\nu_b}}{[A_{\nu_a} B_{\nu_b}]} \quad (2.7)$$

Based on the definition of supersaturation, $\frac{Q}{K_{ideal}}$, a system can vary its supersaturation in a number of ways. For example, in creasing Q by increasing the concentration of liquid species (removal of solvent) or by decreasing its solubility, K_{ideal} , which itself can occur in a number of ways such as altering the solution temperature (cooling or heating dependent on the enthalpy of fusion) or adding an anti-solvent. In the case of cooling crystallization, the value of K_{ideal} can be approximated by the van Hoff equation (Equation 2.8).

$$\ln \frac{K_2}{K_1} = \frac{\Delta H_{fus}^o}{R} \left(\frac{1}{T_1} - \frac{1}{T_2} \right) \quad (2.8)$$

Non-Ideal solutions interatomic forces of ions in solution produces a decrease in ionic mobility. This effect is higher at higher ionic concentration and produces deviation in thermodynamic properties such as osmotic pressure, freezing point and solubility. Although at low concentration the effect is negligible, there are cases where ionic interaction accounts for large deviation from the expected values, Bell (1969). In the case of solubility, the ion iteration yields K_{ideal} to deviate from its ideal value and either be increased or decreased. In order to account for these deviations, the definition of concentration, x_{sol} , is modified by the so called activity coefficient, γ_i . This quantity takes a value of 1 for ideal solution and higher or lower values depending on the ionic interaction. The product of concentration times activity coefficient is the so called activity, α_i .

$$\alpha_i = x \gamma_i \quad (2.9)$$

Various models have been proposed to account for the activity coefficient γ_i (Debye and Huckel, Bromley, Meissner, Pitzer and Chen methods)(Zemaitis, 1986). For example, Debye & Huckel (1954) is a well-known expression which is a valid model for

2.2 Crystallization Theory

Table 2.1: Summary of Debye and Huckel theory based models

Model	Equation	Validity	Reference
Debye-Huckel	$\log\gamma_i = -\frac{0.512z_i^2\sqrt{I}}{1+\sqrt{I}}$	I < 0.01	(Debye & Huckel, 1954)
Extended Debye-Huckel	$\log\gamma_i = \frac{ Z_+Z_- A\sqrt{I}}{1+Ba_d\sqrt{I}}$	I < 0.1	(Gianguzza <i>et al.</i> , 2002)
Davies	$\log\gamma_i = AZ^2 \left(\frac{\sqrt{I}}{1+\sqrt{I}} - 0.2I \right)$	I < 0.5	(Gianguzza <i>et al.</i> , 2002)
Pitzer Models		I < 20	(Zemaitis, 1986)

low concentration which utilizes the ionic strength I ($I = 0.5 \sum z_i^2 x_i$) to account for the amount of ionic charges (z_i) in solution as a function of its concentrations (Debye & Huckel, 1954). The classical expression from Debye and Huckel reads as follows for aqueous solutions.

Further improvement came with the Pitzer model. It allows the calculation of activity coefficient of single and multicomponent solutions based on the variation of osmotic pressure. The improved model relies on temperature dependent semi empirical coefficients, the Pitzer parameters, for each species of the solution which are ionic strength independent. More information on the model can be found elsewhere (Zemaitis, 1986).

Despite the efforts made to obtain a reliable unified activity model, the complex interactions between ions and water have yielded a variety of models each of which is applicable for a range of ionic strengths. Table 2.1 summarizes some of the models available in the literature and its range of ion concentration at which they are applicable.

2.2.3 Nucleation

The nucleation process consists of the creation of a new material phase, either solid, liquid or gas within the matrix of a mother material. For example, the formation of bubbles in the matrix of a gas saturated liquid, the condensation of liquid droplets in a saturated gas phase or, more relevant to our case, the nucleation of solid crystalline material with in a saturated solution.

For a transformation of this kind to take place, a driving force must exist. It is the so called supersaturation which has been described in Section 2.2.2. However, the existence of a driving force is not a sufficient condition for nucleation to occur.

2.2 Crystallization Theory

The energetic penalty for the creation of new surface with a homogeneous matrix is sufficient to maintain a system stability even in the presence of a driving force.

Let us take the case of reactive crystallization as an example to illustrate the nucleation process. Figure 2.1 shows a simplified phase diagram of a liquid-solid system. In it, the precipitation path is represented with the line \bar{AC} . At the initial stage, A, the system commences as undersaturated. A precipitation agent is then slowly added which both, dilutes the initial solution but also decreases the solubility of the solute. If the precipitant is continuously added the system would reach the solubility line (Stage B). However, at this point, no changes are observable. The solubility line represents the equilibrium stage between the solid and the liquid $DG=0$ where supersaturation equals unity. Further addition of the precipitate will increase the value of the supersaturation and drive the system towards stage C, the metastable limit. Despite the supersaturation between stages B and C being greater than 1, the system is very unlikely to nucleate. Supersaturation must reach a value above the metastable limit for the nucleation to not have a negligible probability occur.

As introduced above, the nucleation is very unlikely to occur in the area between the solubility line and the metastable limit, the so called metastable zonewidth (MSZW). However, it is ideal for crystal growth due to the presence of a gentle driving force which prevents consumption of material by nucleation but allows its deposition on crystal surfaces which are already present. If more precipitant is added, the solution enters the saturation area where nucleation is more likely to occur. For a given point in this area, the probabilities of a nucleation event increase with time. In other words, in the presence of sufficient driving force there is no defined lag time for the nucleation to occur.

At the molecular scale nucleation can be pictured as an aggregation phenomenon of molecules into clusters. When the rate of attachment of molecules is greater than the rate of detachment then the nuclei grows and nucleation is more likely to occur. However, the growth of the nuclei has an energy cost as a new surface is being created. If the nuclei grows up to a certain critical size, the penalty disappears and the nuclei is free to grow. Equation 2.10 describes the phenomena. The first term on the right hand side of the expression shows the contribution of the supersaturation as the driving force for the attachment of molecules. Whereas the second term accounts for the energy penalty for the creation of a new surface. Both contributions can be represented graphically in

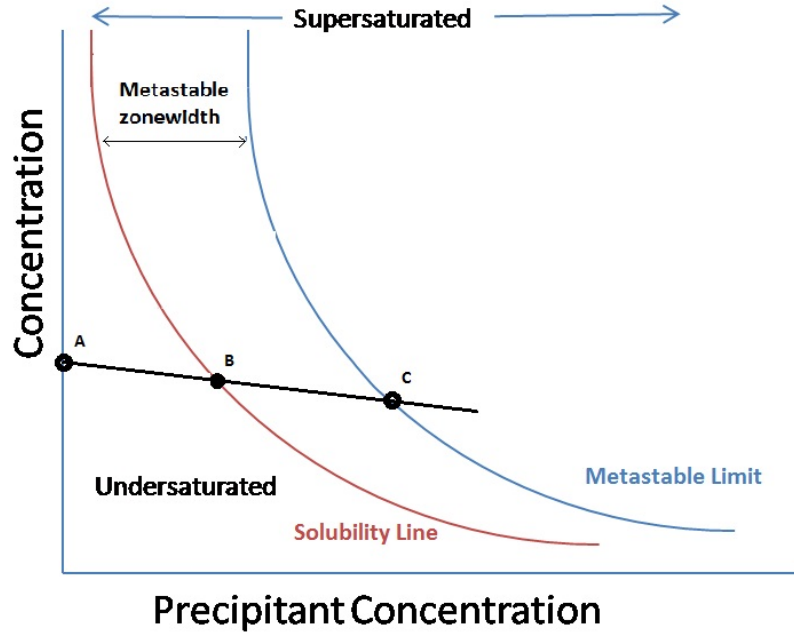


Figure 2.1: Phase diagram showing the crystallization process induced by reactive crystallization. Point A shows an undersaturated solution with not precipitant present. Point B shows a solution with sufficient precipitant for saturating the solution. Point C indicates the amount of precipitant needed for nucleation to commence, when the metastable limit is reached.

the classical representation of the Gibbs free energy as a function of nuclei size, Figure 2.2, in which the nucleation barrier can be visualized. It is worth commenting that the stochastic character of molecular attachment and detachment, driven by thermal fluctuation and Brownian motion, is likely to be the cause of the stochastic nature of the crystallization. This leads to a process difficult to predict due to its large time variability.

$$\Delta G = 4\pi r_{cu}^2 \sigma + \frac{4}{3}\pi r_{cu}^3 \Delta G_{\mu} \quad (2.10)$$

Although all crystals are created based on the same nucleation principle, namely, new surface creation driven by supersaturation, there are a number of ways the nucleation can proceed as a function of process and chemical factors. For example, the value of supersaturation, the surface energy, the presence of foreign surfaces, agitation inten-

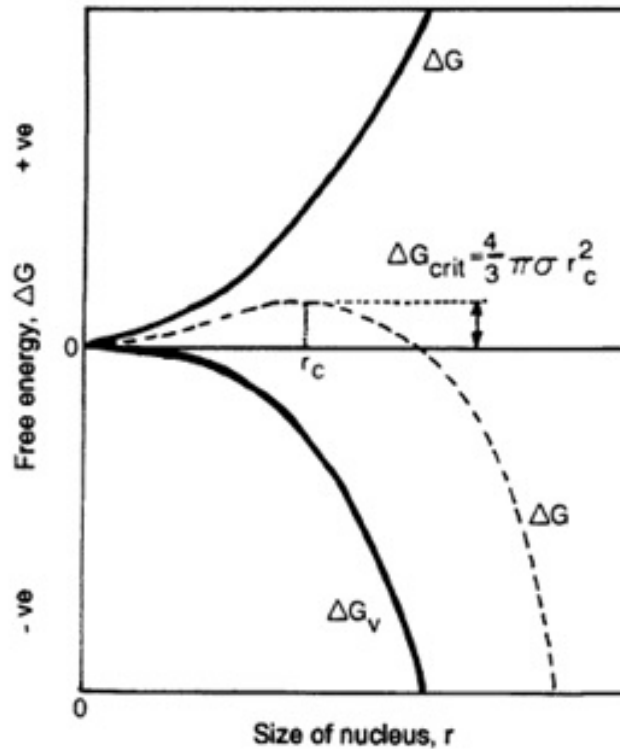


Figure 2.2: Evolution of free energy with nuclei radius. A free energy barrier needs to be overcome for the nucleation to proceed. Before the nuclei reach a critical radius, it cannot grow bigger. Mullin (2001)

sity, tendency of nuclei to break, the rate of supersaturation change or solution history. Depending on the relative importance of the listed phenomena, the crystallization will follow one of mechanism shown in Figure 2.3.

In the first stages, nucleation proceeds under two different mechanism, instantaneous or progressive. In the first case all nuclei appear simultaneously across the whole solution bulk, developing at the same time and the same rate. This is called instantaneous nucleation (IN). On the other hand, it may be occur that the nuclei appears at different times and different parts of the solution, growing at different rates. In this case the new nuclei co-exist with already growing in a polydistribution of sizes. This has been named as progressive nucleation (PN).

After this first stage when nuclei are created, nucleation can proceed in a number

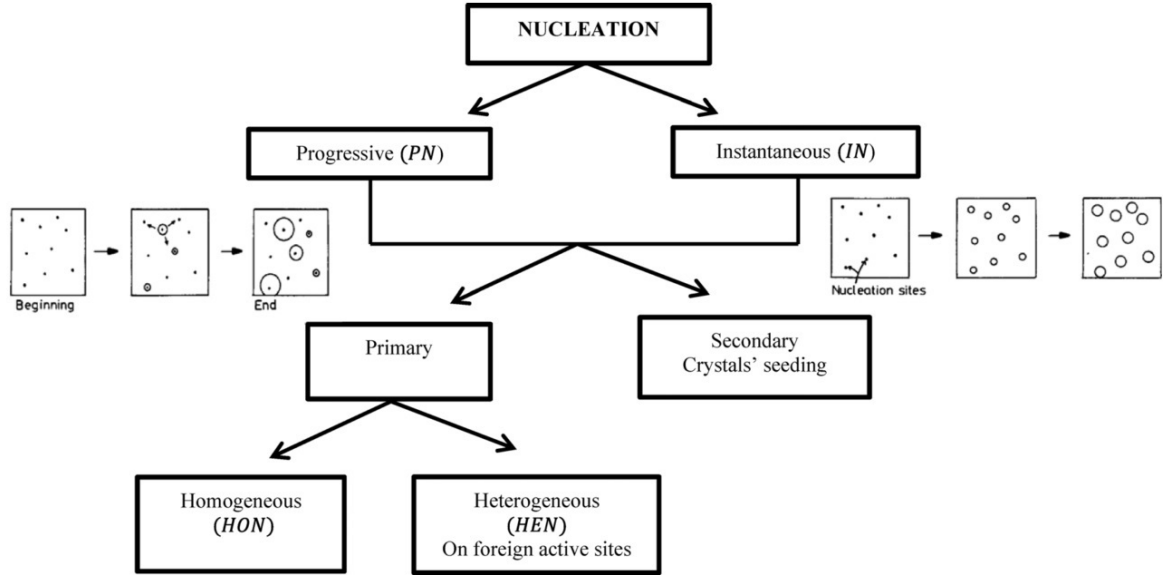


Figure 2.3: Diagram showing the various nucleation mechanisms. Nucleation can commence as progressive or instantaneous, then depending on the availability of crystal surfaces, the nucleation can undergo, primary or secondary mechanism. Under primary mechanism homogeneous nucleation occurs when no foreign surfaces are present, and heterogeneous nucleation in the presence of active sites. (Camacho Corzo *et al.*, 2014)

of ways. In the case of no crystalline matter being present, primary nucleation occurs. Under this mechanism homogeneous and heterogeneous nucleation can be found as function of the supersaturation.

Homogeneous Nucleation, homogeneous nucleation occurs in solutions where no nucleation sites are present and therefore their effect is negligible in the nucleation process. Typically, filtered systems and/or high supersaturation are examples of such cases. The classical nucleation theory, (Volmer, 1939), describes the nucleation rate (number of crystals per unit volume per unit time) with an Arrhenius type of expression shown in Equation 2.11.

$$J = A \exp\left(\frac{B}{\ln(ss)^2}\right) \quad (2.11)$$

Where ss is the supersaturation as described in Section 2.2.2. J is the nucleation rate ($\#/m^3/s$) which is inversely proportional to the induction time (t_i). Brandel &

2.2 Crystallization Theory

ter Horst (2015) provides the following relationship between the variable.

$$J = \frac{3\alpha}{\pi G^3 t_i^4} \quad (2.12)$$

In this equation α represents the detectable volume fraction and G is the growth rate. This expression assumes that the immediate detection of the first crystal is not possible but instead, it occurs after certain growth time of the nuclei. Therefore, the detected induction time would be a summation of the induction time (t_n), and the growth time (t_g) of the cluster to a detectable size ($t_i = t_n + t_g$). Furthermore, the exponential factor B contains information about the size and the surface tension. For example, nuclei size r_i , can be worked out from parameter B using the following expression:

$$B = \frac{16\pi\gamma^3\nu_m^2}{3k_b^3T^3} \quad (2.13)$$

Where γ is surface tension, ν is the mean molar ionic volume, k_b is the Boltzmann constant and T is the temperature in K. Based on the classical nucleation theory free molecules in solution clusters in unstable nuclei. When thermal forces ($3k_b^3T^3$) are overtaken by surface forces ($16\pi\gamma^3\nu^2$) (Equation 2.13 increases to a critical value) then nucleation occurs.

$$r_i^* = \frac{2\gamma\nu_m}{k_bT} \quad (2.14)$$

The minimum stable nuclei has a radius described by Equation 2.14. Nielsen & Söhnel (1971) suggested a simple expression to calculate the interfacial tension of the material in solution. Based on Equation 2.13 he obtained:

$$\gamma = 0.290 (B/\nu_m^2)^{1/3} \quad (2.15)$$

From the molecular point of view, the B factor as shown in Equation 2.13 represents the ratio between the binding energy between the molecules and the thermal forces applied to them. Therefore the CNT describes a process in which the two forces compete.

To finalize the description of Equation 2.11 let us comment on the pre-exponential factor A . Whereas B is a factor depending on thermodynamic properties, A is a

kinetic factor. It accounts for the collision rate of molecules in solution to the nuclei and depends on process factors such as concentration and stirring rate. For example, Forsyth *et al.* (2015) and Liu & Rasmuson (2013), observed an increase of A as a consequence of the turbulent energy in to the system. Mechanical agitation has been shown to accelerate the process of primary nucleation. Liu & Rasmuson (2013) showed that the decreased induction time comes from the decrease in the exponential factor of the classical nucleation theory. The effect of agitation on induction time has also been scaled between equipment with a very well defined shear stress field by Forsyth *et al.* (2015) who found that nucleation rates were scalable with shear stress.

Heterogeneous nucleation describes a nucleation process where surfaces or impurities like dust or walls significantly decreases the nucleation energy barrier, therefore, crystalline material forms around these foreign elements (Mullin, 2001).

Secondary nucleation stands for systems where crystalline material is already present. It was observed by Tina and McCabe (1934) that seeded solutions nucleate much faster than homogeneous ones. The addition of small crystals to a saturated solution is an effective way of enhancing nucleation rates by secondary nucleation. However, it is not the only way. Crystals already present in solution break and undergo attrition when contacting moving parts such as stirrer or other crystals. This is the so called, contact secondary nucleation (Cui & Myerson, 2014).

Induction time determination

Determination of the nucleation rate has been approached from two methodologies fundamentally different in their principle. The literature lists them as the isothermal and polythermal method.

Isothermal methodologies understand nucleation as a thermodynamic process in which a system in equilibrium is exposed to a driving force which shifts it to a new thermodynamic stable stage. These approaches rely on the capture of the lag time between the two stages as variable containing information about the system. The mathematical models used in these methodologies assume that the first crystal nucleates with a probability, $P(t)$, after a lag time, t . They also assume that nucleation follows a random variable process modeled by a Poisson distribution (Jiang & Ter

Horst, 2011). After some simplification, Equation 2.16 can be derived from the mathematical expression of the distribution. In order to obtain the nucleation rate (J) and growth time (t_g), a fitting between expression 2.16 and the experimental induction time distribution is needed which required at least 80 repetitions (Xiao *et al.*, 2017) or some statistical treatment such as Bootstrapping or Monte Carlo simulations (Forsyth *et al.*, 2015).

Approaches in this vein have been successfully used to measure interfacial tension in different solvents (Yang, 2013a), or the effect of shear on nucleation rates (Forsyth *et al.*, 2015). The model contains the parameters J and t_g as optimization parameters and can be read as follows:

$$P(t) = 1 - \exp(-JV(t - t_g)) \quad (2.16)$$

A simple model for obtaining information on the nucleation kinetics is to derive the average and standard deviation of various induction time measurements. In this manner, the induction time obtained (t_i) can be directly fitted to the CNT as a function of the supersaturation (s) to obtain exponential (B) and pre-exponential (A) parameters. This assumes that there is an inverse relation between induction time and nucleation rate.

The polythermal methods comprise the second set of methodologies. Nyvlt *et al.* (1970) understood the nucleation process as a kinetic process influenced not only by the degree of supersaturation but also by the rate of change in this variable. Through the measurement of induction time at different supersaturation and cooling rates, the model is capable of predicting solubility and nucleation rates. The results of this method are in good agreement with the ones from isothermal methodologies with the advantage that they are based on first principles (Camacho Corzo *et al.*, 2014). Since this model is outside the scope of this work, the reader is referred to Camacho Corzo *et al.* (2014) and Nyvlt *et al.* (1970) for further information.

2.2.4 Crystallography

Solids with their atoms arranged in a three dimensional periodic structure are called crystals. The smallest repeatable unit in a crystalline material is the unit cell and its repetition in space creates the so called crystal lattice. They are characterized by

three distances (a , b and c) and three angles (α , β and γ), the lattice cell parameters. Permutations of the possible values of the unit cell parameters yield the 14 Bravais lattice shown in Figure 2.4.

Planes in a crystal lattice, by convention, are represented by the so called Miller Indexes. Under this representation planes are described by three parameters (hkl) defined as the inverse of the interception point of the plane with the axes of the crystal lattice. Let's take Figure 2.5(a) an example. Plane DGF yields $D = 2A$, $G = -2B$ and $F = 3C$ as intersection points with the xyz co-ordinates. Therefore the inverse values would be $\frac{1}{2}$, $-\frac{1}{2}$, $\frac{1}{3}$. The final Miller indexes ($3, \bar{3}, 2$) are computed by multiplying by the lowest common denominator, 6 in this case. Notice that the negative value of the y axes is denoted with a bar.

Miller indexes are used to describe crystal features. For example, morphological features such as shape can be described based on Miller indexes. Also the growth rate of crystal faces can be described using this method. In this case, the Miller indexes are used to uniquely identify growth rates with t crystal surfaces. The rapidly growing surfaces tend to disappear where the slow growing ones control the crystal morphology. Figure 2.5(b) shows the form of calcite crystal with their Miller indexes.

Lattice incorporations In a wide range of scenarios, impurities are either substituted or trapped in the crystal structure which becomes part of the solid product as represented by a and h respectively in Figure 2.6. As a consequence of the altered crystal structure, the number of dislocations per volume increases. Properties such as melting point or solubility are affected by alteration of the lattice which can be seen in the example of quartz (Wintsch & Dunning, 1985). In The pharmaceutical and cosmetic industries utilize the alteration of these properties to modify the solubility and therefore the efficacy of API. This method for tuning solubility falls into the category of crystal engineering (Savjani *et al.*, 2012a).

Goldsmith's Rules are a set of practical rules for assessing the ion incorporation of foreign ions into a host crystal structure. Based on atomic properties such as electronic charge, electronegativity or atomic ratios a probability can be given on whether or not an ion will be incorporated into a crystal structure. For example, the charge criteria states that atoms in a lattice are more likely to be substituted if they have a charge

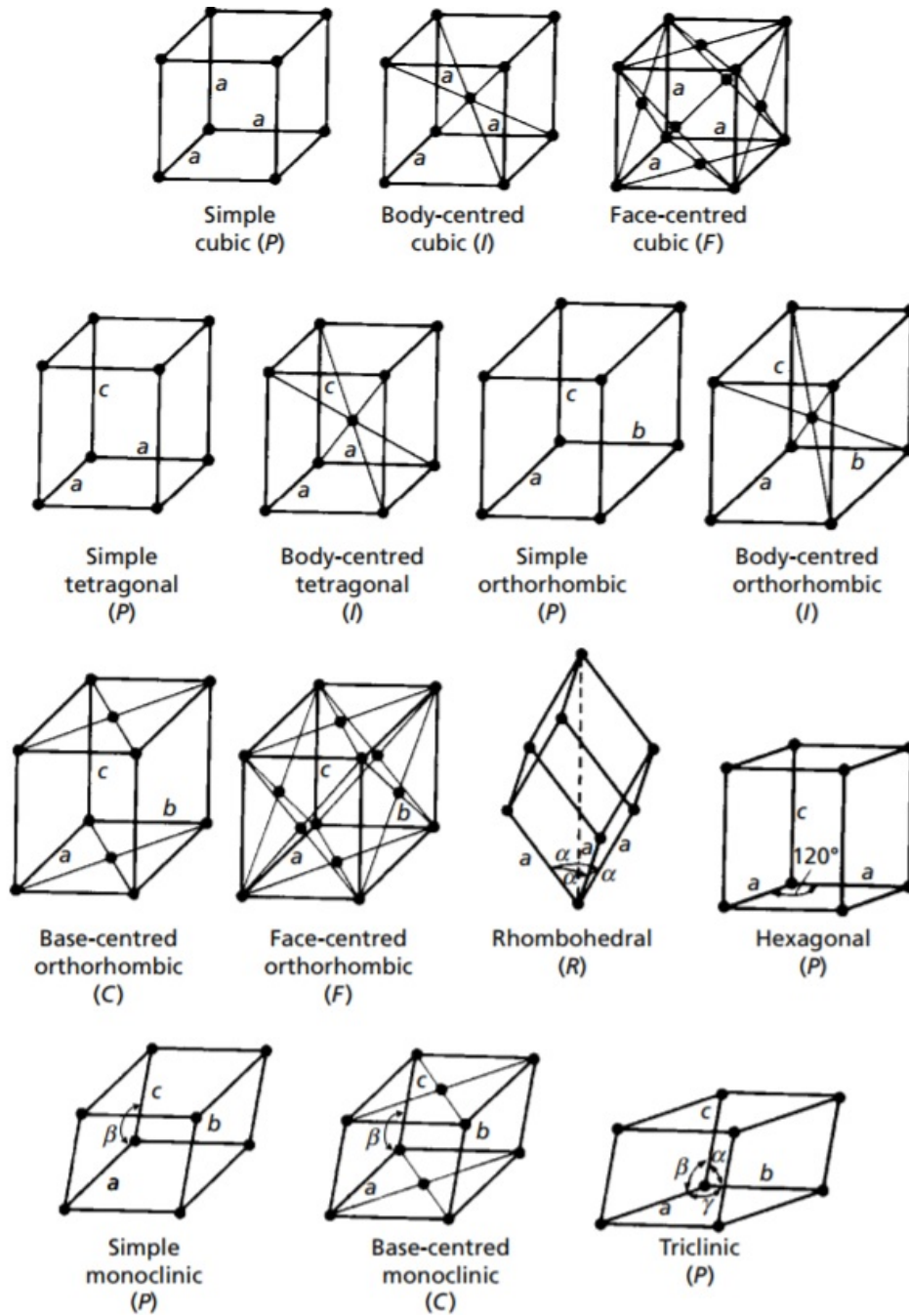
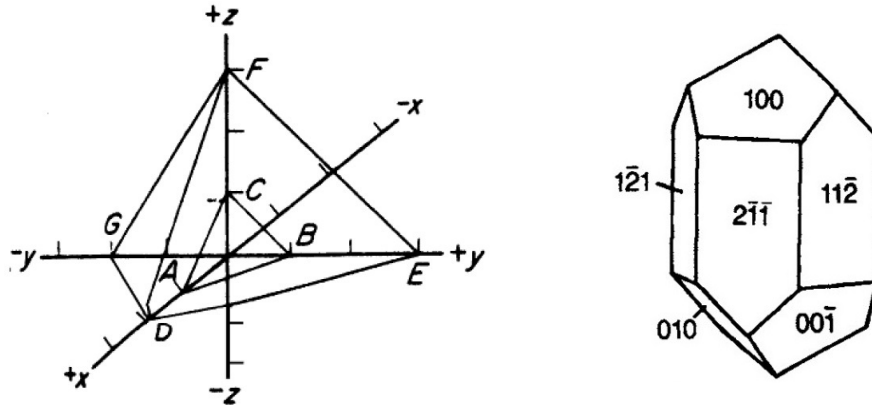


Figure 2.4: The 14 Bravais lattices. Possible structures of the crystal unit cell as function of the combination of the unit cell parameters (Hargittai, 2009)



(a) Illustration of planes as an explanation of (b) Crystal morphology of calcite with its miller indexes (Mullin, 2001)

Figure 2.5: Illustration of the use of Miller indexes for the definition of planes and crystal surfaces.

difference less than two. Similarly, comparable radius between host and substituting ions means that replacement is more likely to occur. Ringwood’s modification to the Goldsmith rules introduced the electronegativity criteria which states that atoms should be not exceed certain differences of electronegativity otherwise they would be rejected from the lattice.

Studies done in calcite doped with Mg Goldsmith *et al.* (1956) and more recently with SO_4^{+4} Kontrec *et al.* (2004) indicates doped ions disrupt the crystal structure increasing the unit cell volume steadily which differs significantly with what was observed in this study. Sarma & Sarma (2016), on the other hand, reported a sudden change in unit cell volume as Mg was incorporated into calcium phosphate.

2.2.5 Growth

Crystal growth is the phenomena by which new solute molecules are added to an existing solid phase. It requires a solid phase with template growth and a driving force, in this case the same as nucleation and supersaturation. However, many other factors may affect its kinetics such as impurity content, surface defects, surface properties.

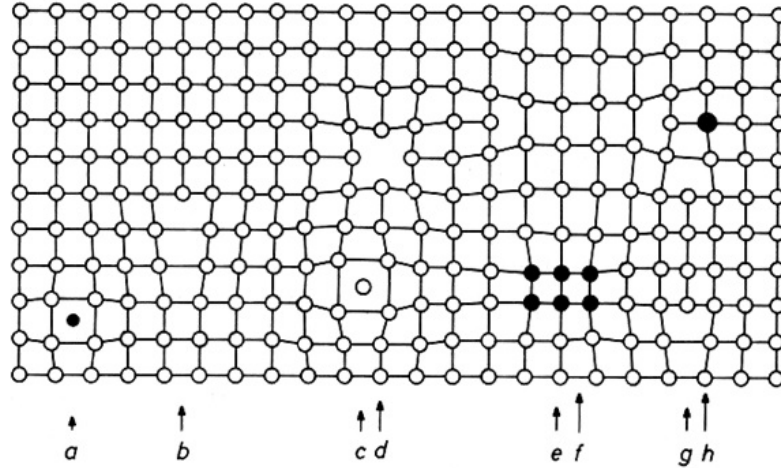


Figure 2.6: Types of crystal defects on a 2D lattice. a) Interstitial impurity atom, b) Edge dislocation, c) Self interstitial atom, d) Vacancy, e) Precipitate of impurity atoms, f) Vacancy type dislocation loop, g) Interstitial type dislocation loop, h) Substitutional impurity atom.

Within the same crystal, faces with different Miller indexes grow at different rates. Wulff (1901) found that the surface energy of each face is related to its growth rate. It is argued that the surfaces with high surface energy (low reticular lattice density) grow faster than the ones with low surface energy.

Crystal growth consist of a number of different processes. The Gibbs-Voulmer theory understands the growth process as a succession of adsorption and diffusion steps. They commence from a free molecule in solution to finally being immobilized onto the crystal surface. The theory rests on the fact that a solute unit is not immediately immobilized when arriving at the crystal surface, but instead it is allowed to move along the surface as a consequence of Brownian motion. The solute molecules are more likely to remain in low energy areas such as kinks or steps. The process of solute addition to the crystal lattice is illustrated in Figure 2.7. Initially, a solvent molecule undergoes Brownian motion in the bulk solution (1). If it encounters a concentration gradient as those found in a surface boundary layer, the molecule would diffuse towards the crystal surface (2). Then, the particle is adsorbed on the surface where its energetic stage is lower, at this point the molecule either accommodates itself to the lower energy stage (3) or is rejected back to the boundary layer (4). Brownian motion remains important

on the crystal surface and the adsorbed molecule is free to move on the surface (4). The molecule can further decrease its energetic stage if it finds a stable location on a step (5) or in a kink (6).

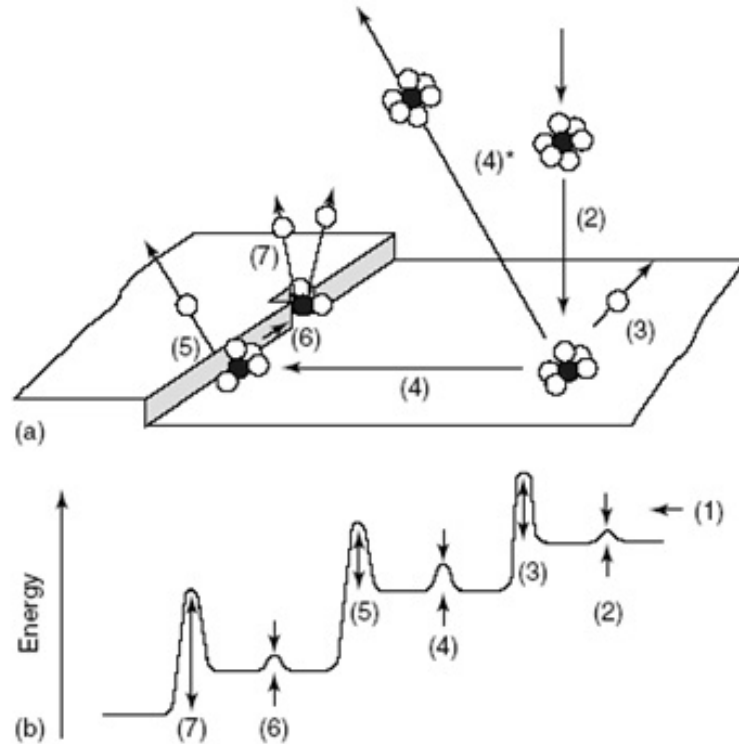


Figure 2.7: (Cubillas & Anderson, 2010) Representation of the different energy levels on crystal surface. (1) Bulk diffusion (2) Diffusion to crystal surface, (3) Molecular attachment, (4) Surface diffusion, (4)* Surface detachment, (5) Step attachment, (6) Step diffusion, (7) Kink attachment.

The lowest energy state of a molecules, the most stable, on a crystal surface is a kink site. However, depending on the relative importance of the kinetics of abortion compared with diffusion, the solute molecules may not reach the lowest energy site. As consequence, different growth regimes arises. In spite of these efforts there is still no unified theory of crystal growth, instead three mechanism of growth have been identified. These are, absorption layers, birth and spread and surface roughening.

Adsorption layers theories (Burton Franc Cabrera) The mechanism proposed by Frank & van der Merwe (1949) is dominant at low supersaturations, when

the bulk diffusion is slower than the surface diffusion(Processes 2 and 4 in Figure 2.7). Under this regime, the solute molecules are allowed sufficient time to find the location of minimum energy in the lattice. It assumes that the crystal presents a dislocation step from which spiral growth occurs. Figure 2.8 show a crystal surface growing under this mechanism which takes the characteristic shape of a spiral.

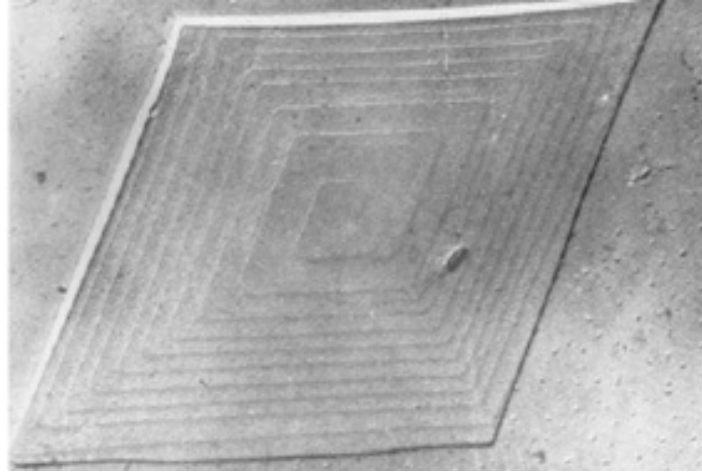


Figure 2.8: Spiral growth from a dislocation in a C36 alkane (Mullin, 2001) as predicted by the BFC theory

In 1951 Burton Cabrera and Frank improved the theory (BCF) by adding a mathematical expression of the growth kinetics The resulting equation can be read as follows:

$$R_g = A_1 s^2 \exp\left(\frac{A_2}{ss}\right) \quad (2.17)$$

Birth and spread models at relatively high supersaturation, the rate of molecular attachment to the surface increases and solute molecules, unable to find their lowest energy point in the lattice, coalesce in isles on the crystal surface. The isles grow and expand across the surface. Under this mechanism processes 2 and 4 in Figure 2.7 are in the same order of magnitude (Mullin, 2001; van der Eerden *et al.*, 1978).

Figure 2.9 shows the aspect of a island on the crystal surface with arrows indicating the direction of growth. The growth rates (R_g) on this regime are a function of supersaturation (s) and system related constants A_1 and A_2 .

$$R_g = A_1 s^{\frac{5}{6}} \exp\left(\frac{A_2}{ss}\right) \quad (2.18)$$

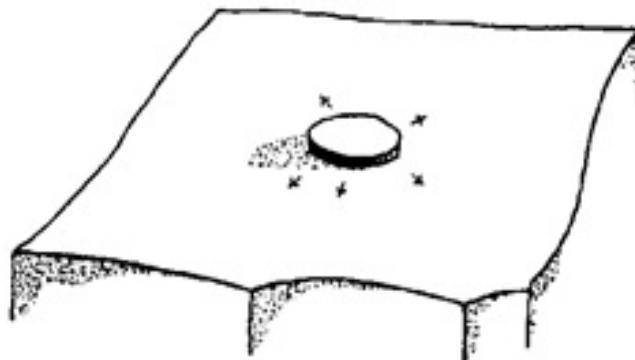


Figure 2.9: Representation of the birth of a new layer on the crystal surface.

Rough interface growth theories when the supersaturation is in excess of a certain value, surface adhesion (process 2) is dominant and solute molecules pile on top of one another creating a rough crystal surface. This is the so-called surface roughening regime. Under this regime there is no preferential growth direction and hence, no crystal morphology can be seen. Instead, surfaces produce dendrite and fractal patterns. (Cubillas & Anderson (2010)) In this case, the growth rate is proportional to supersaturation.

In conclusion, the overall picture of growth is of a process controlled by supersaturation in which adhesion rate and diffusion are the two main processes. When combining the growth laws of the three mechanisms we find that the overall process of growth can be modelled. This is shown in Figure 2.10 Chernov (1961).

2.2.6 Reactive crystallization

Reactive crystallization or precipitation denotes the rapid formation of crystal from solution as a consequence of large supersaturations away from equilibrium. Such a large driving force generally implies the simultaneous occurrence of crystallization-related processes such as nucleation, aggregation growth and Ostwald ripening meaning that they are difficult to study independently. Generation of large supersaturations are characteristic of low solubility materials or also called sparingly soluble compounds which yield small nuclei as predicted by CNT (Equation 2.14). This supersaturation is normally achieved by the reaction of chemical species, where the name reactive crystal-

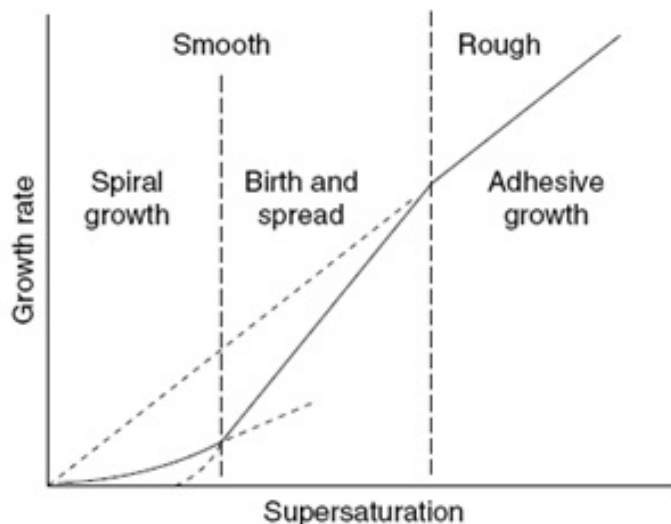


Figure 2.10: Growth rates as a function of supersaturation. Three trends can be identified depending on the growth mechanism, spiral growth from the BFC theory, birth and spread model and adhesive growth or surface roughening.

lization comes from. Under these high supersaturation conditions, primary nucleation plays a major role in precipitation as compared with secondary nucleation or growth. In other words, the importance of foreign surfaces is diminished as solution nucleates homogeneously across the bulk. The low solubility of the resulting compound, yields a sudden decrease in supersaturation after nucleation occurs as illustrated by Figure 2.11. Therefore, subsequent processes driven by the same driving force are less important since driving force is quickly consumed. For example, growth kinetics are greatly reduced as most of the supersaturation is consumed in nucleation. On the other hand, secondary processes, which minimize surface energy, are greatly enhanced by concentrated suspension and small crystal sizes. Typical secondary processes are aggregation and Ostwald ripening.

Colloidal suspensions are a common product of reactive crystallization. As a consequence of the small particle size, surface forces become important as well as Brownian motion. Therefore, the control of the resulting colloidal systems is key in achieving the desired particle size distribution. Colloidal stability will be introduced in Section 2.4.2.

As reaction kinetics accelerate, mixing becomes a limiting step. In order for the system to undergo reaction, the chemical species must be mixed in at the molecu-

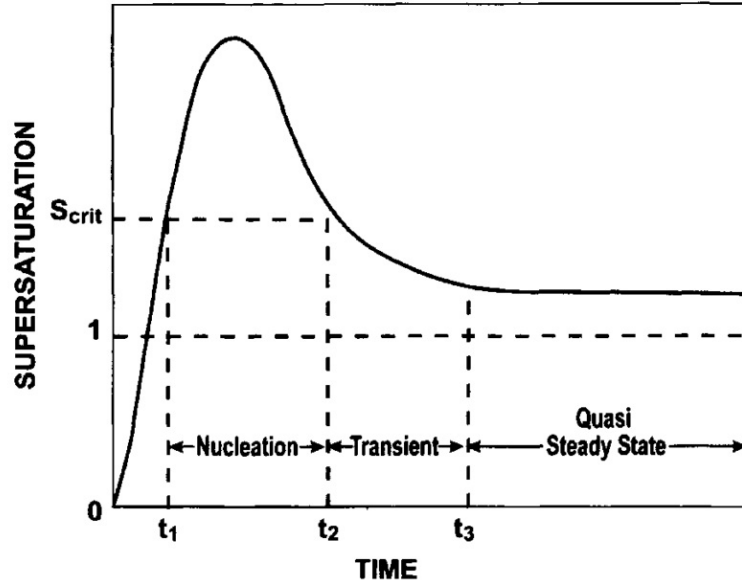


Figure 2.11: Supersaturation vs. time during a precipitation (Myerson, 2002). Supersaturation initially builds as the concentration of precipitant increases. After the first nuclei is formed nucleation occurs and supersaturation decreases as solute precipitates.

lar level. Therefore mass transfer across the various mixing scales, macro, meso and micromixing must be completed. Mixing scales and mass transport across them are assessed in Section 2.3.

A convenient way of understanding the possible outcomes of a reactive crystallization process are precipitation diagrams, introduced by Söhnel & Garside (1992), they consist of a 2D representation of the concentration of metal and the precipitant. They illustrate the variety of outcomes of the precipitation process.

Figure 2.12 shows a generalized precipitation diagram where the axes represent the negative logarithm of the concentration of the two reactants. The contour lines b, c, d and e delimit the surfaces 1, 2, 3 and 4. Line b is the solubility line and delimits unsaturated (1) and the metastable zone. c would represent the crystallization line above which, spherical (3) or dendritic growth (4) would occur. Zones 6, 7 and 5 represent the precipitation product. In the case of an excess amount of positively charged ions Me^+ , the resulting colloidal particles will be negatively charged (7) and the opposite also holds (6). Area 5 represents large supersaturation areas where homogeneous

nucleation would occur. It is delimited by line *e*.

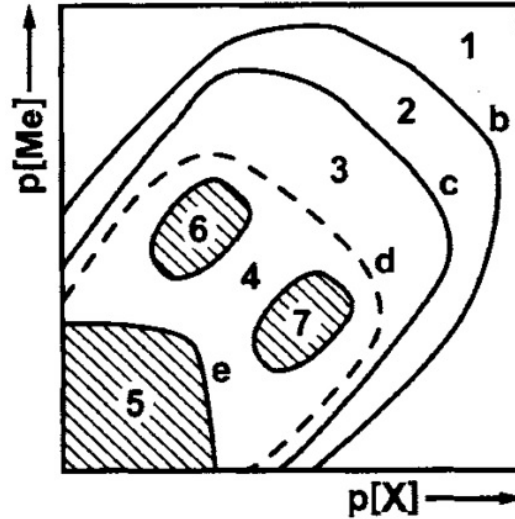
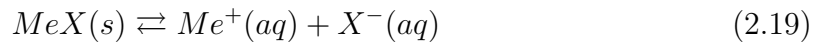


Figure 2.12: Boundaries separating the different precipitation regions as function of the reactant concentration , metal salt [M] and precipitant [X].(1) Under-saturated solution(2)Metastable supersaturated solution,(3) (4) heterogeneous nucleation (5) homogeneous nucleation., (6) positively charged colloids, (7) negatively charge colloids. (Myerson (2002))

Although easy to interpret, this diagram is very limited in terms of what processes it can show. The representations are valid for precipitation processes which obey the following general equation:



Where MeX is the precipitated species in solid state and Me^+ and X^- are the metal and precipitant ionic species respectively. In many cases, this simple equation is not sufficient to describe all the precipitation process. Polymerization reactions or systems incorporating OH^- ions follow a series of reaction where composition is time dependent or the pH of the solution is altered. The former situation presents additional concerns as surface chemistry is altered with the variation in pH. This phenomenon will be further studied in Section 2.6.5 where surface ionization will be studied as function of pH.

Adapted from Brecevic & Kralj (2007), Figure 2.13 illustrates the processes involved in the reactive precipitation. Firstly, reactants mix and react to create a supersaturated solution which then undergoes nucleation either by the formation of nuclei homogeneously across the solution or in specific points. This nuclei growth into crystals which can undergo attrition or breakage and become new growth regions by means of secondary nucleation. Finally, as a consequence of secondary effects, such as aggregation, Ostwald ripening or sedimentation, to yield the lowest energy state, a single crystal.

2.2.7 Ostwald Ripening

Ostwald ripening is part of a chain of physical and chemical processes which comprise the crystallization process. Ostwald ripening is defined as the process by which small crystals undergo dissolution due to their higher solubility whereas the larger bigger ones grows at their expense (Kahlweit (1975)). The driving force for this phenomenon is the minimization of the surface free energy which will eventually finalize when all small particles are dissolved. The gradient in solubility of the crystal as function of their radius is described by the Gibbs-Thomson equation which is as follows.

$$x_s(r) - x_\infty = x_\infty e^{\left(\frac{b}{r}\right)-1} \quad (2.20)$$

where:

$$b = \frac{2\gamma\nu_m}{v_iRT} \quad (2.21)$$

In the expression $x_s(r)$ corresponds to the solubility as a function of the radius (r), x_∞ is the solubility of the compound and b is a set of constants gathering surface tension(γ) molar volume(ν_m), number of dissolution products(u_i), the gas constant (R), and the temperature (T).

It is Interesting for the present study to look at description made by (Kahlweit (1975)) where the kinetics aspect of the Ostwald ripening are described. He assumed the growth rate (R_g) of the crystal to be controlled by diffusion and used Fick's law of mass transport to describe it. The combination of Ficks law with the Gibbs-Thomson equation yields Equation 2.23 which describes the growth rate of a crystal as function of its size and supersaturation.

2.2 Crystallization Theory

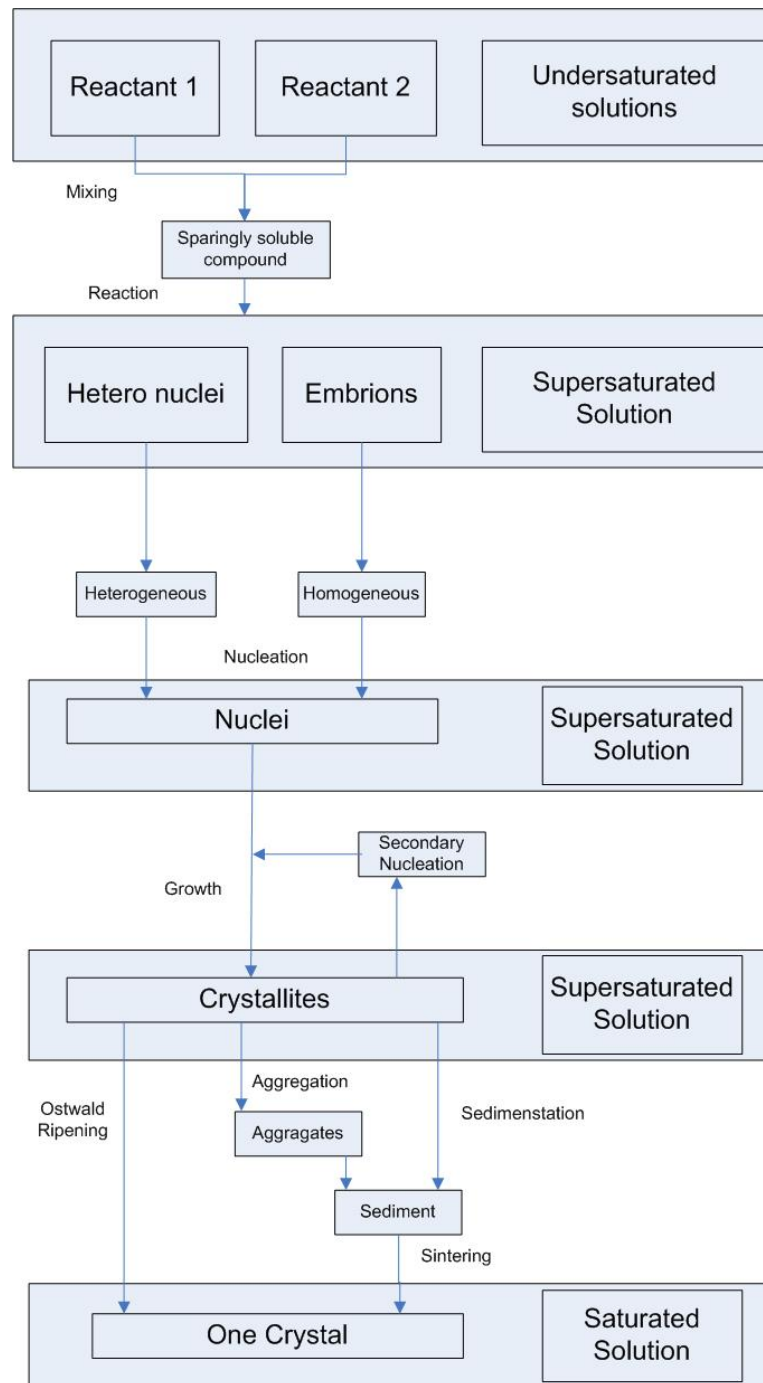


Figure 2.13: Diagram of a precipitation process ((Brecevic & Kralj, 2007)). Reactive crystallization commences with mixing of reactants, supersaturation builds and nucleation commences followed by growth. This may occur by a number of paths such as primary nucleation (homogeneous-heterogeneous) or secondary nucleation. Crystal matter can then undergo aggregation sedimentation or Ostwald ripening. If given enough time one single crystal will be formed.

2.2 Crystallization Theory

$$R_g = \frac{D\nu_m}{\gamma} (\bar{c} - c_s(r)) \quad (2.22)$$

$$R_g = \frac{D\nu_m}{\gamma} \left(\Delta x - x_\infty \frac{b}{r} \right) \quad (2.23)$$

From the theory the concept of critical radius arises. It defines the threshold under which particles dissolve and over which particles grow. The concept is the same as the critical radius of a nuclei described by Gibbs in the classical nucleation theory. Figure 2.14 illustrates this phenomenon together with the growth paths of particles in solution. Notice that r_c increases with solubility and decreases with supersaturation.

$$r_c(t) = \frac{bx_\infty}{\Delta x} \quad (2.24)$$

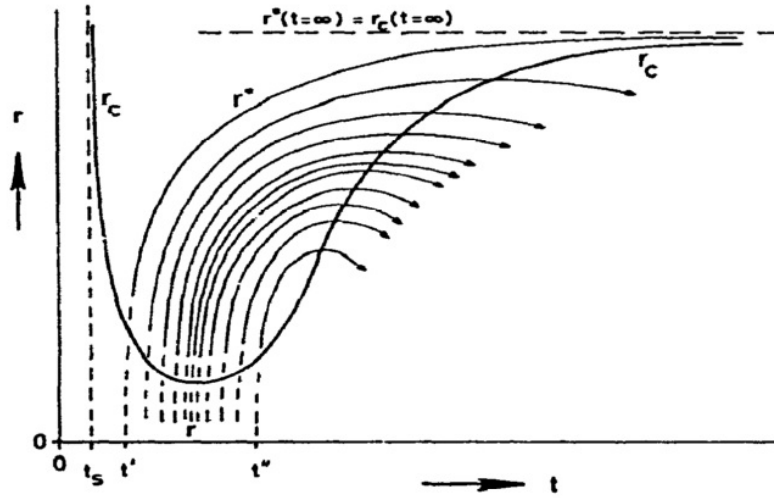


Figure 2.14: Evolution of the crystal sizes as a function of time. Initially, all crystal increases in size under the effect of supersaturation. As it is consumed, smaller particles decrease their growth rate, until they react with the critical size, r_c where they re-dissolves. The largest crystals dissolve last. Only the largest crystals or radius r^* remain at infinite time (Kahlweit, 1975).

2.3 Turbulent Flow and Mixing Kinetics

2.3.1 Introduction

The flow dynamics of precipitation processes are of great importance, especially involving aggregation. For example, at micro-scale level, the flow features will affect the supersaturation distribution hence, nucleation rates and nuclei size. At larger scales, the shear rates distribution defines the aggregation and breakage of solid particles. Therefore, some background is important to explain the observed precipitation phenomena.

In this section, the fundamentals of laminar and turbulent flow will be covered, such as turbulent scales along with a short description of the nature of flow. Then, a description of mixing will be given using the concept of mixing scales. Finally, a description of current micro-mixing models is given.

2.3.2 Laminar and turbulent flows

Fluid dynamic conditions are important in crystallization processes and critical in precipitation since momentum and mass transfer drive the aggregation and mixing phenomena. It will dominate mass and energy transport. Therefore a description of the governing equation is needed. The Navier-Stokes equation (Equation 2.25) describes the velocity field of fluids (Bird *et al.*, 2007). It contains an accumulation terms, a convective term, a pressure terms and a diffusive term.

The solution of the velocity field would be straight forward if it was not for the convective term (second term in the left hand side of Equation 2.25), which is non-linear and causes a strong dependence on initial conditions. At low Reynolds number this term is negligible and the flow is known as laminar. Turbulent flows, on the other hand occur at higher Reynolds numbers when non-linear contributions are important (Badyga & Bourne, 1999).

$$\frac{\partial u_i}{\partial t} + u_j \frac{\partial u_i}{\partial x_j} = -\frac{1}{\rho} \frac{\partial p}{\partial x_i} + \mu \nabla^2 u_i \quad (2.25)$$

Under turbulent flow conditions, the dissipation of energy occurs in the shape of a vortex in opposition to laminar flow where smooth velocity gradients are sufficient to

consume the kinetic energy. Due to the complexity of the flow under turbulent conditions, its theoretical description requires the separation of the phenomena in different scales, called turbulent scales. In the following section a description of these scales will be given.

2.3.3 Turbulent scales

It is important to have in mind that the nature of flows is to dissipate energy. The kinetic energy of the stream decreases due to the friction with the walls and viscous forces within the fluid elements, to finally be dissipated into internal energy by means of viscous forces. The transport of energy from kinetic energy to viscous dissipation occurs at three different scales (macro, meso and micro-scales) each of which has its own characteristic time and spatial scale (Badyga & Pohorecki, 1995).

Figure 2.15 represents the named mixing scales and the phenomena associated with them. A specific description of each of them will be given.

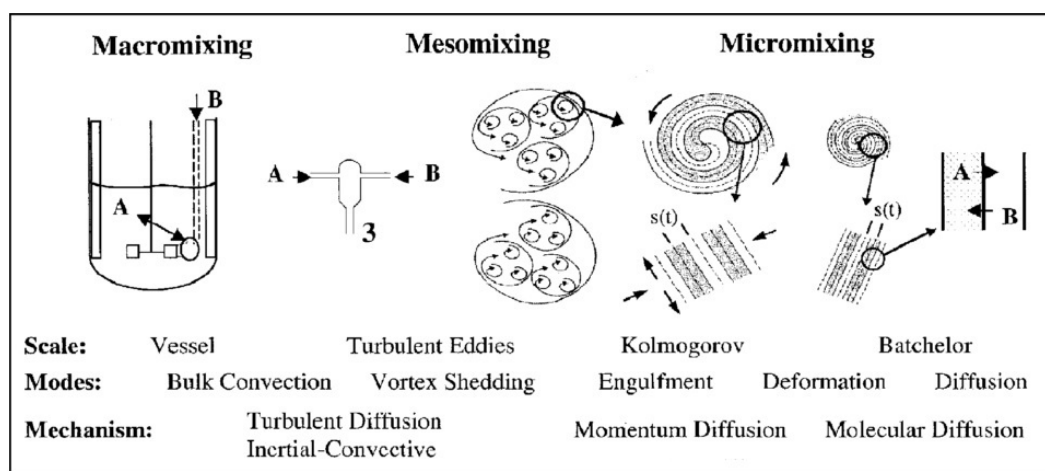


Figure 2.15: Mixing scales in vessels and impinging jets. Macro-scale is of the size of the vessel. Impinging reactors decreases or abolish this scale. Meso-mixing occurs at the size of the turbulent eddies and micro-mixing at the smallest scales, where momentum and molecular diffusion are present (Johnson & Prud'homme, 2003).

Macro-mixing occurs at the largest of the scales. It comprises the transport of energy across the bulk of the mixing volume. For example, the transport of energy from the impeller to the walls in a stirred tank reactor occurs through this mechanism.

2.3 Turbulent Flow and Mixing Kinetics

Under conditions of vigorous agitation in stirred vessels this mechanism is not limiting. Other set-ups working continuously, such as impinging jet reactors and Y-junctions, avoids mass transfer issues by decreasing the macromixing time using equipment of smaller dimensions.

At the **meso-scale** large eddies disintegrate into smaller ones in the so called inertial-convective subrange. Therefore, no diffusive forces occur on this scale but only convective transport is present. Equation 2.26 accounts for the relation between turbulent dissipation rate, ϵ , and characteristic time τ_s . Phenomena associated with this scale is the distribution of residence time in which a fluid element would have a certain probability of spending time in a system depending on the turbulent condition that it experiences. i.e.. intensity of the turbulence, size of the eddies, variation in the velocity fields.

$$\tau_s = \frac{3 L^{\frac{2}{3}}}{4 \epsilon^{\frac{1}{3}}} \quad (2.26)$$

Finally, **micro-scale** energy dissipation occurs at the smallest of the scales where viscous effects finally transform kinetic energy into internal energy. At this scale, the fluid can best be understood as a stack of laminar structures which dissipates energy in the same way as in a laminar flow. This dissipation occurs by means of two transport phenomena at two scales. At the Kolmogorov scale energy is dissipated by convection of the fluid elements in the so called viscous convective sub-range. In other words, internal energy is created by friction between two fluid layers, a consequence of momentum consumption. The Kolmogorov time scale has been approximated as: Badyga & Pohorecki (1995)

$$\tau_k = 17.24 \frac{\nu^{\frac{1}{2}}}{\epsilon} \quad (2.27)$$

The Bachelor scale, on the other hand, dissipates energy by means of diffusion in the molecular scale in the so called viscous diffusive sub-range. Gradients of kinetic energy triggers diffusion of energy between layers of fluid. The time scale of this last scales is defined as:

$$\tau_B = \frac{\eta_B^2}{D_m} \quad (2.28)$$

2.3 Turbulent Flow and Mixing Kinetics

Table 2.2: Mathematical formulations of the time and spatial scales in a turbulent flow shown in Figure 2.15

Turbulent scales			
Scale	Physical scale	Time Scale	Length scale
Macro	Bulk	$\tau_D = \frac{L_0}{D_T}$	L_0
Meso	RTD	$\tau_s = \frac{3}{4} \frac{L^{\frac{3}{2}}}{\epsilon^{\frac{1}{2}}}$	L
Micro(Kolmogorov)	Viscous convective	$\tau_K = 17.24 \left(\frac{\nu}{\epsilon}\right)^{\frac{1}{2}}$	$\eta_K = \left(\frac{\nu^3}{\epsilon}\right)^{\frac{1}{4}}$
Microscale(Batchelor)	Viscous diffusive	$\tau_B = \frac{\eta_B^2}{D_m}$	$\eta_B = \eta_K Sc^{-\frac{1}{2}}$

Table 2.2 summarizes the turbulent ranges, their respective time and length mathematical expressions.

With each scale there is a derived turbulent kinetic energy $E(k)$. Therefore, large eddy wave number k (proportional to the eddy size) contains less energy. The relation between turbulent kinetic energy $E(k)$ and frequency are shown in Figure 2.16. It is observed that smaller eddies contain more energy than larger ones. Based on the studies from Badyga & Pohorecki (1995), the turbulent kinetic energy can be divided into three sub-ranges, inertial-convective, viscous-convective and viscous-diffusive, each of them corresponding to the mesoscale, Kolmogorov and Batchelor scale respectively which have been explained previously.

2.3.4 Mixing kinetics in reactive flows

In reacting flows, momentum transport and diffusion drives mass transfer as expressed by the convective term in Equation 2.29. Similarly to energy transport shown in the previous section, mass is transferred from large scale to small scale to finally end in molecular diffusion. This process is called mixing and occurs in characteristic time scales i.e. macroscale, mesoscale and micro-scale (Badyga & Pohorecki, 1995).

$$\frac{\partial \phi_i}{\partial t} + u_j \frac{\partial \phi_i}{\partial x_j} = D \nabla^2 \phi_i + S_i(\phi) \quad (2.29)$$

The product of reactive precipitation depends on the relative importance of each process: mass transfer, molecular diffusion and reaction (Badyga & Pohorecki, 1995;

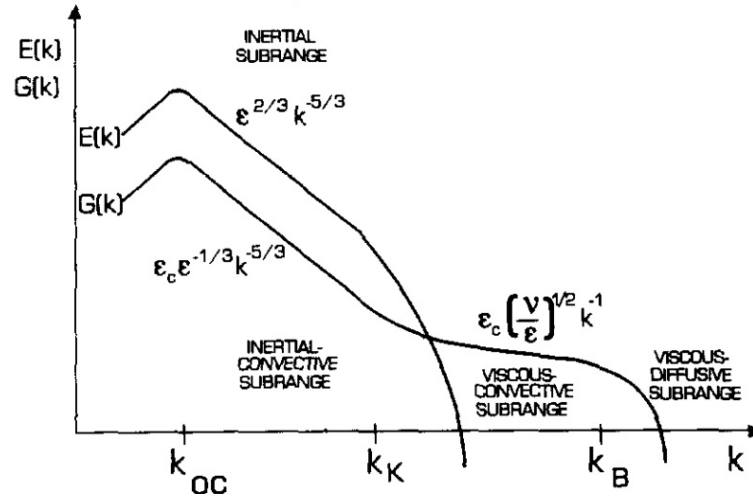


Figure 2.16: Turbulent kinetic energy, $E(k)$, and concentration of fluctuations, $G(k)$ as function of the eddy wavenumber (Badyga & Pohorecki, 1995). Turbulent kinetic energy dissipation can occur in three subranges, inertial-convective, viscous-convective and viscous-diffusive corresponding to the mesoscale, Kolmogorov and Batchelor scale respectively

Villermux, 1994). In processes involving rapid chemical reactions, micromixing time is especially important as is a limiting step. For example, a rapid precipitation with poor micromixing yields an uneven particle size distribution. Polymerization, organic synthesis and competitive reactions are other examples where micromixing is of great importance (Villermux, 1994).

The relative time of micromixing compared with creation kinetics can be estimated using the dimensionless quantities. For example the Damkholer number which is the ratio between micro-mixing time scale and reaction time scale.

$$Da_c = \frac{\text{KolmogorovTimeScale}}{\text{ReactionTimeScale}} = \frac{\tau_k}{\tau_c} \quad (2.30)$$

Large values of Da number represent a diffusion limited mechanism whereas reaction limits the process in the case of low values. Two limiting cases of micromixing can be defined: maximum mixedness and its antagonist complete segregation, depending whether mixing occurs intermediately or is the last step of the process. These models are to be described in Section 2.3.5. Just to say here that maximum mixedness considers

mass exchange between two fluid elements to be instantaneous whereas the complete segregation model excludes mass transfer among the elements of different time age.

2.3.5 Mixing models

Residence time distribution (RTD) functions are widely used in engineering for characterizing reactors of various kinds (Fogler, 2006b).

The method efficiently describes the probability distribution functions, $E(t)$ which describe the fraction of fluid elements that spend a certain time t inside the reactor. Tracer experiments are common methodology to characterize such a property. The so obtained residence time distribution function is sufficient to describe a first order reaction, for example, the decomposition of hydrogen peroxide in water since conversion only depends on concentration of one reactant. A number of models are available for fitting RTD which will be applied in this case, namely, diffusion model and series of reactors. When reaction orders are different than 1 mixing needs be taken into account and a micromixing model is needed. The segregation and complete mixing models described by Villiermaux (1994) are described as two possible extremes between perfect separation and perfect mixing. On the segregation model fluid elements remain unmixed within the reactor for a time corresponding to their $E(t)$ until the moment they react. In order to compute the conversion in the reactor the process would simply consist of summing the contribution to the total conversion of the elements with certain residence time. Equation 2.31 would be applicable in the case of the segregation model.

$$\bar{X} = \int_0^{\infty} x(t)E(t)dt \quad (2.31)$$

The other extreme of micromixing is the complete mixing model. In this model mixing of the elements occurs as soon as they enter the reactor for later spend some residence time in the reactor.

In the case of reactive crystallization, the utilization of micromixing models is desirable since the reaction order does is not equal to one, instead two reactants must be present for reaction to occur. Therefore the utilization of some kind of micromixing model would be preferred. The approach taken in this work does not follow the previous models although their understanding would be of great help.

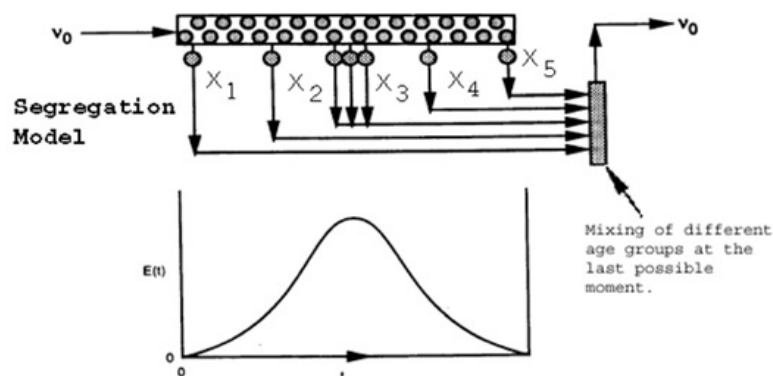


Figure 2.17: Complete segregation model, Fogler (2006b). In this model elements remain unmixed for certain residence time until they leave the reactor.

A number of models have been developed to model the range of situations between these two models. Two representative models are to be mentioned here for their illustrative nature.

Interaction by exchange with the mean model. IEM models shows a partially segregated reactor in which each element exchanged material with the bulk solution which has an average concentration of \bar{c}_1 (Badyga & Pohorecki, 1995; Tavare, 1995). The rate of exchange is given by the micromixing time t_m . They are computationally cheap, simple and versatile as shown by its formulation below:

$$\frac{\partial \bar{c}_i}{\partial t} = \frac{\bar{c}_i - c_i}{\tau_m} + R_i \quad (2.32)$$

IEM neglects the growth in the reaction zone. This is the reason why its results are not accurate Badyga & Pohorecki (1995).

Eddy growth by engulfment (Badyga & Bourne, 1999) In these models the interaction between meso and micromixing scales is resolved. The model for mesomixing scales resolve the mixing of fluid without species. The growth rate of volume of mixed fluid (V_m) is therefore a function of growth rate (E).

$$\frac{\partial V_i}{\partial t} = EV_i(1 - X_i) \quad (2.33)$$

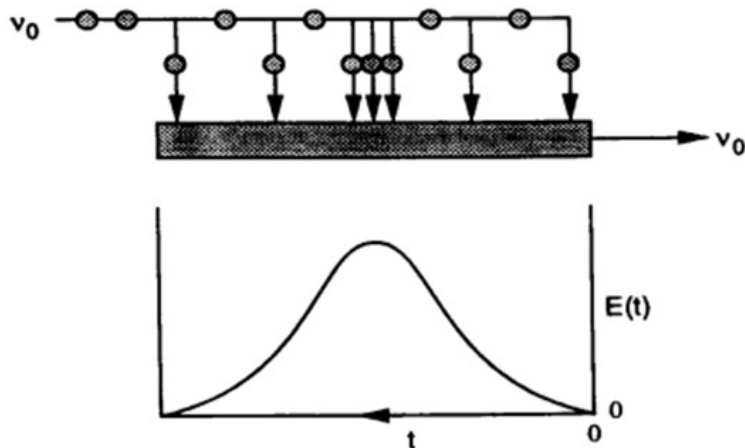


Figure 2.18: Maximum mixedness Fogler (2006b). Elements immediately mix as they enter the reactor to later expend certain residence time

The micromixing scale is resolved assuming four zones in the fluid: pure reactant A (V_A), pure reactant B (V_B), enriched A (V_{mA}) and enriched B (V_{mB}) zones.

$$\frac{\partial c_i}{\partial t} = EV_i(1 - X_i)[\bar{c}_i - c_i] + R_i \quad (2.34)$$

Eddy growth models have been used to fit experimental data and thus obtain the Da number (Gillian & Kirwan, 2008).

Nowadays, advances in computational fluid dynamics allows direct access to detailed analysis an a comprehensive description of the mixing phenomena. Direct numerical simulations are capable of resolving all time scales of turbulence thus avoiding the use of these models. However, they are computational expensive Villermaux (1994). Therefore, the challenge is to incorporate micromixing models or simpler models such as $k - \epsilon$.

2.4 Colloid Stability, Aggregation and Breakage Phenomena

2.4.1 Introduction

Aggregation of colloidal suspensions is a matter of interest for a wide range of scientific and engineering fields, e.g. environmentalists study aggregation which leads to river

2.4 Colloid Stability, Aggregation and Breakage Phenomena

sediments, the oil industry try to avoid it thus preventing pipe blockage, pharmaceutical industries control aggregation to optimize product quality. The variety of study fields has also allowed the variety of terms used to define phenomena very similar in nature. Aggregation and agglomeration are used in the literature as generic terms. On the contrary, flocculation refers to a specific phenomenon in which individual particles are loosely bounded. Repulsive and attractive forces are balanced preventing solid surfaces to contact. The term coalescence refer to the collision of solid particles, bubbles or drops which are then combined to form a single larger entity (Myerson, 2002).

New advances in the last 30 years have increased attention to the problem of aggregation. Computational fluid dynamics, fractal dimension, population balance approach, are major advances leading to the development of this field.

Despite these advantages, aggregation remains a complex problem involving a wide range of disciplines, e.g. colloidal sciences, fluid dynamics or chemistry. This chapter will present the aggregation phenomena starting from the definition of electrical double layer and colloidal stability and then move into the population balance model of aggregation and breakage.

2.4.2 Colloidal stability

Aggregation, similar to nucleation, requires an energy barrier to be overcome in order to reach a more stable state. Whereas for nucleation, it was the work required for the creation of a new surface, in the case of aggregation it is the surface potential between two particles. This section aims to discuss the nature of the forces between particles based on the DLVO theory (Derjaguin & Landau, 1941; Verwey & Overbeek, 1948) and recent amendments (Zhang *et al.*, 2014)

All surfaces present surface potential but it is typically in large surface area systems where the effects are most noticeable. For example, finely dispersed particles smaller than $1\mu m$ suspended in solution are a common example of such a systems. They receive the name of colloidal system and represent a science in itself. Let's review first some concepts.

Electrical double layer charged particles in solution induce a distribution of charges as a result of charge neutralization. Ions of an opposite sign would gather around

2.4 Colloid Stability, Aggregation and Breakage Phenomena

charged particles yielding the so called double layer. Various models have been developed over the years to explain this behaviour. Helmholtz (1853), for example, understood this layer as a simple capacitor with opposite ions attached to the surface, the Gouy-Chapman model interpretation was that ions were placed in a decreasing exponential distribution away from the surface. A combination of these models is given by Stern (1924) who assumed a layer of ions attached to the surface (The Stern or Helmholtz layer) followed by a decreasing exponential distribution.

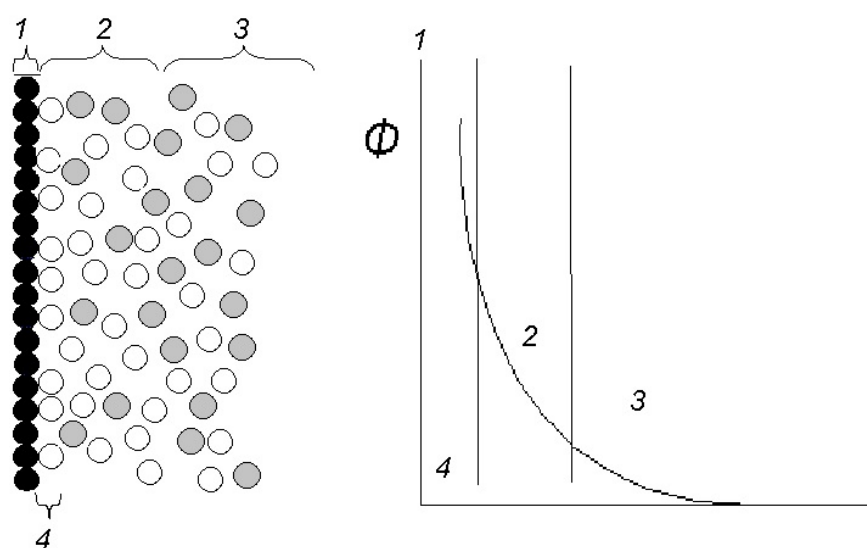


Figure 2.19: Stern model for a charged surface in solution. 1: Charged surface (black circles); 2: Diffuse layer with counter-ions (white circles); 3: Bulk solution; 4: Stern layer.

Refinements carried by Grahame (1947) include a sub-division of the Helmholtz layer, in two new layers, the inner Helmholtz layer would include the solvent molecules accompanying the ions in solution, whereas the outer Helmholtz layer would include the ions in solution. This is the currently accepted theory and is called the Stern-Grahame theory.

Derived from the electrical double layer concept, there are some conclusions arising:

- Firstly, as a consequence of an electrical layer, particles are sensitive to changes in the electromagnetic fields which make them suitable to be analytical techniques such as, electrophoresis or electro-acoustic potential measurements.

2.4 Colloid Stability, Aggregation and Breakage Phenomena

- Secondly, due to the tight binding between the surface and the particles in the Helmholtz layer, the particle surface potential is not accessible experimentally, instead the so called Stern potential is measured.
- Finally, the amount of ions in solution will determine the thickness of the double layer. The surface potential as function of the distance from the particle, $\psi(x)$, is defined by the Poisson-Boltzmann equation which after the Debye-Huckel approximation and terms grouping reads as in Equation 2.35.

$$\psi(x) = \psi_0 \exp(-\kappa x) \quad (2.35)$$

where ψ_0 is the surface potential κ is the Debye-Huckel parameter ($\kappa^2 = (2000F^2I)/(\epsilon_0 \epsilon_r k_b T)$), x is the distance from the surface, F is the Faraday constant, R is the gas constant, T is temperature and I is the ionic strength.

Thus, reduced amounts of ionic species would yield a lower ion density near the surface, and as a consequence the layer would extend further away from the surface. On the other hand, large amount of ions would allow larger densities near the surface and surface potential will decrease sharply as we move away from the particle surface. This idea will be of importance to use in colloidal stability as the thickness of the double layer defines the proximity of other colloidal particles.

Colloidal stability : When two small charged particles approach each other, the electrical double layers overlap and repulsive forces arise from it. The potential between two particles of radius r_i and r_l with Stern potential ψ_{oi} and ψ_{ol} can be derived from the Poisson-Boltzmann equation and reads as follows (Hogg *et al.*, 1966):

$$V_{el} = \frac{\epsilon r_i r_l (\psi_{oi}^2 + \psi_{ol}^2)}{4(r_i + r_l)} \left(\frac{2\psi_{oi}\psi_{ol}}{\psi_{oi}^2 + \psi_{ol}^2} \ln \left[\frac{1 + \exp(-\kappa x)}{1 - \exp(-\kappa x)} \right] + \ln[1 - \exp(-2\kappa x)] \right) \quad (2.36)$$

The force arising between the particles is the repulsive character and decreases exponentially with distance. Compared with other forces it has the longest range of action and hence is the most important.

DLVO theory considers that at short distances, van der Waals forces, created by molecular dipoles, gain greater importance. Hamaker (1937) firstly introduced the concept of London-van der Waals forces into colloidal sciences. The permanent or induced

2.4 Colloid Stability, Aggregation and Breakage Phenomena

dipoles on the electron clouds around molecules, align themselves in the presence of dipoles in neighboring particles. By summing all dipole interactions and taking solvent into consideration he was capable of defining the so called Hamaker constant (A). The potential created by London-van der Waals forces between two particles of different size is defined by the following expression:

$$\frac{V_{vdw}}{kT} = -\frac{A}{6kT} \left(\frac{2r_i r_l}{r^2 - (r_i + r_l)^2} + \frac{2r_i r_l}{r^2 - (r_i r_l)^2} + \ln \left(\frac{r^2 - (r_i + r_l)^2}{r^2 - (r_i r_l)^2} \right) \right) \quad (2.37)$$

The formulation of the DLVO theory contemplates the action of both forces, electrical and van der Waals. The total potential between the particles would be a simple summation of the repulsive and attractive forces. Figure 2.20 shows the evolution of the attractive, repulsive and the resulting forces as a function of the distance between particles. Two possible equilibrium conditions can be observed on the graph. The first one, no always present is a local minimum where particles remain apart from each other in a stable emulsion. The second one is an absolute minimum where at distance close to 0 where the particles irreversibly aggregate. Although DLVO theory has been extended to contemplate other phenomena, such as steric forces, magnetic forces, hydrogen bonding or hydrophobic interaction (Zhang *et al.*, 2014), the theory is still valid and is the basis of many studies in the field of colloid science.

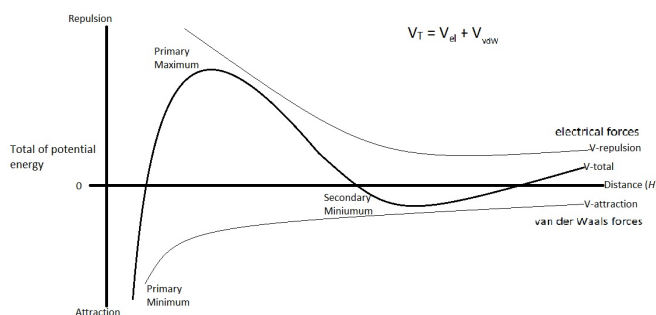


Figure 2.20: Representation of the repulsive and attractive forces between colloidal particles as a function of distance. This is the classical DLVO representation

Among them, steric forces will be briefly commented on as they play an important role in surfactant stabilization. Steric forces arise from the interaction of layers of surfactants or polymers adsorbed on the particle surface (Zhang *et al.*, 2014). Long

2.4 Colloid Stability, Aggregation and Breakage Phenomena

chain molecules tend to adsorb on the surface of colloidal particles. They create layers of 10 to 20 *nm* in thickness. The molecular chains are thermally mobile and can take a number of configurations depending on temperature, concentration or interaction with solvent molecules. The steric interaction occurs when colloidal particles with adsorbed layers approach each other. The compression of the long molecules reduces their possible configurations and hence entropy increases. As a consequence, a steric energy arises between the particles which stabilize the suspension.

In the present study, the DLVO theory will be used to understand the phenomenon of particle aggregation. In the following section the principles of the DLVO theory will be used for:

- evaluating the particle breakage as function of the Hamaker constant and its relative importance against hydrodynamic parameters.
- Explaining the higher colloidal stability showed when surfactants are present.
- Also, the double layer concept will be used when explaining changes in particles fractal dimension.

2.4.3 Aggregation phenomena

The DLVO theory sets the basis of the particles-particle interaction. However, the picture of the aggregation process is not complete without considering the evolution over time. In these terms, thermal motion, sedimentation and hydrodynamic forces must be considered in the context of a time dependent model.

The current aggregation theory is based on Smoluchowski theory of aggregation Smoluchowski (1917). The population balance principle is a convenient way of explaining the aggregation phenomena. In this basic formulation, particle size is discretely divided into a number of ranges, i , to each of which a number, n , is assigned representing the number of particles in that size. In the Smoluchowski theory of aggregation, the number of particles in a certain bin i increases as a consequence of smaller particles aggregating or, oppositely, decreases as particles in bin i aggregate to form larger aggregates. Equation 2.38 represents this phenomena (Smoluchowski, 1917).

2.4 Colloid Stability, Aggregation and Breakage Phenomena

$$\frac{\partial n_i}{\partial t} = \sum_{i+j=k=1}^{k=\infty} K_{k,j}^a n_k n_j - \sum_{j=2}^{\infty} K_{i,j}^a n_i n_j \quad (2.38)$$

Based on this theory, the particle aggregation would be the result of collision between particles which occurs at with frequency ($K_{i,j}$). The two terms on the right hand side of the expression represent the ratio of the particle addition to bin i due to aggregation of the particles in bins k and j and the ratio of particles leaving the bin i due to particle aggregation with particles in bin j . This process would evolve with time as represented by the partial derivative. Notice that this expression by Smolukoski only accounts for aggregation and not for breakage. More terms will be added by following studies. It assumes that all collisions are efficient and that the particles resulting from aggregation fall into one of the preexisting bins.

Smoluchowski suggests a mathematical expression for the collision frequency of three phenomena, thermal movement, flow hydrodynamics and sedimentation. The total amount of collision would be the sum of the three frequencies, although some assumption can be made in neglecting one or two of them. Those are to be explained later in this section. Let's begin with thermal motion. Small particles in suspension undergo Brownian as a motion consequence of the random movement of solute particles. Its movement increases with temperature which increases the chances of collision. It is named perikinetic aggregation and is described by Equation 2.39 where k_B is the Boltzmann constant, μ is the viscosity of the fluid, T is the temperature, $R_{c,i}$ and $R_{c,j}$ are the radius of the two colliding particles.

$$K_{i,j,pk} = \left(\frac{2k_B T}{3\mu} \right) \frac{(R_{c,i} + R_{c,j})^2}{R_{c,i} R_{c,j}} \quad (2.39)$$

Orthokinetic aggregation, on the other hand, names the phenomena in which hydrodynamic forces influence the aggregation frequency. In the following expression, the flow features are summarized by the shear rate, $\dot{\gamma}$.

$$K_{i,j,ok} = \frac{4}{3} \dot{\gamma} (R_{c,i} + R_{c,j})^3 \quad (2.40)$$

The studies of Smoluchowski were the first step in much of the development of aggregation models. Extension of these models was followed by Camp & Stein (1943) who

2.4 Colloid Stability, Aggregation and Breakage Phenomena

extended the concept to sedimentation phenomena in which the differential velocities of sedimenting particles drive particle collision. Equation 2.41 models the phenomena

$$K_{i,j, sed} = \frac{g\pi}{72\mu}(\rho_p - \rho_l)(R_{c,i} + R_{c,j})^3 |R_{c,i} - R_{c,j}| \quad (2.41)$$

Further advances and assumptions have been applied to Smoluchowskis model and therefore extended to a larger range of applications. In the simple case of mono-dispersed particles coalescing in laminar flow, Equation 2.38 can be simplified to the Gregory model (Gregory, 1981) a simple exponential expression which relates the number of particles to the time spent in a laminar flow. The model has been criticized but remains useful for engineers. The product $\phi\alpha_{eff}\dot{\gamma}$ (Solid mass fraction, collision efficiency and shear rate) is the so called Camps number (Ca) which is used as a design parameter in flocculation tanks (Ahmed, 1995).

$$N(t) = N_0 e^{-\frac{4}{3}\phi\alpha_{eff}\dot{\gamma}t} \quad (2.42)$$

where $N(t)$ stands for the number of particles as a function of time, N_0 for the initial number of particles, $\dot{\gamma}$ for the shear rate, ϕ for the volume particle concentration ($\phi = 4/3\pi R^3 N$) and t for the residence time and α_{eff} stands for the collision efficiency. This expression assumes that velocity gradients also cause particles to collide and hence produces aggregation.

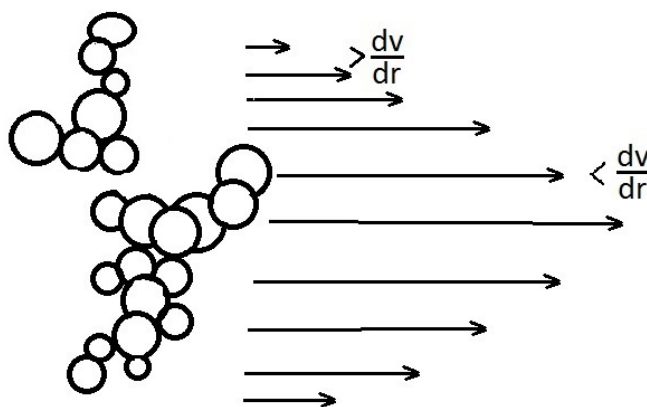


Figure 2.21: Schematic of Orthokinetic aggregation. Velocity gradients enhances changes in particle collision

2.4 Colloid Stability, Aggregation and Breakage Phenomena

In order for a collision to be efficient and produce aggregation, certain conditions must be met, i.e. the approaching velocity between the particles must be sufficient to overcome the repulsive forces of the double layer. Also, the particle bonding forces must be sufficient to resist the collision and the repulsive forces as described by the DLVO theory. Since not all collisions meet the requirements for yielding aggregation, a ratio between effective collision and total collisions can be defined by the so called collision efficiency. As a first attempt to quantify this parameter, van de Ven & Mason (1977) formulated that for completely unstabilized solution (Neutral surface potential), the collision efficiency would depend on the flow number (Fl), represented as the ratio between the Hamaker constant (H) and the flow forces depending on $\dot{\gamma}$. The value of aggregation efficiency α reads as in Equation 2.43:

$$\alpha_{eff} = k_{\alpha}(Fl)^{-0.18} \quad (2.43)$$

where k_{α} is a factor which takes the value of 0.79, 0.87 and 0.95 for particles of radius 2,1 and 0.5 μm respectively and Fl is the flow number:

$$Fl = \frac{H}{6\pi\mu\langle\dot{\gamma}\rangle R_p^3} \quad (2.44)$$

A number of predictions regarding the behaviour of the process can be drawn based on this model. This equation predicts a decrease in aggregation efficiency with increasing shear which means that large flow forces are capable of reducing aggregation kinetics. Since the Hamaker constant is a function of material and solvent, those can be altered in order to change particle stability. Finally, it is observed that collision efficiency increases with decreasing particle size.

Although this formulation is very convenient for easily assessing the aggregation efficiency, it neglects the effect of the electrical double layer. As shown by the DLVO theory, the electrical double layer accounts for the repulsive forces between particles. van de Ven & Mason (1977) introduced information about the importance of this factor. The work suggested the use of a dimensionless ratio between the surface forces and the flow forces as shown in Equation 2.45:

$$C_R = \frac{2\epsilon_r\epsilon_0\psi_0^2}{3\nu\dot{\gamma}R_p^2} \quad (2.45)$$

2.4 Colloid Stability, Aggregation and Breakage Phenomena

where ϵ_r is the dielectric constant of the medium, ϵ_0 is the relative permeability of the vacuum, ψ_o is the surface potential of the particle, ν is the kinematic viscosity, $\dot{\gamma}$ is the shear rate and R_p is the particle radius.

Other more elaborate expression were introduced by Valioulis & List (1984) which directly relates the collision efficiency ($\alpha_{eff,i,j}$) with particle-particle potentials (V_a) considered in the DLVO theory. The expression reads as follows:

$$\alpha_{eff,i,j} = \left(\left(1 + \frac{r_l}{r_i} \right) \int_{1+\frac{r_l}{r_i}}^{\infty} \left(\frac{D_{\infty}}{D_{i,j}} \right) \exp \left(\frac{V_a}{kT} \right) \frac{ds}{s^2} \right)^{-1} \quad (2.46)$$

In this expression, V_a stands for the summation of the repulsive and attractive potentials, van der Waals and electrical ($V_a = V_{vdw} + V_{el}$) which can be read in Equations 2.37 and 2.36. $D_{i,j}$ is the relative diffusion coefficient and D_{∞} is the limiting diffusion coefficient.

Breakage so far, the process of aggregation has been described as a function of the forces interacting between particles, i.e. surface forces, electrical, thermal, hydrodynamic and sedimentation. However these forces not only yield aggregation, they can also produce particle breakage. This phenomenon consists of the fragmentation or loss of particles from a bigger aggregate to yield smaller particles due to external forces acting over the aggregate. Breakage phenomena was latter introduced in the formulation of the aggregation model as two new terms birth and death. Similar to aggregation, birth and dead terms in Equation 2.38, the breakage birth and death terms represent the addition of particles to a bin caused by fragmentation of larger particles and the loss of particles from a bin as a consequence of the their breakage. This phenomena can be represented mathematically as in Equation 2.47 which defines a purely breakage phenomena (Lasheras *et al.*, 2002; Pandya & Spielman, 1983).

$$\frac{\partial n_k}{\partial t} = \sum_{m=k+1}^{\infty} K_m^b n_m(t) \Gamma_{m,k}^b - K_m^b n_k(t) \quad (2.47)$$

K^b is the breakage kernel, or breakage frequency. Various models of the breakage kernel are be covered below. Γ^b is the daughter particle distribution after breakage which would be different for different breakage mechanisms. Jones *et al.* (1996) reminds regarding the two breakage mechanisms suggested in the literature. Those are surface

2.4 Colloid Stability, Aggregation and Breakage Phenomena

erosion and particle splitting which can occur by particle-particle interaction or by particle-fluid.

Various models exist for the modelling of breakage kernels which can be classified as empirical and semi-empirical. Both have been successfully implemented in population balance models. Empirical models consist of a combination of the power laws containing shear rate $\dot{\gamma}$ and aggregate size (R_{ci}). Works in this vein are Pandya & Spielman (1983); Serra & Casamitjana (1998); Soos *et al.* (2007). A general expression for this kind of model can be found in Soos *et al.* (2007).

$$K_i^b = P_3 \dot{\gamma}^{P_1} \left(\frac{R_{ci}}{R_{cp}} \right)^{P_2} \quad (2.48)$$

Semi-empirical models of aggregation consist of a mathematical formulation based on physical principles which contain optimizable parameters, in the case above case, P_1 , P_2 and P_3 . The model developed by K.A. Kusters (1991) is used widely in the formulation of population balance models and considers breakage depending on the turbulent kinetic energy dissipation rate, ϵ . Therefore, this model is more suitable for turbulent conditions. The mathematical expression read as in Equation 2.49:

$$K_i^b = \left(\frac{4}{15\pi} \right)^{\frac{1}{2}} \left(\frac{\epsilon}{\nu} \right)^{\frac{1}{2}} \exp \left(\frac{-\epsilon_{bi}}{\epsilon} \right) \quad (2.49)$$

This expression assumes that aggregates are more likely to break under a certain critical turbulent dissipation energy ϵ_{bi} . Tambo & Watanabe (1979) observed that experimental ϵ_{bi} was inherently proportional to the aggregate size (R_{ci}) ($\epsilon_{bi} = B/R_{ci}$) which implies that the amount of energy required for breaking larger aggregates is lower when compared with smaller ones. If the reader is interested in further coverage of this and other breakage models please refer to Patruno *et al.* (2009). Under turbulent condition the value of $\dot{\gamma}$ can be derived from Equation 3.5.

??

$$\dot{\gamma} = \sqrt{\frac{\epsilon}{\mu}} \quad (2.50)$$

In this study we contemplate a different interpretation of the breakage phenomena. Serra & Casamitjana (1998) discussed the idea that the size is related to the size of the Kolmogorov eddies. Based on this description and the turbulent flow given in Section 2.3.2 the velocity fields consist of eddies which create areas of high vorticity

2.4 Colloid Stability, Aggregation and Breakage Phenomena

and low strain as well as other areas of low vorticity and high strain. It is believed that particles are likely to aggregate in the first ones and would break in the second ones. The size and energy of the vortex would determine the final size and the frequency of the breakage phenomena.

Restructuring internal restructuring of aggregates has been studied only recently in the literature.(Chakraborti *et al.*, 2003; Flesch *et al.*, 1999; Rahimi & Solaimany Nazar, 2010; Selomulya *et al.*, 2003). This property accounts for the structural changes that an aggregate undergoes. It occurs for a number of reasons such as external forces, change in the medium chemistry, frequency of particle attachment or Oswald ripening. In order to measure changes in structure, the variable fractal dimension, described in Section 2.7.1, has been preferred by scientists since it is easy to measure as well as simple to implement in aggregation models. Lin *et al.* (1990) suggests two modes of particle restructuring in a shear field. It is argued that the loss of more exposed branches of the aggregates led to higher fractal dimension aggregates. Alternatively, the exposed branches may bend towards the aggregate core also increasing fractal dimension.

Universality in colloidal aggregation. although different aggregation products vary hugely in structure or size depending on physical properties, aggregation regimen, surface forces. etc. there is some universality in the aggregation process. The shape of the aggregate created under a diffusive regime, for example, changes as a function of the frequency of attachment.

Following the studies by Meakin, (Meakin & Family, 1988), there are two different aggregation mechanism base on the relative importance of diffusion of new particles towards the surface of the aggregate or the attachment of those particles. In the case diffusion is the limiting phenomena the process will be called diffusion limited aggregation (DLA) whereas in the case of attachment controlling the aggregation, the process will called reaction limited aggregation (RLA). Let us set clear that reaction in the context of aggregation does not refer to a chemical transformation, instead, it refers to the process of particles attachment.

Based on Meakin & Family (1988) there are similarities in the shape of the aggregates produced by the same mechanism whatever the material. In their studies they shows high value of fractal dimension, around 2.1 for reaction limited mechanism

2.5 Aggregation in Turbulent Flows

(RLA) whereas lower values around 1.7 were found when aggregation was limited by diffusion of particles to the surface of the aggregate (diffusion limited). This was found to be true for gold, silica and polystyrene particles.

Based on Aubert & Cannell (1986) results there seems to be an equilibrium stage which fractal structures moves towards, regardless of the path followed for its formation. He observed that when left undisturbed, colloidal silica aggregates created by reaction limited mechanism restructures towards structures belonging to the diffusion limited mechanism.

Traditionally, aggregation has been studied in Taylor-Couette cells Serra *et al.* (1997) or batch reactors Kusters (1991). This work explored aggregation in tubular reactors in laminar and turbulent conditions.

Peclet Number in the case of particles sufficiently small, shear forces would not be sufficient to yield aggregation as thermal motion predominates over the shear forces. The Peclet number is a dimensionless number computed from the ratio between flow and thermal forces. It is used to define molecular diffusion as well as being a criteria for colloidal stability. Its formulation reads as follows:

$$Pe = \frac{FlowForces}{ThermalForces} = \frac{6\pi\nu\dot{\gamma}r_p^3}{k_B T} \quad (2.51)$$

2.5 Aggregation in Turbulent Flows

In turbulent flow, the interaction of vortexes with particles produces a number of interactions. Although the properties of the product may vary, such as morphology or fractal dimension, they are all ruled by a balance between particle inertial forces and scale of the turbulence. For example, low density small particles easily follows stream lines, even if vortex are small. They behave as ghost particles. In the opposite extreme, large dense particles do not interact with small, low energy eddies and behave like bullets following the average flow direction. A middle ground case is illustrated in Figure 2.22 where the scale of vortex is sufficient to affect the particles but not enough to make them follow the stream lines. Under these circumstances particles would accumulate in areas of low vorticity (away from eddies) and high strain (high shear areas) Eaton & Fessler (1994).

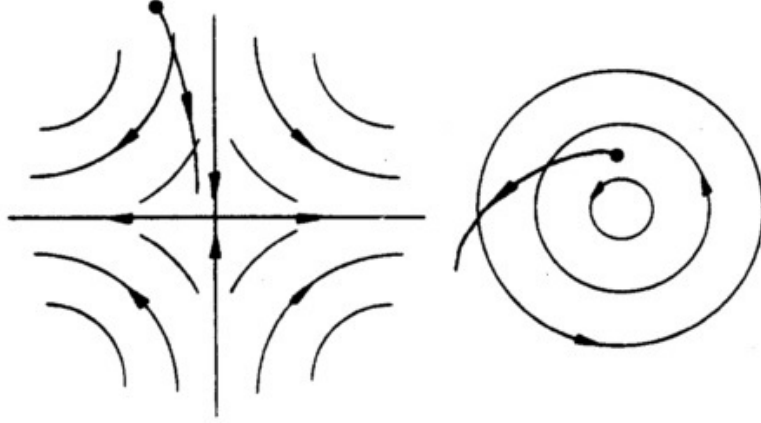


Figure 2.22: Representation of a high strain and low vorticity zone where particles accumulate and a low strain and high vorticity zone is depleted of particles. Eaton & Fessler (1994)

The Stokes number is a dimensionless quantity which evaluates the characteristic time of the particle τ_p against the characteristic time of the flow τ_k and is defined as follows:

$$St = \frac{\tau_p}{\tau_k} = \frac{2\rho_p}{9\rho_l} \left(\frac{r_p}{\lambda_k} \right)^2 \quad (2.52)$$

where ρ_p is the particles density, ρ_f the fluid density, r_p the particle radius and λ_k is the Kolmogorov length scale as computed from Equation 2.27. For low Stokes ($St \ll 1$) number ghost like particles are found. Large, on the other hand, Stokes number ($St \gg 1$) characterize bullet like particles and around $St = 1$ phenomena like clustering or preferential concentrations occurs (Goto & Vassilicos, 2006).

Clustering of particles at Stokes number close to unity is a phenomenon which should not be left unmentioned (Eaton & Fessler, 1994). The name refers to the fact that particles accumulate in certain zones of the flow as a consequence of flow features, such as vortex or high strain zones. Clustering does not necessarily imply aggregation, but allows zones of higher concentration where aggregation is more likely to occur and low strain (vortex) where aggregates remain stable.

Further computational studies on collision efficiency found that Stokes number, among other dimensionless numbers such as the flow number, correlated the collision efficiency in turbulent flow (Balakin *et al.*, 2012).

2.5 Aggregation in Turbulent Flows

Experimental studies on aggregation in turbulent flow have been carried out traditionally in Taylor-Couette cells (Oles, 1992; Serra *et al.*, 1997; Soos *et al.*, 2007) where turbulent conditions are homogeneous and well described mathematically. The material normally consisted of latex particles, colloidal silica or polystyrene. Serra *et al.* (1997) found larger aggregation rates as shear increases with smaller steady state particle size. The research also found that for larger shear stress particle size decreases whereas exponentially it increases when shear is small. This indicates a critical concentration at which the behaviour of the suspension completely changes. Oles (1992) found similar aggregation behaviour in a system of mono-disperse polystyrene latex particles. In order to destabilize the system and favor aggregation a highly electrolyzed aqueous solution was chosen as continuous media. The results of the dimensionless particle size vs dimensionless time can be seen in Figure 2.23. This study revealed that high shear rates yields fast aggregation and small equilibrium particle size. It is assumed that the equilibrium stage is caused by stable equilibrium between aggregation and breakage.

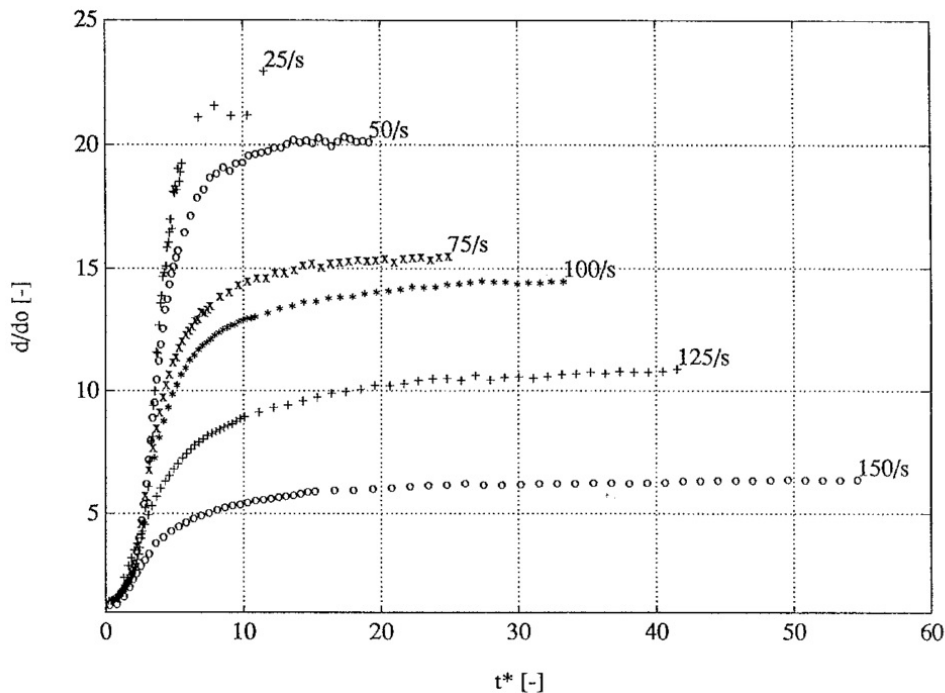


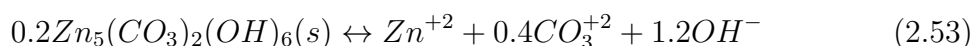
Figure 2.23: Evolution of dimensionless particle size with the dimensionless number of collisions in the system ($t^* = t\dot{\gamma}\phi$) polystyrene latex-water. Smaller equilibrium size was found with increasing shear (Oles, 1992).

2.6 Literature Review of Zinc Carbonate Hydroxide.

2.6.1 Introduction, properties and applications

Hydrozincite is found in nature (Alwan & Williams, 1979) but can also be artificially synthesized. It is referred to in the literature with by various other names such as zinc carbonate hydroxide, zinc hydroxide carbonate co-crystal or zinc layered compound. They respond to the chemical formula $Zn_5(CO_3)_2(OH)_6$.

A summary of the physical, and chemical features of hydrozincite will be given in this section. Its carbonated structure gives the material similar chemical properties to others in the same family, such as calcite or magnesite. Those can be listed as: low hardness (2-2.5 in Moh's scale), medium density (around $3500kg/m^3$), low solubility, and white in colour. For its low solubility, hydrozincite, is classified as a sparingly soluble compound (Clever *et al.*, 1985) which is interesting as it increases its bio-compatibility and slows its dissolution kinetics. It is different in specific gravity with respect to water yielding unstable suspensions and high precipitation rates. The solubility product has been measured by Schindler *et al.* (1969) as $10^{-14.01}$ based on the following solubility equilibrium:



The hydrozincite double layer structure, further described in Section 2.6.4, gives the material adsorbent properties. For example, is been observed that foreign molecules incorporate within the double layer structure in substitution to carbonate ions. Studies in this area comprises the ones from Lee *et al.* (2010); Miao *et al.* (2006) and Sun (2016) with surfactants and of Hasan *et al.* (2012) with active pharmaceutical compound API. They conclude that these structures can be used to control solubility and hence to tune bio-availability.

As a consequence of the small particle size after precipitation, hydrozincite's surface area is relatively large, around the $50m^2/g$ (Turianicova *et al.*, 2016). Therefore, it makes an excellent material for filtering small size molecules such as SO_2 and HCN gases (Abler & Company), 1995). It is used in hospital respirators.

2.6 Literature Review of Zinc Carbonate Hydroxide.

In cosmetic applications, it is added to shampoo for improving the efficiency of zinc based anti-dandruff formulations such as zinc pyrithione (Cardin *et al.*, 1992). Its efficiency is believed to be dependent on its solubility (Schwartz & Johnson, 2004). This is, in fact, the motivation of this work, as solubility is controlled by particle size and crystallinity.

Hydrozincite is also a precursor of ZnO which has applications in photocatalysis, chemical sensors, gas sensors, biosensors, solar cells, electrochemical cells and varistors. By calcination of hydrozincite at above 600 °C, the carbonate ions are lost and a structure of ZnO is left as residue.

2.6.2 Synthesis methods for the production of hydrozincite

Reactive crystallization is the main route for its production in laboratory and industrial scale and which can be classified in two methods. On one hand, the hydrothermal method utilizes urea ($(NH_3)_2CO_3$) as a source of carbonate in conjunction with other zinc salt (acetate (Hu *et al.*, 2010), nitrate (Musić *et al.*, 2002) or sulphate (Wang *et al.*, 2012)). The advantage of this method is that it is heat transfer controlled and hence allows certain control over reaction. Thanks to the property of urea to decompose into carbonate at high temperatures, this material can be used to switch mass transfer limitation into heat transfer problems. Although the yields are inferior to other methods, the potential for increasing crystallinity is higher. On the other hand, direct precipitation from solution consists of a zinc salt and carbonate salt, normally sodium carbonate (Bems *et al.*, 2003; Shamsipur *et al.*, 2013a) but also sodium bicarbonate (Fujita *et al.*, 1995), ammonium carbonate (Chen *et al.*, 2011) or potassium bicarbonate (Zhang *et al.*, 2004a). Since carbonate is available initially from solution, mixing is the limiting step in this kind of set-up. Consequently, the variety of experimental apparatus is larger than in hydrothermal methods, i.e. impinging jets (Kickelbick *et al.*, 2012), microfluidic reactors and micro-emulsions.

Among the methods listed above, a direct precipitation method in a continuous Y-junction reactor has been chosen for the purpose of this study. Its geometry allows well mixing conditions as well as an easy construction and maintenance which make it a good candidate for continuous applications when compared with impinging jets or

2.6 Literature Review of Zinc Carbonate Hydroxide.

microfluidic devices. Regarding the reactants, zinc nitrate and sodium carbonate have been chosen as they are widely used in the literature.

Other non-conventional methods for hydrozincite preparation are: CO_2 bubbling, microemulsions or synthesis from ZnO in CO_2 atmosphere etc. A summary of the literature found in hydrozincite synthesis is given in Table 2.3.

2.6.3 Speciation of zinc in solution

Speciation of zinc species in solution, such as zinc hydroxide or zinc carbonate, defines the solubility product and hence the supersaturation. Therefore the definition of species in solution is paramount. The equilibrium water-carbonate-zinc has been studied using individual solubility products for each of the species. Similar to other authors, such as Grauer & Feitknecht (1967); Schindler *et al.* (1969); Zirino & Yamamoto (1972), this work utilizes solubility product to compute species in solution. The final speciation diagram, computed in Section 4.2.3, will serve the purpose of understanding the solubility data.

The method here, ideal species contribution (ISC) computes the concentration of soluble species in solution based on solubility data from the literature. Solubility product and equilibrium equations are listed in Table 2.5. Firstly, a range of pH was chosen arbitrarily and its corresponding OH^- and H_3O^+ concentration computed. Secondly, the concentration of carbonate and bicarbonate was worked out based on equilibriums k_7 and k_8 . Then dissolved zinc ions can be easily determined using equilibriums k_5 and k_6 . Finally soluble zinc species are extracted from equilibrium k_1 , k_2 , k_3 and k_4 .

Once the speciation of hydrozincite is been described, the supersaturation of hydrozincite in water can be defined. Supersaturation, ss , is defined in its thermodynamic form as the ratio between species in solution and the solubility product (see Section 2.2.2). Therefore the final expression would read as:

$$ss = \frac{[CO_3^{-2}]^{0.4}[Zn^{+2}][OH^-]^{1.2}}{K_{sp}} \quad (2.54)$$

However other forms to express supersaturation were available, this expression was chosen as it was derived from the equilibrium equation of hydrozincite Equation 4.2.3. The expression of supersaturation of these terms allows the use of the solubility product

2.6 Literature Review of Zinc Carbonate Hydroxide.

Table 2.3: Literature review of the synthesis method of hydrozincite classified by their operation modes and reactants used.

Hydrozincite synthesis methods			
Method	Operation	Features	References
Precipitation	Semibatch	$Zn(NO_3)_2$ and Na_2CO_3 $Zn(NO_3)_2$ and $NaHCO_3$ $ZnCl_2$ and K_2CO_3 $Zn(NO_3)_2$ and $(NH_4)_2CO_3$ Counter Ions	Shamsipur <i>et al.</i> (2013b) Fujita <i>et al.</i> (1995) Zhang <i>et al.</i> (2004b) Li <i>et al.</i> (2005) Chen <i>et al.</i> (2008) Pudukudy & Yaakob (2014)
	Continous	Impinging Jets Spray drying Spray drying	Kickelbick <i>et al.</i> (2012) Kaluza <i>et al.</i> (2008) Wang & Muhammed (1999)
Hydrothermal	Semibatch	$ZnCl_2$ Microwave $Zn(NO_3)_2$ pH effect $Zn(O_2CCH_3)_2$ Paramerts $Zn(O_2CCH_3)_2$ $Zn(NO_3)_2$ $Zn(NO_3)_2$ $Zn(O_2CCH_3)_2$ aditives	Tseng <i>et al.</i> (2012) Wu <i>et al.</i> (2011) Hu <i>et al.</i> (2010) Li <i>et al.</i> (2010) Kakiuchi <i>et al.</i> (2008) Liu <i>et al.</i> (2007) Wu <i>et al.</i> (2006) Bitenc <i>et al.</i> (2008)
	Continous	Microfluidics Flow injection analysis	Li <i>et al.</i> (2011) Bitenc <i>et al.</i> (2008)
Microemulsion	Batch	$Zn(NO_3)_2$ and $NaHCO_3$ $Zn(NO_3)_2$ and $(NH_4)_2CO_3$	Alhawi <i>et al.</i> (2015) Sarkar & Khilar (2009)
Electrochemical	Batch	Surfactants	Pourmortazavi <i>et al.</i> (2015) Picca <i>et al.</i> (2017)
Solid-gel		$Zn(SO_4)$ and $(NH_4)_2CO_3$	Wu & Jiang (2006)
ZnO Conversion	Mill	ZnO , H_2O and CO_2	Turianicova <i>et al.</i> (2016)

2.6 Literature Review of Zinc Carbonate Hydroxide.

Table 2.4: Summary of alternative expressions for the definition of supersaturation. They are based on the work of Schindler *et al.* (1969)

Turbulent scales		
Equilibrium equation	Supersaturation expression	Solubility constant
$0.2Zn_5(CO_3)_2(OH)_6(s) \leftrightarrow$ $Zn^{+2}(l) + 0.4CO_3^{+2}(l) + 1.2OH^-(l)$	$ss_1 = \frac{[Zn^{+2}][CO_3^{-2}]^{0.4}[OH^-]^{1.2}}{K_{sp1}}$	$K_{sp1} = -14.01$
$0.2Zn_5(CO_3)_2(OH)_6(s) + 0.8H_2O(l) \leftrightarrow$ $Zn^{+2}(l) + 1.6CO_2(g) + 2HCO_3^-(l)$	$ss_2 = \frac{[Zn^{+2}][HCO_3^-]^2 P_{CO_2}^{1.6}}{K_{sp2}}$	$K_{sp2} = -6.43$
$0.2Zn_5(CO_3)_2(OH)_6(s) + 2H^+ \leftrightarrow$ $Zn^{+2}(l) + 0.4CO_3^{+2}(l) + 1.6OH_2O(l)$	$ss_3 = \frac{[Zn^{+2}][CO_3^{-2}]^{0.4}[OH^-]^{1.2}}{K_{sp3}}$	$K_{sp3} = 9.199$

K_{sp} as obtained from literature (Schindler *et al.*, 1969). The expression of the supersaturation in its differential form was not convenient in this case as the contribution of all species would not have been taken into account. Alternatively, other forms of the equilibrium equation could have been used instead of Equation 4.2.3. However, the value of the solubility products was defined as a function of bicarbonate concentration which is unavailable from experimental data or process conditions. Table 2.4 shows alternatives expressions for supersaturation.

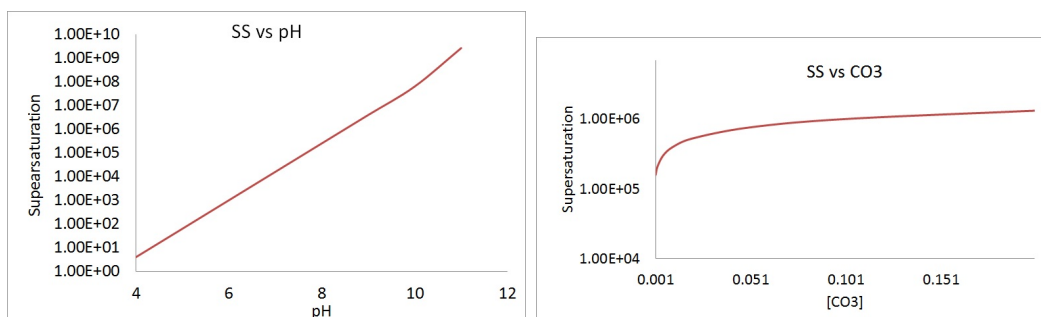
Figures 2.24(a) and 2.24(b) show the dependence of the supersaturation variable from pH and carbonate concentration. Carbonate importance seems to decrease with increasing concentration as its asymptotic behaviour demonstrates. However, pH seems to be important throughout the whole range. The supersaturation dramatically increased in order of magnitude with pH. The logarithmic character of this variable is the cause of such behaviour. The importance of pH on the supersaturation will become obvious in the characterization of the induction time.

2.6 Literature Review of Zinc Carbonate Hydroxide.

Table 2.5: Equilibrium equation of the species involved in the equilibrium of hydrozincite with water

Zn-OH-CO ₃ equilibrium			
Equilibrium	Solubility product	K_{sp}	Reference
$ZnOH^+ \leftrightarrow$ $\leftrightarrow Zn^{+2} + OH^-$	$k_1 = \frac{[Zn^{+2}][OH^-]}{[ZnOH^+]}$	-4.4	Zirino & Yamamoto (1972)
$Zn(OH)_2^0 \leftrightarrow$ $\leftrightarrow ZnOH^+ + OH^-$	$k_2 = \frac{[ZnOH^+][OH^-]}{[Zn(OH)_2^0]}$	-8.49	Zirino & Yamamoto (1972)
$Zn(OH)_3^{-1} \leftrightarrow$ $\leftrightarrow Zn(OH)_2^0 + OH^-$	$k_3 = \frac{[Zn(OH)_2^0][OH^-]}{[Zn(OH)_3^{-1}]}$	-1.11	Zirino & Yamamoto (1972)
$Zn(OH)_4^{-2} \leftrightarrow$ $\leftrightarrow Zn(OH)_3^{-1} + OH^-$	$k_4 = \frac{[Zn(OH)_3^{-1}][OH^-]}{[Zn(OH)_4^{-2}]}$	-1	Zirino & Yamamoto (1972)
$ZnCO_3(s) \leftrightarrow Zn^{+2} + CO_3^{+2}$	$k_5 = [Zn^{+2}][CO_3^{+2}]$	-10.26	Reinert (1965)
$0.2Zn_5(CO_3)_2(OH)_6(s) \leftrightarrow$ $Zn^{+2} + 0.4CO_3^{+2} + 1.2OH^-$	$k_6 =$ $[Zn^{+2}][CO_3^{+2}]^{0.4}[OH^-]^{1.2}$	-14.01	Schindler <i>et al.</i> (1969)
$H_3O^+ + HCO_3^- \leftrightarrow$ $\leftrightarrow H_2CO_3 + H_2O$	$k_7 = \frac{[H_2CO_3]}{[H_3O^+][HCO_3^-]}$	6.352	Zirino & Yamamoto (1972)
$H_3O^+ + CO_3^{2-} \leftrightarrow$ $\leftrightarrow HCO_3^- + H_2O$	$k_8 = \frac{[HCO_3^-]}{[H_3O^+][CO_3^{2-}]}$	10.33	Zirino & Yamamoto (1972)
$2H_2O \leftrightarrow H_3O^+ + OH^-$	$k_W = [H_3O^+][OH^-]$	14	-

2.6 Literature Review of Zinc Carbonate Hydroxide.



(a) The graphic shows the supersaturation dependence from pH. An exponential increase of this variable is observable. Zinc and carbonate concentration set to 0.05M and 0.1M respectively.

(b) The graphs shows the supersaturation dependence on carbonate concentration. The influence is limited to the low concentration of carbonates. Zinc and pH values were set to 0.2 and 8pH respectively.

Figure 2.24: Dependence of supersaturation from the variables pH and Carbonate concentration.

2.6.4 Solid phases and hydrozincite crystal structure

The system Zn-CO₃-H₂O has been reported to have three thermodynamic stable solid forms. Smithsonite, Hydrozincite and Zincite. Studies performed on the thermodynamic stability of the system indicated that the three forms are function of temperature, partial pressure of carbonate and pH. Initial studies by Schindler *et al.* (1969) showed vapour pressure of carbonate as the main definer of thermodynamically stable material. At high concentrations of carbonate, $< 10^{-3}$ smithsonite ($ZnCO_3$) is the most stable product. At low concentration, $< 10^{-5}$ zincite (ZnO) at intermediate values, between 10^{-3} and 10^{-5} hydrozincite seems to be the most thermodynamically stable product.

Later studies in the series of articles by Preis & Gamsjäger (2001) and ? found that the system is dependent on temperature, zinc concentration and pH as well as vapour pressure. Thus, the ideal phase diagram can be presented in a 3D diagram as in Figure 2.25

The previous studies, based on thermodynamic properties such as heat and entropy of fusion as well as on thermodynamic solubility are ideal for a rapid reacting system. They do not consider the route of production neither its kinetics to predict the final product. In the present work, no other predicted product of the crystallization was

2.6 Literature Review of Zinc Carbonate Hydroxide.

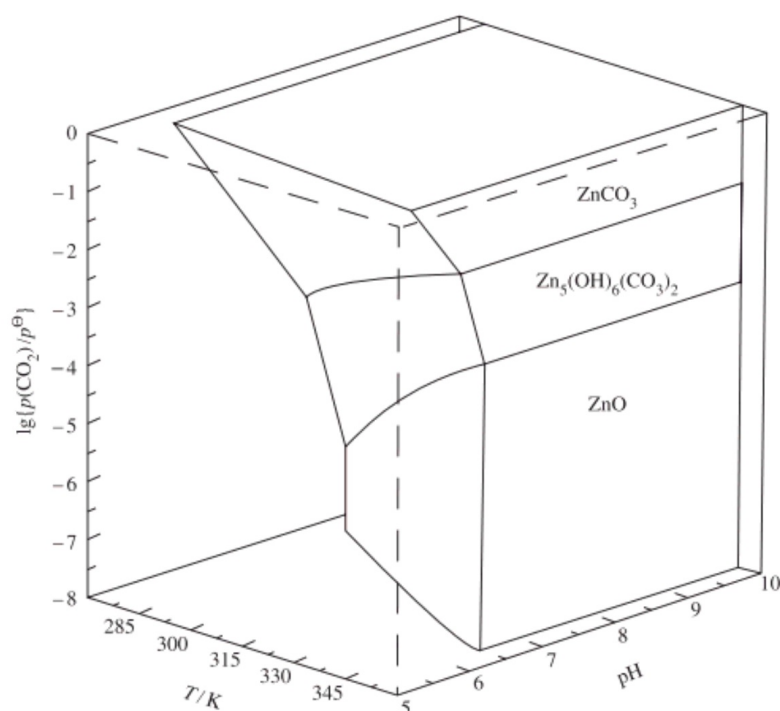


Figure 2.25: Predominance diagram of the system $Zn-CO_3-H_2O$ for zinc concentration $[Zn^{+2}] = 10^{-4}$

found at the range precipitating condition used but hydrozincite. Based on the current knowledge of crystallization it is understood that hydrozincite is probably a kinetic product of the rapid crystallization in the zinc-carbonate-water system. For the reader's reference, the XRD patterns are shown in Figures 2.26(a) and 2.26(b).

Understanding the crystal structure of hydrozincite will allow understanding of the source of crystal defects as well as the mechanism of ion absorption. The structure of hydrozincite consists of the arrangement of three basic structures to create the so-called zinc layered compound. Octahedral Zinc $Zn(OH)_8^{-4}$ structures create double layers linked by tetrahedral zinc hydroxide $Zn(OH)_4^{-2}$ and carbonate. Ghose (1964). Figure 2.27(b) shows the arrangement of the structures in a 3D representation.

The molecular structure of hydrozincite crystal is shown in Figure 2.27(a) together with the plane corresponding to the double layer (200). When simulating the XRD pattern of this structure in Mercury software we found the peak corresponding to 100 planes to be the most significant (Figure 2.28). This is a common feature in the

2.6 Literature Review of Zinc Carbonate Hydroxide.

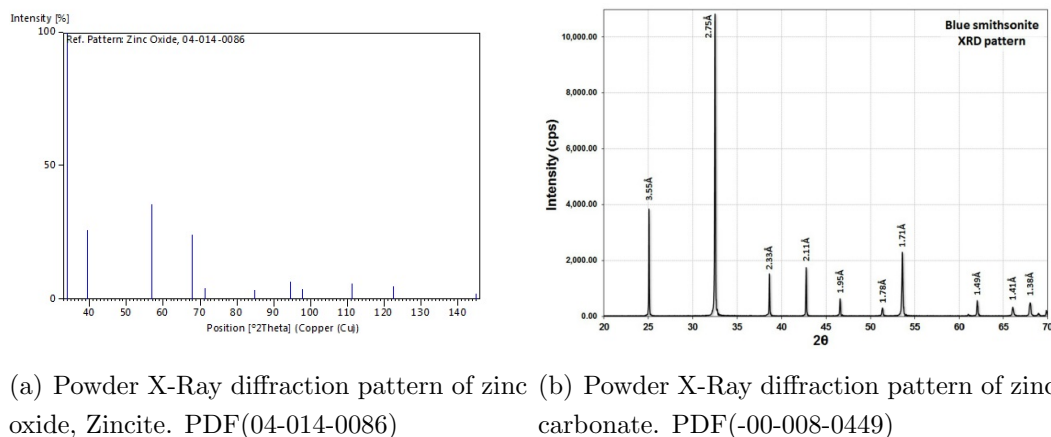


Figure 2.26

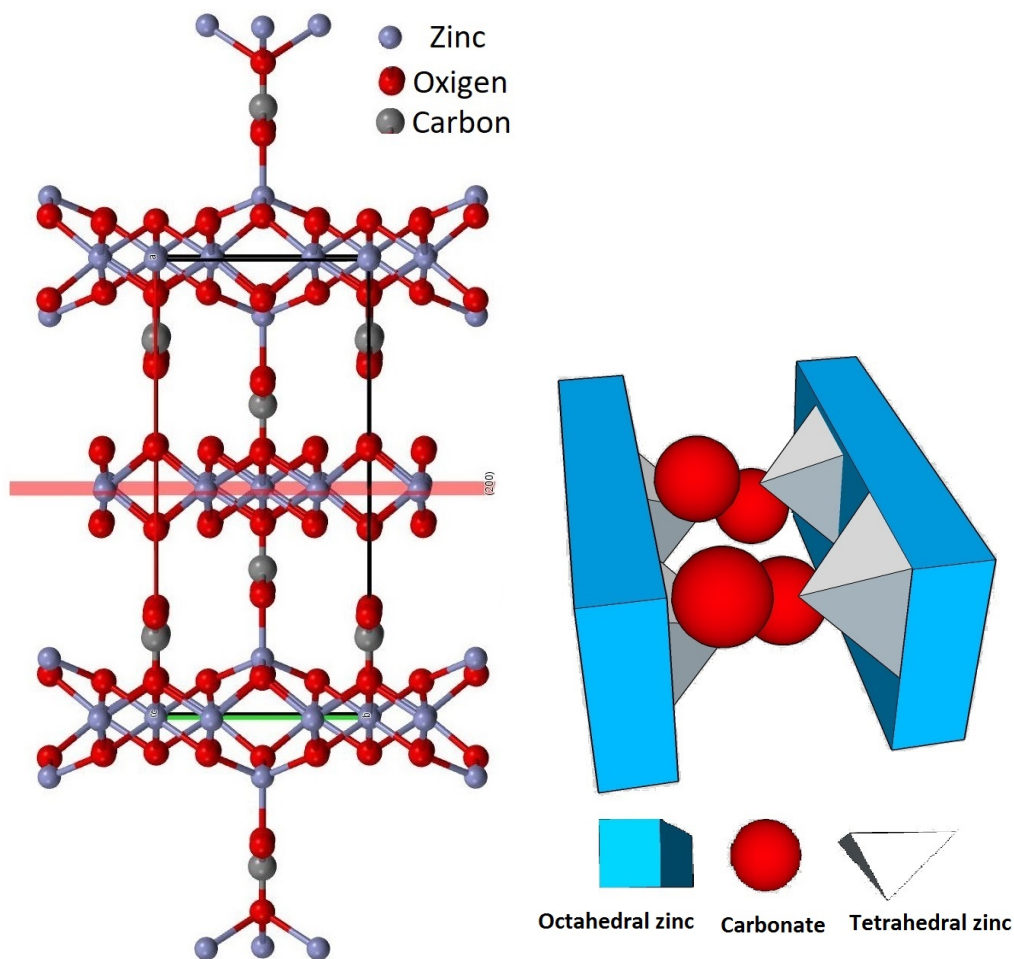
literature, (Alhawi *et al.*, 2015; Fujita *et al.*, 1995; Hu *et al.*, 2010; Liu *et al.*, 2007; Pudukudy & Yaakob, 2014; Zhang *et al.*, 2004b), where the XRD pattern shows the same characteristic peak with a variety of intensities.

The ratios between peak high remain the same for the same crystalline structure, it will be use to account for the perfection of the structure.

The height of this peak is, therefore, related with the ideality of the crystal structure. In other words, as the peak gets broader, the crystal structure will be distorted and less perfect whereas a sharp peak will characterize an ideal crystalline arrangement close to the one in Figure 2.27(a). The perfection of a crystalline structure is called crystallinity and is related to the peak broadening. For more on XRD theory and crystallinity see Section 2.7.2.

When observing the XRD patterns of hydrozincite reported in the literature, it can be concluded that the experimental condition alters the relative importance of the 100 peak. Therefore, factors such as the type of zinc salt, aging time or synthesis method, show their importance on the final crystallinity of the sample. For example, Pudukudy & Yaakob (2014) found zinc sulphate to yield lower crystallinity as a consequence of the larger electrical interaction of sulfate compared with other salts such as nitrate zinc salt. Among the synthesis method, the hydrothermal methods seems to yield the best crystallinities. Liu *et al.* (2007) and Hu *et al.* (2010) report sharp peak in comparison

2.6 Literature Review of Zinc Carbonate Hydroxide.



(a) Crystal structure of hydrozincite based on (b) Zinc layered compound model with its CIF file using Mercury. The 200 plane has three building blocks, octahedral zinc, tetrahedral zinc and carbonate.

Figure 2.27: Zinc carbonate hydroxide structure, as extracted from mercury and modelled using blocks. The double layer structure is represented in as blue blocks. It is linked by carbonate and tetrahedral zinc.

2.6 Literature Review of Zinc Carbonate Hydroxide.

with other precipitation methods. This is a consequence of the controlled release of carbonate along the precipitation process.

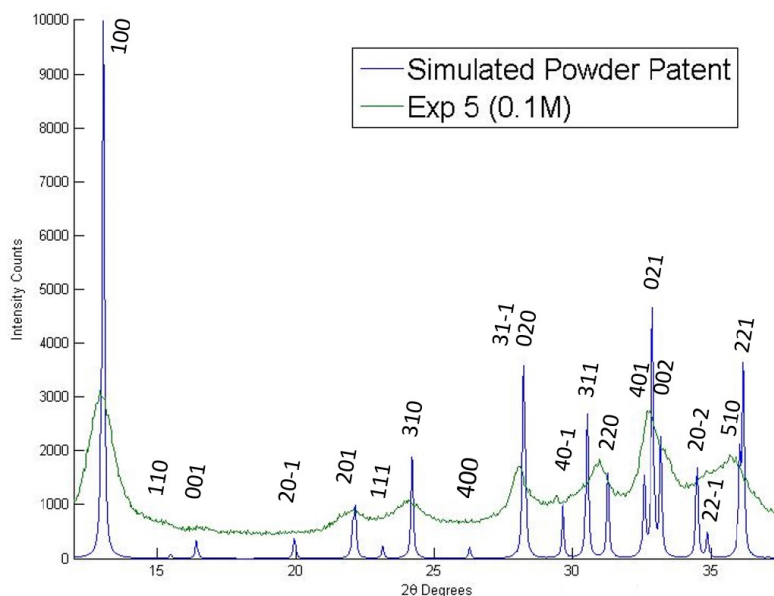


Figure 2.28: Hydrozincite $Zn_5(CO_3)_2(OH)_2$ simulated spectrum and its corresponding planes against synthesized hydrozincite.

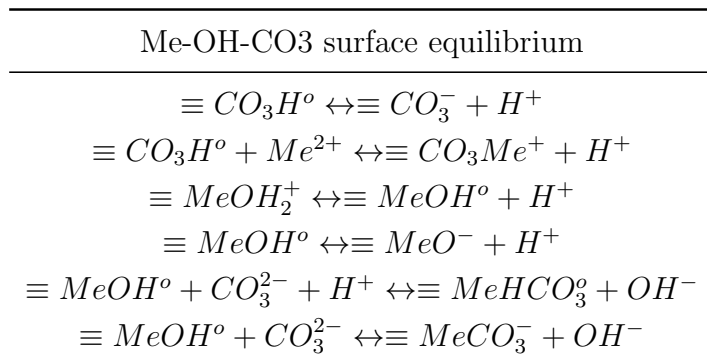
2.6.5 Surface chemistry of carbonates

The surface chemistry of carbonate material is greatly affected by pH changes as well as concentration changes (Wolthers *et al.*, 2008). An initial model for calcite was proposed by Van Cappellen *et al.* (1993) where a homogeneous surface consisting of $\equiv CaOH^o$ and $\equiv CO_3H^o$ sites was assumed. An optimization of the ionization constant of this species with water would yield a dependence on the surface chemistry with pH. The equilibrium reaction would read as in Table 2.6 which would explain physical features such as the dependence of the zero point charge on CO_3 partial pressure or the pH dependence of the dissolution kinetics. This feature plays a major role in suspension stabilization.

The electrical double layer is closely related to with the concentration of ions in the surface of the particle. Based on Table 2.6, the surface charge of a particle σ can be calculated as a summation of all surface charge. Then, the surface potential ψ_0 can be

2.6 Literature Review of Zinc Carbonate Hydroxide.

Table 2.6: Surface chemistry of carbonated atom base on Van Cappellen *et al.* (1993)



calculated using any of the available models in literature (Wolthers *et al.*, 2008) from which the distribution of surface charge $\psi(x)$ can be obtained as a function of distance (x).

Although the model from Van Cappellen *et al.* (1993) is a general model, it provides guidance for the design of experiments and an explanation of features such as isoelectric point, or decrease of surface charges. Predictions on the behaviour of surface potential as a function of pH can be derived from this model. Surface charge is expected to decrease as a function of pH. Positively charged surfaces are expected at low pH as the metal ions lose hydroxide whereas negatively charge hydroxides are promoted at high pH. The isoelectric point, or zero charge, is expected to be found in between the two extremes. Under isoelectric conditions repulsive forces are minimum and aggregation is the greatest.

The model of surface ionization presented in Table 2.6 is not completed as it lack fundamental information on the surface features such as Me and CO_3 density for each crystal surface. Different particle surfaces will have different densities of steps, kinks and faces (microtopological features) and therefore ionization of each surface would be different. Other models such as the charge distribution multisite ion complexation or CD-MUSIC for short incorporates this information, although it will not be explained here since it is outside the scope of this study. For more information on this models please refer to Wolthers *et al.* (2008).

2.7 Scattering Theory

Light scattering relies on the interaction of light and matter to obtain information on the size and shape of particles in suspension.

2.7.1 Light scattering theory

Particles subjected to an electromagnetic field undergo a movement in electric charges, such as electrons, which themselves serve as a new source of electromagnetic radiation. This phenomenon is the base for a number of interactions between light and matter which all together comprise the light scattering effect. The term absorption refers to the attenuation of light occurring when the laser beam interacts with a particle. Diffraction is a consequence of the interaction between the remitted radiation by the same particle. Refraction is a change in direction of light as a consequence of the different velocities of light in two media and reflection occurs when light is not observed but instead is rejected. (Stojanović *et al.*, 2010)

Among this phenomenon, diffraction is the most relevant for size measurement since it is a function of particle size. For larger particles, for example, different parts of the molecule behave as new sources which interact with each other creating constructive and destructive interference producing very distinct diffraction patterns as a function of the angle. On the contrary, smaller particles, also produce patterns but in this case are more diffused. The information contained in this diffraction pattern allows us to extract the particle size.

Present techniques using light scattering are classified into two categories, static and dynamic light scattering. The first one uses information on the light intensity as a function of the angle, to reconstruct the particle size distribution. It captures the time averaged size distribution as a function of the angle and combines it with Mie scattering theory as will be explained in Section 2.7.1. On the other hand, dynamic light scattering refers to the measure of light intensity as a function of time. By comparing information on time-dependent light scattering, information about the mobility of the particles can be obtained from where particle diffusion coefficients can be captured. This parameter is related to the size of the particle.

Dynamic light scattering is a very flexible technique. If electrodes are placed in the measured solution, the mobility as a function of the electrical field can be obtained,

Table 2.7: Light scattering regimes found in a typical Guinier plot.

	1	$qR_{gy} \ll 1$	Rayleigh
S(q)	$1 - \frac{1}{3}q^2$	$qR_{gy} \approx 1$	Guinier
	$cc_p(qR_{gy})^{-d_f}$	$qR_{gy} \gg 1$	Power Law

thus yielding its ζ -potential. Other pieces of equipment allow the capture of light intensity as a function of angle and concentration. In that case the so called Zimm plot can be drawn from which the radius of gyration and the molecular weight can be obtained using the Rayleigh Ratio.

Static light scattering

Static light scattering (SLS) has been used in this study to obtain the distribution of sizes and particle shape information. This technique will be used inline as shown in Section 3.3 to capture the dynamics of the process. This section will comment on the principles of the measurement and the models below.

As introduced in the previous section, SLS relies in the collection of time averaged scattered light from particles and aggregates at different angles. In this manner, the shape of the scattering pattern can be obtained and correlated with scattering models. Mie's model (Mie, 1908) is widely used to explain the pattern containing the diverse phenomena of light scattering. Intensity values I collected at each angle θ can be transformed into the q space ($q = 4\pi/\lambda \sin(\theta/2)$) thus, the normalized intensity $S(q)$ can be obtained. When plotting $\text{Log } S(q)$ against $\text{Log}(q)$ three different scattering regimens are identified, each of which correspond to a region in Figure 3.2.

The Rayleigh regime is found at low q and is constant and proportional to the number of aggregates in the measurement volume. The suspension is seen as a whole and therefore, the size distribution can be calculated from it. The Guinier regime is a transition regime which leads to the power law regime. Finally, the power law regime is found at $qR_{gy} \gg 1$ and is dependent of the surface features of the aggregate. Fractal dimensions (concept discussed in the following section) can be obtained from fitting the power law to a straight line in a $\log S(q)$ - $\log(q)$ plot. (Ibaseta & Biscans, 2010)

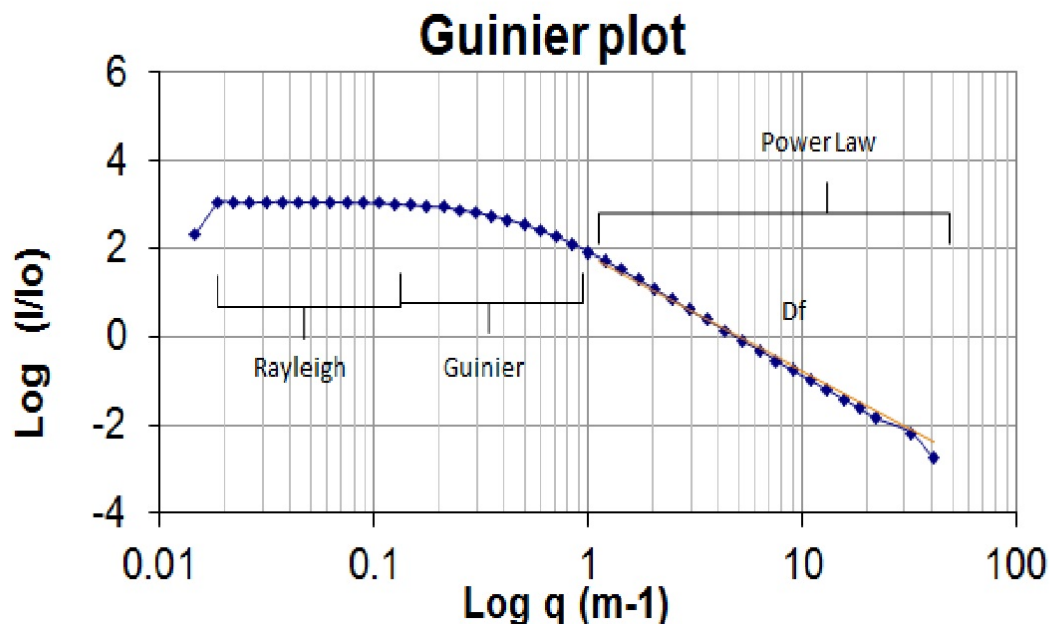


Figure 2.29: Guinier plot showing the three light scattering regions. Rayleigh, Guinier and power law regime.

Fractal Dimension

Fractal dimension, d_f , is a measurement of the amount of space filled with relation to the total volume occupied by self-similar systems. Mandelbrot (1967) accounts for features such as ramification or porosity. It can be understood as an extension of the classical Euclidian dimensions where fractional numbers are permitted between the integers 1, 2 and 3. Many natural systems can be described in terms of fractal dimension including aggregates. In this case of d_f values around 3 corresponding to compact aggregates close to a sphere, d_f of 2 is expected from ramified aggregates or flat flake like surfaces. Finally, d_f around 1 are characteristic of string like aggregates.

Therefore, the calculation of the d_f provides useful information about the degree of ramification, porosity and surface features of aggregates. In fact it can provide information about its mechanism on formation. Based on the concept of colloidal universality, developed in Section 2.4.3 and introduced by Meakin (1992), fractal dimension of 1.7 is a consequence of diffusion limited aggregation whereas 2.6 is characteristic of reaction limited aggregation.

Although studies have been carried around colloidal aggregation and fractal dimension, the concept can be used in a number of other crystallization processes to extract structural changes, also known as restructuring (section 2.4.3) for example, increase in porosity along Ostwald ripening is described by Chun Zeng (2007). He argues that aggregates increase porosity due to the loss of small particles from within the structure. Therefore, they could be tracked looking at the fractal dimension as variable. Additionally, d_f can give clues about the habit of a crystal. Although not entirely sufficient to fully characterize the crystal, SLS allows identification of flat surfaces. SEM is ideal to corroborate the results from SLS and also to reveal details of the surface of the crystal (Ibasetta & Biscans, 2010).

2.7.2 X-Ray Diffraction

In a similar way to light diffraction, X-ray diffraction utilizes the interaction of electromagnetic waves with matter to produce diffraction patterns unique for each crystal structure. However, in the case of X-ray diffraction, the wave length is much lower, in the range of 0.01 to 10 *nm*, which allows interactions with atoms instead of particles. Therefore, atoms excited with X-ray radiation will become sources of radiation themselves. Since the new sources have coherence arrangements diffraction patterns are created. For each atomic array the diffraction pattern would be unique which allows its characterization. X-ray diffraction or XRD for short, was first used for crystal characterization by Max von Laue in 1912 (von Laue, 1915) in Munich and was later developed by W.H Bragg in Leeds and Cambridge (Bragg, 1913). Their discoveries allowed among others, the resolution of the DNA double helix structure by Watson & Crick (1953). Nowadays, the use of XRD is wide spread among biologists, geologist and the pharmaceutical industries as it capable of resolving complex protein structures and identify crystalline materials or mixtures of them.

Information about the unique arrangement of atoms, characteristic of crystalline molecular structures (see Section 2.2.4) can be accessed using this technique. Bragg's Law assumes a crystal comprised of planes of repeatable atomic arrays as described by the Miller indexes. The incident radiation will excite the atoms in the array which will then become sources of radiation as shown in Figure 2.30. The new sources will create interference patterns with each other. Thus, only constructive interferences would be

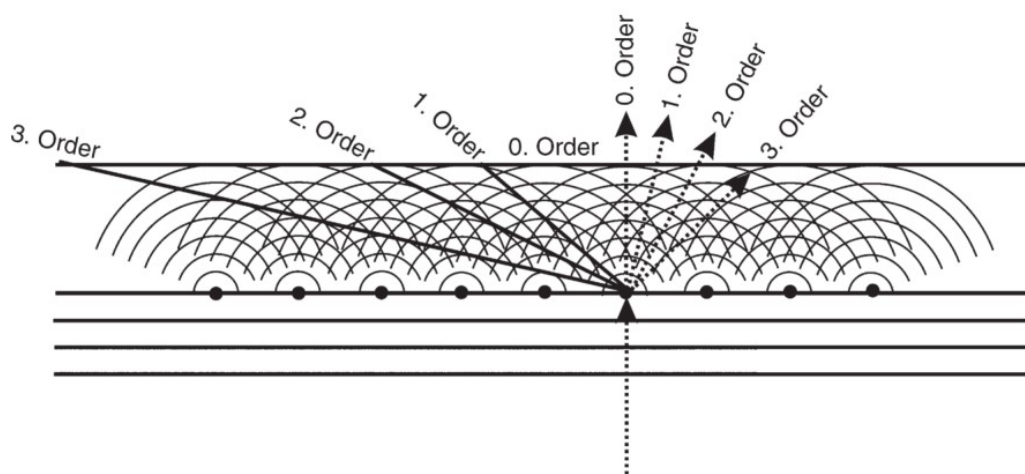


Figure 2.30: Array of atoms scattering electromagnetic radiation. Only constructive interferences (orders from 0 to 3) are allowed (Dinnebier & Billinge, 2008)

allow. Bragg's Law defines the direction of the diffracted bins (θ) as a function of the spacing between the atomic planes (d) and the frequency of the radiation (λ):

$$n\lambda = 2d\sin(\theta) \quad (2.55)$$

In the case of x-ray diffraction for a single crystal of NaCl, the diffraction pattern resembled the one in Figure 2.31. From it we can observe an array of points corresponding to the constructive interference allowed by Bragg's Law.

2.7.3 Sources, filters and monochromator

Copper lamps are the most common radiation sources in crystallography laboratories. However, they can also be found in synchrotrons or radioactive materials. Copper lamps and synchrotron relies on the deceleration of electrons which would emit light by the so called photoelectric phenomena described by Einstein (Einstein, 1965). Based on this principle, the kinetic energy of an electron is transformed in radiation when decelerated. Whether is by mechanical impact against a copper cathode or centripetal acceleration in the case of synchrotron, the decelerated electrons would yield electromagnetic radiation as indicated by Einstein's equation:

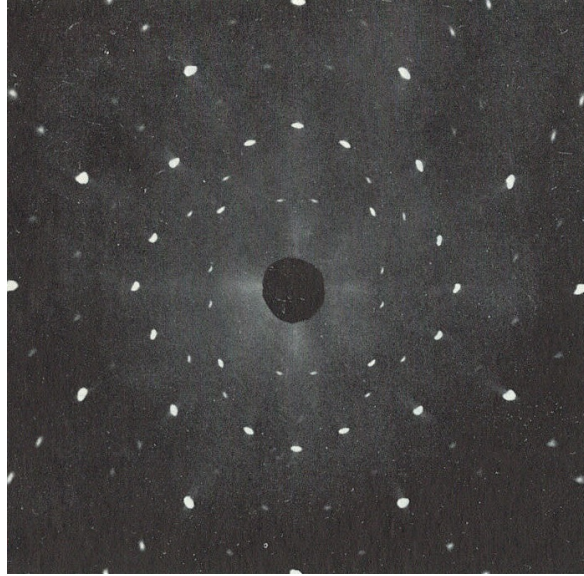


Figure 2.31: Single crystal X-ray diffraction for a single crystal of NaCl

$$KE = \frac{1}{2}m_e u_o^2 = eV = h(\nu - \nu_o) \quad (2.56)$$

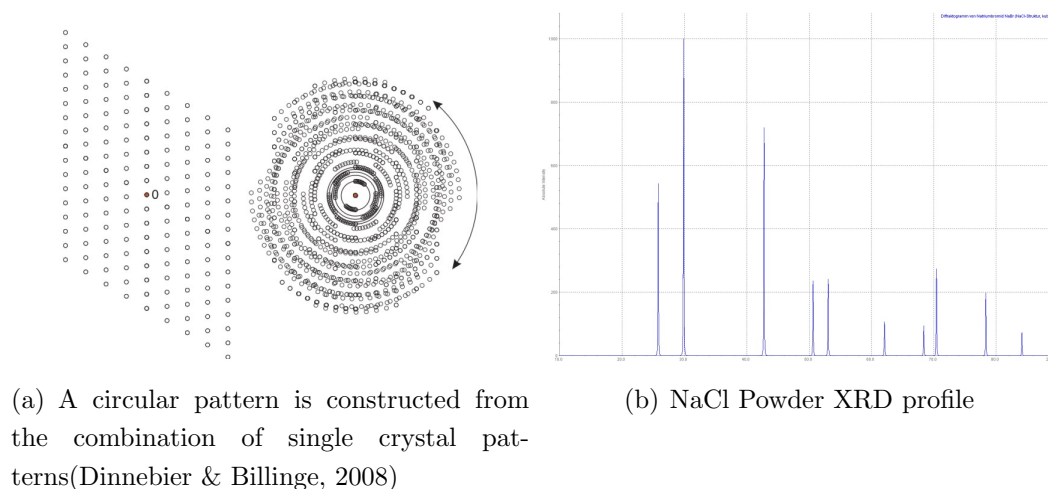
Let us take a laboratory copper lamp as example, as is the case in this project. In Equation 2.56 KE is the kinetic energy carried by an electron which is equivalent to the classical mechanics expression involving the mass of the electron m_e , and its velocity u_o . In a laboratory lamp the kinetic energy can be achieved by applying a potential (V) between the anode and cathode across which an electron of charge (e) will be accelerated. The frequency of the outgoing radiation (ν) is proportional to Plank's constant (h) minus a certain cut-off frequency (ν_o) characteristic of the material below which the effect does not occur.

At the atomic level, the photoelectric effect is explained as the energy emitted by an electron moving from outer orbitals to a K shell of the copper atom. The empty K shell is left as consequence of a high KE electron from the anode colliding with electrons in the inner shell K. Ideally only electrons from the L shell should be promoted to shell K however, electrons from shell M are sometimes promoted. Radiation from L shell electrons is $K_{\alpha 1}$ and $K_{\alpha 2}$ (depending on the orbital) from radiation of electrons from M orbitals is K_{β} which have different frequencies. Since the desired radiation for X-ray diffraction is of a single frequency, a monochromator is needed to select the $K_{\alpha 1}$

radiation consisting of a set of crystals capable of absorbing the unwanted radiation in 99%. Higher radiation quality can be achieved with a nickel filter which removes a further 99% of the K_{β} .

2.7.4 Powder X-ray diffraction

Powder XRD is a well used technique useful for a variety of purposes. i.e. phase composition, crystal structure, crystallite size determination, etc. It relies in the diffraction of X-ray, similarly to a single crystal, although in this case the sample is a randomly orientated collection of crystals (powder). As a consequence of this new arrangement, a point in Figure 2.31 becomes a circle, as shown in Figure 2.32(a). Then, a radial profile can be drawn from the centre outwards yielding the typical powder XRD pattern found in Figure 2.32(b). In a powder XRD pattern, the peak position is characteristic of the crystalline structure and retains information of the hkl plane distances.



(a) A circular pattern is constructed from the combination of single crystal patterns (Dinnebier & Billinge, 2008)

(b) NaCl Powder XRD profile

Figure 2.32: Construction of powder XRD pattern from single crystal XRD.

The sample to be used in the Powder XRD must meet certain criteria. The crystal must be randomly orientated otherwise preferential orientations would occur (see further explanation later in this section). The size of the particles must be over 120nm otherwise peak broadening would occur. (see peak broadening). Sample milling is normally required for achieving the desired particles size.

Peak broadening the width of the peaks change with a variety of factors. For example, a sample with a distribution of d-spacing between khl planes yields a broad peak centered in the average planar distance (see Figure 2.33). Also, sources with a distribution of wavelengths, instead of monochromatic, yield peak broadening. Finally, a smaller crystalline domain produced peak broadening. In the former case, the broadening of the peak provides information about the polycrystallinity of samples, for example metal samples. The Scherrer equation (Equation 2.57) relates the peak width (broadening at half maximum (β)) with the mean size of the crystallites (r_c).

$$r_c = \frac{K\lambda}{\beta \cos\theta} \quad (2.57)$$

where K is a dimensionless factor with a typical value of 0.9, θ is the location of the peak, λ is the X-ray wavelength and β is the full width at half maximum of the peak.

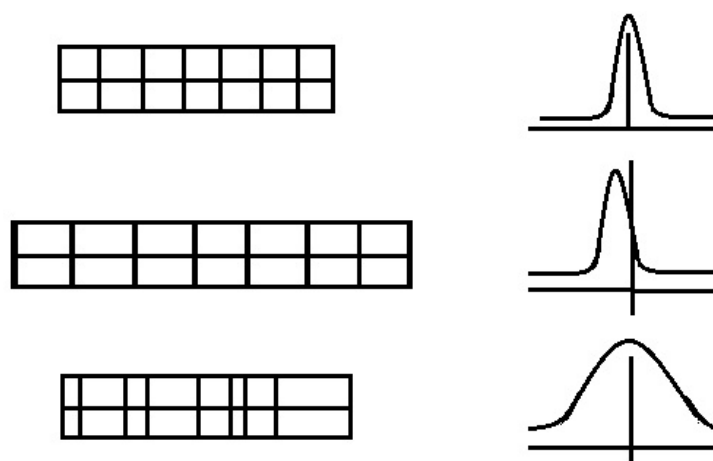


Figure 2.33: Crystal structure defects and their effect on the powder diffraction pattern. (Dinnebier & Billinge, 2008)

Background. the NaCl pattern in Figure 2.32(b) shows sharp peaks over a flat background. This is not always the case as samples may present non-crystalline structures or detector may be exposed to cosmic rays which produce background noise. In the first case, were non-crystalline structures are present, diffraction does not occur, instead a broad shape is captured as shown in Figure 2.34. A way of understanding this pattern is to imagine a crystalline material consisting of a wide distribution of planes

distances with no special arrangement. Rapid precipitating carbonates such as the one studied in this project present some extent of amorphous material, this is typical of rapid crystallizing carbonates (Brecevic & Kralj, 2007; Dosch *et al.*, 1986).

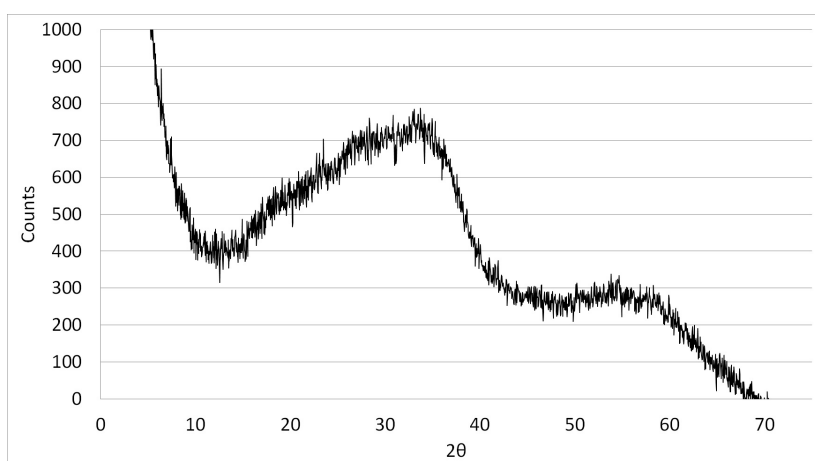


Figure 2.34: Typical amorphous pattern

Preferred orientation. The relative intensity of one peak with respect to other is expected to be equal if the powder grains are randomly orientated. However, some samples are difficult to prepare as they tend to align preferentially in certain directions. For example, needle like crystals tend to align in a specific direction when pressed into a sample holder or when introduced in a capillary tube. As a consequence the relative intensity of the peak does not remain constant or peaks would be missing. This phenomenon is known as , preferred crystallographic orientation. Regarding peak intensity, it is important to say that materials with naturally layered structure, as in the case of lamella structures of hydrozincite, present a characteristic peak in the XRD pattern corresponding to the hkl plane. (Sun, 2016).

Chapter 3

Materials and Methodologies

3.1 Introduction

This chapter describes the methodologies both, experimental and mathematical, used in this work along with the materials used to perform the studies. It commences with a description of the materials used in the experimental section for later detailing the methodologies used to achieve the objectives of this study. Methodologies include: an inline light scattering set-up, electron microscopy, solubility determination, atomic absorption spectroscopy, turbidity measurements, electrostatics spectroscopy, population balance modelling in gPROMS, CFD and determination of residence time distribution by tracers.

3.2 Materials

For the main experimental work zinc nitrate hexahydrate recrystallized grade from Sigma Aldrich has been utilized as well as sodium nitrate of analytical grade from the same vendor. These were used as purchased with no further purification.

Hydrozincite was synthesized in house using the reactive crystallization method. The C mixing solutions consist of zinc nitrate and sodium carbonate (both soluble salts) which yielded a cloudy suspension. The product of this reaction was filtered using Whatman filter paper (cellulose or Nylon ($0.2\mu m$) depending on the suspension concentration), washed with distilled water, dried in a vacuum oven at 36 degrees

and grained for later be characterized by XRD to confirm hydrozincite as synthesized product.

The materials used in this research are listed below for the reader's reference:

- Magnesium chloride- analytical grade from Sigma Aldrich as supplied.
- Sodium bicarbonate- analytical grade from Sigma Aldrich as supplied
- Nitric acid 70% reagent grade. Sigma Aldrich
- Sodium hydroxide, reagent grade, $\geq 98\%$, pellets (anhydrous),
- Sodium Dodecyl Sulphate- analytical grade from Sigma Aldrich as supplied.

3.3 Light scattering

As described in Section 2.7, light scattering is a powerful tool to obtain size information of a suspension or a powder. Time averaged light intensity scattered by a suspension of solids is recorded as a function of the angle to be later fitted to the Mie scattering theory. The result is a particle size distribution containing information about the size and the morphology of the suspension.

3.3.1 Inline Light scattering

Apparatus

The dynamics of the aggregation process within the tubular reactor were characterized by mean dynamic light scattering. An equipment arrangement has been designed aiming to capture the desired phenomena. Figure 3.1 illustrate the experimental set-up for in-line measurements. It consists of a 60° glass junction ($\phi 5\text{mm}$) where zinc and carbonate solutions were continuously mixed. Attached to the junction, various lengths of silicon tubing (from 0.5 to 4m, $\phi 8\text{mm}$) allowed diverse residence time. A peristaltic pump (Marlow Watson 520s) provided the desired flow rates in the range 167 to 442 ml/min. Under these conditions micromixing is believed to be completed after the junction as CFD results will show later on in Section 7.8. Additionally reservoirs and waste tanks were conveniently placed to recover the products and contain reactants.

3.3 Light scattering

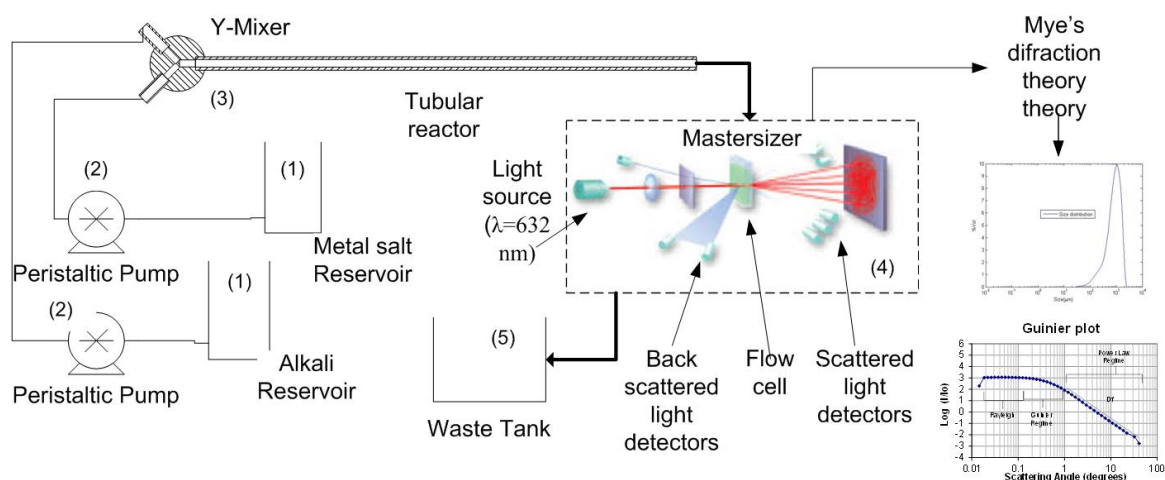


Figure 3.1: Flow diagram of the inline light scattering system showing the equipment set-up for the continuous synthesis and analysis of the PSD. (1) Reactant reservoir, (2) Peristaltic heads, (3) Y-Mixer, (4) Light scattering equipment, (5) Product recovery.

This set-up is similar to others reported in the literature (Yang, 2013b); although, a continuous precipitation and particle analysis has not been reported until this work. The present set-up allows the study of suspensions at various flow rates from 0.14m/s to 0.39 m/s as well as various reactor lengths (from 0.5 to 4 metres). The concentration of solids allowed is limited by the obscuration range set by the light scattering detector. Values used in this work are 0.33 to 0.54%w.

Analysis

Light intensity data, captured by the detectors, was recorded and analyzed using the software provided by Malvern, thus obtaining size distribution. This allowed the capture of size distribution descriptors, $d[4,3]$, $d(0.5)$ and $d(0.9)$. Additionally, Guinier's plot was construed by plotting the logarithm of relative intensity vs the logarithm of the q space. The slope of this plot at small q is used in this study to approximate fractal dimension (d_f) Ibaseta & Biscans (2010). Figure 3.2 shows the three different regimes: Rayleigh, Guinier's and power law. Refer to Section 2.7 for further references.

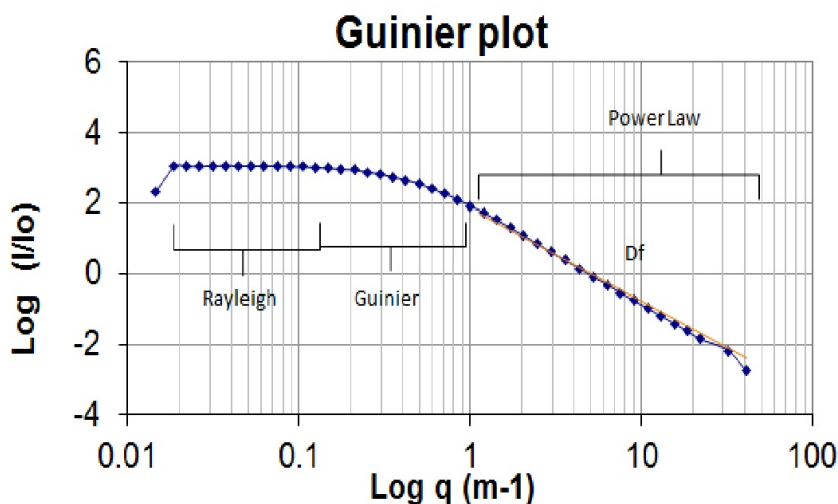


Figure 3.2: Guinier plot showing the three light scattering regions. The Rayleigh regime provides information on the particle size, the Guinier regime is a transition regime, whereas power law contains information of the particle shape.

3.4 X-ray diffraction

3.4.1 Equipment

A Bruker D8 advanced XRD diffractometer was used routinely to characterize and confirm the purity and phase of hydrozincite. The copper slab source produces X-ray radiation which is then filtered using a germanium primary monochromator to obtain K_{α} radiation. The detector is a Vantec-1 position sensitive detector. The XRD source was set to 35kV and 45mA. 2θ angles from 10° to 50° were covered with a step size of 0.033° at 0.8 sec/step.

3.4.2 Sample preparation

The powder for XRD analysis was prepared following the present procedure. First, suspensions were filtered with cellulose filter paper, unless the sample had low concentration or very fine particle size, in which case a Whatman filter paper (ϕ $0.20\mu m$) was used. Then, the solid sample was washed 3 time with water, following standard procedures (Chen *et al.*, 2008). A low temperature vacuum drying at $30^{\circ}C$ followed intending to avoid form change. The sample was then ground in a mortar to obtain a

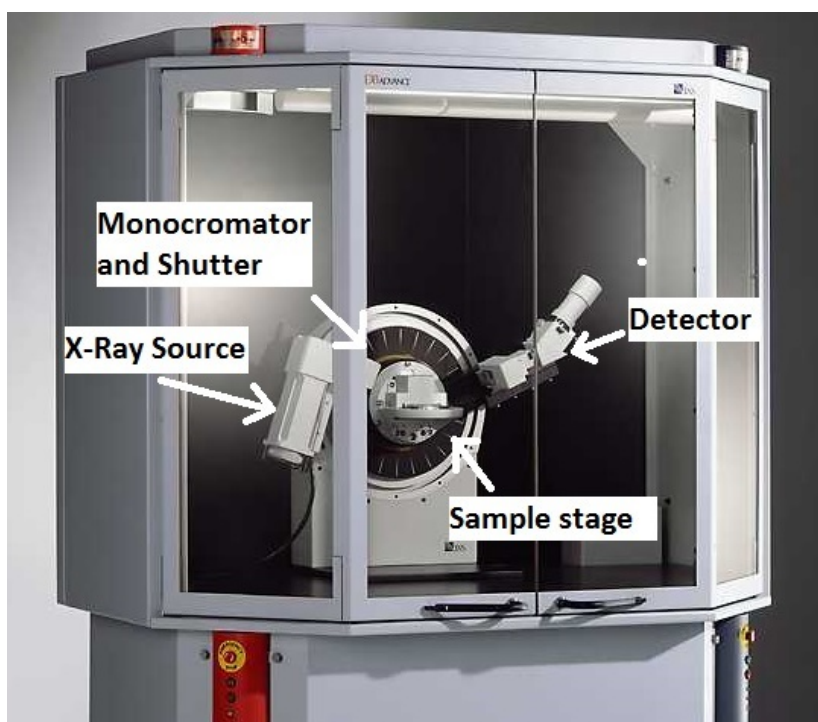


Figure 3.3: Bruker D8 power X-ray diffraction equipment used for hydrozincite characterization

fine powder suitable for XRD. Finally, the sample was placed in the Bruker D8 sample holder ensuring a smooth and flat surface.

3.4.3 Analysis

For patent identification, the peaks were tagged using HighScorePlus and automatically compared with peaks reported in the data base to find the best match. Structural analysis on the other hand used TOPAS where the routine reported in Appendix B.1 was used to obtain the angles and distances of the unit cell parameters. The so called Pawley analysis was used for this purpose. It utilizes the peak position and compares it with the one derived patent from the ideal crystal structure. TOPAS then runs a minimization routine which optimizes the unit cell parameter to minimize the difference between the model pattern and the experimental spectrum.

3.5 Electron Microscopy

Morphology characterization was carried out on a scanning electron microscopy (SEM) equipment Hitachi SU8230 in secondary electron detection mode (SE). A feature of this equipment is the low operating voltage (2kV) which allowed observation of carbonate samples without degradation.

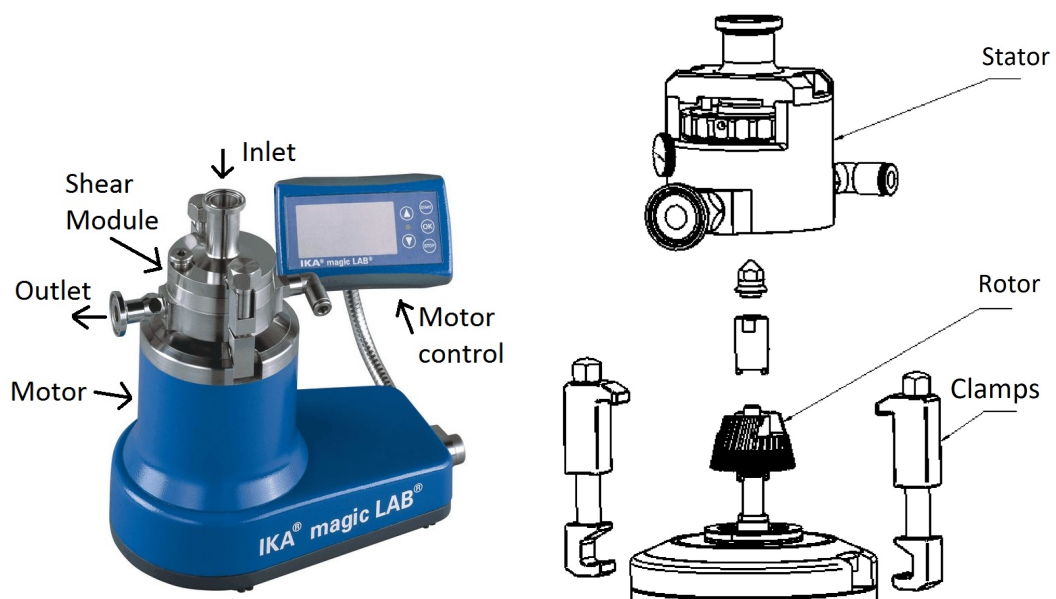
SEM relies on accelerated electrons interacting with the sample. Absorbed or scattered electrons are detected and images can be constructed from this data. The electrons produced by the electron gun possess higher energy (higher frequencies $E = h\nu$) rather than visible light. Therefore they provide higher image resolution.

Sample preparation required re-dispersion of the dried powder in ethanol by ultrasound since powder was found to agglomerate after drying. A drop of the suspension was placed in the SEM stub and left to dry for 20min. The stubs with the dry suspension were placed in an ozone cleaner to avoid sample residue left in the SEM vacuum chamber. The low voltage operation permitted the use of uncoated samples although it was found that image quality increased sensibly with 3 nm Pt coating.

3.6 High Shear Mixer

Studies on the influence of high shear on particle size were performed using an IKA Magic Lab with a MK module (Figure 3.4(a)). This equipment was designed for the production of micro suspensions and emulsions. The speed control system allowed the selection of variable tip velocities (rpm).

In the present case, the equipment was used in inline mode as shown in Figure 3.5. Similar to Section 3.3, the set-up consisted on a Y-junction as a continuous mixer with reservoirs for reactants and products. However, in this case the IKA Magic Lab was attached to the reactor outlet. The arrangement of the Mastersizer differs from previous arrangements. In this case, the measurement of particle size was performed off-line which is represented by a thinner line in Figure 3.5. Around 10ml of sample was collected and stabilized with a 1% SDS solution in order to be transferred to the Mastersizer dispersion unit. Particle size distribution were obtained from the analysis of the intensity data from the Mastersizer.



(a) Ika Magic lab wet mill equipment. The (b) The Ika Magic Lab consists of a rotor shear module powered by a 900W motor is stator configuration which is secured by two controlled from a control module from where clamps. temperature and torque are read.

Figure 3.4: Wet mill diagram

3.7 Zinc solubility and adsorbed magnesium determination

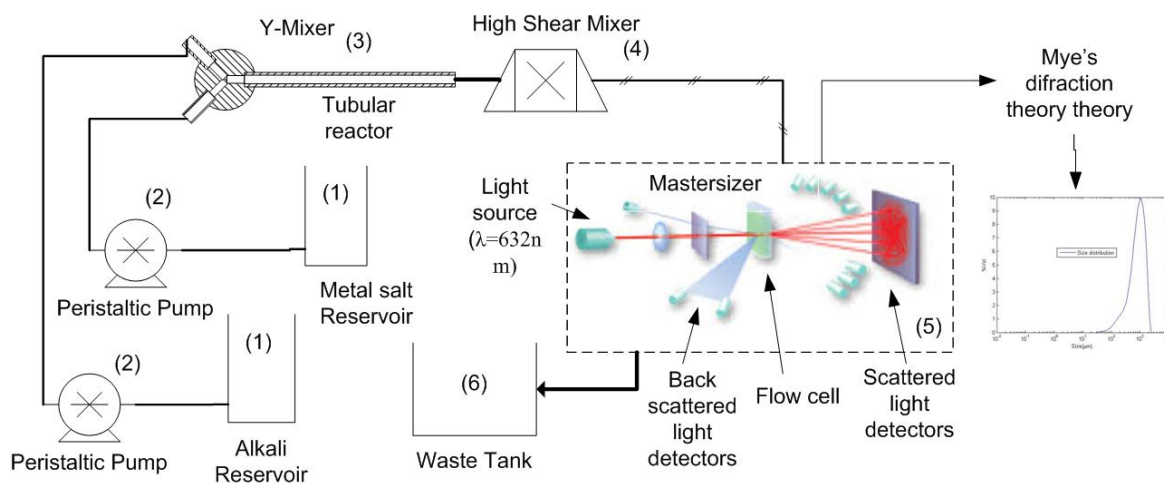


Figure 3.5: Flow diagram showing the experimental set-up for the continuous synthesis and milling of hydrozincite under high shear conditions. (1) Reactant reservoir, (2) Peristaltic heads, (3) Y-Mixer, (4) High shear mixer, (5) Light scattering equipment, (6) Product recovery.

3.7 Zinc solubility and adsorbed magnesium determination

The determination of concentration of metal ions in solution has been carried out by atomic absorption spectroscopy (AAS) in a Varian AA240. This technique was used in the solubility determination of hydrozincite, as well as on the quantification of adsorbed magnesium ions. The procedures of sample preparation and concentration determination are described as follows.

3.7.1 Atomic Absorption Spectroscopy

Atomic absorption spectroscopy was used as the analytical technique to quantify zinc and magnesium ions in solution. The technique is classified as a spectro-analytical technique and relies on the absorption of optical radiation by ionized chemical elements. An optical radiation source, normally a hollow cathode lamp, generates radiation tuned to the element of interest. Then this radiation is absorbed by ions produced after nebulization and ionization of the solution. This is achieved by the high temperatures

3.7 Zinc solubility and adsorbed magnesium determination

produced by an acetylene-air flame. The intensity of the remaining radiation (transmittance) is recorded and amplified electronically to then be compared with a calibration standard. The Beer-Lambert law ($(T_r - 1) = e_B L_p c$) relates the transmittance (T_r), opposite of absorption, Abs , with the length of the flame L_p , the solution concentration c and a proportional constant e_B .

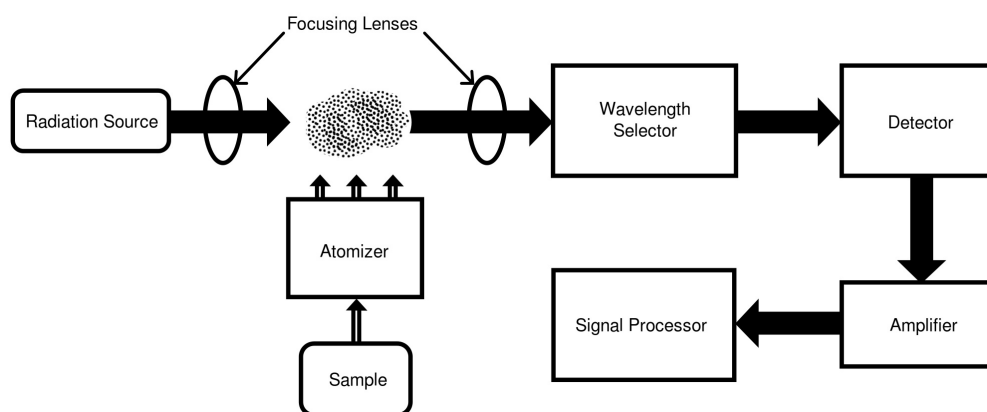


Figure 3.6: Flow diagram of an atomic absorption spectroscopy system. The sample is neutralized and ionized with an acetylene flame. A light source interacts with the flame and absorbance is recorded, cleaned and transformed to concentration by a calibration model.

Mg and Zn calibration solutions were prepared from standard solutions for AAS calibration. Figure 3.7 shows an example of intensity vs concentration calibration curve.

Hydrozincite solubility product determination

For experimental determination of solubility an excess amount of in-house synthesized hydrozincite was placed into a 20 ml vial containing $NaOH$ solutions ranging 0.025 to 0.2M. Vials were then sealed. Under these conditions the system was considered as a closed system as no gases were allowed to leave or enter the container. Then, mixtures were left for 4 days to reach equilibrium in a thermostatic shaker at $20^{\circ}C$ after which samples were analysed. Firstly a Mettler Toledo pH meter was used to determine the proton concentration. Then using a syringe filter, the mother solution

3.7 Zinc solubility and adsorbed magnesium determination

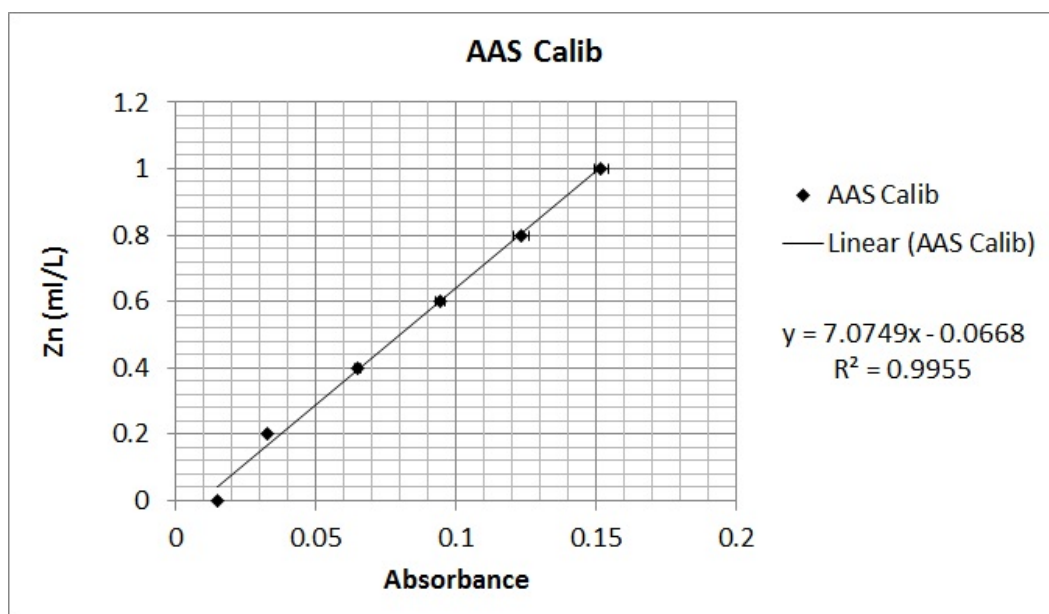


Figure 3.7: Example of a calibration curve for AAS. Reference sample was automatically diluted by the AAS sampler in ranges from 0 to 1 ml/L. Absorbance correlates adequately with zinc ion concentration.

was separated from undissolved hydrozincite. Then, two drops of nitric acid were added to prevent any solid deposition before AAS analysis. Sample dilution was required for the concentration to fall into the AAS calibration range. Three samples were prepared and then measured three times with the AAS. Solubility product was computed using Equation 3.1 assuming that the concentration of carbonate remains in stoichiometric relation with zinc and none is lost as CO_2 to the atmosphere since low pH shifts the equilibrium towards CO_3^{2-} and vials are sealed.

$$K_{sp,hyz} = [Zn][CO_3^{2-}]^{0.4}[OH^-]^{1.2} \quad (3.1)$$

Magnesium determination in hydrozincite

Magnesium doped hydrozincite was synthesized in-house using a reactive crystallization method similar to the one described in Section 3.2 for hydrozincite. However, in this case, Mg chloride was added to the zinc solution at various concentrations. Sodium carbonate concentration was chosen to be 2:1 with respect to zinc concentration. Table 3.1 shows the experimental conditions chosen for this experiment.

3.7 Zinc solubility and adsorbed magnesium determination

Table 3.1: Experimental conditions for the quantification of Mg^{+2} in precipitated hydrozincite. The table shows the concentration of zinc salt and the mass percentage of magnesium in relation with the amount of zinc salt.

Exp ID	$Zn(NO_3)[M]$	$w\%Zn(NO_3)/MgCl_2$
32	0.02	10
36	0.02	6
30	0.1	10
35	0.1	6
31	0.1	15
28	0.5	10
34	0.5	6
37	0.5	15
51	0.02	15
40	0.02	3
39	0.1	3
38	0.5	3
52	0.5	0

3.8 Induction time determination

The solutions were then pumped at a flow rate of 0.140ml/s through a Y junction to induce precipitation. After that, suspensions were recovered, filtered, washed and dried as described in Section 3.2. For AAS analysis a known mass of powder was dissolved in acidic solution and diluted to match the AAS calibration curve.

The amount of Mg transferred from the solution to the sample in the precipitation process can be measured by means of atomic absorption spectroscopy AAS. For this purpose, a known amount of product was weighed and placed in a volumetric flask, then a small amount of acid was used to dissolve the powder, finally the volumetric flask was filled up to the mark. The resulting solution was shaken and analyzed using the AAS from which its concentration can be taken as described in Section 3.7.1.

PHREEQC Simulations

In addition to experimental determination of solubility, PHREEQC (Parkhurst & Appelo, 2013) was used to compare results from experiments and ideal species in solution. PHREEQC is a software package developed in C++ by the U.S. Geological Survey which utilizes the solubility products of mineral species to compute equilibrium values of ions in solution or in contact with gases under the existence or not of chemical reactions. Hydrozincite solubility product was introduced in the data base manually using the K_{sp} value provided in the literature Schindler *et al.* (1969). Excess mass of hydrozincite was added to a solution of water and *NaOH* at different molarities yielding a pH of 8.23, 8.36, 9.49, 9.89, 10.63 and 11.16. An example of the code can be found in Appendix A.1.

3.8 Induction time determination

The introduction time of crystallization was measured by tracking changes in the turbidity of the solution. Turbidity was found to follow a first order plus delay behaviour where the induction time corresponded to τ_0 in Equation 3.2. Therefore, fitting this equation to the turbidity plot in Figure 3.9, would allow the determination of the induction time.

3.8.1 Measurement

Induction time was measured using H.E.L. AutoMATE multi-reactor system equipment with turbidity probes (Figure 3.8). It allows independent control and monitoring of temperature for four 100ml vessels. For each of the vessels turbidity probes were used to obtain solution obscuration against time.

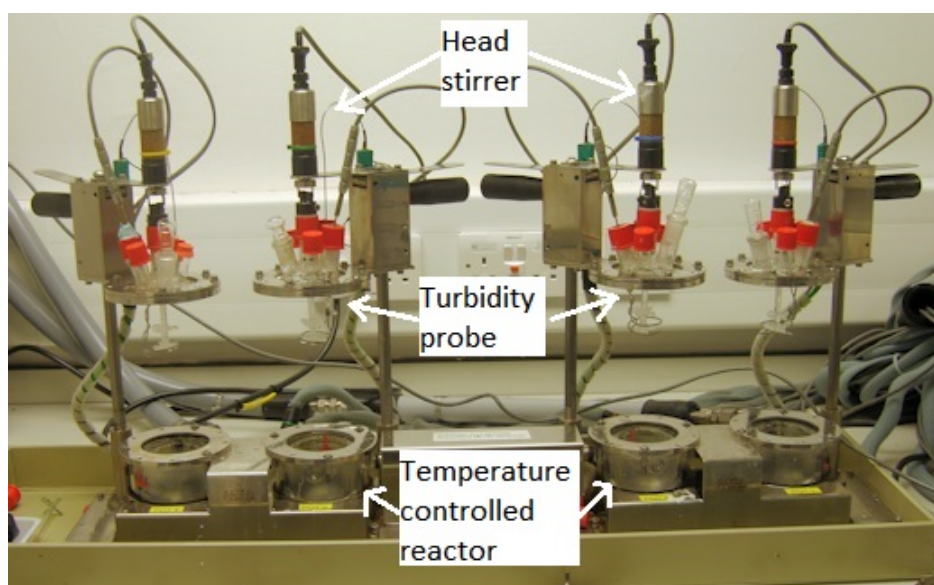


Figure 3.8: Automate equipment for recording turbidity as function of time.

For measuring induction time the following procedure has been followed: A 100 ml reactor was half filled with 50 ml of zinc nitrate solution at various concentrations and stirred vigorously with a glass impeller in order to increase convective mixing. At time 0 (τ_0), 50 ml carbonate solution was added and turbidity recorded against time. Data was finally normalized and induction time was taken as the delay between τ_0 and the first turbidity increment (τ_i).

Figure 3.9 exemplifies the increase of turbidity with time after precipitation. A latent time is observable from time 0 and the first change in turbidity which was taken as the induction time. In some cases the fitting of the step change was fitted to a first order plus delay system 3.2 conveniently obtaining induction time as one of the optimization parameters.

$$Tur = 1 - \exp(-K_{\tau}(t-\tau_i)) \quad (3.2)$$

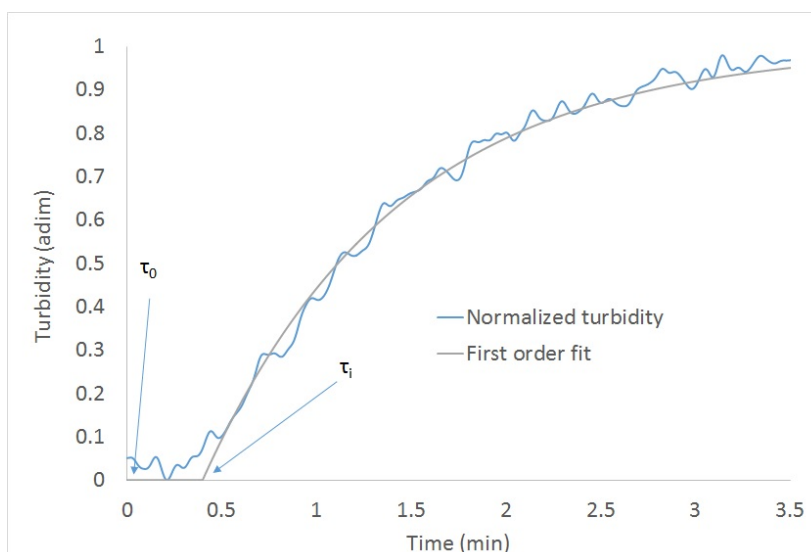


Figure 3.9: Turbidity vs time. Mixing occurs at time τ_0 . Turbidity increases after induction time τ_i

3.9 Electroacoustic spectroscopy

A Zeta Probe by Agilent was utilized to measure the ζ -potential as a function of pH. The equipment relies on the relation between ultrasonic excitation of the sample and the yielded electric potential. The periodic displacement caused by the sound waves in the suspension causes displacements in the electrical double layer of the particles which produces an electric field. This is detected by a probe submerged in the slurry. By scanning different sound frequencies and their associated electrical response, a spectrum can be obtained and then fitted to a theoretical expression proposed by Dukhin & Goetz (1996) which provides the particle θ -potential.

The Zeta Probe allows titration as it incorporate two syringe pumps. Therefore the ζ -potential can be recorded as a function of pH and the isoelectric point determined.



Figure 3.10: Electroacoustic spectroscopy equipment (Zeta Probe) used for measuring the ζ -potential as function of pH

3.10 Population balance model and gPROMS methodology

Population balance models have been chosen for mathematical description of the aggregation phenomena commented on Section 2.4. A number of phenomena defines the outcome of the aggregation phenomena, namely: collision efficiency, aggregation rate or breakage rate which themselves are driven by gradients in momentum (shear rates) or minimization of surface energy (attractive surface forces). The expression derived in this work includes these factors and their evolution in time and space.

Intrinsic properties of particles such as particle size L , or particle volume V can be represented by an internal set of coordinates (x_i) and external co-ordinates (x_e) such as time(t) or spatial co-ordinates (x, y, z). A certain number of particles (population) are therefore, characterized by a combination of internal and external coordinates as a number density function, $N(x_i, x_e)$. An interesting point of the population balance is that it easily incorporates functions to account for the process influencing the number density function (NDF) such as aggregation, thermal diffusion, nucleation, growth or

3.10 Population balance model and gPROMS methodology

breakage. When considering time as an external co-ordinate and size as an internal co-ordinate, the NDF can be expressed as $n(t, L)$. A general formulation can be found in Cheng *et al.* (2009) where all the above processes (nucleation, growth...) are taken into account.

$$\begin{aligned}
 \frac{\partial n(t, k)}{\partial t} + \nabla \bullet \mathbf{un}(t, k) - \nabla \bullet D\nabla(n(t, k)) + \frac{\partial(G(L)n(t, k))}{\partial L} = \\
 = \frac{\alpha}{2} \sum_{i+j=k}^{\infty} K_{i,j}^a n(t, i)n(t, j) - n(t, k) \sum_{i=1}^{\infty} K_{i,j}^a n(t, i) + \\
 + \sum_{m=k+1}^{\infty} K_m^b n(t, m)\Gamma_{m,k}^b - K_k^b n(t, k) \quad (3.3)
 \end{aligned}$$

The first two terms on the right are the mathematical description of the aggregation phenomena proposed by (Smoluchowski, 1917). Thus, particles of size i and j collide with a frequency $K_{i,j}^a$ and on the driving mechanism, weather, thermal, convective or sedimenting as described in expressions 2.40, 2.39 and 2.41 respectively. The last two terms on the right hand side correspond to the breakage terms. They model the creation of particles of size k through the breakages of size m with a frequency K_m^b . It is been observed that breakage occurs in a number of ways. First, fragmentation would be the splitting of the particle in two involving a significant loss of mass of one of them. Attrition on the other hand, would be the lost of smaller surface particles with no significant depletion of the mother particle. These breakages modes are considered by the breakage function $\Gamma_{m,k}^b$. Terms on the left hand side refer to accumulation, convective transport, thermal diffusion and growth.

After various assumptions supported by experimental results as well as with CFD simulations, Equation 7.4 was chosen to be the final mathematical expression to implement.

$$\begin{aligned}
 \frac{u}{X} \frac{\partial n_k}{\partial \tau} = \frac{1}{2} \sum_{j=k-i}^{j=\infty} \alpha_{eff}(i, j) K_{i,j}^a (AggFac) n_i(\tau) n_j(\tau) - n_k \sum_{i=1}^{\infty} K_{i,j}^a n_i(\tau) + \\
 + \sum_{m=k+1}^{m=\infty} K_m^b n_m(\tau) \Gamma_{m,k}^b - K_m^b (P_1, P_2) n_k(\tau) \quad (3.4)
 \end{aligned}$$

3.10 Population balance model and gPROMS methodology

This expression has been tailored for the specific case of a tubular reactor and therefore contain characteristic features. For example, on the left hand side of the expression the dimension less reactor length has been used as the independent variable instead of time. That allowed the incorporation of reactor length and flow velocity to characterize the residence time. Also the collision efficiency (α_{eff}) has been assumed to be a function of i and j . Therefore it will be placed inside the summation operator. Assumption and other considerations are described in Section 7.8.

Population balance formulation and coding

Once the equation was developed, it was implemented in a gPROMS code. This equation-based programming language is a very useful tool for engineers as it contains a tool for easy model implementation and parameter estimation. The methodology of model implementation followed for the population balance model is described here whereas the complete code can be found in Appendix C.1

1. A number of variable types were defined in the tab Variable types, those being: number of particles [#], first[# m], second [# m^2], third [# m^3] and fourth [# m^4] momentum of the size distribution, aggregation rate [#/ s], shear rate [s^{-1}], fractal dimension [$adim$], velocity [m/s] length [m].
2. The model was then developed. Declaration of the variables was required: size ($L(Nogrid)$), shear rate (G), number of bins ($Nogrid$), number of particles ($n(Nogrids)$), aggregation kernel (Kr), collision efficiency(α), aggregation birth rate ($BirthA$), aggregation death rate ($DeathA$), Breakage birth rate ($BirthB$), Breakage death rate ($DeathB$), Initial particle size ($minL$), size of the first bin ($DeltaL$), reactor length (X), flow velocity (u), Solid volume fraction ($Volume\ fraction(Nogrid)$), fractal dimension (df), first second third and fourth momentum of the size distribution ($m1, m2, m3, m4$), initial solid fraction (Phi) and dimensionless length (xl), ($P1$) and ($P2$)
3. In the model section, the variables were then defined either with mathematical expressions or with values following the aggregation theory in Section 2.4. As pointed out before, the complete code is reported in Appendix C.1.

3.10 Population balance model and gPROMS methodology

4. Results of the experiments were then introduced in Chapter 6.1. For each of the 5 flow rates, size distribution was introduced for 4 to 6 different reactor length. Each size distribution contained information for 26 bin sizes. A uniform variance of 0.06 was chosen.

Discretization schemes and parameter estimation

gPROMS also provides tools for discretization and parameter estimation. These are to be used for obtaining values of collision frequency factor (k_α) shear rate scale factor on aggregation rate ($AggFac$), Shear exponent scale factor on the breakage term (P_1) and size scale factor on the breakage term (P_2). After the PB equation was coded and variables defined, the software solves the ordinary differential equation (ODE). Then it defines an objective function between experimental and calculated size distribution which is minimized thus estimating process parameters. gPROMS utilizes the following methods for the solution of ODE's and parameter estimation.

- gPROMS contains two solvers for ODE's, DASOLV and SRADAU. Where as the first one is based on backwards difference method, the second is based on the fully implicit Runge-Kutta method. Based on the documentation DASOLV has been chosen as solver for the length domain as it is good enough to solve ODE's with no oscillatory behaviour.
- For parameter estimation, only one solver was available on gPROMS. MAXLKHD firstly will solve the ODE' using the DASOLV solver, as pointed out above. The combination of the ODE with the set of constrains supplied by the user, turns the problem into a nonlinear programming problem (NLP) which can be solved using the sequential quadratic programming (SQP) method. More information on the solution methods can be found in the gPROMS documentation.

The results of this routine are a set of estimated values for k_α , $AggFac$, P_1 and P_2 one for each flow rate and their respective confidence intervals.

Estimation of the shear rate in turbulent flows

Under turbulent condition the value of $\dot{\gamma}$ can be derived from the following equation:

$$\dot{\gamma} = \sqrt{\frac{\epsilon}{\mu}} \quad (3.5)$$

where μ is the kinematic viscosity (taken as the one for water 1.00×10^{-6}) ϵ is the turbulent dissipation rate (m^2/s^3) estimated as:

$$\epsilon = \frac{2fU^3}{D} \quad (3.6)$$

where $4f = 0.316Re^{0.25}$, U is the flow velocity (m/s) and D is the pipe diameter (m)(Roelands *et al.*, 2003). It was found that the relation between U and G can be linearized. For the present geometry and fluid properties the linearized expression of the shear rate against the flow velocity reads as follows: $\dot{\gamma} = 0.5294U - 340.61$

3.11 CFD methodology

Introduction

CFD simulation provides a comprehensive analysis of flow features where other methodologies cannot. For example, it allows the analysis of systems where experiments are not possible, as well as providing comprehensive visualization of flow variables which would be inaccessible otherwise (turbulent dissipation rates, local shear rates, etc.).

In order to create a simulation it is important to gather as much information about the system as possible, i.e. geometry, flow specifications, fluid properties, boundary conditions and initial conditions. Once this information is gathered a CFD analysis can be performed by using an adequate software which usually requires the following information (Eesa, 2009):

- A matrix of points where the CFD variables can be stored. Velocity, turbulence kinetic energy, concentrations.
- Boundary conditions. Needed to define velocity, concentration, turbulence level at the boundaries of the problem. Inlets, outlets, walls, symmetries.

- Fluid properties which will define the behaviour of the fluid. For example, viscosity, thermal conductivity or density.
- A fluid model which determines the equations to be solved. Examples are: $k - \epsilon$, $k - \omega$, Shear Stress Transport (SST), Large Eddies Simulations (LES) or Direct Numerical Simulations (DNS).
- Initial conditions. They are an initial guess from which the equations start the iteration routine.

The following diagram shows the stages involved in a CFD simulation including feedback loops aiming to amend common bugs in the programming routine (Eesa, 2009).

Turbulent and laminar regimes were simulated in both, the mixing and contacting zone after the Y-junction where kinetic energy dissipation, shear stress and micromixing time were characterized. Firstly, for the mixing area Y-Junctin 2D geometry was built in DesignModeler ANSYS® and discretized using the ICEM meshing tool to a total of 35090 elements.

Geometry and meshing

Geometry A 2D geometry was created based on the experimental design used for laboratory testing. It consist of a Y junction with a 60 degree angle between the sort arms. A long pipe of 90cm makes the outlet where mixing occurs. Details of the dimensions are shown in Figure 3.12. In order to increase the mesh quality and avoid triangular elements, the junction element was considered as a trapezoidal region.

A 2D geometry was selected as the problem is symmetric along the vertical plane although it limits the systems description. For example, features such as mixture in the horizontal plane are not identified. Also, engulfment of the jets as described in literature (Fani *et al.*, 2013; Schikarski *et al.*, 2016) cannot be simulated with 2D geometry.

Meshing The geometry was discretized utilizing a structured grid of rectangles. A bi/geometric law was used to increase resolution near the walls and around the junction section where high velocity gradients are expected. Additionally, in order to assure that the solution is not influenced by the discretization and optimize computational resources, a mesh independent test was carried out. This required the generation of

various meshes with an increasing number of nodes until the solution showed independence from mesh size. The so obtained mesh contained 35090 cells. Mesh quality is high, yielding 68% of the elements between 1 and 4.8 aspect ratio.

Before exporting the mesh to the pre-processing software, mesh was extruded by one element, as is required by CFX.

Pre-processing For model set-up, ANSYS CFX 17-Pre was used. A shear stress transport (SST) model with automatic wall function provides a higher level of accuracy for modelling flow in pipes. It is based on $K - \omega$ models although it utilizes a bending function which switches to $k - \epsilon$ far from the wall.

Transported species (Zn , OH^- and CO_3^{-2}) were introduced into the material section. CFX treated material as transport scalars was ruled by Equation 2.29. Where diffusion terms were neglected as convection it is believed to be the most important contribution (discussed in Section 7.8).

Inlets were defined with velocity and concentration boundary conditions. A range of normal speeds were fed into the model with values of 0.075, 0.115, 0.16 and 0.32 m/s. Outlets were considered as pressure outlets with a 0 Pa pressure and walls as 0 velocity. A symmetric boundary condition was used on both the two vertical planes. Concentration was introduced as a mass fraction of the following components Zn, CO₃ and OH. They were introduced as user defined functions (UDF) with a value of 0.1M, 0.1M and pH=8 respectively which were latter converted to mass fraction using the following UDF:

$$W\%_i = \frac{c_i * Mm_i}{1000 + c_i * Mm_i} \quad (3.7)$$

For modelling the driving force of the reaction, supersaturation (ss), Equation 3.8 was defined using the K_{sp} value of hydrozincite Schindler *et al.* (1969) ($\log K_{sp} = -14.85$). In order to avoid indetermination with logarithms, the supersaturation will avoid unity values by using a maximum function which limits the value of supersaturation to 1.000001.

$$ss = \max \left(\frac{[CO_3^{-2}]^{0.4} [Zn^{+2}] [OH^-]^{1.2}}{K_{sp}}, 1.000001 \right) \quad (3.8)$$

The source term of the scalar transport equation $S_{i\alpha}$ has been computed using a classical nucleation expression (Mullin, 2001) from which the nucleation rate J (number

of crystals per second per volume) is obtained. Exponential and pre-exponential factors were obtained from induction time experiments ($AB=3.98e21$ and $BB=449$).

$$J = AB \exp\left(\frac{-BB}{\ln(ss)^2}\right) \quad (3.9)$$

The nucleation rate ($\# m^{-3}s^{-1}$) was then converted into production rate ($kg m^{-3}s^{-1}$) in the source terms S_α by Equation 3.10 from which the nuclei radius was assumed to be 28nm as shown by the XRD diffraction pattern.

$$S_{i\alpha} = -\nu_i \frac{\pi}{6} R_{crys}^3 \frac{\rho_{cry}}{M m_{crys}} M m_i J \quad (3.10)$$

Post-processing A number of variables has been studied in this work aiming to obtain information about the mixing dynamics of the system. They were introduced as an expression in the CFD-Post and then contour plots were extracted. The selected variables were: viscosity ratio, eddy viscosity, dissipation rate, Kolmogorov scale and Damkohler number. Mathematical definitions of this variable were given in Section 2.3. Visualization of the data will be given in the shape of contour plots.

Turbulent models

Reynolds Averaged Navier-Stokes (RANS) equations were solved using the shear tensor model (SST) which switches between $k-\epsilon$ and $k-\omega$ for accuracy near the walls You *et al.* (2015). Non-slip conditions were applied on the walls. A range of velocities (0.07, 0.115, 0.16 and 0.32 m/s) were set as the inlet boundary condition and 0 pressure in the outlet. Properties were taken as those of water at 25°C. Calculation of micromixing time follows the method described in Roelands *et al.* (2003).

3.12 Tracer experiments

Introduction

Complementary to CFD simulations, tracer experiments were performed to obtain further information on the flow dynamics in the Y junction and the tubular reactor. For example, residence time distributions (RTD) were obtained experimentally from time-pH profiles. Standard models of tank in series and plug flow reactor were then

fitted to the RTD thus obtaining the number of ideal reactor and the Peclet number. This section covers the description of the apparatus as well as the mathematical models.

Theory

Modelling the residence time distribution, these models are derived from ideal reactor models, such as CSTR or PF. The series of reactors, for example, account for the number of serial reactors needed to obtain certain RTD. The parameter to optimize in the serial reactors is the number of reactors (M). Although, preferable for batch reactors it could be used for plug flow and hence obtain the number of batch reactors needed to obtain the same RTD as a PF. The derivation of this model from a single batch reactor can be found in Fogler (2006b) where Equation 3.11 was obtained.

$$E(\Theta) = \frac{M^M}{(M-1)!} \Theta^{M-1} e^{-M\Theta} \quad (3.11)$$

Another one-parameter model utilized in this work is the dispersion model. It is derived from a laminar reactor with mass diffusion where convective and diffusive transport of species occurs. The parameter to optimize is the dimensionless number Peclet (Pe) and is obtained from a pulse experiment. Similar to the series of reactors the dispersion model is more appropriate to non-ideal plug flow reactors although is applicable to other types. The model equation in this case reads as follows:

$$E(\Theta) = \frac{1}{2\sqrt{\pi Pe}} e^{-\frac{(1-\Theta)^2}{4Pe}} \quad (3.12)$$

The application of these models together with impulse experiments will provide understanding of the residence time distribution.

Apparatus

The set-up used in this experiment is similar to the one described for inline SLS, only in this case a pH meter from Mettler Toledo was placed at the reactor outlet for measurement of OH^- concentration. It consisted of a Y-junction pipe followed by a tubular reactor 90cm long, a Marlow Watson 520s peristaltic pump and reservoirs for containing the reactants and the residues. The reactant reservoirs were filled with water.

Methodology

Initially the pump was set to pump 29.23ml/min of water through the pipe. A low flow rate was required as the time resolution of the pH meter is poor.

A tracer compound consisting on a *NaOH* solution was introduced into one of the inlets at time t_0 as an impulse. The outlet concentration ($C(t)$) is then followed with time. From this data $E(t)$ can be then calculated.

$$E(t) = \frac{C(t)}{\int_0^{\infty} C(t)dt} \quad (3.13)$$

A Mettler Toledo pH probe was place at the reactor outlet which read pH values 3 time every 5 min. The time resolution, although it could be improved, was sufficient for the purpose of the study. Delay is a common issue with pH measurements since equilibrium between electrodes is not reached immediately.

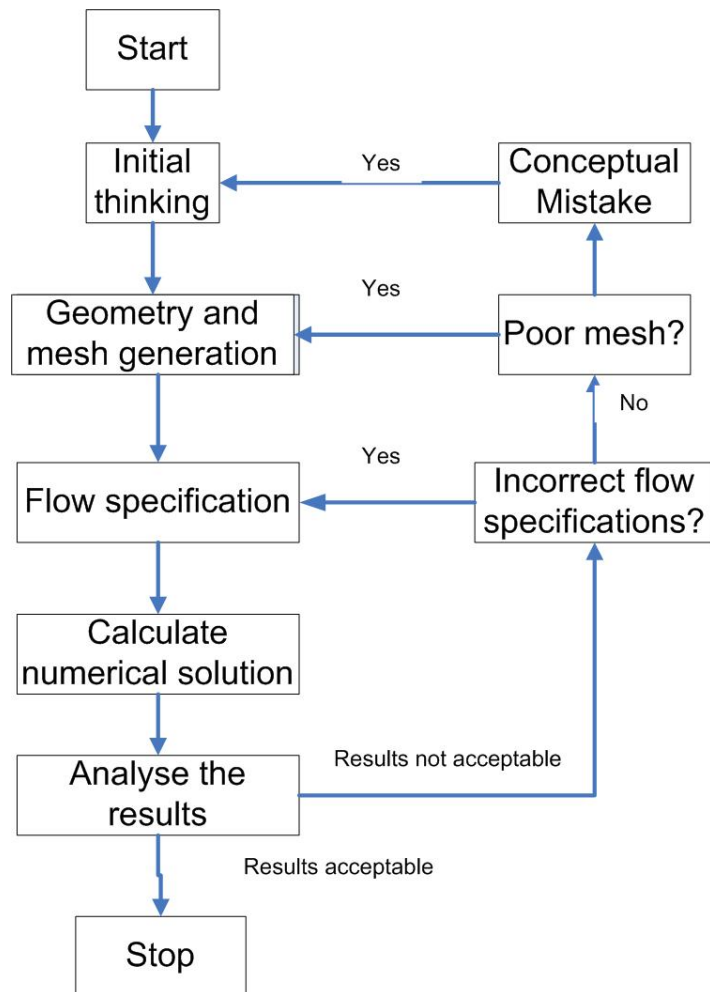


Figure 3.11: Flow diagram for the preparation of a CFD simulation. Feedback loops represent common problems found in simulation set-up Eesa (2009).

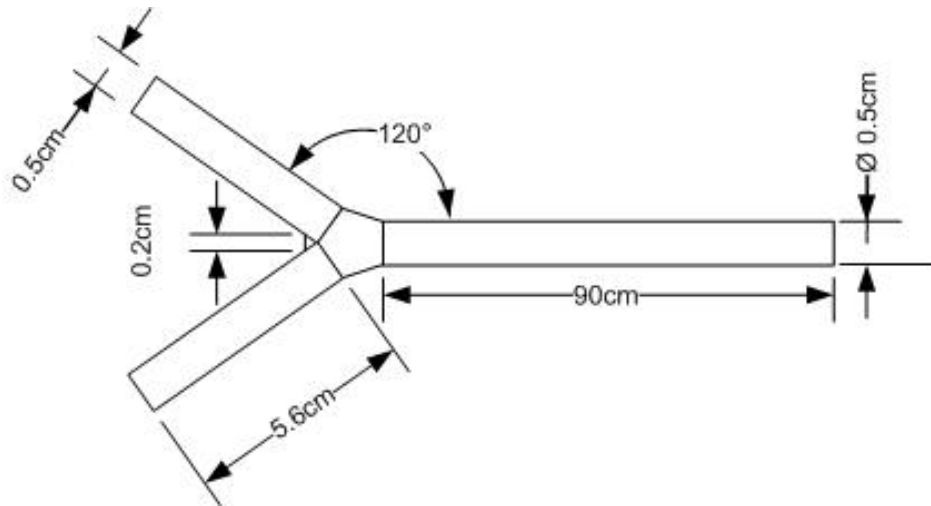


Figure 3.12: Y-Junction dimension utilized in the definition of the geometry for CFD study.

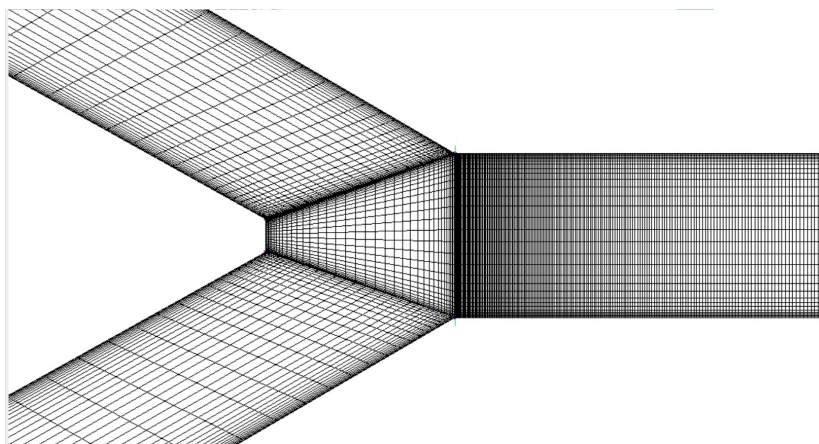


Figure 3.13: Details of the refined mesh used in this work after the mesh independence test.

3.12 Tracer experiments

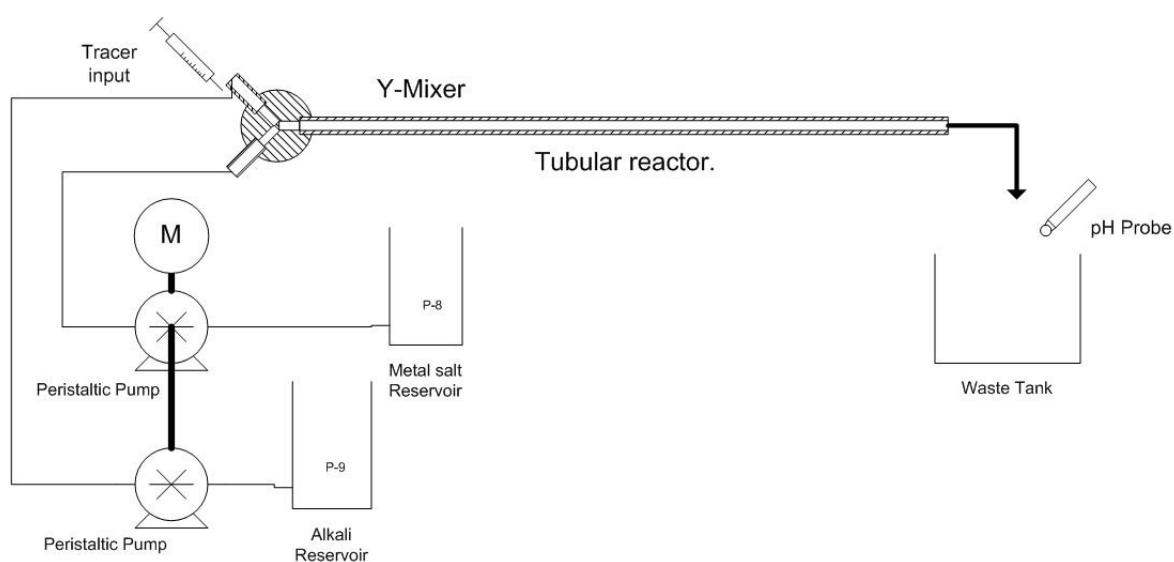


Figure 3.14: Experimental set-up for tracer experiments. A tracer was injected into one of the inlets and pumped through the system and its concentration recorded by a pH probe at the end of the reactor

Chapter 4

Zinc Carbonate Properties: Induction time, solubility and distortion of crystal structures

4.1 Introduction

Hydrozincite has caught the attention of researchers in materials with unique properties: when calcined it decomposes into ZnO a transparent semiconductor, its small crystal size makes it a highly porous material perfect as an adsorbent for medical catalytic purposes, The layered crystalline structure allows organic molecules to be included in the interstitial space between zinc structures, thus being suitable for use drug delivery system. The knowledge around this compound increases everyday although the perturbation of the crystalline structure, reaction rates and mechanism of precipitation still remain unclear. The vigorous character of this reaction impedes adequate control of crystal structures and morphology since kinetic products prevail over thermodynamic ones. In this work we measure the nucleation rate of hydrozincite from aqueous solution at over a wide range of supersaturations obtaining classical nucleation behaviour similar to other sparingly soluble compounds also observing the great interfacial tension, this being the reason for its insolubility.

The results of this study will allow engineers and scientists to design equipment which better controls the vigorous character of the precipitation of hydrozincite.

4.2 Hydrozincite equilibrium properties. Crystal structure, solubility and induction time

4.2.1 Experimental conditions

The products synthesized by the continuous Y junction reactor, described in 3.3.1, will be characterized in this section. The product will be described in terms of its crystal structure, including crystallinity and crystallite size, solubility and induction time. In order to achieve these objectives, analytical techniques such as powder XRD, atomic absorption spectroscopy and turbidity will be used.

4.2.2 XRD and crystal structure characterization

Phase identification of the synthesized product by XRD was carried out under a wide range of conditions such as pH, concentration, Zn^{+2}/CO_3^{-2} and magnesium dopant. They all found hydrozincite to be synthesis product corresponding with reference PDF 04-013-7572 (Figure 4.1). However, significant differences with respect to the reference were found in terms of crystal imperfections. The differences can be observed in larger peak widths which were found to vary with process conditions. The literature reports wider peaks for synthesis methods involving reactive crystallization, as in the present study (Fujita *et al.*, 1995; Hu *et al.*, 2010; Liu *et al.*, 2007). On the other hand, hydrothermal synthesis reports increased crystallinity due to the slower release of carbonate into the solution (see section 2.6.2).

Hydrozincite presents a particular structure consisting of the repetitive arrangement of $Zn(OH)_8^{-4}$ and carbonate in a layer type of structure. Section 2.6.4. Figure 4.2 shows the molecular arrangement of this structure as well as the crystal plane 100 which is parallel to the layers. The characteristic structure can be observed on the XRD patterns where the peak at $13^\circ 2\theta$ presents high intensity indicating that this plane is dominant in the crystal structure.

In order to illustrate the changes in crystal structure, hydrozincite has been synthesized in the Y-junction reactor under a number of Zn^{+2}/CO_3^{-2} ratios (0.4, 0.5, 1, 2, 2.5) with a zinc concentration of 0.1M. A summary of the experimental conditions is given in Table 4.1The product was then dried and milled in preparation to be analysed by XRD, these results are shown in Figure 4.3. A spectrum refinement performed

4.2 Hydrozincite equilibrium properties. Crystal structure, solubility and induction time

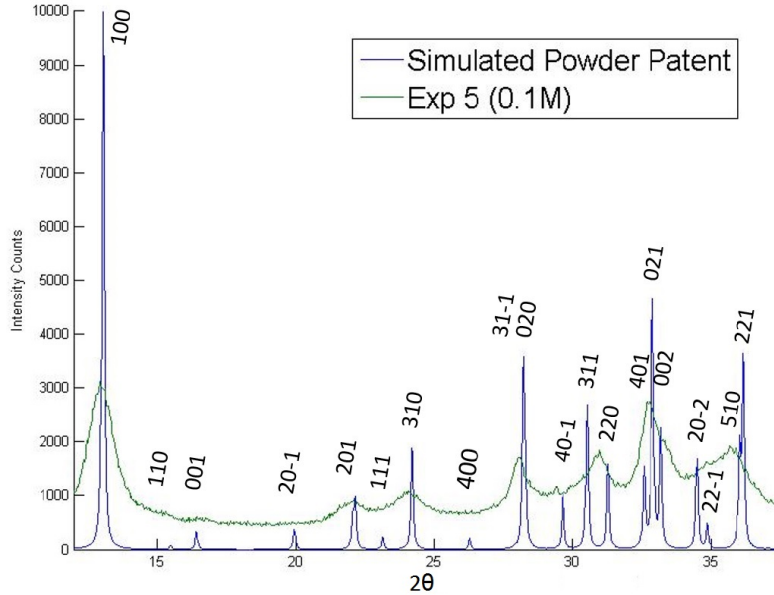


Figure 4.1: Hydrozincite $Zn_5(CO_3)_2(OH)_2$ reference spectrum and its corresponding planes against synthesized hydrozincite. Preferential plane 100 is found at 13 2θ .

on HighSoftwarePlus software revealed a crystallinity between 40 and 65%. The low crystallinity is believed to be the consequence of crystal imperfection transforming the structure into a more amorphous material. The crystallinity was found to increase as the Zn^{+2}/CO_3^{-2} ratio approached 1:1 where its maximum was found. Similarly, crystallite size computed from the Scherrer expression followed similar trend. Values can be seen in Table 8.1

Pawley analysis showed lattice distortions mostly, in the a direction. The standard deviation of this lattice parameter is significantly higher compared with b and c indicating that the preferential orientation characteristics of the layered compounds were distorted mainly in the direction perpendicular to the $Zn(OH)_8$ (Medas *et al.*, 2014).

Figure 4.4 shows the evolution of cell parameter a in Angstroms as a function of the zinc-carbonate ratio. It is observed that close to the stoichiometric ratio the cell parameters were similar to a perfect crystal (13.62Å). However, as the ratio increases the planar distances initially increase and then suddenly decrease. It is believed that the relative scarcity of CO_3 at high Zn/ CO_3 ratios prevent the inter layers structures to form normally the best crystalline structures were found when the carbonate was in large stoichiometric excess.

4.2 Hydrozincite equilibrium properties. Crystal structure, solubility and induction time

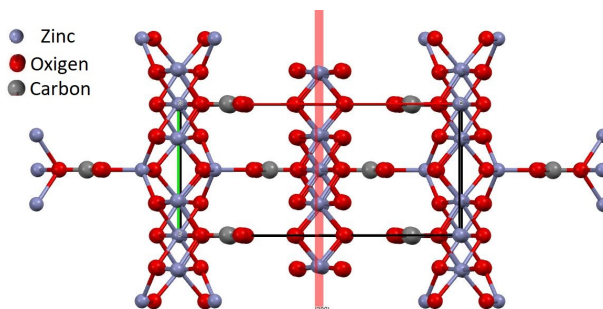


Figure 4.2: Molecular structure of hydrozincite showing the 100 plane. Interplanar distance of this plane widens or shortens as a function of the $ZnCO_3$ ratio

Table 4.1: Experimental conditions used for the assessment of crystal structure changes in hydrozincite synthesized in a Y-junction reactor

ExpID	$[ZnNO_3]$	$[Na_2CO_3]$	Ratio	Flow Rate (ml/min)
5	0.1	0.1	1	50.2
53	0.1	0.25	2.5	476.3
54	0.1	0.2	2	476.3
55	0.1	0.1	1	476.3
56	0.1	0.05	0.5	476.3
57	0.1	0.04	0.4	476.3

4.2.3 Solubility

This section evaluates the solubility of hydrozincite showing its speciation products, the solubility values were computed from Pitzer model simulation and experimental solubility studies. It attempts to understand core factors in the pre-crystallization stages of hydrozincite which will allow the understanding of the solid-solvent equilibrium as well as critically revising the data from the literature.

Firstly, this study describes the solid-solvent equilibrium using the equilibrium constants given in the literature for the expected species in the so called Ideal Species Contribution model (ISC). Please refer to Section 2.6.3 for the list of equations. Secondly, the same problem was solved using a commercial package, PHREEQS, which incorporates the Pitzer model to account for the ionic strength of the free molecules

4.2 Hydrozincite equilibrium properties. Crystal structure, solubility and induction time

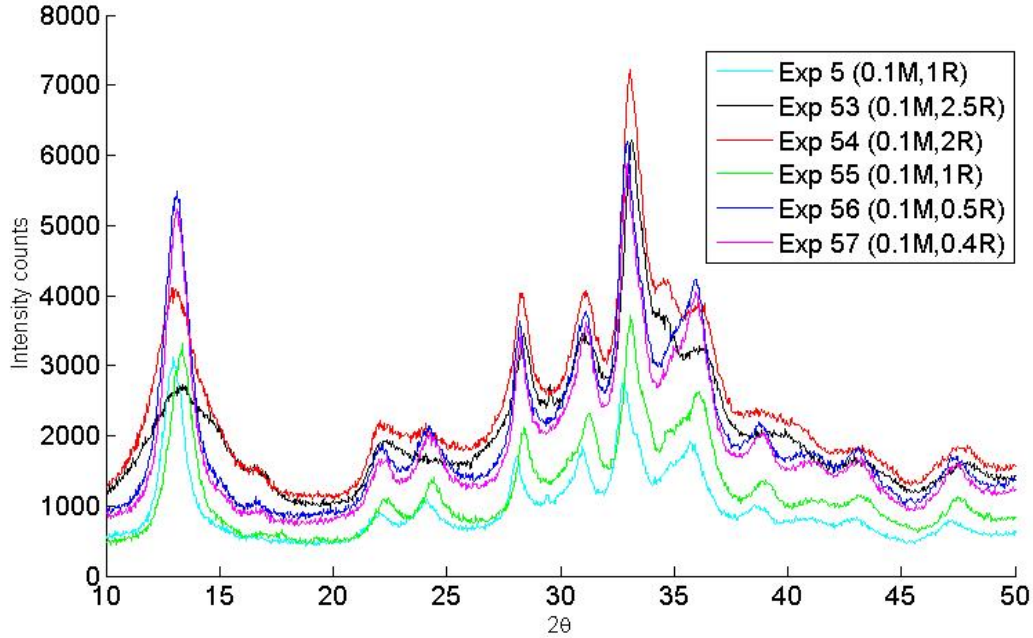


Figure 4.3: Hydrozincite spectrums synthesized at various Zn/CO_3 ratios showing widening of peaks. Peak at 12 2θ seems to widen as ratio increases.

(Reference to the software is made in Section 3.7.1). Finally, the experimental values of zinc ion concentration in solution were acquired by atomic absorption spectroscopy (AAS) following procedures in Section 3.7.1 which are to be compared with the results from ISC and PHREEQS.

When looking at the speciation diagram in Figure 4.5 computed using the ISC method it is observed that soluble zinc ions are most abundant at low pH. On the other hand, $Zn(OH)_2^0$, $Zn(OH)_3^-$ and $Zn(OH)_4^{2-}$ are the most common species at high pH, all of them being soluble. Along the intermediate region soluble species are instable against insoluble ones. Therefore around a pH of 7.5 the minimum solubilized zinc is found.

It is been reported that zinc ions in solution are capable of ionizing water molecules thus increasing its coordination number above four. Therefore species such as $[Zn(OH)(H_2O)_x]^+$ and $[Zn_2(OH)(H_2O)_x]^{3+}$ are present in the solution which in the presence of carbonate (either atmospheric or solubilized) precipitate in the form of hydrozincite or other species such as Smithsonite or zinc hydroxide Wang & Muhammed (1999). The ioniza-

4.2 Hydrozincite equilibrium properties. Crystal structure, solubility and induction time

Table 4.2: Crystallinity (%), Scherrer radius (\AA) and unit cell parameters (\AA) obtained from the XRD spectrum refinement of hydrozincite powder synthesized at various ratios of Zn^{+2}/CO_3^{-2}

	Zn/CO3 ratio					σ
	2.5R	2R	1R	0.5R	0.4R	
Crystallinity	51.15	57.15	59.54	44.97	42.86	
$r_c(12\ 2\theta)$	52.01	50.15	91.43	42.15	28.34	
a (\AA)	13.36	13.70	13.82	13.76	13.68	0.177
b (\AA)	6.43	6.30	6.401	6.39	6.42	0.051
c (\AA)	5.28	5.45	5.51	5.45	5.49	0.089
α	90	90	90	90	90	0
β	96.09	96.24	95.36	95.36	95.17	0.482
γ	90	90	90	90	90	0

tion effect of the zinc ions is likely to be the start of the crystallization of hydrozincite. Zinc ions arrange them-selves into high coordination number structures also found in the crystalline structure of hydrozincite.

The PHREEQS software for species simulation has been introduced in Section 3.7.1. Table 4.3 summarizes the conditions at which the equilibrium stage was calculated which contains a range of ionic strengths and pH as well as results for the concentration of zinc in solution. Figure 4.6 shows the results plotted as a function of pH. The minimum in the concentration of zinc ions is found at around pH 10. The presence of this minimum is comparable to the minimum found in the ISC model. However, its position is displaced by 2 pH units towards higher pH as well as the concentration of zinc in solution was found to be one order of magnitude lower. The additional consideration of the Ionic Strength using the Pitzer model is likely to be the cause of the discrepancy between the models.

Finally, in the case of the experimental solubility studies, the samples were prepared following the methodology described in the Section 3.7.1. Table 4.4 shows the values of pH, zinc concentration and carbonate concentration as calculated from the pH meter and AAS data. The concentration of carbonate was computed from the concentration

4.2 Hydrozincite equilibrium properties. Crystal structure, solubility and induction time

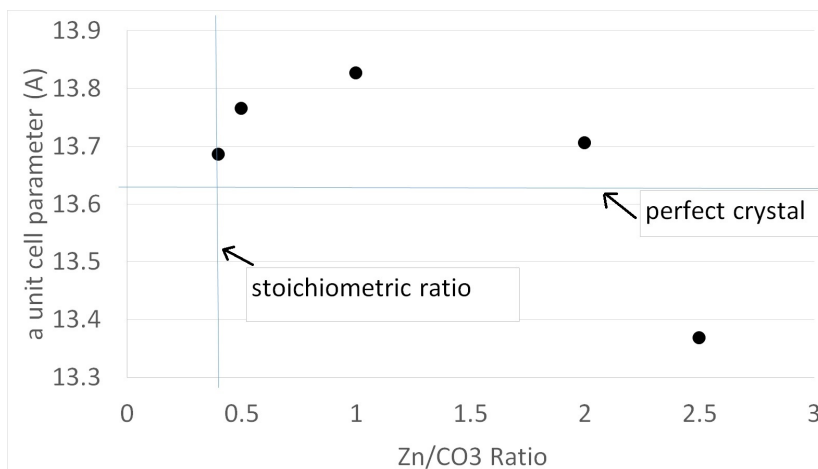


Figure 4.4: Unit cell parameter a as function of the ratio between reactants. Close to stoichiometric ratio, the unit cell parameters resemble those of the perfect crystalline structure. After an initial increase, the value of a suddenly decreases.

of zinc assuming that they were in stoichiometric ratio and that there is not exchange with the atmosphere and that containers were sealed from the atmosphere.

Results from AAS are shown in Figure 4.6 and indicate the presence of a minimum in solubility around pH=10. When compared with thermodynamic calculations it shows certain deviations probably caused by non-ideal behaviour. Simulations by PHREEQS and ISC both predict the same minimum but a difference in the order of magnitude both in the amount of zinc dissolved and in the pH range. It is believed that this difference arises from the method followed to obtain the equilibrium data. For example,

Table 4.3: Set of conditions used for the simulation performed in PHREEQS.

pH	Ionic Strength	$[Zn]$	Temperature
8.23	0.104	2.08×10^{-5}	20
8.361	0.105	1.68×10^{-5}	20
9.492	0.139	2.52×10^{-6}	20
9.898	0.163	1.19×10^{-6}	20
10.635	0.192	1.64×10^{-6}	20
11.159	0.198	1.27×10^{-5}	20

4.2 Hydrozincite equilibrium properties. Crystal structure, solubility and induction time

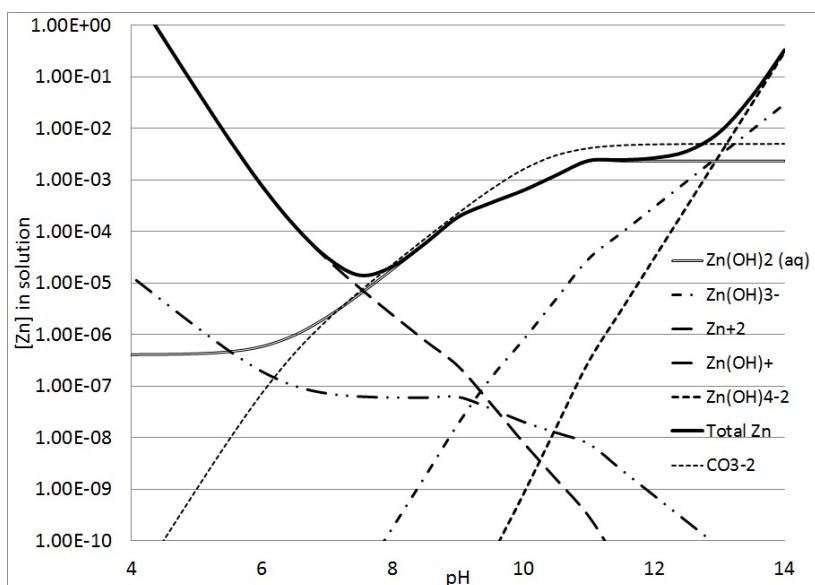


Figure 4.5: Speciation diagram in the system zinc-carbonate-water as function of pH calculated from the species ideal equilibrium (ISC). It includes the species, Zn^{+2} , $Zn(OH)_2^0$, $Zn(OH)_3^-$, $Zn(OH)_4^{2-}$ and CO_3^{2-} .

PHREEQS utilizes the Pitzer model which incorporates ionic interaction between the species, therefore reducing the activity of the Zinc ions which shows in the simulation, as lower solubility. ISC, on the other hand, only uses solubility products at 0 ionic strength where no ionic interactions are present hence showing the largest value of solubility. In spite of this trends which occurred on three similar cases.

Regarding the experimental results of solubility, it needs to be clarified that despite precipitation occurring at higher or lower pH, the final product remains zinc carbonate, see Figure 5.13. Thermodynamic studies reported in the literature for the system $Zn-CO_2-H_2O$ predicts $ZnOH_2$ ZnO at high pH and $ZnCO_3$ $ZnOH_2$ at low pH (Preis & Gamsjäger, 2001). However, despite the intensive XRD analysis performed on fresh and riped samples, such products were not found. The fast kinetics of the precipitation enhanced kinetics products, this is believed to be the reason behind the consistent synthesis of hydrozincite across experiments regardless of the conditions.

4.2 Hydrozincite equilibrium properties. Crystal structure, solubility and induction time

Table 4.4: pH, zinc ion concentration and carbonate ion concentration used for computing the solubility product, K_{sp} , of hydrozincite. Temperature was set to 20C using a heating block and a chiller.

ExpID	pH	[Zn] (mol/L)	[CO ₃ ⁻²] (mol/L)	log K_{sp}
7	11.02 ± 0.14	7.117x10 ⁻⁶ ± 2.117x10 ⁻⁷	2.847x10 ⁻⁶	-10.95
8	8.62 ± 1.07	4.977x10 ⁻⁵ ± 2.107x10 ⁻⁵	1.991x10 ⁻⁵	-12.64
9	8.69 ± 0.01	1.026x10 ⁻⁵ ± 2.687x10 ⁻⁵	4.103x10 ⁻⁶	-13.51
10	10.08 ± 1.04	8.736x10 ⁻⁶ ± 5.281x10 ⁻⁶	3.495x10 ⁻⁶	-11.95
11	13.47 ± 0.42	1.198x10 ⁻⁴ ± 7.031x10 ⁻⁵	4.792x10 ⁻⁵	-6.27
12	7.31 ± 0.05	1.606x10 ⁻⁴ ± 1.924x10 ⁻⁵	6.423x10 ⁻⁵	-13.50

4.2.4 Induction time

Figure 4.7 presents a typical induction time measurement in which turbidity sharply increased after reactants were mixed. A latent time is observable between reactants being mixed and the first change in turbidity which was taken as induction time. As mentioned in Section 2.2.3 the value of this induction time is not a fixed value but instead is distributed around in a probability distribution of stochastic a nature.

In this case, induction times were obtained from averaging at least 3 results of latent times from turbidity measurements. In some cases the obscuration change was fitted to a first order plus delay system thus conveniently obtaining induction time as one of the optimization parameters.

It is well known that induction time measured in a batch reactor greatly depends on the power input supply given by the stirring system (Mullin, 2001). In the present study the stirring rate was not considered as a variable but it was kept constant throughout the experiments. Recent studies under controlled power input and shear rate have shown the decreasing exponential correlation of induction time with power input (Liu & Rasmuson, 2013). When a classical nucleation expression was applied a change in the pre-exponential factor was observed. This indicates that the nucleation barrier remained constant but it was the frequency of attachment which decreased the nucleation rate. With this evidences, we can assume that all measurements in the present study are equally displaced from an ideal nucleation rate by an unknown factor which is

4.2 Hydrozincite equilibrium properties. Crystal structure, solubility and induction time

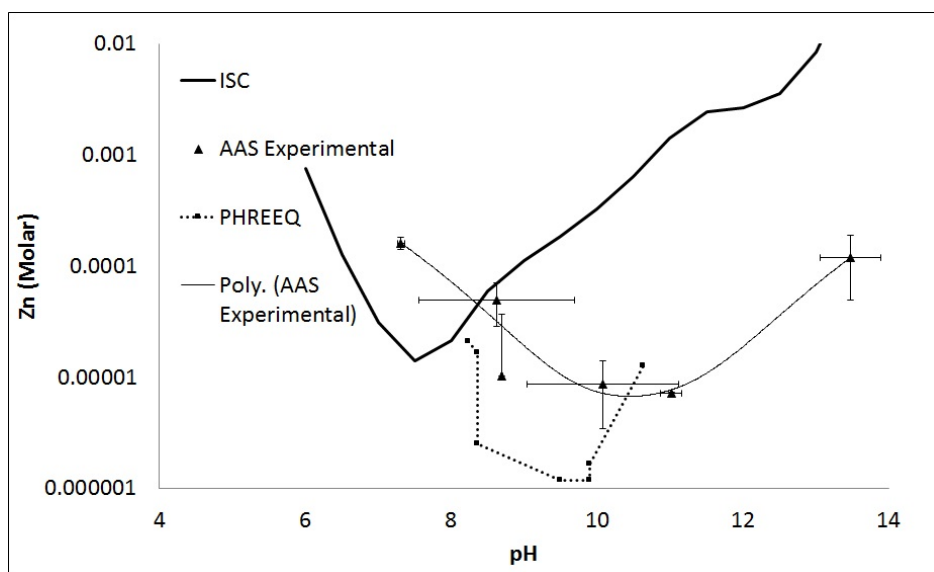


Figure 4.6: Comparison of zinc ion concentration obtained by AAS, simulated with PHREEQ and computed from the ideal species contribution (ISC). A common minimum is found in all the results. Displacement among them may be a consequence of the method used.

constant as stirring rate is constant (Liang *et al.*, 2004). Therefore, interfacial tension measurements remain valid as it is only function of the nucleation barrier.

Data collected from turbidity experiments are shown in Table 4.5. In order to cover the whole range of supersaturation, concentration of reactants and pH have been varied. Sodium carbonate and sodium and bicarbonate provided high and low pH in the desired range whereas tuning concentration provided further refinement. Various experimental limitations were found in the course of these experiments. Firstly, a maximum supersaturation of 5×10^7 was found to be the upper limit since the time resolution of the H.E.L Automate equipment was reached. In this venue we observe how the standard deviation of the induction time is in the order of magnitude of the measurement. Also measurements taken under these conditions raise concerns about the validity of the assumptions such as if mixing time needs to be considered. The lower limit, on the other hand, was found at low concentrations, where turbidity is in the order of magnitude of the noise detected by the turbidity probe.

Induction time values of hydrozincite synthesized by bicarbonate precipitation were

4.2 Hydrozincite equilibrium properties. Crystal structure, solubility and induction time

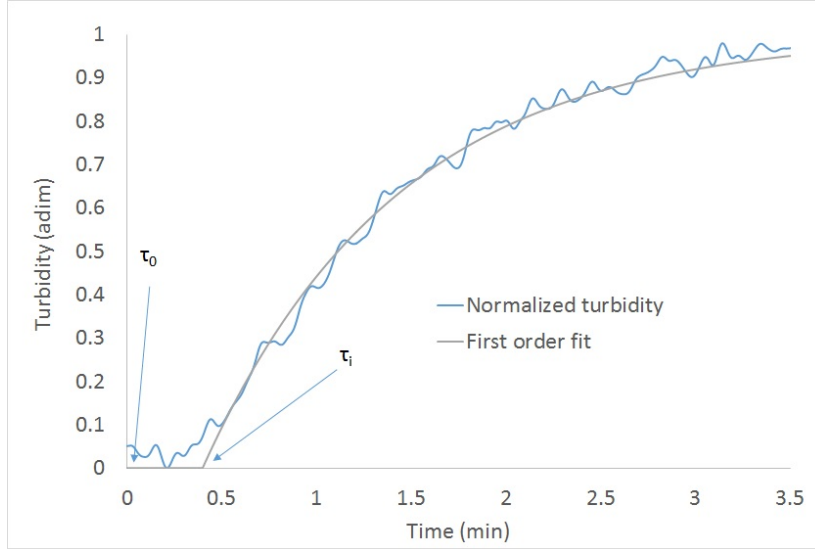


Figure 4.7: Turbidity vs. time. Mixing occurs at time τ_0 . Turbidity increases after induction time τ_i

found to have the lowest values. As the classical nucleation predicts, induction time increases with decreasing supersaturation. A simple observation of the definition of supersaturation for this system, as Equation 3.8, shows the sensitivity of this expression from the hydroxide ion concentration. In other words, from pH. Therefore, a decrease in pH hugely decreases the supersaturation and hence the induction time. From the point of view of chemistry, the decrease in supersaturation is a consequence of the presence of a bottleneck in the equilibrium carbonate bicarbonate. The predominance of bicarbonate at low pH does not favour precipitation since the bicarbonate ions are not part of the crystalline structure whereas carbonate is. This means at low pH carbonate ions required for precipitation are not readily available to form the hydrozincite structure which as a consequence slows the crystallization process.

The values of standard deviation shown in Table 4.5 are large compared with their averaged values. They were computed from the results of 3 to 6 repetitions of turbidity measurements. The large variability is an expected consequence of the stochastic nature of crystallization. The literature has shown that Poisson distribution is a reliable model to predict this variability (?). This one-variable distribution has the property of having its variance equal to its mean which means that its standard deviation will always be in the range of the average value. Therefore, the large variations were expected as they

4.2 Hydrozincite equilibrium properties. Crystal structure, solubility and induction time

Table 4.5: Results of the induction time of hydrozincite with a variety Zinc and coprecipitants (carbonate or bicarbonate) concentration. The use of carbonate or bicarbonate defined the pH. Supersaturation was defined based on expression 3.8. t_{ind} is the induction time in minutes and $t_{ind}\sigma$ is the standard deviation of the induction time measurements.

[Zn]	[HCO ₃ ⁻]	[CO ₃ ⁻²]	pH	SS	t_{ind} (min)	$t_{ind}\sigma$ (min)
0.01	0.02	0	6.7	2572.8	110	-
0.005	0.01	0	6.8	1285.2	180	-
0.0025	0.005	0	7	846.3	588	-
0.02	0.02	0	7	11788.1	6.15	2.7
0.01	0.01	0	7	4466.8	15.051	2.34
0.01	0	0.01	10	17782794.1	1.5	0.34
0.02	0	0.02	10	46929075.0	0.435	0.295
0.3	0.3	0	7	522359.8	2.85	0.21
0.1	0.1	0	7	112201.8	3.83	1.23

are intrinsic properties of the crystallization process.

Classical nucleation theory takes nucleation rate (J) as being inversely proportional to induction time (t_{ind}). For this reason, this proportional factor depends on factors such as detectable volume fraction α_c of crystal as well as growth rate G_c as expressed in Equation 4.1 (Brandel & ter Horst, 2015) which are not easily accessible. The logarithmic plot of $1/t_{ind}$ against $\ln(ss)^2$ is a well accepted method to obtain the surface tension (γ) Utilizing the Log-Log plot the influence of the stirring rate will be moved to the same proportional term as explained above. However, the surface tension is believed to depend on concentration, but it was not possible to separate this factor from the surface tension.

$$J = \frac{3\alpha}{\pi G^3 t_i^4} \quad (4.1)$$

$$\frac{1}{t_{ind}} = J = -A \exp\left(\frac{16\pi\gamma^3\nu^2}{3k^3 T^3 \ln(ss)^2}\right) \quad (4.2)$$

4.2 Hydrozincite equilibrium properties. Crystal structure, solubility and induction time

Where γ is the surface tension in (J/m^2), ν is the ionic volume k_b is the Boltzmann constant and T is the temperature in kelvin.

The log-Log plot of inverse induction time ($1/t_{ind}$) and supersaturation squared (SS^2) was utilized to obtain the slope of the trend (B) which corresponded to the activation energy of the process. Also the pre-exponential factor can be obtained although, as pointed out previously, is not significant as its value is a function of the power input and detectable volume fraction.

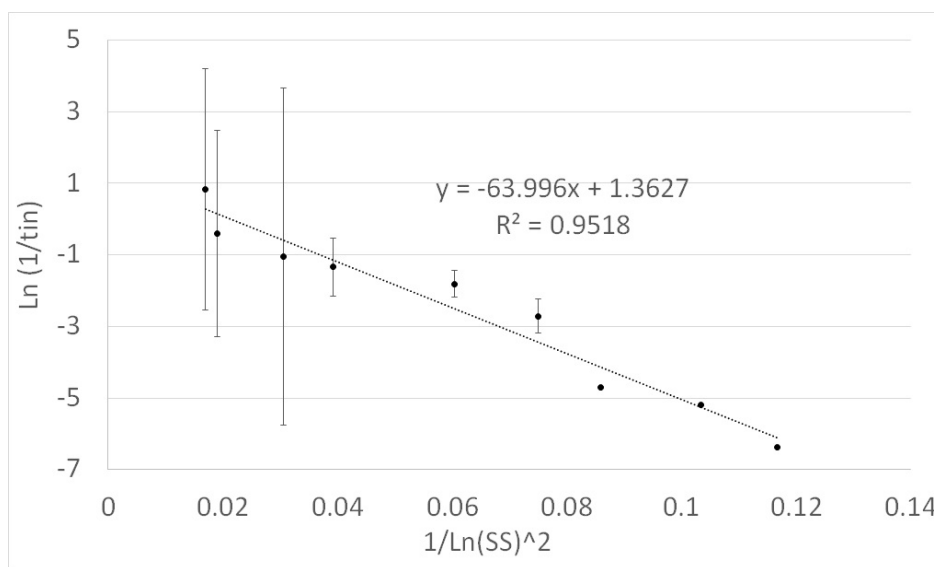


Figure 4.8: Nucleation rate ($\ln(J)$) vs. $\ln(SS)^{-2}$ obtained from induction time experiments. Large error bars are inherently linked with stochastic process such as nucleation. The linear trend indicates a good agreement with classical nucleation theory

The slope of the fitted curve can be compared to similar systems such as calcium carbonate, barium carbonate etc. Söhnel & Mullin (1978). Table 4.6 compares the values of slope for the different compounds. Notice that the slope is a measure of the nucleation barrier which the classical nucleation theory assumes to be independent of process conditions such as agitation or set up. Although, hydrozincite present high values compared with other reference, This compound has shown similar behavior in other works where was found to have the smallest of the induction times Bucca *et al.* (2009). It indicates that molecules encounter a low interfacial tension to overcome in the process of precipitation

4.2 Hydrozincite equilibrium properties. Crystal structure, solubility and induction time

Table 4.6: Slopes of classical nucleation theory fittings from various references compared with this work. Hydrozincite shows the highest of the slopes which coincides with the largest pK_{sp}

Compound	Slope	Reference	pK_{sp}	Reference
Calcite	8.12	Söhnel & Mullin (1978)	8.48	Benjamin (2002)
Struvite	9.93	Hanhoun <i>et al.</i> (2013)	13.36	Bhuiyan <i>et al.</i> (2007)
Witherite	27.2	Söhnel & Mullin (1978)	8.56	Busenberg & Plummer (1986)
Hydrozincite	64.0	This work	14.85	Schindler <i>et al.</i> (1969)

Based on the slope (B) of Figure 4.8 and the high values of super saturation the systems resemble an homogeneous system. Although, based on Mullin (2001) a straight line is inconclusive for characterizing homogeneous nucleation, when compared with other systems, the high value of the slope leads one to think that homogeneous nucleation is even more likely in the case of hydrozincite. From the value of the slope the surface tension can be calculated clearing γ from Equation 4.2 (Nielsen & Söhnel, 1971):

$$B = \frac{16\pi\gamma^3\nu^2}{3k_b^3T^3} \quad (4.3)$$

B takes the value of the slope (63.9955), ν is the molar volume computed as ($3.25\text{cm}^3/\text{mol}$) and temperature (T) is 300K. Calculation of the interfacial tension, using Equation 4.3 shows values in the order of magnitude of similar compounds, however its value is the lowest of all ($0.0512\text{J}/\text{m}^{-2}$). This indicates a small energy barrier for molecules to attach to the nuclei.

Results from Medas *et al.* (2014) showed that induction time values for hydrozincite have a similar order of magnitude than those for calcite (Söhnel & Mullin, 1978). In the present case, the results for hydrozincite differ in one order of magnitude with the ones from Medas *et al.* (2014) 0.24 to 0.38 (Jm^{-2}).

Although the value of slope and interfacial tension are larger compared with similar compounds, hydrozincite shows the lowest induction time of them all. Also its solubility value is the lowest which indicates the difficulty of this compound to remain solubilized

4.2 Hydrozincite equilibrium properties. Crystal structure, solubility and induction time

compared with Struvite, calcite or witherite (Hanhoun *et al.*, 2013; Söhnel & Mullin, 1978).

Nuclei radii was calculated using the expression proposed by Mullin (2001) which includes the volume of molecules in a unit cell ν ($3.24 \times 10^{28} m^3$). The expression reads as:

$$r_c = -\frac{2\gamma\nu}{kT \ln(ss)} \quad (4.4)$$

Equation 4.4 implies an inverse law between r_c and $\ln(ss)$ hence a hyperbolic trend is expected. The relation describes the observed decrease of nuclei size with supersaturation.

The values of radius resulting from the Equation 4.4 present an unusual small value ranging between 1.3 and 0.5 nm. However it is understandable that large values of supersaturation yield smaller crystals.

Table 4.7: Nuclei size computed from Equation 4.4. The nuclei size decreases with increasing supersaturation. However, due to the small interfacial tension the variation in size with supersaturation is not extremely acute.

SS	t_{ind}	Nuclei size (nm)
2572.8	110	1.073
1285.2	180	1.177
846.3	588	1.250
11788.1	6.15	0.899
4466.8	15.051	1.002
17782794.1	1.5	0.585
46929075.0	0.435	0.477
522359.8	2.85	0.640
112201.8	3.83	0.725

4.3 Phase and Morphology of the Hydrozincite Product.

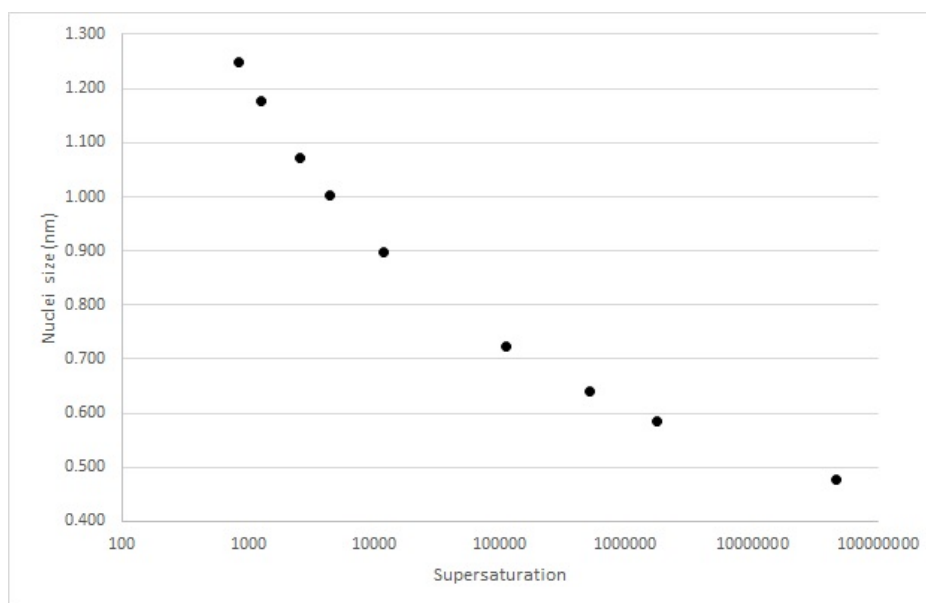


Figure 4.9: Nuclei radius vs. supersaturation based on Equation 4.4 for interfacial energy = $0.051(J/m^2)$. It shows small nuclei radius.

4.3 Phase and Morphology of the Hydrozincite Product.

4.3.1 Structure change of hydrozincite as function of pH

Figure 5.13 shows XRD patterns of samples synthesized in a tubular reactor (as introduced in Section 3.3.1) at various pH. Experiments with ID 41, 42 and 43 were obtained by precipitation of zinc nitrate with a mixture of carbonate and bicarbonate salts with a yielded pH of 6.84, 6.44 and 6.23 respectively. On the other hand, Sample 54 was synthesized with only carbonate salt as precipitant.

Sample 54 was found to have an acute amorphous character observable from the broad peaks and high background. The amount of crystalline material in the sample content has been previously quantified as 59.54% based on the ratio, background area/pick area shown earlier in this chapter (Section 4.2.2). Oppositely, spectrums found at low pH seem to have an increased crystalline content as the shaper peaks indicate. It is necessary to clarify at this point that, although the background does not change, the peak area increases due to the increased height of the peaks. Therefore,

4.3 Phase and Morphology of the Hydrozincite Product.

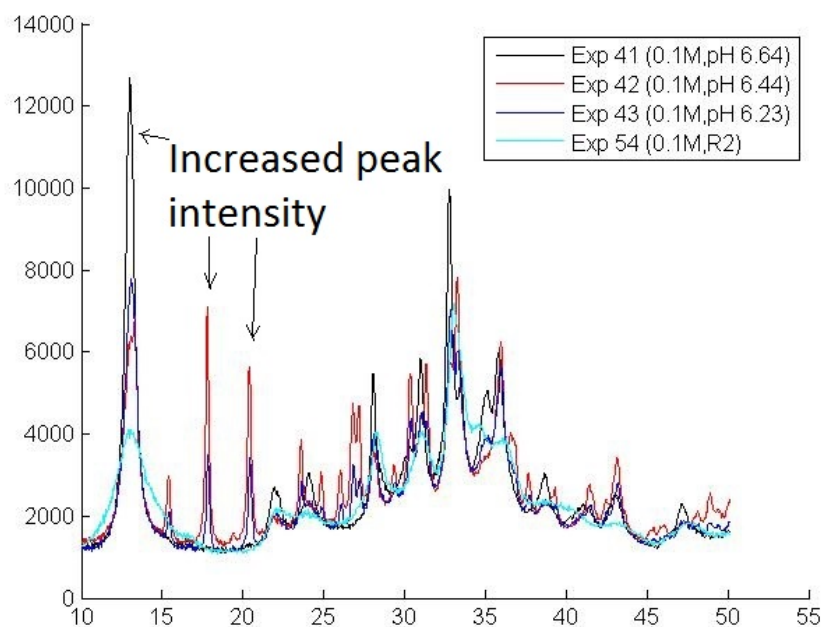


Figure 4.10: XRD of spectrum of hydrozincite synthesized at various pH compared to a reference sample. Experiment 54 was prepared with sodium carbonate at 7.2 pH. A higher number of counts were found at lower pH indicating a better crystalline structure.

the total crystallinity increases.

Phases were characterized using HighScorePlus from which a single phase of hydrozincite was identified. Despite the presence of extra peaks at lower pH, the position of the remaining peaks is sufficient for the software to pick up the right solid phase. When comparing the hydrozincite ideal spectrum (Figure 4.2) with the product synthesized in this work (Figure 4.2), both at high and low pH it can be concluded that the low pH product shares more peaks with the ideal sample. As explained in section 4.2.2, those differences are only a function of the increased crystallinity of the sample, in other words, how well the atoms are arranged in the crystal structure.

Therefore, base on results from HighScorePlus, and the comparison of the ideal spectrum with the samples at low and high pH, it is concluded that, despite the presence of extra peak in the low pH, all the products, independently of the pH, correspond to hydrozincite.

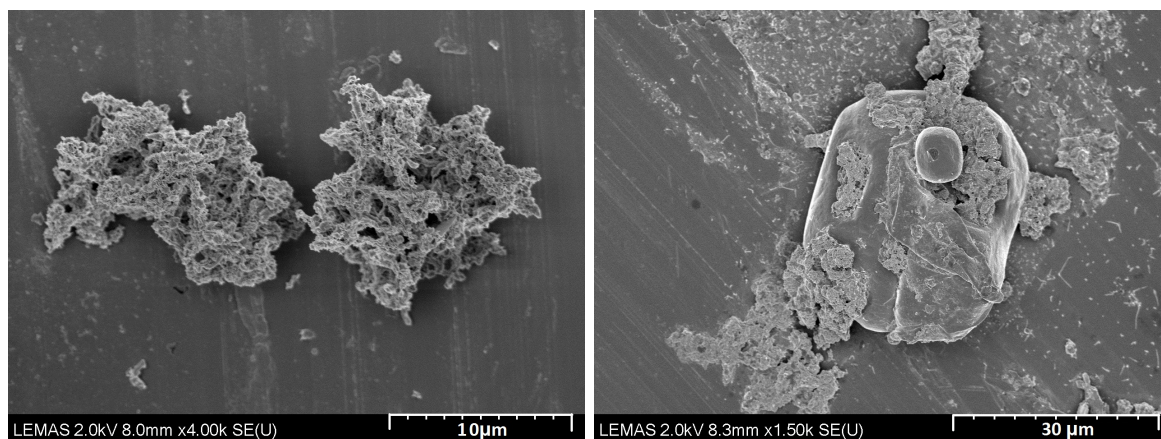
4.3 Phase and Morphology of the Hydrozincite Product.

Morphology also seems to be largely influenced by the pH conditions. For example, Figures 4.11(a) and 4.11(b) show products synthesized with zinc nitrate salt and two different sodium salts, carbonate and bicarbonate. Aggregates of plate like structures are easily observable at low pH ranges, whereas aggregates of rounded particles are readily observable in the carbonate products.

In order to explain this change in morphology the effect of supersaturation, speciation as well as surface chemistry are to be considered. On one hand, the decreased supersaturation at which the lower pH precipitation takes place (which also implies larger induction times) allows the atoms to find a lower energy location in the crystal structure. As a consequence, more crystal like structures can be found. On the contrary, larger supersaturation yields smaller particles with less crystal-like features which easily aggregate. On the other hand, pH alters the surface chemistry of the carbonates. The change on the surface charge distribution, a consequence of different pH, is likely to additionally contribute to the final appearance of the product.

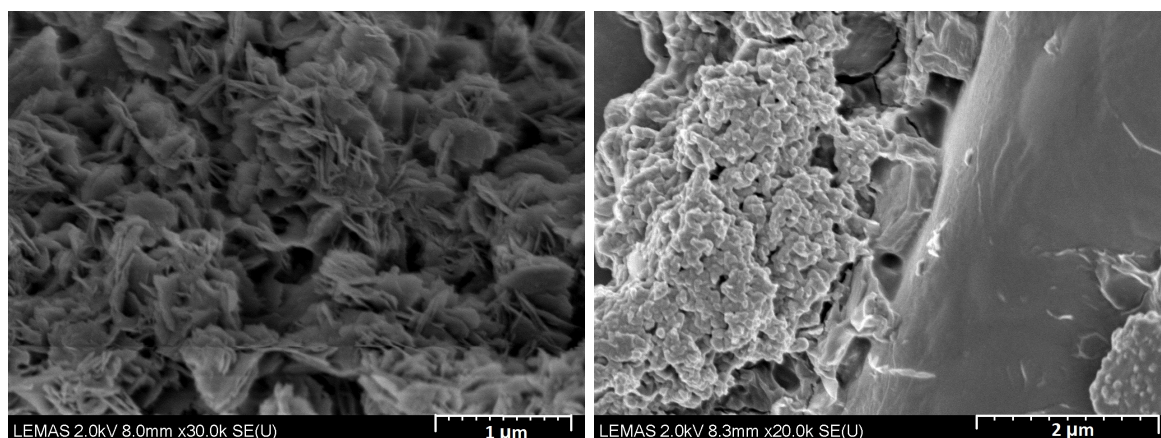
The speciation of carbonate and bicarbonate species in solution needs to be discussed in order to understand the morphology changes. On one hand, from the equilibrium equation presented in Section 2.6.3 one can observe that carbonate needs to be present for hydrozincite to be synthesized. This means that the concentration of carbonate is directly related with the rate of production of hydrozincite as indicated by the formulation of supersaturation. ON the other hand, the relative predominance of carbonate in solution is strictly related with pH as described by the $CO_2-HCO_3^{-1}-CO_2^{-2}$ equilibrium equations. For example, the amount of carbonate is maximum at high pH above pH 10.5 on the contrary bicarbonate is predominant between 6.5 and 10.5 pH, Low pH. Due to the plentiful amount of carbonate ion at high pH, hydrozincite quickly precipitates out of the solution. This yields round like particles with high amorphous content, which are characteristic of kinetic products. However, at low pH, the amount of carbonate is limited and requires to be converted through $HCO_3^{-1}-CO_2^{-2}$ equilibrium. This is an slower reaction compared with hydrozincite precipitation which crease a bottleneck in the synthesis. Therefore more crystalline features are found in hydrozincite at low pH as the kinetics of its production are slower. This agrees with the larger induction times found at low pH.

4.3 Phase and Morphology of the Hydrozincite Product.



(a) Product synthesized at low pH (6.2pH) using bicarbonate salt after 1 day. Scale = $10\mu m$

(b) Product synthesized at high pH (7.2pH) using carbonate salt after 1 day. Scale = $30\mu m$



(c) Magnification of product synthesized at low pH (6.2pH) using bicarbonate after 1 day. Scale = $1\mu m$

(d) Magnification of product synthesized at high pH (7.2pH) using bicarbonate after 1 day. Scale = $2\mu m$

Figure 4.11: SEM images of hydrozincite product synthesized at low and high pH conditions. Low pH shows aggregates of flake like particles, whereas high pH present rounded primary particles. The morphology changes found in both samples are a consequence of differences in supersaturation as well as the difference in surface chemistry

4.3 Phase and Morphology of the Hydrozincite Product.

4.3.2 Hydrozincite ripening

Hydrozincite properties are altered with time spent in aqueous media. Processes such as Ostwald ripening or particle arrangement transform both morphology and crystal structure. In this section, these changes are going to be assessed by means of XRD and SEM as a function of time and pH. The intention of this study is to explain particle agglomeration observed in hydrozincite while in transportation.

XRD analysis XRD shows the increase in crystallinity expected in recrystallized material. Sharper peaks and narrower widths are characteristic of crystallized material. Wider peaks are characteristic of small crystal domains, found after an intensive nucleation event. The new bigger crystals then make the peaks sharpen. Notice that most of the change in the peak intensity occurs in day 2. Figure 4.12 shows the evolution of XRD pattern of particles in a suspension when ripped for several days. Features such as background reduction or increase of peak intensity along time, observed in Figure 4.12, indicates particles increasing crystalline size and decreasing amorphous content.

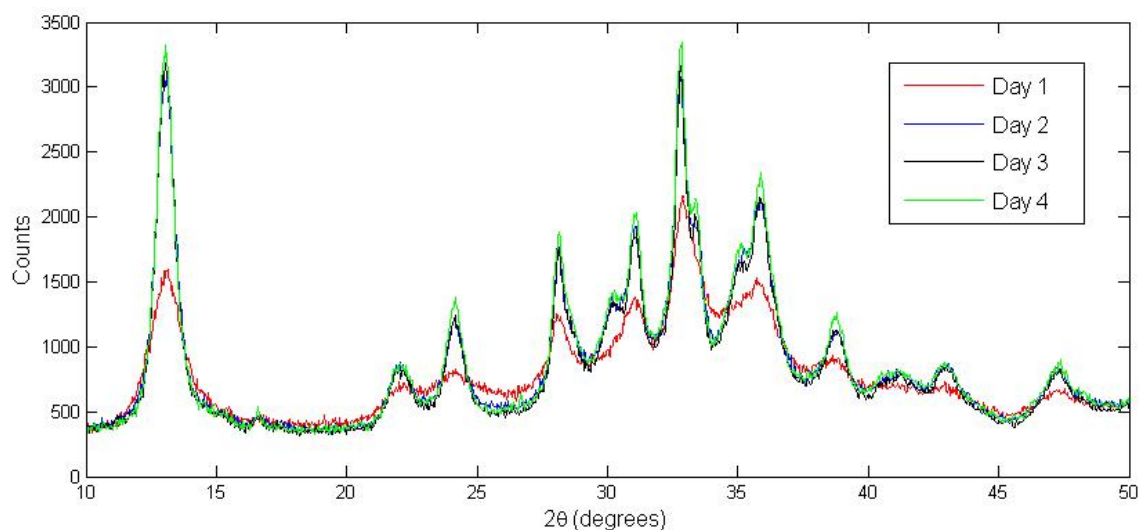


Figure 4.12: XRD spectrum obtained for products ripped for 1 2 3 and 4 days after synthesis. Crystallinity increases greatly after one day as a consequence of Ostwald ripening and particle rearrangement

4.3.3 Morphology changes as a function of ripening time

Figure 4.13 shows SEM images of aggregated particles of hydrozincite after a period of 2 and 3 days of ripening respectively. A defined aggregated of plate like particles is observable from all the images. Magnification of these images show that plates grow in size and eventually form, either block or fibers as shown in Figure 4.13(d).

The plate like morphology is characteristic of compounds with layered structure. In XRD this layer would correspond to the plane 100 in Figure 4.2. The predominance of this structure is a consequence of an Ostwald ripening effect which is enhance by a low pH. Under these conditions, the solubility of hydrozincite is enhanced thus, allowing the smaller crystal to dissolve and crystallize in a more dynamic way.

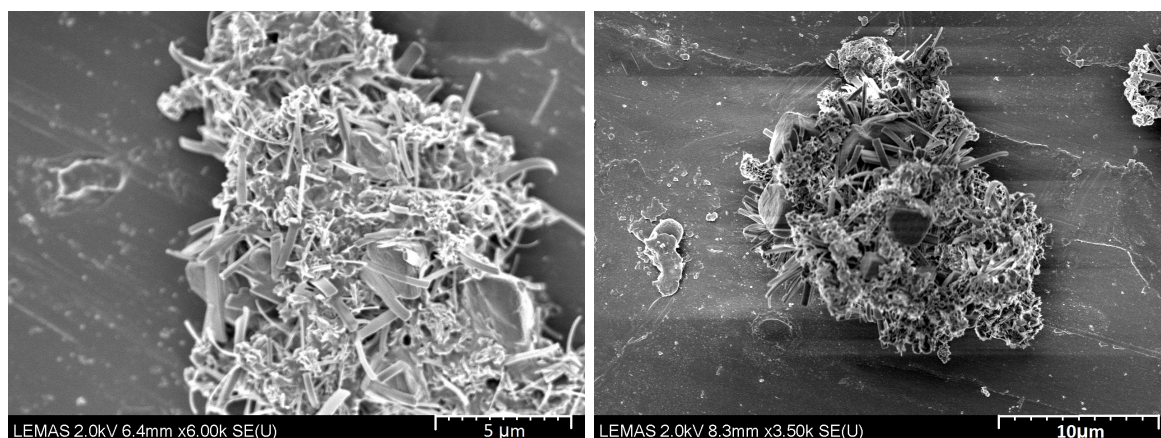
This contrasts with a stiffer solid-liquid equilibrium at high solution pH. As observed in the images in Figure 4.14, the morphology of crystals ripped at high pH present more block like structures. It is believed that a process of rearrangement occurs in this case where low solubility particles migrate towards lower energy locations in a crystal like matrix. The process of particle rearrangement has been described in previous studies (Aubert & Cannell, 1986).

The driving force of both processes, Ostwald ripening and particle rearrangement, is the same, surface area minimization. However, the particles yielded differ greatly. Where plate like particles are favoured at low solution pH larger bulky structures are formed at lower pH. Those have been controlled by means of solution pH.

4.4 Conclusions

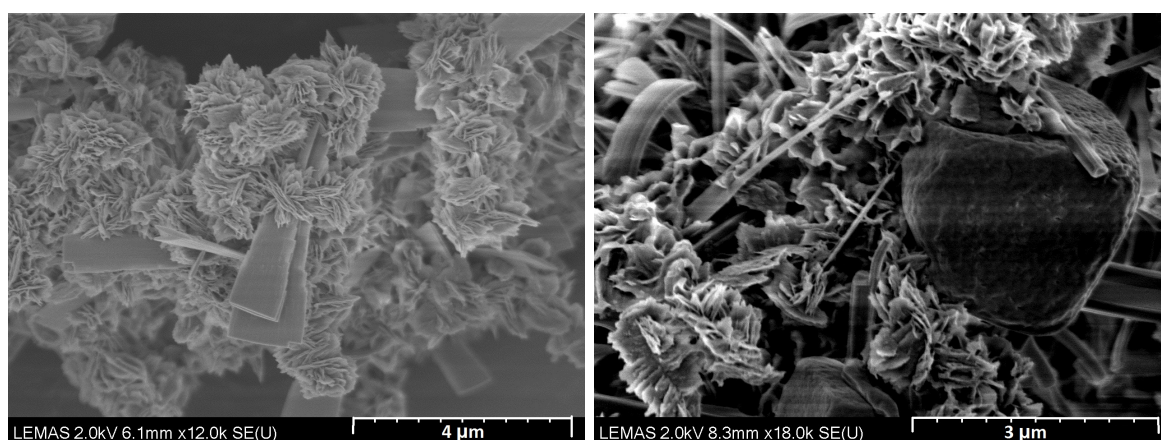
The studies in this work aim to cast some light on the crystallization behaviour of hydrozincite. Solubility, crystallinity, interfacial tension and unit cell parameters have been investigated. The results will help to understand the precipitation behaviour of the material.

- We identified lack of carbonate ions as the source of the distortion of crystalline structure of zinc layered compounds based on XRD analysis. The distortion mainly occurs in the direction a , in the direction of the zinc hydroxide double layer. Crystallinity was found to be the maximum at ratio 1:1 Zn^{2+}/CO_3^{2-} .



(a) Product synthesized at low pH (6.2pH) using bicarbonate salt after 2 days. Scale = 5 μm

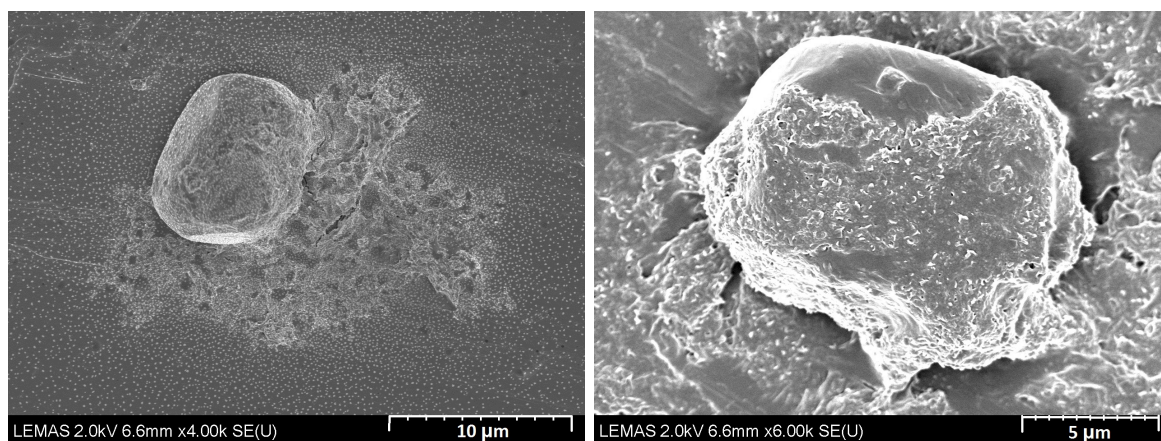
(b) Product synthesized at low pH (6.2pH) using bicarbonate salt after 3 days. Scale = 10 μm



(c) Magnification of product synthesized at low pH (6.2pH) using bicarbonate after 2 days. Scale = 4 μm

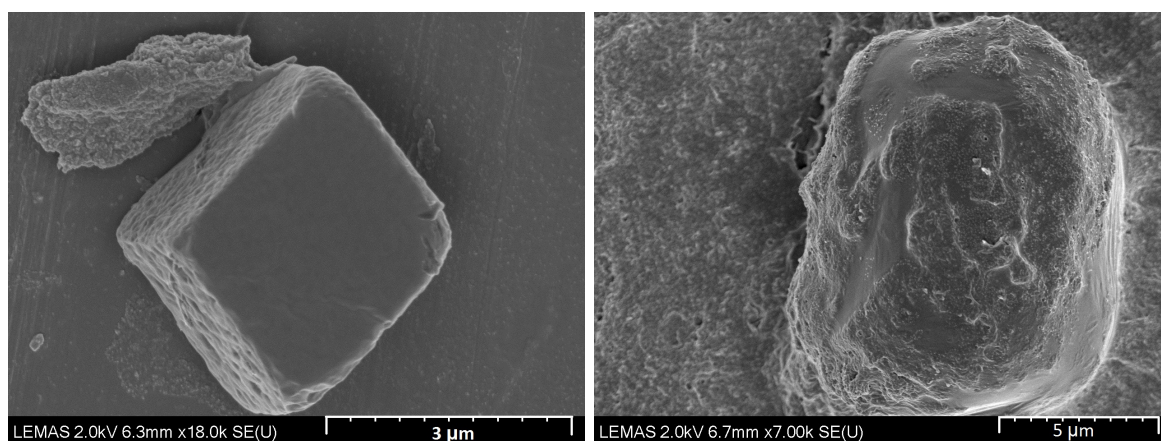
(d) Magnification of product synthesized at low pH (6.2pH) using bicarbonate after 3 days. Scale = 3 μm

Figure 4.13: SEM images of samples after 2 and 3 days synthesizes at low pH. Plates like structures are found.



(a) Product synthesized at high pH (7.2pH) using carbonate salt after 2 days. Scale = 10 μm

(b) Product synthesized at high pH (7.2pH) using carbonate salt after 3 days. Scale = 5 μm



(c) Magnification of product synthesized at high pH (7.2pH) using bicarbonate after 2 days. Scale = 3 μm

(d) Magnification of product synthesized at high pH (7.2pH) using bicarbonate after 3 days. Scale = 5 μm

Figure 4.14: SEM images of samples after 2 and 3 days synthesizes at high pH. Larger single particles with flat surfaces were found. Particle rearrangement into ordered structures is believed to be the cause of these features.

- Induction time analysis indicates that nucleation kinetics of hydrozincite are rapid compared to other similar compounds as a consequence of the low surface tension. A value of $0.051 J/m^2$ has been obtained from slope of the log-log plot. It is believed that low pH decreases the availability of CO_3^{2-} ions on favour of the creation of HCO_3^- which decreases the supersaturation.
- The decrease of solubility of hydrozincite at around pH 7 was observed by various techniques and found to be a consequence of the lack of soluble complexed species. Additionally, hydrozincite has been identified out as the major product of precipitation from aqueous solutions.
- Morphology changes were found to occur when bicarbonate was used or when material was left to ripen. Carbonate derived material at high pH was found to yield compact aggregates of particles which become tighter with ripening time due to particle rearrangement. On the other hand, bicarbonate products synthesized at low pH were found to yield flake-like particles which undergo Ostwald ripening yielding larger flakes or fibres.

Chapter 5

Influence of Synthesis Conditions on the Hydrozincite Properties

5.1 Introduction

The lack of knowledge around large scale production of zinc carbonate nanoparticles has motivated studies aiming at improving synthesis at an industrial scale. Parameters identified as influencing reactive precipitation such as pH, dopant concentration, ratio between reactants etc. all which lack depth of comprehension. As a consequence, the industrial production of hydrozincite incorporates the use of a final step of wet milling aimed at controlling the final particle size.

The aim of this chapter is to exhaustively investigate the influence of such parameters in quality defining properties such as crystallinity, particle size or fractal dimension. Understanding the relation between both parameter and final properties is essential when preserving the quality across the different scale up stages.

Final product properties have been obtained through the use of analytical techniques such as static light scattering (SLS), scanning electron microscopy (SEM) or Powder X-ray diffraction (XRD). SLS was used to observe particle size distribution under conditions such as pH or reactant ratios whereas X-ray was used to observe the quality of the crystalline structure.

This chapter consists of several different studies focused on the previously named process parameters, those being: pH, concentration, shear rate Zn^{+2}/CO_3^{-2} ratio and presence of surfactant. The chapter will conclude with an analysis of the relative

importance of each parameter in relation to the others thus identifying the important ones.

5.2 Results and Discussion

5.2.1 Product characterization.

Products studied in this section were synthesized utilizing the setup described in Section 3.6. The set-up consists of a tubular reactor which provided the mixing required for reaction followed by a high shear mixer (HSM) where shear was applied. The HSM speed can be tuned for further controlling shear stress. Samples after HSM were stabilized in SDS for later analysis in SLS to obtain size distribution as well as bring prepared for SEM analysis following the procedure described in section ??.

Regarding the solid phase obtained through the process of reactive precipitation, it was found that, although the spectrum varies in peak intensity as well as in peak width, the position of the peaks remains the same. In the process of peak separation and identification run in High Score, no alternative phases to hydrozincite were identified, only the pattern (04-013-7572), corresponding to hydrozincite, was found to explain the spectrum. For example, it has already been shown that products obtained at various pH present variability in the number of peaks present in the spectrum due to the selective disorder of crystal structure planes containing the index h in their Miller index. This was also shown to be true for aged product. In another set of experiments the influence of flow rate on crystal structure was studied which showed no alteration of the XRD pattern (See Figure ??).

Aging of the product also affects particle properties such as crystallinity and particle-particle interactions. Product ripened for 3 days has been exposed to a range of shear and particles size studies. SEM was used to identify surface features affecting aggregation.

5.2.2 Physical factors influencing size

In this section the influence of process parameters such as flow rate, shear rate and aging are going to be assessed in the precipitation of hydrozincite. The influence

5.2 Results and Discussion

Table 5.1: Experimental conditions for the characterization of the particle size distribution of hydrozincite synthesized in tubular reactor. A range of flow rates as well as reactor lengths were tested.

Exp ID	[Zn]	[CO ₃ ²⁻]	Final pH	Reactor length (m)	Flow Velocity (m/s)	Flow Rate (ml/m)
106	0.01	0.01	N/A	1.09, 2.19 3.82, 4.22	0.392	442.92
106	0.01	0.01	N/A	1.09, 2.19 3.82, 4.22	0.331	373.97
106	0.01	0.01	N/A	1.09, 2.19 3.82, 4.22	0.269	305.02
106	0.01	0.01	N/A	1.09, 2.19 3.82, 4.22	0.208	236.07
106	0.01	0.01	N/A	1.09, 2.19 3.82, 4.22	0.147	167.12

on the particle size distribution is of special interest, however, the morphology and hydrozincite polymorph are going to be assessed.

Influence of flow rate in hydrozincite precipitation in a tubular reactor

The importance of laminar and turbulent regimes on the aggregation process have been introduced in Section 2.4.3. Velocity gradients and vortex drive the movement of particles yielding aggregation or breakage phenomena. Additional to the influence on solid particles flow rate it also affects the mixing rate of the reactant streams which could have an effect on the final polymorphic form of hydrozincite.

Figure 5.2(a) shows a series of particle size distributions obtained in the set-up described in Section 3.3.1. The complete experimental conditions are shown in Table 5.1. It shows 5 PSD was found at steady state which is to say, far away from the junction and after allowance of some time for the readings to be stable. A steady progression towards smaller particle sizes is observable as flow velocity increases. Some small fluctuations are present in the higher particles range. The equipment manufacturer reports a size limit of 2000 μm which is reached in the case of large sizes of the PSD for 0.147m/s, that being the cause of the deep decrease of the curve at the named range.

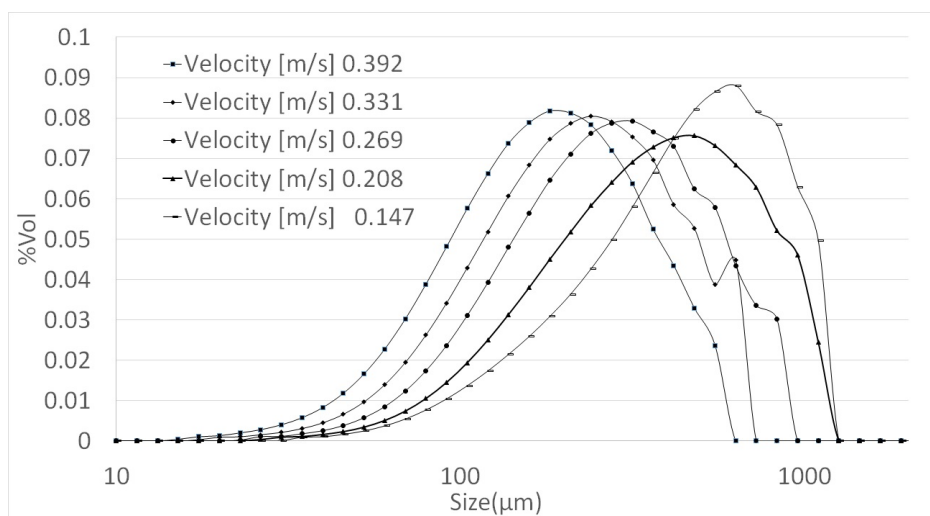


Figure 5.1: Particle size distribution of hydrozincite synthesized in the plug flow reactor and its variability with flow velocity. Reactor length was set to 4.22m

The steady decrease of the particle size as a function of velocity indicates the tight relationship between the two variables which has already been shown in the literature. The nature of this relation lays in the flow forces influencing the movement of the particles. For example, a high energetic vortex in a large flow rate stream creates high strain areas around it which are likely to yield particle breakage if the binding forces of the aggregates are weak.

Figure 5.2(a) shows the XRD spectrum obtained from two samples precipitated at low and high flow rates. A complete description of the experimental conditions can be found in Table 5.2. The good match between them suggests that flow rate does not have an influence on the product obtained. The morphology of the sample at high flow rate shows an aggregate of small particles as is observed in the SEM image in Figure 5.2(b).

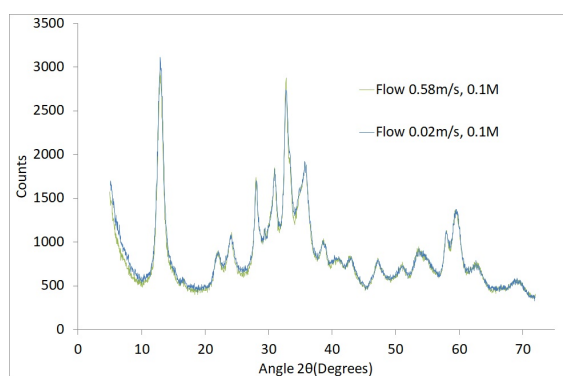
Effect of wet milling on particle size after hydrozincite precipitation in tubular reactor

Among the available methods for colloidal stabilization, the use of HSM is widely applied. In this section the behaviour of hydrozincite under shear is to be studied. The aim is to assess the capabilities of this technique for drug stabilization purposes

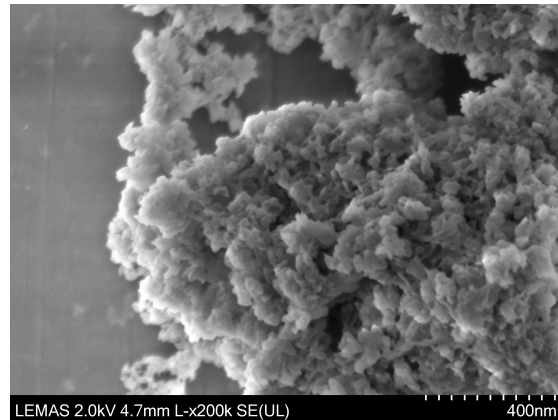
5.2 Results and Discussion

Table 5.2: Experimental conditions for the characterization of hydrozincite synthesized in at tubular reactor. Maximum and minimum flow rates were tested for phase changes and morphology.

Exp ID	[Zn]	[CO ₃ ⁻²]	Final pH	Reactor length (m)	Flow Velocity (m/s)
5	0.1	0.1	6.75	0.9	0.02
6	0.1	0.1	6.91	0.9	0.58



(a) Comparison of XRD spectrum of hydrozincite synthesized at high and low flow velocities. The results show no difference between the spectrum.



(b) SEM Image of Hydrozincite synthesized at high flow rate. An aggregate of small particles is observable.

Figure 5.2: Phase and morphology of hydrozincite precipitated in the tubular reactor.

5.2 Results and Discussion

Table 5.3: Experimental conditions for the study on the influence of shear over freshly synthesized product in a wet mill. The variables concentration and wet mill rpm were studied at a flow velocity of 0.04m/s were studied

[Zn]	[CO ₃ ⁻²]	HS rpm	Flow Velocity (m/s)	Flow rate (ml/min)
0.1	0.1	0,3000,5000 7000,9000	0.04	64
0.01	0.01	0,3000,5000 7000,9000	0.04	64

and obtain guidance for its application at industrial scale.

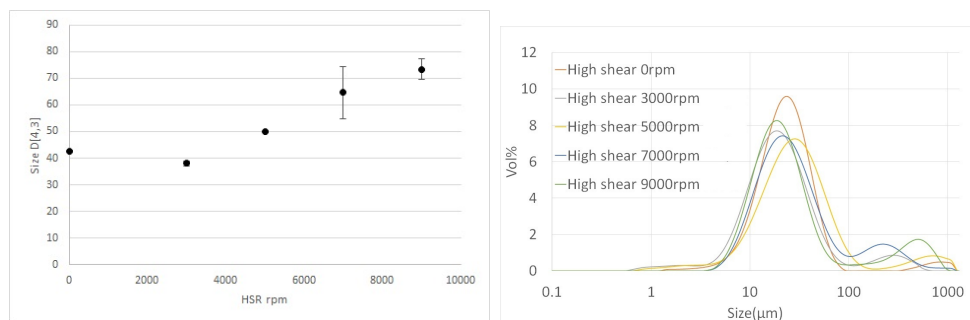
Fluid shear affects particle suspension in various ways. For example, if hydrodynamic forces overcome gravitational forces, then sedimentation is avoided hence particle remain suspended. This is beneficial as agglomeration at the bottom of the container is avoided. Another aspect of shear is that it yields aggregation or breakage depending on particle size, concentration and shear intensity. The case of intense shear is especially interesting as under these circumstances breakage prevails. This is the case with high shear mixers which is covered in the following section.

The particles size distribution and D[4,3] of particles has been used as an indicator of the grade of particle breakage after shearing. Samples were taken at various HSM rpm and in some cases at various flow rates. A summary of the conditions is shown in Table 5.3. The continuous set-up combining synthesis and milling, described in Section 3.6, was used.

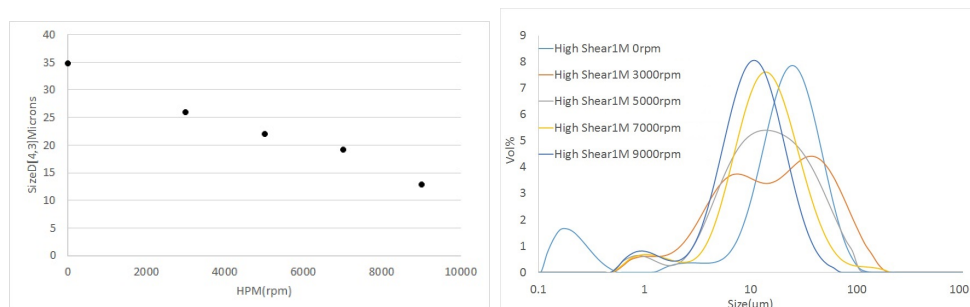
Figure 5.3(d) shows the D[4,3] of fresh hydrozincite samples obtained at 0.01M and 0.04m/s (see Table 5.3 for details) from which an obvious increase of particle size with rpm is observed. The effect of shear in this case does not yield breakage but aggregation as the the PSD clarifies in Figure 5.3(b). On the contrary, product synthesized at higher supersaturation (Figure 5.3(c)) present the opposite trend. The PSD shows a bimodal distribution which moves towards the smaller particle sizes as the rpm of the high shear mixer increases.

The balance of shear forces and particle-particle collision appears to be changing the behavior of the suspension under shear for low and high concentrations. The flow features created at high shear seems to bring particles together due to the strong

5.2 Results and Discussion

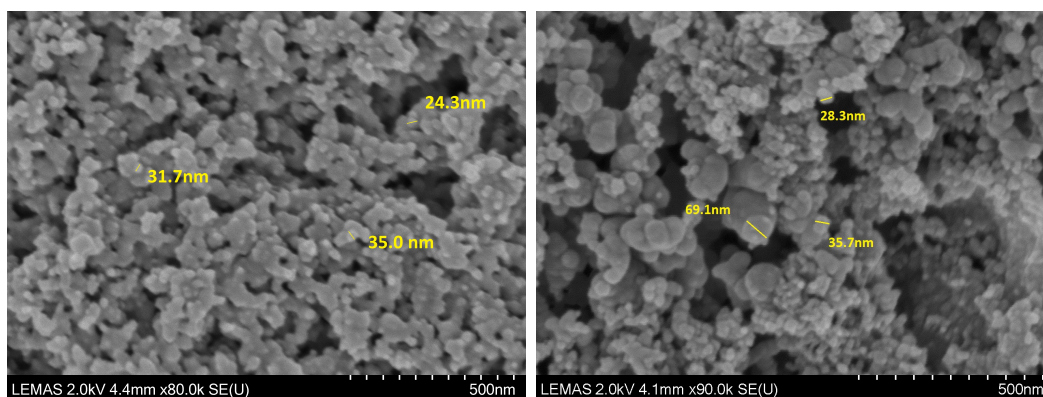


(a) D(4,3) Vs High shear mixer rpms for product synthesis at 0.01M with no ripening. (b) PSD of hydrozincite synthesized at 0.01M with a flow rate of 20rpm at various High shear rpm. Particles aggregate in larger cluster as the shear rate increases as seen from the binodal distribution of high RPM.



(c) D(4,3) Vs High shear mixer rpms for product synthesis at 0.1M with no ripening. 65% reduction in particle size was achieved. (d) PSD of hydrozincite synthesized at 0.1M with a flow rate of 20rpm at various High shear rpm. Binodal modes in the small particle sizes indicates breakage of particles.

Figure 5.3: Evolution of D[4,3] and particle size distribution (PSD) at two concentrations 0.01M and 0.1M. Lower concentrations shown particle aggregation whereas breakage is observed at higher concentrations. The relative importance of shear forces against particle-particle collision produces the change in behaviour.



(a) SEM image of Hydrozincite synthesized at 0.01M to which no shear was applied. Particle average size was found to be 25nm with a very narrow distribution

(b) SEM image of Hydrozincite synthesized at 0.1M to which no shear was applied. Particle average size was found to be 43nm with a wide distribution

Figure 5.4: Studies of freshly synthesized particles under shear for low (0.01M) and high (0.1M) concentration of Zinc. 5.3(d) and 5.3(c) shown particle size $D[4,3]$ against Mixer rpm. 5.4(a) and 5.4(b) shows SEM images of the synthesized particles.

inter-particle forces and low particle-particle collisions, a consequence of the low concentration, the process results in particle aggregation. On the other hand, an increase of particle-particle collision driven by an increase in concentration, produces breakage of particles.

Figure 5.4(a) and 5.4(b) shows the crystallized particles observed through a SEM microscope from which differences in structure can be identified. Crystal size seems to be more heterogeneous in the case of hydrozincite synthesized at the higher concentration. Whereas small rounded particles are observed at low concentration, see Figure 5.4(a). An increase in the surface area could be the cause of the shift in behaviour. As particle size is reduced at low concentrations (5.4(a)), surface area increases thus increasing the importance of inter-particle forces.

An increase in surface forces in combination with the high shear which enhances particle collision, is believed to be the cause of the observed increasing size at low concentration. On the other hand, more heterogeneous particles were observed at high concentration and these are believed to have weaker surface forces as a consequence of

Table 5.4: Experimental conditions for the study of shear on the 3 days ripened product. Concentration of reactants, rpm of the wet mill head and flow rates through the wet mill volume.

$[Zn]$	$[CO_3^{-2}]$	HS rpm	Flow Velocity (m/s)	Flow rate(ml/min)
0.1	0.1	0,3000,5000	0.04	64
		7000,9000	0.12	201
0.01	0.01	0,3000,5000	0.04	64
		7000,9000		

their larger sizes. This feature in combination with reduced particle-particle interactions at high concentrations is believed to increase particle breakage and hence yield smaller particles.

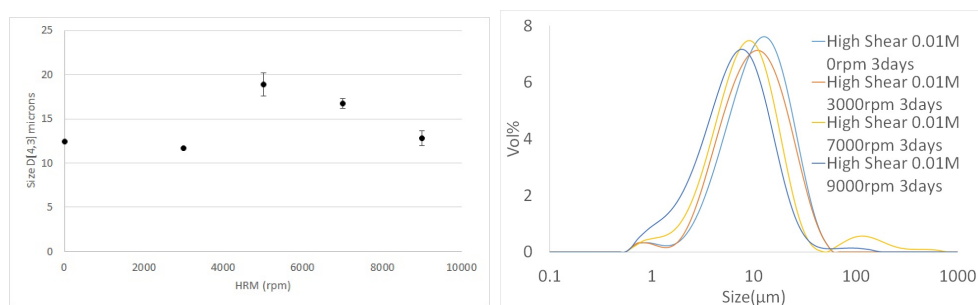
Influence of aging (ripening) in the behaviour of hydrozincite suspension under shear

Suspensions produced as described in Section 3.6 were left to ripen for 3 days in a sealed beaker and then pumped through the high shear mixer. The complete set of experimental conditions are found in Table 5.4. This study aimed to identify if ripening could be used as a method for particle control.

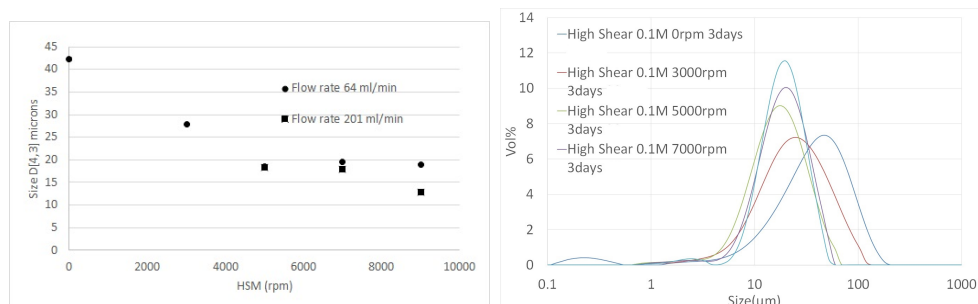
The typically named Ostwald ripening, consist of physical phenomenon occurring in crystalline materials in solution where small particles shrink and large ones grow by transferring matter through the solution (see Section 2.2.7) (Kahlweit, 1975). This yield changes with the size and morphology of the precipitated crystals. Although this phenomenon has been covered in Section 4.3.3 regarding morphological changes, emphasis is going to be put on the effect of shear on ripened product. It has been observed that shear influence ripened and unripened crystals differently. For this reason, this section will focus on the effect of shear on ripened particles.

In this study, crystal suspensions, as synthesized in a tubular reactor (Section 3.3.1), have been left to ripen for 3 days, the latter to be sheared in a HSM at a range of rpm from 3000 to 9000. Similarly to the concentration study, surface morphology will be studied by means of SEM imaging.

5.2 Results and Discussion

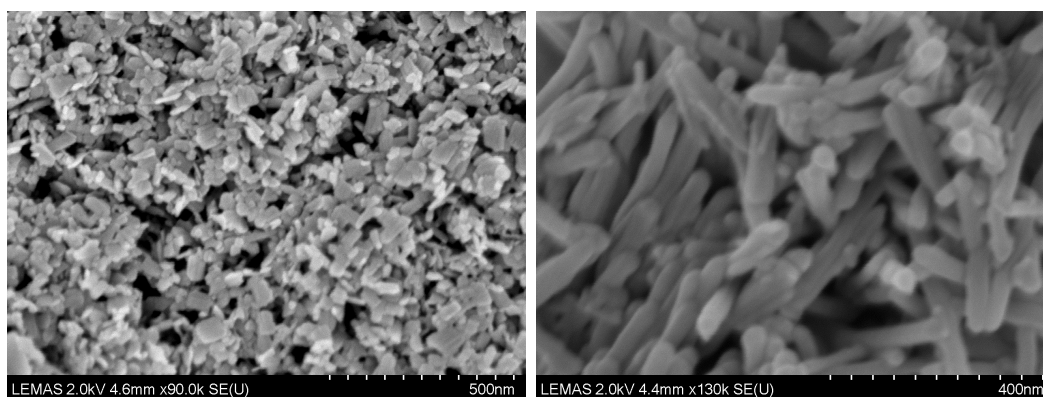


(a) $D(4,3)$ Vs High shear mixer rpms for product synthesized at 0.01M after three days ripening. Smaller particles are observed (b) PSD of product synthesized at 0.01M was pumped at 0.147m/s. Slightly larger aggregates are found at higher wet mill RPM.



(c) $D(4,3)$ Vs High shear mixer rpms for product synthesized at 0.1M after three days ripening. 66% reduction in particle size was pumped at 0.147m/s. Distribution get narrower and move towards smaller sizes as RPM increases. This indicates a disruption on larger particles. (d) PSD of product synthesized at 0.1M

Figure 5.5: Evolution of $D[4,3]$ and particle size distribution (PSD) of 3 days ripened product at two concentrations 0.01 and 0.1M. Larger concentrations are shown to be more sensitive to shear due to the larger particle-particle collision rate.



(a) SEM image of Hydrozincite synthesized at 0.01M after three days ripening. Small agglomerates of flake like particles.

(b) SEM image of Hydrozincite synthesized at 0.1M after three days ripening. Large rod like agglomerates easily break under shear.

Figure 5.6: Studies of ripened particles under shear for low (0.01M) and high (0.1M) concentration of zinc. 5.6(a) and 5.6(b) shows SEM images of the synthesized particles at 0.01 and 0.1M respectively.

Figures 5.5(a) and 5.5(c) show the results for high shear experiments of ripened particles. Particles synthesized at high concentration and ripened for three days are larger in size than low concentration ones, although high concentration samples seem to be more sensitive to shear (63% reduction of the initial particle) than product created at low concentration (only 33% reduction). Additionally, reduction of particles at low concentration seems to show uneven results with scattered points round the size vs. rpm plot, whereas reduction of high concentration products is rather defined by a steady decreasing trend. Further observation of the particle size distribution (5.5(d)) indicates that the variability of the product synthesized at low concentration comes from a minimal aggregation or fracture effect which leaves the main node of the size distribution relatively unchanged. Oppositely the sheared suspension synthesized at higher concentration (Figure 5.5(d)) shows an alteration of the whole of the PSD towards the smaller sizes.

In order to explain the behavioural change of particles under shear, SEM images have been obtained for ripened product at two different concentrations (0.01 and 0.1M). When comparing images of unripened and ripened material obtained at low concentra-

tion (Figures 5.4(a) and 5.6(a)) morphological changes were observed. Round particles are the rule for unripened material as observed in previous experiments, whereas flake like particles and flat surfaces are common after 3 days those being characteristic of crystalline material. More acute changes were found at high concentrations where rod like morphologies appeared after ripening (Figures 5.4(b) and 5.6(b)). This suggests morphological changes as a consequence of rearrangement of the crystal structure into a more crystalline like material.

As a consequence of these morphological changes, particles present different behaviours against shear. For example: small ripened flake-like particles synthesized at low concentration present a tight network of crystals which prevent breakage of particles hence explaining the 33% reduction on size. On the other hand, large particles consisting of flakes seems to rule the behaviour at high concentrations. These bulk particles break easily under shear conditions although they do not decrease in size below $15 \mu\text{m}$ as the decreasing exponential trends shows in Figure 5.5(c).

As shown in Section 4.3 the product does not change during the ripening time, only crystallinity and particle arrangement does. These two factors also influence the evolution of inter-particle forces along time and hence affect aggregation. For example, the increased particle arrangement caused by ripening decreases the surface energy. However, it was found that for some concentrations at similar shear conditions, products synthesized at high concentrations behaved similarly regardless of the ripening time. This can be observed in Figures 5.5(c) and 5.4(b) where trends are similar with the same percentage of particle reduction. Therefore, we can conclude that at high concentration, particle reduction is mainly driven by shear whereas for low concentration surface energy is probably more important.

In conclusion, morphological changes caused either by concentration or by ripening were observed using SEM imaging which, in combination with increased crystallinity observed via XRD, explains the differences in behaviours under shear. In general, the response to increasing shear is decreasing size although, in the case of round small particles synthesized at low concentration without shear the trend is ascending, a consequence of the increased surface forces.

5.2.3 Chemical factors influencing size and colloidal stability

Effect of surfactant on colloidal stability

The use of surfactants for suspension stabilization is well documented in the literature. They have the capability of adhering to the particle surface and changing the surfaces properties. For example, an ionic surfactant such as sodium dodecyl sulphate (SDS) attaches its polar head to the positive charged particle surface where as the non-polar extends along the axial direction which prevents other particles from aggregating. Other molecules such as acetic acid, on the other hand, attaches to the particle surface changing the interfacial energy and surface tension (Bitenc *et al.*, 2008). With the intention of testing such properties, a study on the stability of hydrozincite suspension was carried out utilizing SDS as surfactant. For this purpose, a experimental matrix has been designed consisting on the following two variables, amount of solids in suspension and amount of surfactant. Then, turbidity was measured by image analysis of the vials to finally be plotted against the experimental variables.

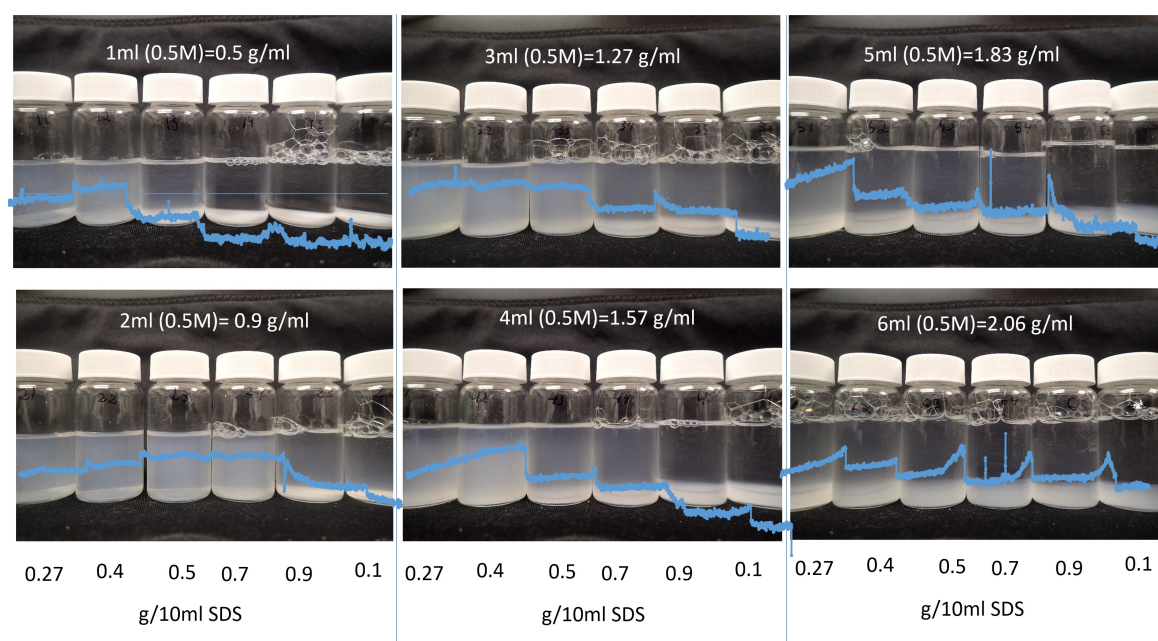


Figure 5.7: Suspensions prepared from different ratios of surfactant and solid. Suspensions were kept at room temperatures. Values of turbidity across a horizontal line are shown by blue lines.

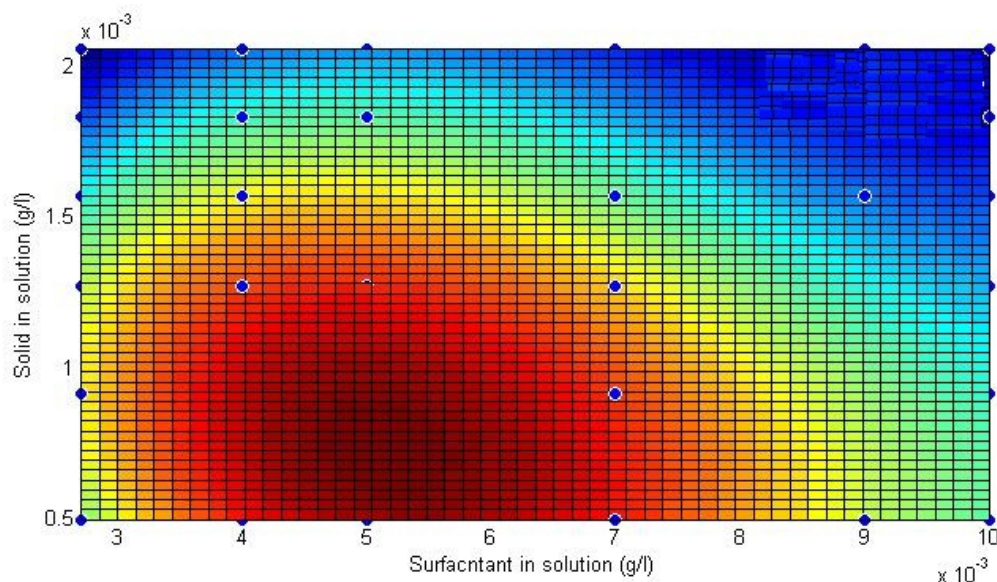


Figure 5.8: Turbidity map extracted from image analysis. Solution concentration was computed from the volume of hydrozincite suspension and its concentration (both shown in Figure 5.7) . Red indicates high turbidity. A localized area of stability was found.

Figure 5.7 shows the process of measuring the turbidity by image analysis. It consisted of measuring the intensity of the gray scale of the images of the vials captured after 1 day. The samples were prepared with a range of solid and surfactant concentration. Figure 5.8 shows the contour map of the turbidity as extracted from image analysis values from Figure 5.7. A third degree polynomial was fitted to the data thus allowing the identification of high stability areas as indicated by warmer colours. An area of stability was found in the ranges 0.6 to 1 g/L of SDS and 4 to 6 g/L of solids in suspension.

The confined stability area indicates that there is no constant ratio solid/surfactant capable of stabilizing the suspension. Instead, there is a confined area of concentrations where a stable suspension was found. As a consequence, surfactant concentration cannot be increased indefinitely along with solid concentration as sedimentation would occur.

The efficiency of a surfactant is a function of the amount of particle surface covered by it, thus, particles completely covered would be stabilized. However, an excess

Table 5.5: Experimental conditions and d(90) Results obtained from the study of the influence of solution pH and concentration on particle size.

Exp ID	[Zn]	[CO ₃ ⁻²]	[HCO ₃ ⁻]	Final pH	d(0.9) μm
41	0.1	0.08	0.12	6.64	50.59
42	0.1	0.04	0.16	6.44	30.06
43	0.1	0	0.2	6.23	25.34
44	0.02	0.008	0.0032	6.97	30.30
45	0.02	0.016	0.024	6.74	21.01
46	0.02	0	0.04	6.51	7.06

of surfactant would enhance particle binding and undesired aggregation would occur instead. Surfactant efficiency is also a function of the amount of solids dispersed. For example, a large concentration would increase the frequency of collisions between particles and, although surfactants would decrease the number of effective collisions leading to aggregation, some collisions remain yielding aggregation. Therefore, high solid concentrations decrease stability. It is believed that the confined stability area is a consequence of the balance of both effects: surfactant and concentration.

Effect of concentration and pH on particle size

This section will investigate the role of concentration and pH variable on particle size. For this purpose, hydrozincite was synthesized at various ratios CO_3^{-2}/HCO_3^{-} which yielded a final solution pH in the range 6.2 to 7. Concentration also has an influence on particle size therefore it was also considered a parameter in the experiment taking values of 0.02 and 0.1M.

Static light scattering was used for the characterization of the particle size distribution. In order to explain the changes in size a characterization of the ζ-potential was necessary. Finally, as a way to confirm the crystalline phase, powder XRD analysis was used.

Table 5.5 summarizes the experimental conditions of both the zinc and the carbonate solution. In this case, the carbonate solution contained a mixture of sodium carbonate and sodium bicarbonate as shown in the ratios given in the table.

5.2 Results and Discussion

Values of $d(0.9)$, also included in Table 5.5, seem to indicate a relation between solution pH and the particle diameter, shown in Figure 5.9. Increasing solution pH produces larger particles. Similarly, concentration consistently affect the product by increasing the size when concentration increases.

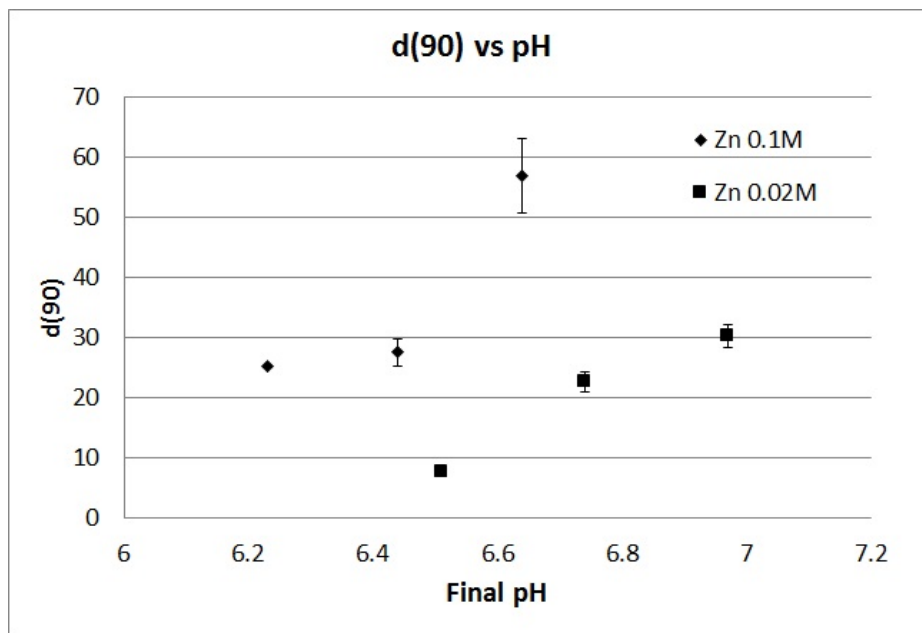
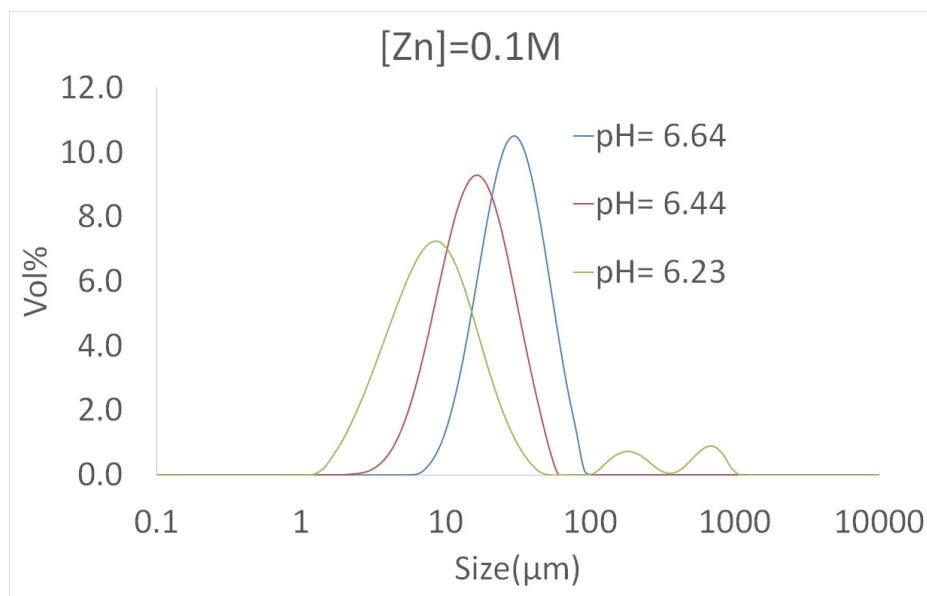


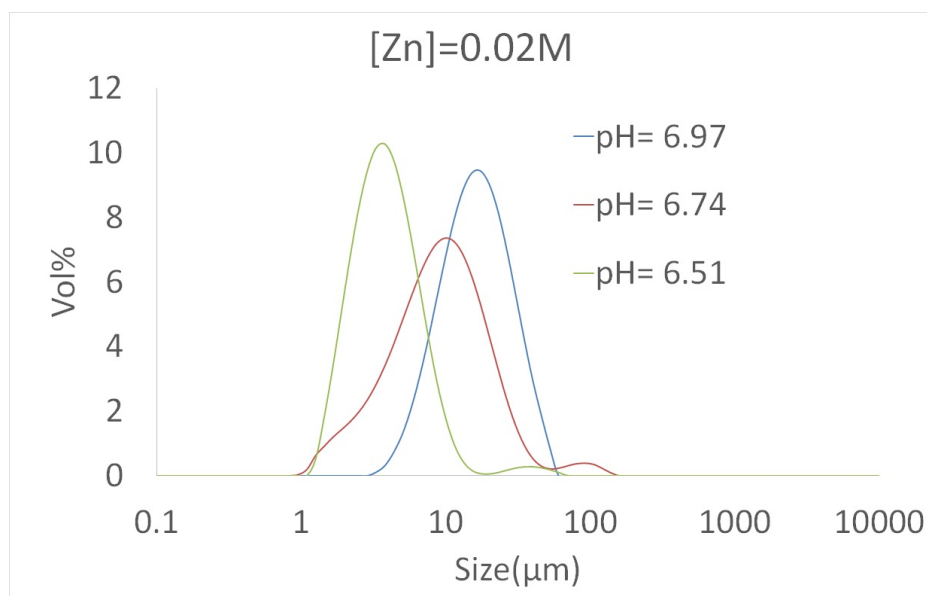
Figure 5.9: $D[0.9]$ of particles synthesized at various pH by changing CO_3^{2-}/HCO_3^- and two different concentrations.

In order to complete the whole picture of the problem the complete size distribution of the experiments shown in 5.5 is presented in Figure 5.10. In the case of high particle concentrations (0.1M) a steady decrease in particle size was observed with decreasing pH. For pH 6.64 and 6.44 the PSD is a well defined monodispersed distribution as expected from a product yielded from a tubular reactor. However, in the case of the lowest pH a small portion of larger aggregates is present which is believed to be caused by the larger tendency of smaller particles to aggregate. Notice that in a volume based size distribution such as the present one, particles in the larger sizes have a large weight in the overall fraction of particles. This means that the polydispersity of the sample is negligible for the present case.

For the case of low concentration (0.02M) a similar trend between size and pH was found. However, in this case, the dispersion the of sample increased for the in-



(a) Particle size distribution of suspended hydrozincite precipitated in tubular reactor at pH 6.64, 6.44 and 6.23. The size distribution shows a steady shift towards smaller sizes as pH decreases.



(b) Particle size distribution of suspended hydrozincite precipitated in a tubular reactor at pH 6.97, 6.74 and 6.51. The smallest sizes are found at low pH and is consistent with a direct relationship between pH and size

Figure 5.10: Particle size distribution of the hydrozincite product precipitated under the conditions summarized in Table 5.5. Distributions towards the smaller particle sizes are found at low pH and low concentrations.

intermediate pH value. This shape is probably a consequence of a longer measure time in the Mastersizer where particles underwent uncontrolled aggregation and breakage phenomena.

Solid concentration

Increasing the zinc concentration in the reactant stream from 0.02 M to 0.1 M increases the amount of hydrozincite solids from 2.19g/l to 10g/l which dramatically changed the aggregation kinetics.

It is believed that this change in concentration directly influences the final particle size through the variation of collision frequencies. In order to elucidate this relation we should look at the population balance equation as shown in Section 3.10 to which appropriate simplification was applied:

$$\frac{u}{X} \frac{\partial n_k}{\partial \tau} = \frac{1}{2} \sum_{j=k-i}^{j=\infty} \alpha_{eff}(i, j) K_{i,j}^a (AggFrac) n_i(\tau) n_j(\tau) - n_k \sum_{i=1}^{\infty} K_{i,j}^a n_i(\tau) + \sum_{m=k+1}^{m=\infty} K_m^b n_m(\tau) \Gamma_{m,k}^b - K_m^b (P_1, P_2) n_k(\tau) \quad (5.1)$$

From examination of Equation ?? it can be observed that the number of particles per liter (n_i) is an important parameter in the expression. It directly influences the aggregation and breakage terms.

In order to assess the importance of the concentration the expression was coded in gPROMS, see Appendix C.1, and a sensitivity analysis was performed. It consisted of systematically increasing the volume fraction of the solid and observing the computed $D[4,3]$ of the size distribution. Results of this study are shown in Figure 5.11. Four parameters in the equation, $AggFrac$, k_{alpha} , P_1 and P_2 were chosen based on experimental results from Section 7.1 and were assigned as: 2.14, 7.04 -0.87 and 2.35 respectively.

The observed increasing trend in Figure 5.11 indicates that the aggregating system increases its final particle size with an increasing amount of suspended solids, probably a consequence of the increase in particle collision.

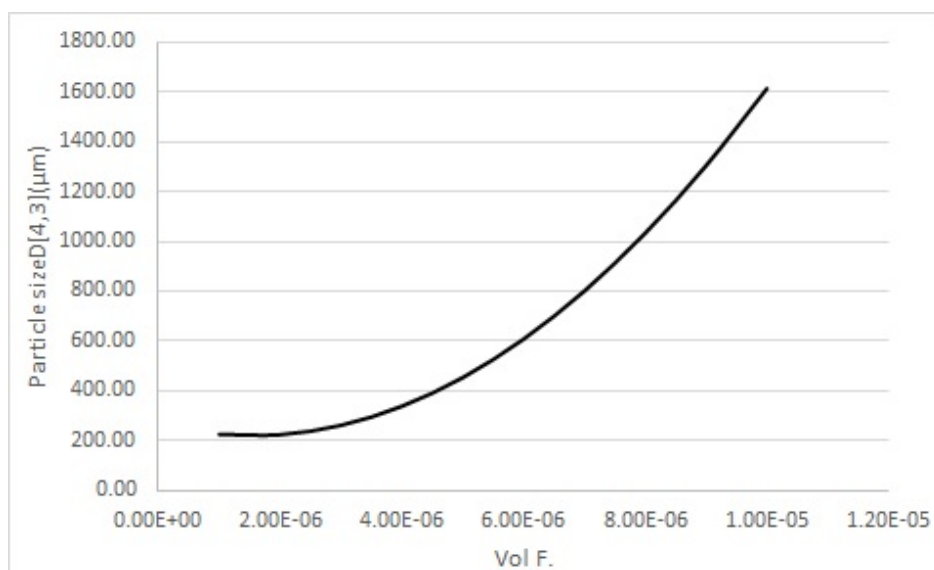


Figure 5.11: Theoretical evolution of final particle size with volume fraction of solids in suspension. Computed using the population balance equation shown in Equation ?? in gPROMS.

Influence of solution pH on particle size

As observed in Figure 5.9, particle size presented an increasing trend with increasing pH. It is believed that the observed change in size is caused by alteration of surface chemistry.

Surface chemistry is well known to be an important factor in the aggregation or coagulation of particles. The case of carbonates has been studied widely in the literature Van Cappellen *et al.* (1993) which concludes that the surface charge is altered by ionization of carbonate and calcium (following equilibria in Table 2.6). Therefore, the role of surface charge on the aggregation process is believed to be of great importance.

In order to assess its influence on aggregation, surface potential (ζ potential) was measured by electrostatic techniques as a function of pH. A general rule of colloidal science indicates that in order to maintain a stable colloidal suspension, an electrostatic repulsive force between particles must be maintained. A ζ potential above 30 mV or below -30 mV is a general rule of thumb to judge whether a suspension would remain stable.

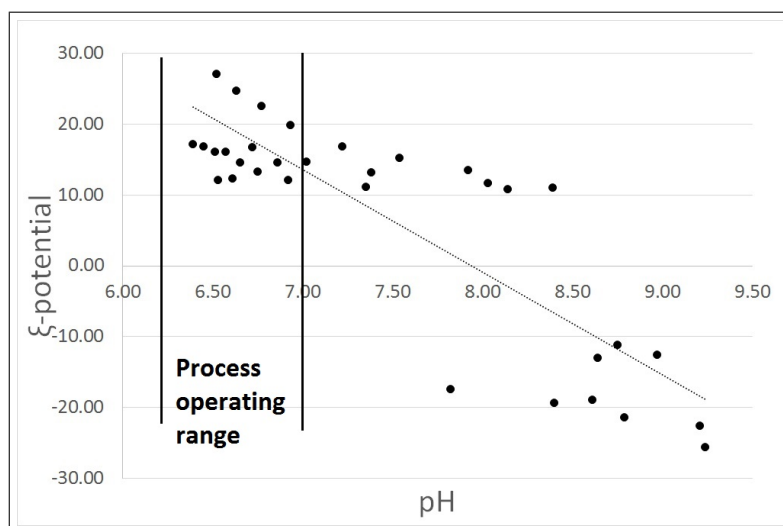
ζ -potential measurements are plotted in Figure 5.12(a). Potential is comprised of

the range 30 mV to -30 mV which is not sufficient to maintain a stable suspension, hence aggregation is inevitable. Although, it is observed that pH's around 6.5 yield the highest absolute values, which corresponds to the pH at which particles were found to have the smallest size as observed in Figure 5.9. Therefore, it is believed that the large value of the surface potential, although not enough to maintain a stable suspension, yield the smaller particle size.

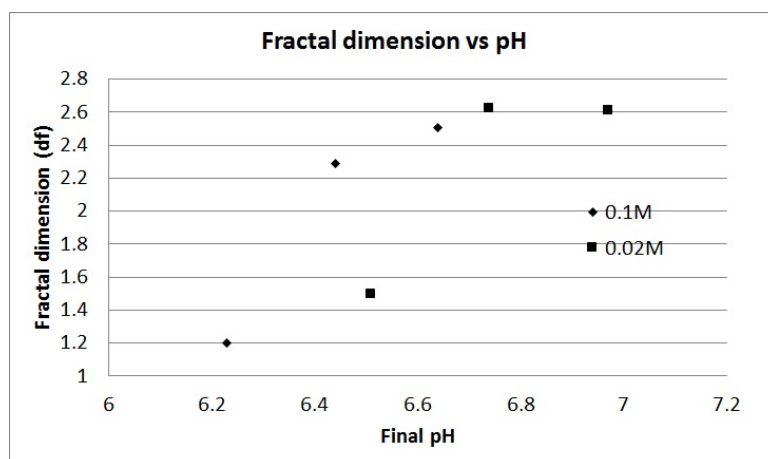
As a consequence of the change in ζ -potential, the aggregated structure is also expected to alter. In order to assess changes in particle arrangement, the fractal dimension of the particle was measured as a function of solution pH. Figure 5.12(b) shows the results. An increase in fractal dimension is observed as pH increase indicating a more compact organization of the aggregates. As a consequence of the decrease in the particle surface potential, particles within the aggregates are allowed closer to each other hence they pack closer together. Therefore fractal dimension increases as pH increases.

The resulting fractal dimension provides an indication of the aggregation mechanism which yielded the final product. It could be either reaction limited or diffusion limited. From Meakin's theory of universality of colloidal particles (Klein & Meakin, 1989) we can conclude that particles formed under reaction limited conditions, would have more compact structures, whereas diffusion limited would yield an open branched structure. Based on this claim, high pH conditions would favour reaction limited conditions since fractal dimensions are high, whereas in the opposite case open fractal structures, the characteristics of diffusion limited conditions, would be formed at low pH.

An XRD analysis of samples obtained at high concentration (0.1M) is shown in Figure 5.13. There, the samples obtained at various CO_3^{2-}/HCO_3^- ratios (yielding pH of 6.2, 6.4 and 6.6) are compared against a reference sample (R2) of hydrozincite synthesized with carbonate ions alone. A search and match analysis found that all peaks corresponded to hydrozincite pattern number 04-013-7573 (Ghose, 1964). However, the intensity of the peaks greatly differs among samples. For example, Sample R2, prepared with carbonate, presented the widest of the peaks which indicates a poor crystallinity. This is especially noticeable at peak 13° (plane 200) which is an indicator of the layered structure of the hydrozincite (see Figure 5.14). The best of the layered structures was found at the highest pH (6.6).



(a) ζ -potential as function of pH as obtained by titration of a suspension of hydrozincite



(b) Fractal dimension as a function of pH. as measured by SLS

Figure 5.12: ζ -potential and fractal dimension as function of pH. We observe that as the ζ -potential becomes close to 0, the fractal aggregates becomes tighter

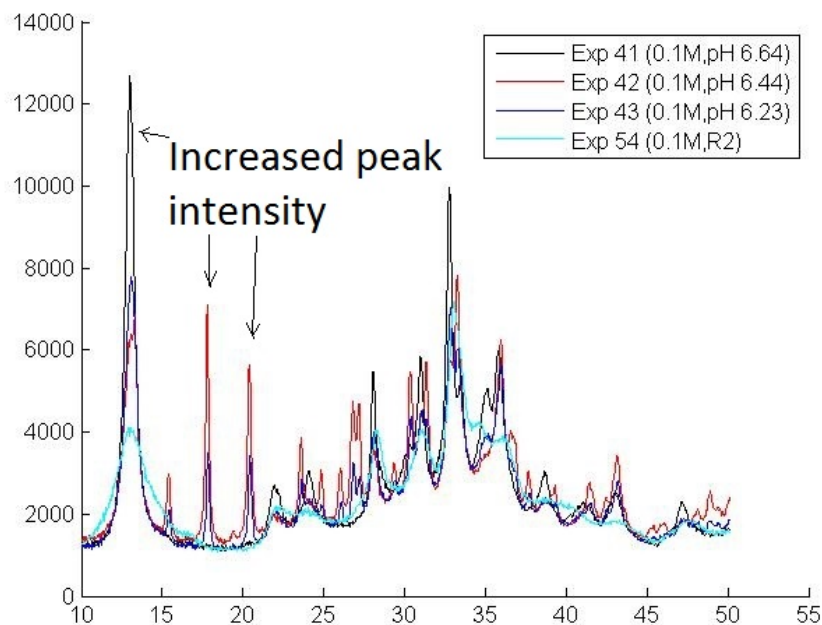


Figure 5.13: XRD of spectrum of hydrozincite synthesized at various pH compared to a reference sample. Experiment 54 yielded 7.2 pH. A higher number of counts was found at lower pH indicating better crystalline structure.

Other crystalline features seem improved at low pH. For example, peaks at 16.4° and at 20° (Planes 001 and 20-1) show a large number of counts when compared with a peak at 13° . The planes corresponding to these peaks are perpendicular to the 200 plane as observed in Figure 5.14 which indicates that not only the double layer structure but also the ZnO structures have their arrangement improved.

The variable supersaturation is believed to be the source of the described changes in the crystal structure. As expressed by Equation 5.2, low pH leads to low supersaturation which eventually produces large nuclei size as Equation 5.3 shows (Mullin, 2001). The gentle crystallization conditions found at low pH allows molecules to arrange in more ideal structures. Hence crystalline features are enhanced.

$$ss = \frac{[Zn^{+2}][CO_3^{+2}]^{0.4}[OH^-]^{1.2}}{k_{sp}} \quad (5.2)$$

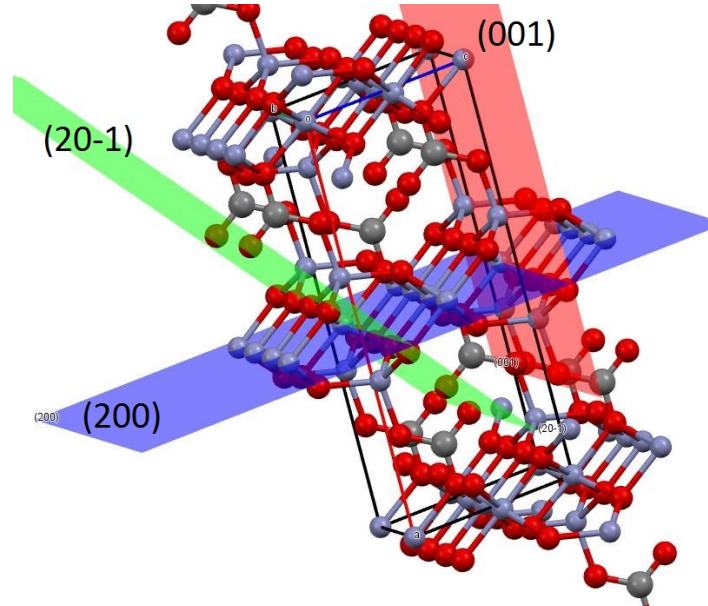


Figure 5.14: Planes 200, 001 and 20-1 showed in the hydrozincite structure.

$$r_c = \frac{2\gamma\nu}{kT\ln(ss)} \quad (5.3)$$

In Equations 5.2 and 5.3 $[Zn^{+2}]$, $[CO_3^{+2}]$ and $[OH^-]$ indicates the concentration of zinc, carbonate and hydroxide ions respectively. K_{sp} stands for the solubility product of hydrozincite. γ is the surface tension, ν the molar volume, k the Boltzmann constant, T temperature and s supersaturation as defined by Equation 5.2.

In summary, pH alters the size of the final particle by two different means. Firstly the surface potential, which increases with decreasing pH, increases repulsions among primary particles and eventually decreased the final particle size. The second mean would be through the alteration of the primary particle size. In this case, the size of the primary crystal was larger as pH decreased. It is believed that additionally to surface potential, the larger size of the primary particles may also decrease the size of the final aggregate by means of a decreased surface area. In other words, the colloidal character of the suspension may decrease as a consequence of the reduced surface area or larger particles.

Influence of temperature on particle size and reaction kinetics

Although no experiments on the study of temperature have been carried out, a brief discussion of its influence in the precipitation process is to be given. Temperature is known to have influence on various phenomena around crystallization such as the polymorph yielded, supersaturation, nucleation rate, growth, mixing kinetics, aggregation and ripening. Increasing temperature is expected to slightly increase the mixing kinetics as it influences the fluid viscosity and the species diffusivity in a limiting extend. Nucleation and growth, on the other hand, are believed to be much more affected. Increased temperature considerable increase in the solubility which would decrease the supersaturation and hence the nucleation and growth rate. Consequence of the same effect larger primary crystal size are expected. Finally, the this variable is expected to have a considerable impact on the aggregation and breakage kinetics. Increased temperature is expected to increase the thermal forces, Brownian motion, and the mobility of the smaller particles in the colloidal systems. Therefore, larger aggregation rates and larger particles are expected. Increased mobility is expected to allow particles to separate from each other more frequently increasing the breakage rate. Since the equilibrium between breakage and aggregation defines the final particle size, the effect of temperature on them would be the crucial when compared with mixing, nucleation, growth, etc. However, we lack tools to evaluate the importance of one over the other. The ripening processes are also greatly affected by the influence of temperature on solubility and ion mobility. Both of this variables increase thus causing the kinetics of the ripening and the final crystalline features to be more acute.

5.3 Conclusions

Particle size and morphology has been studied in this chapter as function of process parameter such as pH, concentration, and ripening time. These results will provide useful information for design of experiments in further studies on aggregation dynamics, as well as information about the behaviour of particulated hydrozincite under shear conditions, and different concentration as well as in the presence of surfactant.

- Shear has diverse effects at different conditions of concentration or ripening. It does reduce the size at high concentrations and in ripened material. However, it

has the reverse effect on fresh material. This is believed to be a consequence of the increased importance of surface forces against hydrodynamic forces.

- When stabilizing the suspension with SDS a defined area of stability was found, this was identified in the range from 0.6g/l to 1g/l of SDS and from 4 to 6g/l of solids in suspension. This occurred as a consequence of the combined effect of excess surfactant and large solid concentration.
- pH and concentration were found to have the greatest influence on the suspension stability. Particle size was found to decrease greatly when the pH of the concentration was decreased. pH acts on surface potential whereas concentration increases aggregation rate by increasing particle collisions. Alteration of crystal structure and fractal dimension were also observed. Based on the d_f data we can conclude that the aggregation mechanism is mainly reaction limited as large values of d_f indicates. However, lower pH moved the mechanism towards a diffusion limited mechanism.

Chapter 6

Aggregation Kinetics of Sparingly Soluble Compounds in Turbulent Tubular Reactor

6.1 Introduction

The mechanism of the aggregation of fractal structures remains unclear despite being a common problem in the pharmaceutical, cosmetics, food or metallurgy industries. This study aims to cast some light on the problem through the analysis of aggregation after reactive crystallization using a novel in-line scattering equipment. The analysis of the $d(0.9)$ of the size distribution and fractal dimension shows the dynamic nature of the aggregation-breakage equilibrium. Three regimes, Brownian growth, exponential growth and equilibrium were found to be driven by changes in turbulent conditions and residence time. Fractal dimension was found to decrease when particles evolved from fundamental particles towards final dynamic equilibrium. The novel equipment designed for this work and its methodology will allow the study of aggregation in continuous processes.

6.2 Results and Discussion

Table 6.1: Experimental conditions for the characterization of the particle size distribution of hydrozincite synthesized in tubular reactor. A range of flow rates as well as reactor lengths were tested.

Exp ID	[Zn]	[CO ₃ ²⁻]	Final pH	Reactor length (m)	Flow Velocity (m/s)	Flow Rate (ml/m)
106	0.01	0.01	N/A	1.09, 2.19 3.82, 4.22	0.392	442.92
106	0.01	0.01	N/A	1.09, 2.19 3.82, 4.22	0.331	373.97
106	0.01	0.01	N/A	1.09, 2.19 3.82, 4.22	0.269	305.02
106	0.01	0.01	N/A	1.09, 2.19 3.82, 4.22	0.208	236.07
106	0.01	0.01	N/A	1.09, 2.19 3.82, 4.22	0.147	167.12

6.2 Results and Discussion

The size of precipitated hydrozincite was measured in a novel set-up consisting of a Y junction to which a tubular section of variable length was attached. In order to assess the kinetics of aggregation SLS equipment was placed at the exit of the tubular pipe. A description of this setup and the assumptions associated with it are discussed elsewhere (Section 3.3). The flow conditions, velocity(u), flow rate(Q), Reynolds number (Re), and shear stress ($\dot{\gamma}$), tested in this work are summarized in Table 6.2. Reynolds in the range 2000 to 6000 are tested thus covering the range of turbulent and laminar regimes.

6.2.1 Size analysis

Figure 6.1 shows the evolution of the $d(0.9)$ as a function of dimensionless time t^* . $d(0.9)$ has been proven to represent the size distribution as well as being an intuitive tool for its interpretation. A dimensionless number of collisions, t^* stands for the product of residence time, τ shear rate, $\dot{\gamma}$, and volume fraction of particles, ϕ . ($t^* = \dot{\gamma}\phi\tau$). The trend of the $d(0.9)$ in Figure 6.1 illustrates a similar evolution to experiments performed in Taylor-Couette flow devices such as Flesch *et al.* (1999); Oles (1992);

Selomulya *et al.* (2003); Serra *et al.* (1997). In them three different aggregation regimes can be identified.

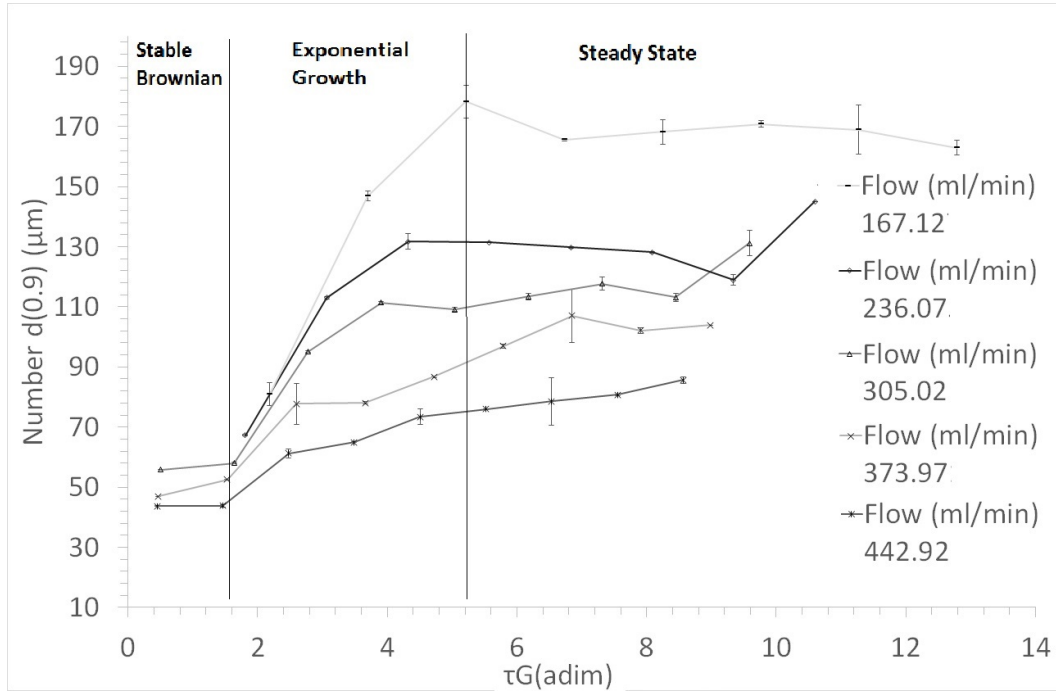


Figure 6.1: Evolution of $D[0.9]$ with dimensionless number of collisions $t^*(= \dot{\gamma}\phi\tau)$. (*) $442.92\text{ml}/\text{min}$, (\times) $373.97\text{ml}/\text{min}$, (Δ) $305.02\text{ml}/\text{min}$, (\diamond) $236.07\text{ml}/\text{min}$, ($-$) $167.12\text{ml}/\text{min}$. Three regimes were found: Stable Brownian, exponential growth and steady state.

1. At the initial stage, particles size remains relatively unchanged, independently of flow conditions. When computing the Stokes number (Figure 6.2(b)), it is observed that particles are below the Kolmogorov sub-range, indicating that they are unaffected by fluid features such as eddies, high strain or vorticity zones. see Section 2.5. Additionally, the small Peclet (Figure 6.2(a)) number suggest that Brownian motion driven the process.
2. Accelerated agglomeration is characteristic of the second regime. The Peclet number suggests that particles are large enough to feel the effect of eddies. However, Brownian motion may still be important. In the present case, faster growth

rates for the smallest shears are observed. On the other hand, equilibrium is reached more rapidly under the same vigorous turbulent conditions.

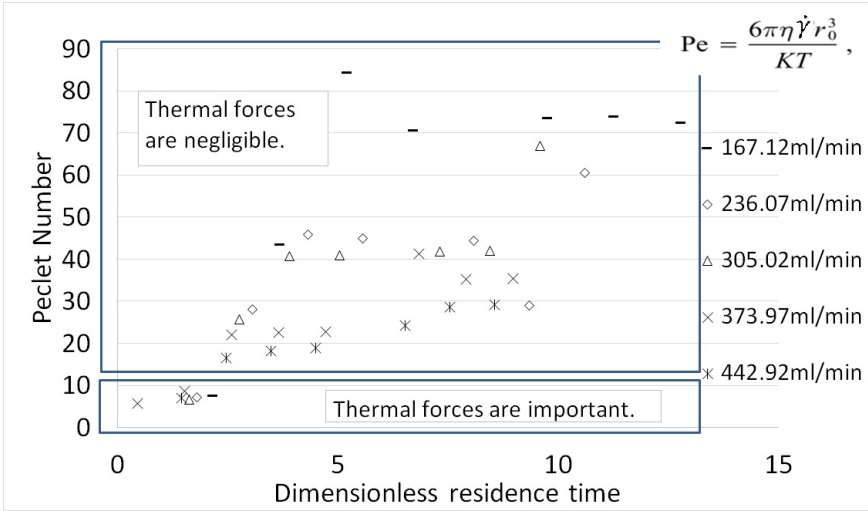
3. Equilibrium is reached in this last stage. Particles are now in the Kolmogorov range being sensitive to flow changes. Diffusive forces are negligible. Equilibrium is reached more rapidly under increasingly vigorous conditions, although aggregation rates are smaller since particles do not need to grow to large sizes.

At the initial stage of aggregation, Kusters (1991) suggested that the formation of doublet by particle diffusion is the main mechanism for particle growth. It is believed that the equipment used is not sensitive enough to capture this phenomena and a particle size of $50\mu\text{m}$ was observed instead. Serra *et al.* (1997) suggested that Brownian motion drives growth which would yield an increase in size independent of shear rate, therefore having the same slope for all flow conditions. However, the present study has found this not to be the case. Instead of shear dependent, the growth was found to follow an exponential growth law which depends on shear stress. Probably, the flow conditions of the tubular reactor makes a difference to how the shear influences the particle aggregation when compared with Taylor-Couette cells. In order to study the growth the Gregory model was used (see Section 2.4.3).

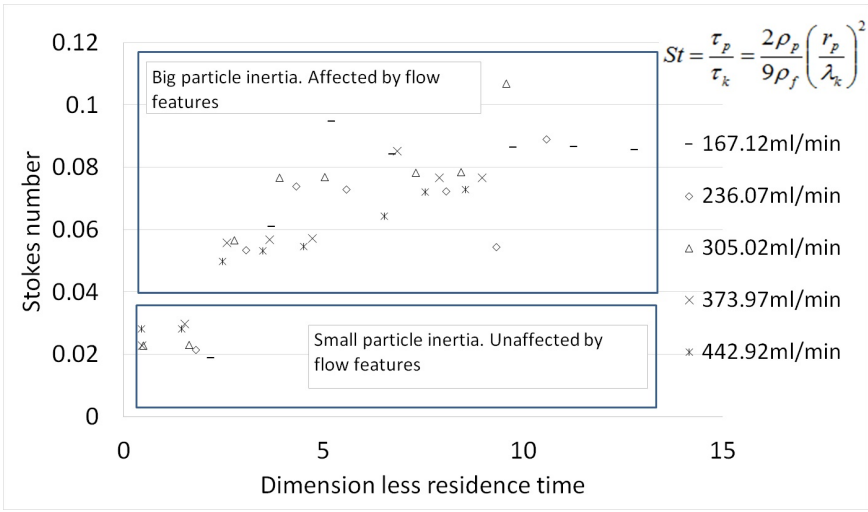
Exponential growth obeys Gregory's model presented previously in Equation 2.42. Due to this assumption, the expression has been criticized in the literature Casson & Lawler (1990). However, it is still useful for the simple case of exponential growth. Gregory's model assumes round particles colliding in couples with efficiency α . He also neglects breakage thus considering only aggregation driven by shear. In spite of this, it provides a way to qualitatively evaluate the effect of shear in the aggregation process.

Results from the fitting of the model to the total number of particles in the system in the range 0.2 to 0.6 dimensionless length are shown in Figure 6.3. A summary of the results is given in Table 6.2 where $\dot{\gamma}$ is the shear rate computed as described in Section 3.10, α is the collision efficiency and ϕ is the concentration of solids which is constant and equal to 0.51% which correspond to a concentration of 0.01M of hydrozincite in suspension. An overview of the phenomena shows a decrease in aggregation kinetics as flow rate (shear rate) increases. The factor of the exponential law decreases with flow rate indicating the slower character of the aggregation.

6.2 Results and Discussion



(a) Peclet number against dimension less residence time for various flow rates $t^*(= \dot{\gamma}\phi t)$. Brownian forces are important at the beginning of the reactor. However not sufficient to stabilize the suspension. As residence time increases particle growth and shear forces dominate.



(b) Stokes number against dimensionless residence time for various flow rates $t^*(= \dot{\gamma}\phi t)$. Initial small particles behaves as ghost particles, following stream lines. As they grow larger, closer to the Kolmogorov scale, effects of preferential concentration may happen which promotes aggregation.

Figure 6.2: Study of dimensionless numbers, Peclet and Stokes, with dimensionless residence time and size. (*) 0.38m/s, (x) 0.35m/s, (Δ) 0.26m/s, (◇) 0.208m/s, (-) 0.140m/s. Peclet number increases with larger residence time, Suggesting greater importance of flow forces against thermal forces. Stokes number also increases which indicates ghost like particles gain inertia becoming less flow driven.

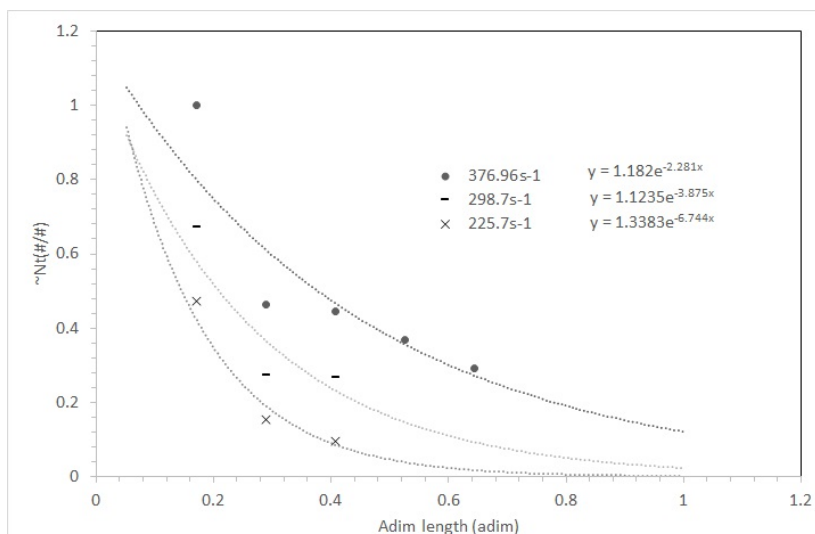


Figure 6.3: Dimensionless number of particles vs. dimensional length for exponential growth regime for three shear rates: (\bullet) $376.96s^{-1}$, ($-$) $298.7s^{-1}$, (\times) $225.7s^{-1}$. Exponential growth kinetics were found to increase with decreasing flow rate.

It is believed that due to the increasing vigorousness of the flow conditions, the collision efficiency decreases therefore slowing the process of aggregation, thus opposing to the the Brownian. This theory is supported by the values of $\phi\alpha$ reported in Table 6.2. They show a steady decrease as the shear increases.

This differs significantly from the results found by Serra *et al.* (1997) and Oles (1992) in Taylor-Couette where the rapid aggregation regime was found to be independent of shear. This divergence is believed to be a consequence of the different flow features between Taylor-Couette and plug flow regimes. For example, the quadratic velocity profile in plug flow and the vortex like features are more heterogeneous than those found in Taylor-Couette which is probably more homogeneous.

Size remained constant in the last regime as a consequence of larger particles being more sensitive to flow stress forces and hence breaking as a consequence of this. In the last stage of aggregation, equilibrium between aggregation and breakage is reached (Oles, 1992). Hydrodynamic stresses to which particles are subjected exceed the bounding forces of the larger particles and hence breakage occurs. Smaller particles, on the other hand do not experience excessive hydrodynamic forces. It is believed that the size of the eddies drives the breakage of particles in the last stage of aggregation (Serra

Table 6.2: Values of the exponential factor of the Gregory model. Aggregation efficiency decreases as shear rate increases.

$\dot{\gamma}$ (s^{-1})	$(\phi\alpha\dot{\gamma})$	$\phi\alpha$
377	2.281	0.006
299	3.87	0.013
225	6.744	0.030

et al., 1997). In other words, particles find difficulties in growing out of the Kolmogorov scale due to the increase of internal stresses.

Although there are significant similarities between the data collected in this work in a tubular reactor and the data from Taylor-Couette flow, there are divergences that cannot remain unnoticed. In spite of the advantages of using inline SLS analysis, the proposed set-up produces more scattered results, more unstable values of $D[0.5]$ compared with the set-up proposed in the literature. Therefore, the stable floc size is not resolved as clearly as in the previous work of Oles (1992). Another thing to notice is the decreasing delay in reaching a stable flow size with increasing flow rate. For example, for the lowest flow rate, the stable size is found at a dimensionless time equal to 5, whereas in the largest flow rate the stable sizes were found at around 2.5. This is believed to be a feature of the plug flow at which the aggregates are obtained.

Whereas in Taylor-Couette and stirred tanks the number of collisions, t^* , depends only on residence time and shear, in plug flow it is also believed that the distance travelled by the fluid has an affect, since the longer the distance, the more eddies will form. This variable is not taken into account in the dimension less collision frequency, t^* . Another possible explanation for the discrepancies between batch and continuous is that the unsuitability of the number of collisions as a variable to accurately describe the aggregation phenomena. Instead other features such as eddy frequency, which holds the same units, may better account for the effect of turbulence on aggregation. However, this study is beyond the scope of this project since it would involve the use of tools like CFD to estimate the value of Kolmogorov eddy frequency.

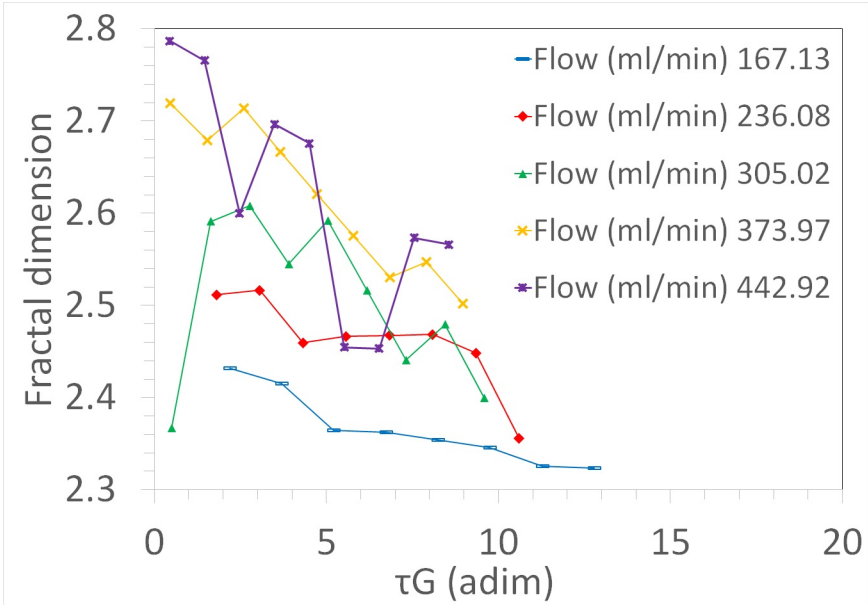
6.2.2 Fractal dimension analysis

For the purpose of analysing the restructuring of fractal aggregates, fractal dimension (d_f) was obtained using the Guinier plot by linear regression of the low q region as shown in Section 3.3.1. d_f is a representative indicator of the particle arrangement and compaction of fractal aggregates. It has been used previously by numerous authors for the purpose of modelling particle restructuring (Aubert & Cannell, 1986; Lin *et al.*, 1990; Oles, 1992; Selomulya *et al.*, 2003). In the present study fractal dimension d_f has been obtained as a function of the dimensionless number of collisions t^* . Figure 6.4(a) shows the evolution of d_f as a function of t^* at various flow rates. Similarly to the case of size, d_f data is significantly scattered. Although the variation of the experimental data is problematic when deriving regression, trends are easily detectable. It is believed that the observed decrease in d_f observed in Figure 6.4(b) is a consequence of the aggregated growth.

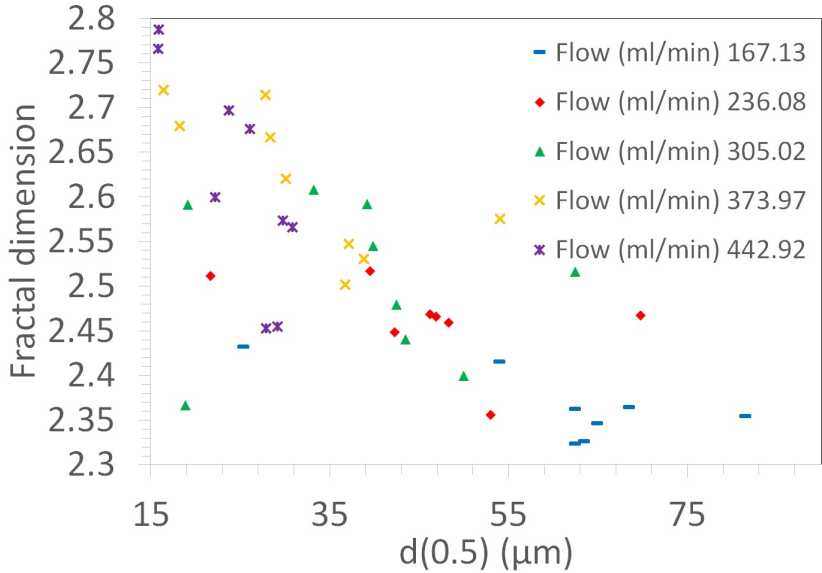
Chakraborti *et al.* (2003) on the other hand, suggests that growth of natural fractal structures inherently decreases fractal dimension. Thus, when doublets or triplets are created in the first stages of aggregation, primary particles are closely bounded hence holding high fractal dimensions. Later on in the process clusters of primary particles collide increasing the size and decreasing d_f since the voids left between particles increase in size. Finally, the increase of fractal dimension is expected to decelerate or even increase as a consequence of the mechanism proposed by Lin *et al.* (1990) such as loss of exposed aggregates of their fouling towards the center of itself.

When plotting fractal dimension against particle size a decreasing linear trend is observed independent of flow conditions (Figure 6.4(b)). Decrease in d_f is believed to be a consequence of kinetic structures created by the attachment of new units as explained previously (Chakraborti *et al.*, 2003).

Under rapid aggregation conditions, like the ones found in this work, kinetics structures are significantly different to stable equilibrium structures, which implies the increasing in fractal features. It is believed that aggregation-breakage equilibrium influences the decrease of d_f . The dynamic equilibrium creates a continuous stage of growth/breakage, since particles gain new entities as they lose them as a consequence of breakage. This stage of dynamic equilibrium would enhance the creation of kinetic aggregates hence favouring the mechanism proposed by Chakraborti *et al.* (2003) where



(a) Trend of the fractal dimension (d_f) for various shear rates with t^* ($= \dot{\gamma}\tau$). Aggregates seem to become less compact as they flow along the pipe. Probably as a consequence of the aggregation-breakage equilibrium.



(b) Fractal dimension (d_f) vs median of the size distribution ($d(0.5)$). The linear correlation found between d_f and size indicates that particles become less compact as size increases.

Figure 6.4: Study of fractal dimension with dimensionless residence time and size. (*) 442.9ml/min, (×) 374.0mL/min, (Δ) 305.0mL/min, (◇) 236.1mL/min, (—) 167.1mL/min. Under the present experimental conditions, fractal dimension seems to correlate with particle size better than with dimensionless residence time.

d_f decreases as a consequence of growth. In this study we observed a steady decrease in fractal dimension suggesting such an effect.

6.2.3 Concentration analysis

Various concentrations have been tested in order to assess the particle size evolution in the tubular reactor. 0.01M, 0.008 M and 0.006 M of zinc salt were used respectively. These values have been chosen based on the detection limits of the Mastersizer. Two repetitions at different flow rate aimed to capture the difference between laminar and turbulent flow rate. Various lengths of tubular reactor were used in order to vary the residence time.

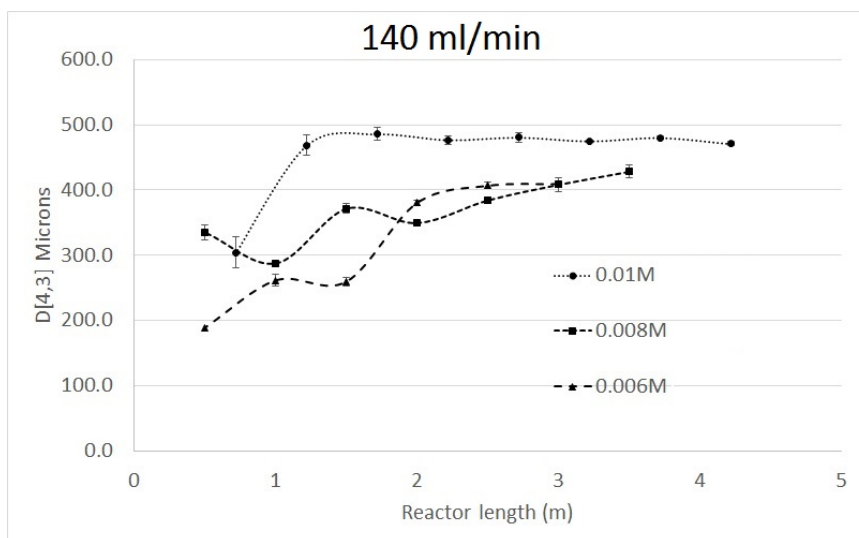
Figure 6.5(a) shows the evolution of $D[4,3]$ with time for various concentrations at low flow rate (140ml/min). $D[4,3]$ has been chosen as a identifier of the particle size as it contains the required information for the size analysis.

Similarly to the 0.01M results in Figure 6.1, the aggregates follow an increasing trend from which the three main stages of aggregation can be identified. This, as pointed out previously, is a consequence of an aggregation event of shear stress affecting larger particles. A final stable particle size seems to be found for the case of 0.006 M, however it is not as clear for 0.008M. This stable particle size decreases with concentration.

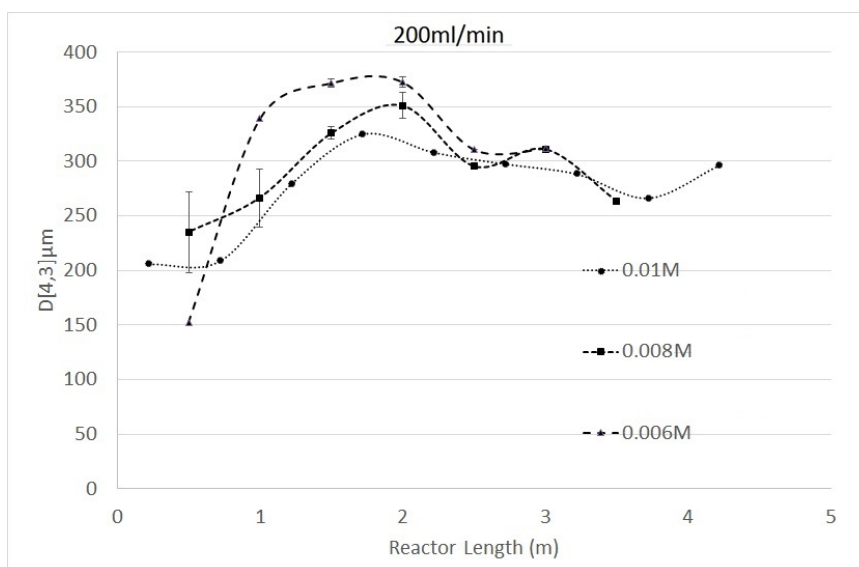
The trend of particles size as a function of reactor length at a flow rate of 200ml/min for various concentrations (0.01M, 0.008M and 0.006M), is shown in Figure 6.5(b). As expected the overall particle size is smaller at higher flow rate as a consequence of flow velocity.

An indication of behavioural change appears when the flow rate is increased. In this case all final sizes seem to be similar with a slight decreasing trend. This indicates that the aggregation-breakage equilibrium has probably not been reached and longer residence time is required to reach stability. It is interesting that for the section near the reactor entry the size increases with decreasing concentration which is the reverse of the trend found at low flow rate. This may be explain by an experimental as the deviation of size values for 0.008M are large.

From experiments performed at different concentrations we can learn that there is a decreasing relationship between size and concentration which only applies to low flow



(a) Evolution of $D(4,3)$ with reactor length for various concentrations for a flow rate of 140ml/min. Aggregation kinetics seem slowed as concentration decreases. However the final particle size seems to be independent of concentration.



(b) Evolution of $D(4,3)$ with reactor length for various concentrations for a flow rate of 200ml/min. Initial particle size is reversed when compared with low flow rate (Larger sizes were found at low concentration). Decreasing trend of the particle size indicates that equilibrium was not reached.

Figure 6.5: Particle size as a function of reactor length for two flow rates (140 and 200ml/min) and three solid concentrations 0.54%, 0.44% and 0.33% corresponding to 0.01M 0.008M and 0.006M of zinc salt. Similar to previous results, aggregation progressed in the three regimes towards a stable final particle size.

Table 6.3: Experimental conditions for the characterization of hydrozincite synthesized in at tubular reactor. Maximum and minimum flow rates were tested for phase changes and morphology.

Exp ID	[Zn]	[HCO ₃ ⁻¹]	Flow Rate (mil/min)
214	0.02	0.04	167
214	0.02	0.04	98
214	0.02	0.04	64

rates. On the other hand, particle size seems to depend upon concentration. Instead, they remain constant after steady state is reached.

6.2.4 pH influence on the aggregation kinetics

Surface chemistry has a great influence on the aggregation of particles. Large absolute value of surface charge (about 30mV or below -30mV) are normally sufficient for a suspension to remain stable. In the case of carbonates the surface chemistry is well defined (Wolthers *et al.*, 2008) which shows a decreasing trend in surface potential with pH. Values normally remain between 40 and -40 mV for low and high pH respectively (7 and 12). whereas in previous cases pH has been kept stable around 9.5 due to an excess of carbonate ions, in this section the process dynamics are going to be tested for a pH around 7.5. This was achieved by using bicarbonate as a reactant instead of carbonate. A summary of the experimental conditions for the study of size in the continuous reactor at low pH is shown in Table 6.3.

Results are shown in Figure 6.6 where particle size is plotted against reactor length. It should be noticed that repeatability of this experiment was poor compared with carbonate experiments (high pH). The system took longer to stabilize as a consequence of the slower reaction not being completed or particle fouling on the instrument windows. Another consequence of the slow reaction kinetics, was that the flow rate needed to be decreased, thus increasing the required residence time for completing crystallization. Finally, as solubility of hydrozincite increases with decreased pH, the concentration used was increased to 0.02 M in order to achieve the required obscuration for the SLS system to work.

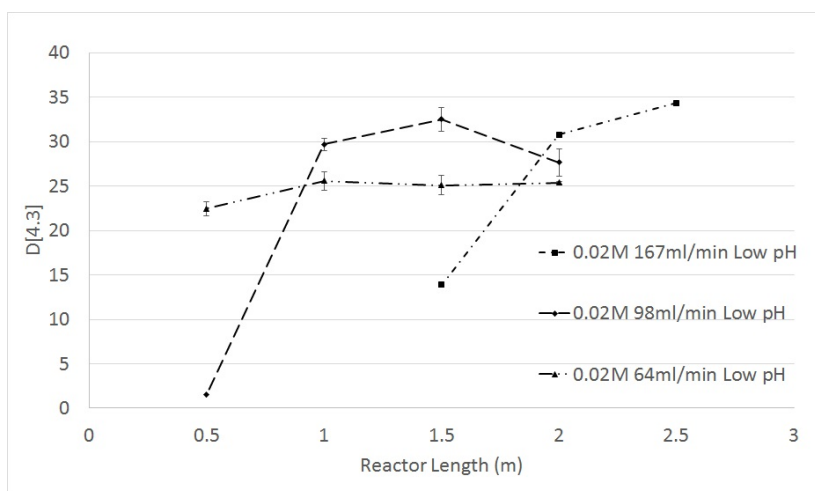


Figure 6.6: Evolution of $D[4,e]$ with reactor length for low pH and three flow rates (63ml/min, 98ml/min and 167ml/min). The particle size is 10 times lower than at high pH. The reading seems to be less consistent. However, particle size increases with reactor length.

Apart from the operating issues, the particle size showed the lowest values of all the experiments being as low as $1\mu\text{m}$ for the shortest residence times and 98ml/min. It is believed that the combination of decreased solid concentration and increased surface potential were, in fact, the cause of size reduction. Since the solubility is high for lower pH, the amount of solids in suspension is lower, as observed in the lower obscuration values from the Mastersizer. As a consequence, the aggregation kinetics were decreased hence yielding a product of smaller size. On the other hand, the effect of lowered pH is transformed into increased surface potential Wolthers *et al.* (2008), which would be added to the decrease of reactor kinetics.

Although the precipitated particles at low pH present the lowest particle size, stability under shear flow seems to be an issue, as suggested by the rapid increase in size from 5 to $20\mu\text{m}$. It is believed that, although Brownian motion is larger, surface potential maintained particles in suspension, eventually, the effect of shear overcomes the repulsive barrier yielding a rapid aggregation.

6.2.5 Aggregates restructuring

Fractal dimension has been chosen to characterize the morphology of the aggregates. It provides information about the space filled by the aggregate primary particles which combined with the in-line data obtained by the SLS system allowing the study of the aggregates restructuring.

Fractal dimension, d_f , of aggregates synthesized at high pH differs significantly to particles synthesized at low pH, whereas high pH yields d_f of around 2.6, values at low pH are in the range of 1 to 1.8. It indicates a greater degree of openness in the aggregated structure. Figure 6.7(a) is a plot of the data obtained by the Mastersizer showing the structure change. This change in structure is probably the result of the increased surface potential which enhances particle repulsion.

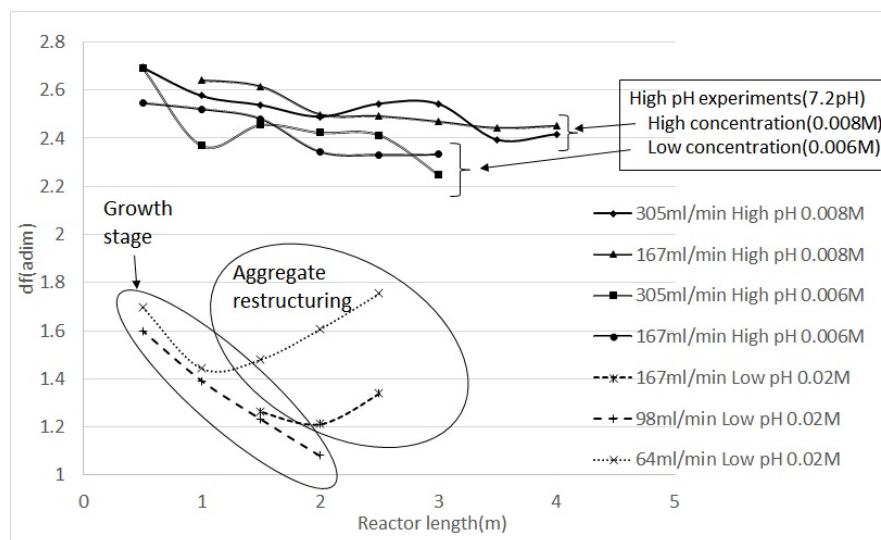
Low d_f observed at low pH indicates a change in the aggregation mechanism towards a more limited by diffusion (Meakin & Family, 1988). As particles attach to the aggregate they find the position of minimum energy, away from other aggregates. The structure observed in SLS is therefore one of an open aggregate with particles separated from each other.

For samples synthesized at low pH it is interesting to observe the initial decrease in d_f as later it sharply increased in a parabolic manner. It is believed that an initial stage of particle growth occurs where the primary particles built up consecutively. Later in the process, growth would be combined with rearrangement of the fractal structure thus yielding the observed curved shape. The mechanisms of rearrangement consist of the lost or bending of the most exposed branches of the aggregate (Lin *et al.*, 1990). This would explain the uneven growth mechanism observed in Figure 6.6.

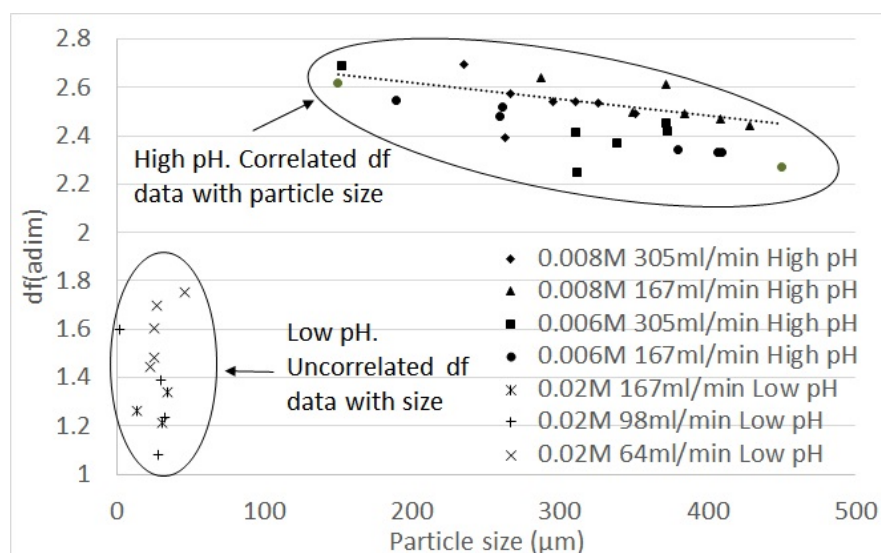
The structure of particles synthesized at low pH seemed to have a stronger relationship with flow rate, whereas size seems to govern the behaviour of particles at high pH. This can be observed in Figure 6.7(a) where the d_f values decrease for increasing values of flow rate, i.e. Flow rates of 350 ml/min showed the lowest of the values whereas 167 ml/min stands for the highest.

d_f from high pH samples plotted in Figure 6.7(a) also seem to have a dependence on concentration, while no as acute on flow rate. Increase in flow rate seems to only enhance the dispersion of the readings, those showing a steadier trend for lower flow rates. The effect of concentration, on the other hand, is observable in two sets of

6.2 Results and Discussion



(a) Fractal dimension vs. reactor length. Test run at various pH, concentrations (0.008M and 0.006M) and flow rate. The higher the pH and concentration, the more compact the particles are. At low pH, aggregates initially expand along the growth process and latter restructure by losing or rearranging exposed branches.



(b) Fractal dimension vs. particle size. Test run at various pH, concentrations (0.008M and 0.006M) and flow rate. At high pH particles correlates with particle size since the process is driven only by growth. At low pH no correlation was found since restructuring was present.

Figure 6.7: Fractal dimension as a function of reactor length and particle size. d_f correlates adequately with particle size at high pH but it does not for low pH ones. At low pH the particles initially decrease d_f for latter increase possibly due to growth and list of the exposed branches.

data which represent experiments at 0.008 M and 0.006 M, where lower concentrations yielded larger fractal dimensions.

Similar to the study performed in Section 6.2.2, Figure 6.7(b) shows fractal dimension against particle size. From it, the two data-groups corresponding to experiments at low and high pH can be identified. For high pH, the behaviour at lower concentration remained similar to the observed at 0.01 M. Therefore, similar conclusions can be drawn. For example, d_f is mainly dependent on particle size, and not on flow rate in the case of high pH. For low pH, on the other hand, no relation of d_f with size could be found which indicates that main contribution is residence time, expressed as reactor length, and fluid forces, expressed as flow rate. This leads one to wonder about the importance of fluid forces in the growth of particles at low pH.

It is believed that large surface potential found in low pH media yields weaker and more open aggregates as the repulsive force increases. Here, the structures would be more sensitive to external forces such as shear. Similar observations were found in Flesch *et al.* (1999) when studying polystyrene particles in turbulent flows. Oppositely, high pH causes repulsive inter-particle forces to weaken, hence increasing strength within the aggregates which makes them more compact and resilient to velocity gradients.

6.3 Conclusions

In this chapter the behaviour of hydrozincite has been observed under various conditions using the inline light scattering equipment in order to study aggregation kinetics. The surface forces, driven by changes in pH, seems to define aggregation kinetics against other factors, i.e. the sensitivity of the flocs to shear stresses or the time evolution of size. Smaller particle sizes were found when repulsive surface forces were the strongest which occurred at low pH. Under these same conditions, aggregates are less dense and decrease in density with increasing flow rate. Only after a certain residence time, when particles have already reached steady state, did the density steadily increase.

- We report a new experimental set-up for studying aggregation kinetics after reactive crystallization under laminar and turbulent conditions consisting of a 60° Y mixer, a contacting zone and a particle analyser.

- Three different aggregation regimes have been found at three residence times. Namely, stable Brownian regime, exponential growth and steady state, which are the result of the competition of three different processes Brownian motion, shear rates and breakage.
- The aggregation phenomena captured with the proposed in-line SLS differs significantly from the one observed in the Taylor-Couette devices. This is believed to be a consequence of the different nature of the flow and the shear stress distribution.
- It is hypothesized that the nature of the process of aggregate restructuring is a consequence of the nature of the flow conditions. Therefore, particles could not grow outside the Kolmogorov turbulent scale and decrease in fractal dimension is inherent to the dynamic equilibrium found under these conditions.
- Changes in size and shape in precipitated hydrozincite have been observed under various conditions affecting the aggregation kinetics. The surface forces, defined by pH seems to define aggregation kinetics. i.e. the sensibility of the flocs to shear stresses or the time evolution of size. Smaller particle sizes were found when repulsive surface forces are the strongest which occurs at low pH. Under these same conditions, aggregates are less dense and more likely to decrease density with increasing flow rate. Only after a certain residence time, when particles have already reached a steady state, did the density steadily increase.

Chapter 7

Aggregation Kinetic Modelling: Population balance model in a tubular reactor

7.1 Introduction

In previous chapters it has been learned that hydrozincite present a variety of particle properties depending on the conditions under which it is synthesized, e.g. pH, flow rate and time. On one hand, thermodynamic variables such as induction time solubility or surface tension have been measured in Chapter 4.1 and then other kinetic properties such as particle size have been measured in Chapter 5.1. Finally, the dynamic behaviour of the PSD of hydrozincite in a tubular reactor has been characterized as a function of concentration pH and residence time in Chapter 6.1.

In this chapter a general descriptive model is derived aiming to explain the general behaviour of precipitating hydrozincite observed in previous sections. Features, such as changes in fractal dimension or final particle size, are described based on concepts, such as surface potential, particle re-arrangement or aggregation-breakage equilibrium. Finally, a population balance model is used to mathematically describe the aggregation phenomena observed in Section 6.1. The model, consisting of a combination of aggregation and breakage, is then fit to the experimental data obtained through the inline SLS thus distinguishing between the aggregation and breakage individual contribution in

the overall process. The limits on the application of the model are given by its assumptions which consist of: plug flow assumption, negligible growth rate and instantaneous reaction.

7.2 Qualitative Hydrozincite Precipitation Model

From the data presented in Sections 4.1, 5.1, and 6.1 a model for the aggregation of hydrozincite in a tubular reactor will be derived. In this model, features of the aggregation process will be contemplated in the context of an overall system. For example: the aggregation event and the stable particle size observed in Figure 6.1, as well as the changes in fractal dimension in Figure 6.7(b) (its size dependence at high pH and its residence time dependence at low pH). A number of concepts developed in the literature, covered in Chapter 2, will be used to explain the features observed in Chapters 4.1, 5.1, and 6.1 (nucleation kinetics (Mullin, 2001), reactive mixing (Badyga & Bourne, 1999), Brownian motion (Smoluchowski, 1917), exponential growth (Gregory, 1981), aggregation- breakage equilibrium (Oles, 1992), colloidal universality (Meakin & Family, 1988), particle rearrangement (Lin *et al.*, 1990), surface potential (Harbottle, 2008), Kolmogorov scale (Serra *et al.*, 1997), shear breakage (Soos *et al.*, 2007), and Ostwald ripening). The story of reactive crystallization of hydrozincite will be developed from these very same constituents from the molecular stage to final particle size.

Figure 7.1 summarizes the different section of the model. It shows the driving forces with their associated phenomena and their different outcome as a function of important process conditions (pH and flow rate). Other process conditions, such as concentration, were found to have an influence on the final results but since they are not as influential, they will not be included in figure, however they will be commented on at the right moment.

The outcome of the process was found to hugely depend on the source of carbonate used in the synthesis. On one hand, nucleation rate decreased when pH was lowered in opposition with fast reaction found at high pH 4.8. Based on the supersaturation expression (Equation 5.2) it can be said that there is a limiting step in the hydrozincite reaction which is the transformation of bicarbonate ions (HCO_3^-) into carbonate ions (CO_3^{2-}). This would be a bottleneck in the nucleation kinetics for hydrozincite

7.2 Qualitative Hydrozincite Precipitation Model

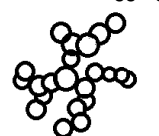
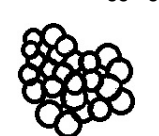

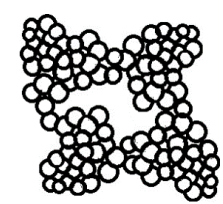
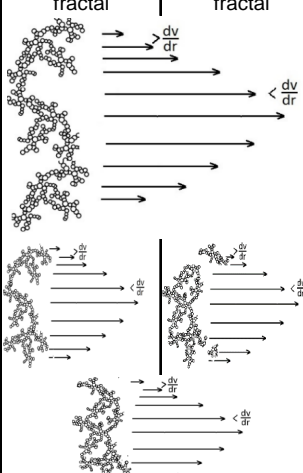
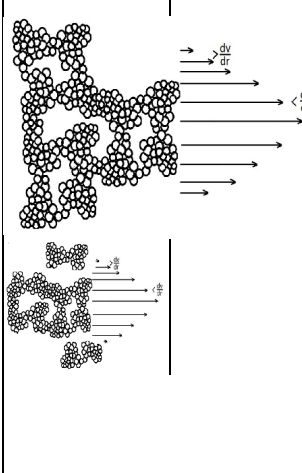
		Experimental conditions			
		Low pH (7.5)		High pH (9.5)	
Driving force	Phenomena	High flow (200ml/min)	Low flow (140ml/min)	High flow (200ml/min)	Low flow (140ml/min)
Chemical Potential	Reaction	ZnNO ₃ (0.01M)	NaHCO ₃ (0.01M)	ZnNO ₃ (0.2M)	NaCO ₃ (0.4M)
		Reaction Limited (Slow Reaction & Fast mixing)	Reaction Limited (Slow Reaction & Slow mixing)	Reaction Limited (Fast Reaction & Fast mixing)	Mixing Limited (Fast Reaction & Slow mixing)
Supersaturation	Nucleation	Homogeneous		Homogeneous	
Surface energy	Aggregation	Moderate strong surface repulsive forces Diffusion limited aggregation		Weak surface repulsive forces Reaction limited aggregation	
					
		Increase particle size Decrease of fractal dimension			
					
Surface energy Shear stresses	Restructuring	Breakage enhanced Early lost of external Increase of fractal	Breakage enhanced Late lost of external Increase of fractal	Breakage enhanced	Aggregation enhanced
					
Surface energy	Ostwald Ripening	Relative large solubility Recrystallization in flakes		Low solubility Particles rearrange to form blocks	

Figure 7.1: Representation of the descriptive model for the reaction, aggregation and ripening of hydrozincite in turbulent flows. High and low pH conditions are contemplated as well as high and low flow rates.

7.2 Qualitative Hydrozincite Precipitation Model

synthesized at low pH. Under these circumstances the mixing does not influence the reaction as it occurs at a faster rate compared with nucleation (Badyga & Bourne, 1999). Hence, for low pH, the precipitation would be reaction limited whatever the mixing conditions are.

On the other hand, solution pH drives the surface ionization of carbonates particles. As shown in Section 5.2.3 the surface potential increases from around 1 to 30eV when pH is decreased from 9.5 to 7.5. As a consequence, a moderately strong repulsive force keeps the precipitated primary particles apart, which although not sufficient for maintaining a stable colloidal suspension, it produces smaller aggregated particles. Increased repulsive forces also yields open aggregates of low fractal dimensions as shown in Sections 5.2.3 and 6.2.5. As final consequence of the high surface potential it has been found that a diffusion limited mechanism drives the aggregation kinetics. This mechanism has slow kinetics and yields small fractal dimensions (Meakin & Family, 1988).

Flow rate is also a key factor which will affect mixing kinetics and particle breakage. Primarily, flow rate is of great importance as it drives the mixing kinetics in tubular reactors. It is shown in Section 7.8 that mixing is the limiting step when flow rate is low. At this variable it is not as important as it is at high flow rate since reaction is slow and limits the overall process of nucleation.

However, at low pH (bicarbonate as reactant), flow rate presents itself a greater influence in later process stages such as aggregation and breakage. The smaller particle size found under low pH conditions (Section 5.2.3) are believed to be a consequence of the effect of shear under weaker aggregated particles. The binding energy of primary particles within the aggregate, would not be sufficient to maintain the particle together as the energy of the Kolmogorov scale eddies is too strong (Serra *et al.*, 1997). Under these circumstances the particles would break or rearrange by the following two mechanism, loss of the external branches or bending towards the inside of the particle (Lin *et al.*, 1990). This is illustrated in Figure 7.1. As consequence, particles increased in fractal dimension as they tighten and lose external branches.

Flow features in combination with phenomena associated with particles, such as Brownian motion, aggregation and breakage, yields the different regimes of aggregation, as found in Section 6.2.1, namely, stable initial size, exponential growth and steady state. The first one would occur after nucleation where particles are small and subjected

7.2 Qualitative Hydrozincite Precipitation Model

to Brownian motion. This movement of small particles would derive the aggregation phenomena at the initial stage (Smoluchowski, 1917). After particles have reached a certain size (around $Pe=50$) shear stress would drive them together at higher rates as shown in Figure 6.1 and 6.6 (Gregory, 1981). Finally, breakage gains importance as particles grow since stress forces accumulates within them (Soos *et al.*, 2007).

Similarly to low pH conditions, samples synthesized with carbonate salts (High pH) presents characteristic features. Firstly, as carbonate ions are present in solution, reaction and later nucleation occurs more rapidly. As a consequence, mass transfer, in other words, mixing is a limiting step which becomes an issue at low flow rate as CFD simulation shows 7.8. Aggregation stages are believed to be driven by the same effects observed at low pH (i.e. Brownian motion, shear stress and breakage). Although in this case surface potential is weaker and particles are tightly packed (larger fractal dimensions). Consequently, particles are more difficult to break (larger inter-particle forces) and reach larger sizes in the order of $500\mu m$. Eventually, when particles reach a certain size, internal stresses become too strong and particles break, this would be a function of flow rate.

Crystal growth was considered as negligible in this model. The low value of solubility in contrast with the large values of supersaturation yields a rapid and homogeneous nucleation which rapidly consumes supersaturation. As a results, growth cannot occur or if it does it occurs to a small extent, negligible in the scale we are working. This is supported by SEM images of freshly synthesized particles, where individual small particles are observable. Also, the rapid aggregation kinetics observed in Figure 6.1 are characteristic of pure aggregation phenomena.

At larger time scales (in the order of days), Ostwald ripening plays a major role in the restructuring of aggregates. Once again the differences between low and high pH are significant. In the case of low pH the increased solubility allows the equilibrium between solid and liquid material to be more balanced between the two stages. This allows ions to dissolve and recrystallize easily. Under these circumstances, the final particles are closer to the thermodynamic crystal characteristics of hydrozincite (Flake like structures observed in Section 4.3.3). On the contrary, under high pH, the solubility is low which shifts the equilibrium towards the solid state. This allows very little exchange of ions and recrystallization is difficult. Instead, in order to decrease its

7.3 Micromixing Time Characterization and Damkohler Number by means of CFD Simulations

surface energy, the system moves entire crystal domains, primary particles. They find location in the crystalline structure and create a bulk of aggregated particles.

The intention of this model is to provide a summary of the experimental findings in this work in a way that they would be useful to researchers in understanding the overall process. It provides a comprehensive explanation of the aggregation phenomena of hydrozincite in tubular reactors. The next step is to use a mathematical model to explain the data which belong to the following section, Population balance modelling.

7.3 Micromixing Time Characterization and Damkohler Number by means of CFD Simulations

Mixing and reaction inside a tubular pipe is to be evaluated in this section. For this propose, the CDF methodology explained in the Material and Methods, Section ??, has been implemented consisting in the definition of a geometry, meshing and simulation.

Firstly, the boundary conditions and variables are going to be listed in Table 7.1 for the reader's reference. Then the variables Kolmogorov Time scale, supersaturation and Damkohler number will be studied in detail which will yield information about mixing and reaction processes inside the tubular reactor.

Table 7.1 lists the boundary conditions (BC), the variables and the Reynolds number used for the CFD simulations studied in this section. The inlet is defined as a velocity inlet with a flat profile. The geometry allows certain residence time for the evolution of the profile to a parabolic or quadratic depending on the conditions. The values of velocities are also listed in Table 7.1. The outlet condition was set as a zero pressure outlet which allows the definition of a flow discharged to the exterior. The BC for walls was set to zero-velocity, non-slip. Finally, The definition of a symmetry in the z axis allows the simplification of the geometry from 3 to 2 dimensions.

Additional to the boundary conditions, some process variables and constants were defined based on the literature or experimental results from previous sections. Exponential and pre-exponential factors of the nucleation rate term were obtained from experiments as shown in the hydrozincite characterization sections ?. The values of the mass fraction of OH , Zn and CO_3 correspond to $pH=8$ and $0.1M$ of Zn and CO_3 ions in the inlet streams. Regarding the solid properties of hydrozincite, a nuclei radius

7.3 Micromixing Time Characterization and Damkohler Number by means of CFD Simulations

of $28nm$ has been chosen as observed in the SEM images in section ???. The hydrozincite density has been reported to be around the $3500 kg/m^3$ and its $\log K_{sp}$ of -14.85. These process variables were considered to be the same for the four simulations.

Kolmogorov Time Scale Due to the rapid character of precipitation, the time that species take to contact at the molecular level needs to be considered since it may be limiting for the overall precipitation. In other words, unreacted material may remain in the reactor as mixing is not completed. The methodology for the evaluation of reaction/mixing consists of evaluating the micromixing time or the Kolmogorov time, as defined in Equation 2.27. There are experimental methods available consisting of a set of mixing sensitive reactions, Bourne reactions, and evaluating its conversion (Fournier *et al.*, 1996). However in this case, the use of computational techniques was preferred. Despite the assumption made on the simulations, 3.11 and the lack of experimental back up, CFD is a widely used tool in academia and industry to evaluate variables difficult to access otherwise.

The variable turbulent energy dissipation rate, ϵ , is used to compute the micromixing time from Equation 2.27. Then it was plotted on a contour plot, see Figure 7.2. Colder colours represent zones of lower Kolmogorov time scale and hence better mixing.

Figures 7.2(a) to 7.2(d) show the evolution of the Kolmogorov time as a function of flow rate. As expected, the time is reduced with flow rate. A stabilization zone is found after the Y-junction for low flow rates. Within this area lower Kolmogorov times are found.

Further insights into the distribution of the micromixing time within the reactor are shown in Figure 7.3 by the plot of the Kolmogorov time scale along the central line of the reactor (commencing at the junction and ending at the centre of the outlet). Around the junction (0.05m), low micromixing times are found due to the collision of the two streams. Then, a maximum is found around 0.25m a consequence of the presence of a mixing front and transition between mixing located on the walls towards an homogeneous mixing across the whole section of the pipe. Finally, a stable regime is reached where homogeneous mixing is found in a steady state. Figure 7.3 shows that the steady regime is reached after 0.4 m independent of the flow rate.

As consequence of the increased flow velocity, the mixing time of the two streams decreases significantly in one order of magnitude. The enlargement of the mixing zone

7.3 Micromixing Time Characterization and Damkohler Number by means of CFD Simulations

Table 7.1: Boundary conditions, variable value and Reynolds number of the CFD simulations.

Boundary	Simulation ID	Boundary Velocity@Inlet
Inlet1=Inlet2	Simulation 1	0.075 [m s ⁻¹]
Velocity BC	Simulation 2	0.115 [m s ⁻¹]
	Simulation 3	0.16 [m s ⁻¹]
	Simulation 4	0.32 [m s ⁻¹]
Boundary	Simulation ID	Reynolds Number@Outlet
Outlet	Simulation 1	1562.46
Zero pressure	Simulation 2	2395.48
	Simulation 3	3332.42
	Simulation 4	6662.96
Boundary	Simulation ID	Boundary Condition
Wall	Simulation 1,2,3,4	Zero velocity
Symmetry	Simulation 1,2,3,4	Zero gradient
Variable	Simulation ID	Variable Value
Nucleation Pre-exponential factor	Simulation 1,2,3,4	3.9810 ²¹ [m ⁻³ s ⁻¹]
	Simulation 1,2,3,4	449
Nucleation exponential factor	Simulation 1,2,3,4	449
<i>OH</i> Mass Fraction	Simulation 1,2,3,4	1.710 ⁸
<i>Zn</i> Mass Fraction	Simulation 1,2,3,4	0.00696
<i>CO</i> ₃ Mass Fraction	Simulation 1,2,3,4	0.005966
Nuclei Radius	Simulation 1,2,3,4	2.810 ⁻⁸ [m]
Crystal Density	Simulation 1,2,3,4	3500 [kg m ⁻³]
Log <i>K</i> _{<i>sp</i>}	Simulation 1,2,3,4	-14.85

7.3 Micromixing Time Characterization and Damkohler Number by means of CFD Simulations

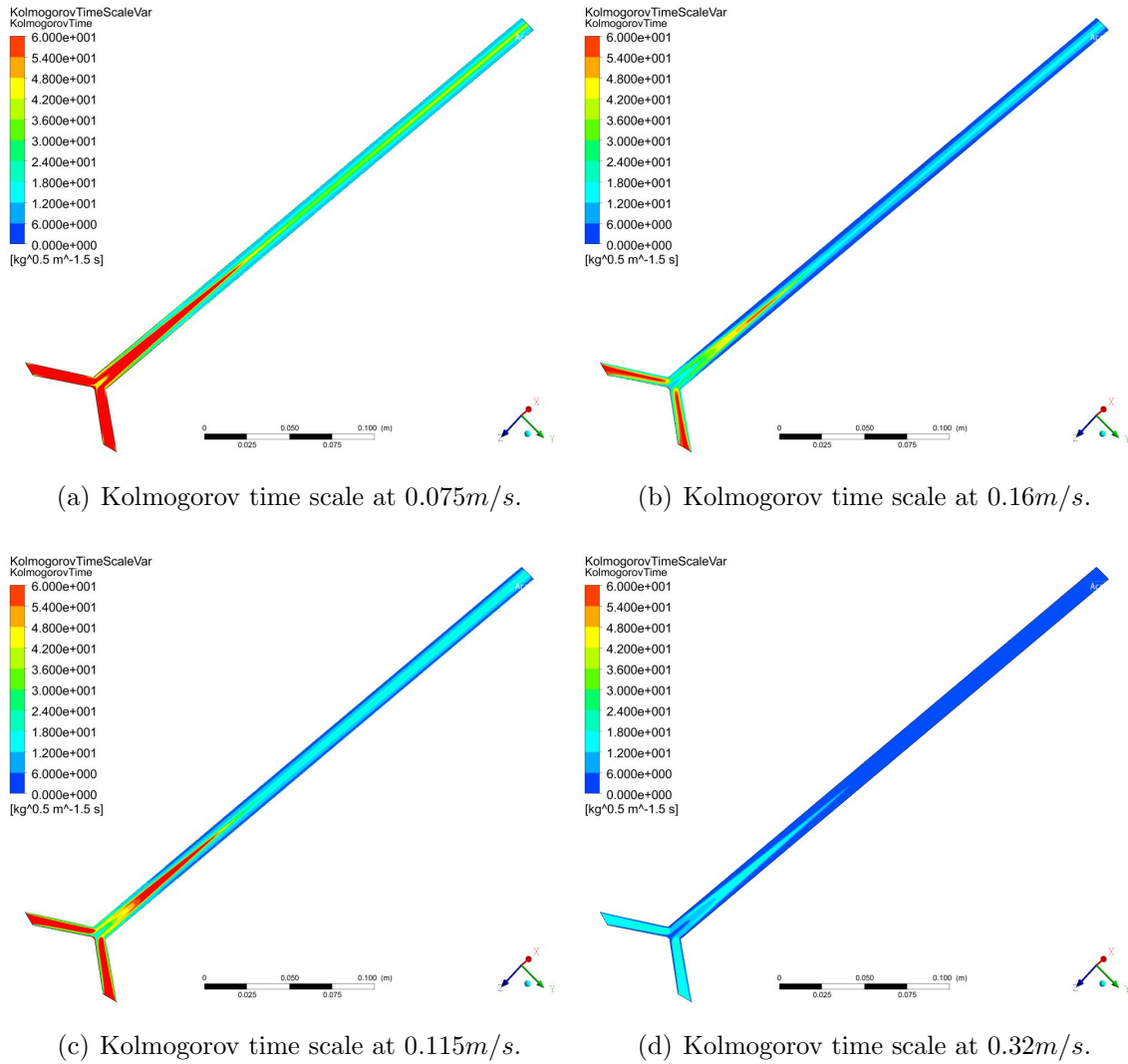


Figure 7.2: Kolmogorov time scales at various flow rates. A decrease in the Kolmogorov time scale is found as flow rate increases. A zone of decrease Kolmogorov time scale is found between the two jets which is probably going to have a great impact in mixing since where both species coincide.

7.3 Micromixing Time Characterization and Damkohler Number by means of CFD Simulations

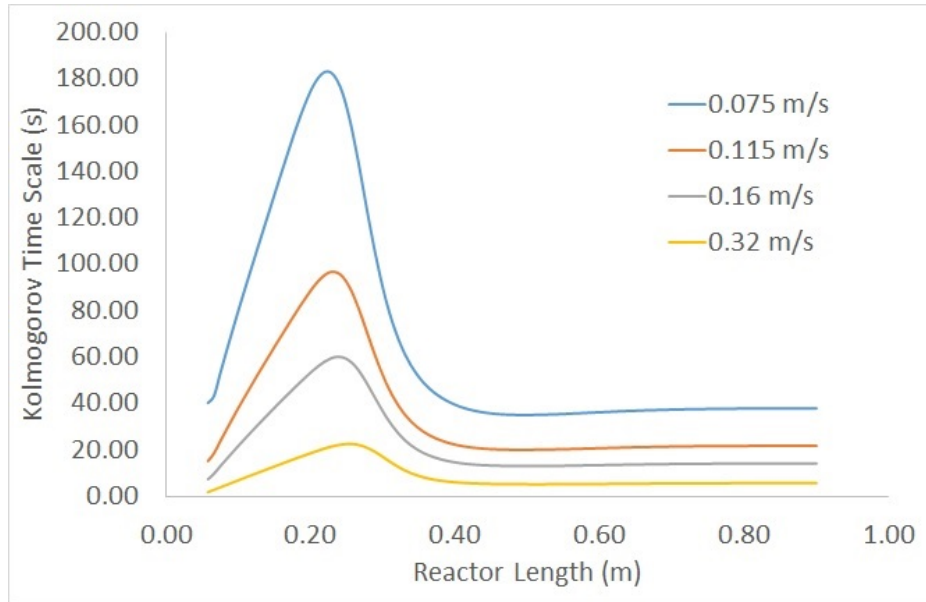


Figure 7.3: Kolmogorov time scale as a function of reactor length for flow velocities 0.075, 0.115, 0.16 and 0.32m/s. The initial low value around 0.05m indicates a high energy collision between streams. The maximum mixing time is found after the streams collide and create a mixing front. Finally, the time scales homogenizes across the reactor section. As expected, the largest values of Kolmogorov time scales correspond to the lowest flow rates as a consequence of the less energy being dissipated.

around the junction (low Kolmogorov time zone located between 0.05 and 0.2m) as a function of flow velocity is expected to greatly enhance the mixing between species as both species are present in that area. The decrease of the Kolmogorov time as a function of flow velocity is a consequence of a larger energy dissipation rate. As introduced on the literature review, Section 2.3.2, the larger the flow rate, the smaller the turbulent eddies and hence the larger the energy dissipation rate. Smaller eddies enhance convective diffusion at smaller scales which drives more efficient mixing. Therefore the mixing time, in other words the Kolmogorov time, is smaller as it is observed in the maximum values of the curves plotted in Figure 7.3.

Supersaturation Profiles Supersaturation was defined by a UDF using the expression 7.1 introduced in literature review 2.6.3

7.3 Micromixing Time Characterization and Damkohler Number by means of CFD Simulations

$$s_s = \frac{[CO_3^{-2}]^{0.4}[Zn^{+2}][OH^-]^{1.2}}{K_{sp}} \quad (7.1)$$

Figure 7.4 shows the evolution of the supersaturation as a function of reactor length. As an alternative to the central line used in the Kolmogorov scale plot, the Supersaturation was taken as the length average value across the reactor diameter to obtain values across the length. 13 lines were drawn perpendicularly to the reactor length and its average value was then obtained and plotted against reactor position. It has been observed that this a more significant representation of the variable since it accounts for the phenomena in the whole section and is more efficient as supersaturation is a more localized phenomena when compared with Kolmogorov time. From Figure 7.4 we can observe the sharp build-up of supersaturation around the junction independent from the flow rate. Then, further build-up is observed. The rate of supersaturation build-up increases as a function of the flow velocity which suggests a mixing dependent phenomena. Finally, the nucleation consumes reactant at a greater rate than they are mixed and supersaturation decays, this corresponds to the third reactor section. Notice that the graph shows the location of the phenomena but not the rate since the curves are not plotted against residence time. However, it goes without saying that all this process occurs at a much faster rate as flow velocity increases.

Region 1 in Figure 7.4 shows a steady increase in supersaturation as a function of reactor length which seems independent of the flow velocity. This indicates that the two streams remain completely unmixed for 0.1m after the junction. Figure 7.5 shows that the supersaturation is localized around the reactor centre where the two streams meet which creates a confined reaction front.

The second length of the reactor shows a steady increase in supersaturation dependent of the flow velocity. The Figures show a steep increase in the supersaturation as flow rate increases. This indicates that flow rate promotes the mixing between species which yields to larger supersaturations. Additionally, the mixing increasing supersaturation, nucleation influences the slope by consuming supersaturation. However, this effect is not obvious in the second region of the graph. Instead, it shows its weight in the third section where reactants commence to exhaust and nucleation plays a more important role. As a consequence the supersaturation curve changes behaviour towards a the decreasing trend expected as reaction evolves. Figure 7.5 shows the distribution

7.3 Micromixing Time Characterization and Damkohler Number by means of CFD Simulations

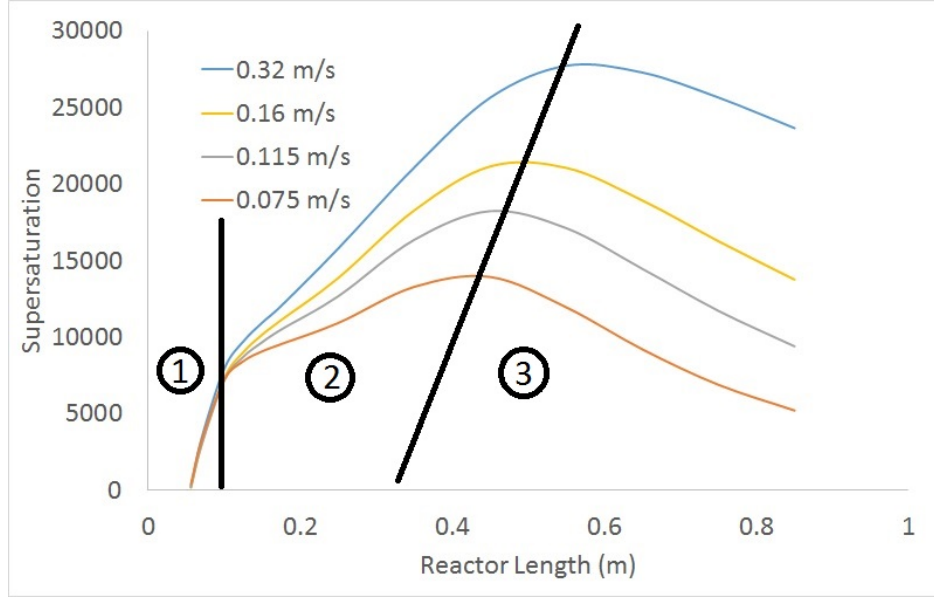


Figure 7.4: Length average supersaturation across the reaction section as a function of the reactor length. Three section can be identified as functions of the trend. (1) supersaturation buildup independent of flow rate. (2) mixing driven supersaturation build-up. (3) Reactant exhaustion and consequent supersaturation decrease.

of supersaturation across the reactor. Opposite to region 1, the distribution is a lot of more homogeneous across the diameter when compared with regions 2 and 3. This supports the idea that the reaction is mixing driven in those areas. In order to assess the real weight of mixing over reaction the Damkohler number is going to be computed and its value across the reactor assessed.

Damkohler Number In order to characterize the relevance of mixing and reaction, the Damkohler number is going to be defined. The Damkohler number is a dimensionless number which is expressed as the ratio between Kolmogorov time scale and reaction time scale. Kolmogorov comes as described previously whereas reaction rate is a ratio between initial concentration and reaction rate. However, due to the nature of crystallization, the definition of reaction rate corresponds to nucleation rate J_r , different to a normal reaction.

$$Da_c = \frac{KolmogorovTimeScale}{Reactiontimescale} = \frac{\tau_k}{\tau_c} \quad (7.2)$$

7.3 Micromixing Time Characterization and Damkohler Number by means of CFD Simulations

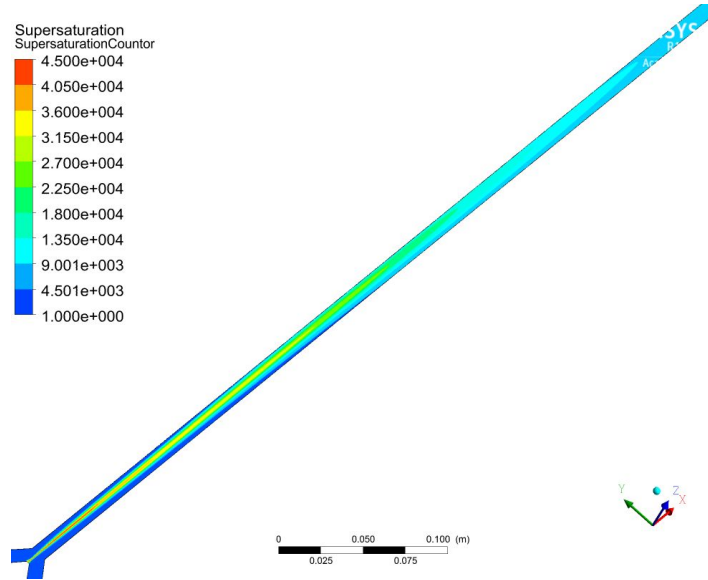


Figure 7.5: Contour plot of supersaturation at 0.075m/s. A localized mixing front is found at the reactor entrance. Supersaturation then spreads homogeneously across the reactor section driven by mixing. Finally, supersaturation is consumed around the reactor outlet.

$$\tau_c = \frac{[Zn]_0}{J_r} \quad (7.3)$$

User defined functions in CDF-Post were used to create a plot of the Damkohler number along the reactor central line, Figure 7.6, and the contour plot shown in Figure 7.7 for various velocities. In Figure 7.6 large values of Da number indicates that mixing as limiting factor for the completion of the reactor. Lower values of Da suggest fast mixing and slow reaction. Similarly, in Figure 7.7, warmer colours indicate high Da numbers where mixing controls reaction (reaction is faster than mixing). On the contrary, blue areas represent where reaction is slow and mixing is more important, hence reaction is the limiting step.

Figure ?? shows low values of Da around 0.1m, near the junction, which suggest that both, mixing and reaction occurs at slow rate. As shown in Figure 7.3 The Kolmogorov scale is low but also the large reaction rate driven by the large concentration gradient yields low Da numbers. As the concentration gradient decreases and the Kolmogorov time increases, the Damkohler number increases up to a maximum at around 0.25

7.3 Micromixing Time Characterization and Damkohler Number by means of CFD Simulations

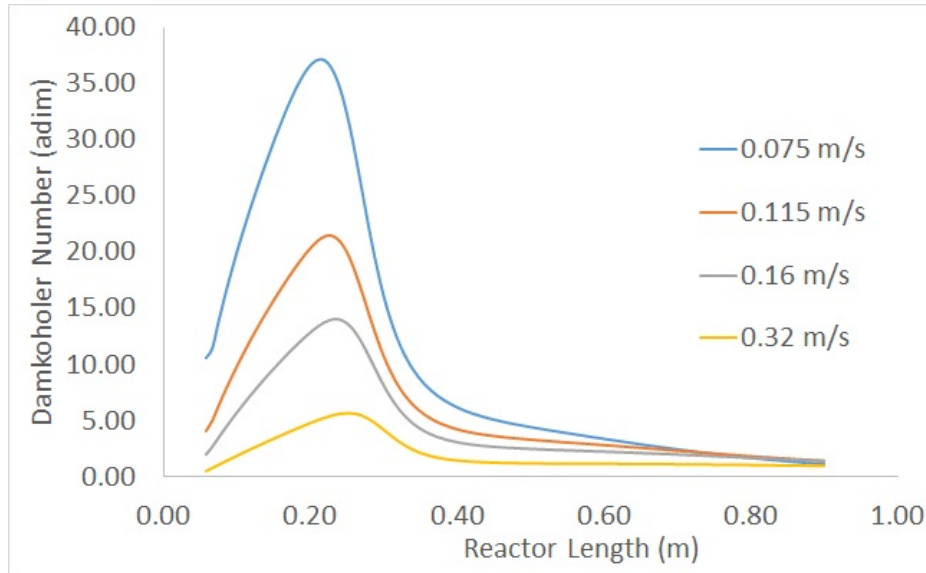


Figure 7.6: Damkohler number across the reactor central line for flow velocities of 0.075, 0.115, 0.16 and 0.32m/s. Low Da number near the junction indicates a reaction limiting process due to the low supersaturation. After the junction (0.2m) mixing controls as indicated by large Da numbers. Finally, reaction limits the process consequence of the reactant exhaustion.

m away from the junction point. The exhaustion of reactants and the homogeneous mixing far from the junction drives the Da value towards values close to 0. The decrease of Da due to the flow rate is a consequence of the decreasing mixing time as the energy dissipation rate increases. The similar shape between Figures 7.3 and ?? indicates that the process is mainly driven by mixing. This is also supported by the fact of a larger reaction rate. Only at the end of the reactor the trend seems to change as the reaction rate takes the smallest values.

In the case of low velocities (Figure 7.7(a)) intense red areas in the shape of a plume after the junction points can be observed. This indicates that mixing controls on those areas. Although the supersaturation is enough for reaction to occurs at a maximum rate, species are not transported at the same rate, hence reaction is limited by mass transport. On the other hand, in Figure 7.7(d) the greener area indicates a situation where reaction is less limited by mixing. Values of Da , moves from $Da=11$ to $Da=4$ for increasing flow rate. Hence, for this set up, the reaction is not limited by mixing

when flow rate is sufficiently high.

7.4 Population balance model

The mathematical model used in this section will cover only a portion of the whole range of the experimental conditions since generalization to the whole of it is not yet possible. For example, consideration of surface potential in the aggregation model is not included and hence, weak repulsive forces will be assumed. Also, nucleation kinetics was excluded assuming that nucleation is instantaneous and not limited by mixing. Therefore, the scope of the modelling will cover the conditions show in Figure 7.8 which includes aggregation by shear and breakage of will mixed rapid reaction in tubular reactors.

The equation used for the PBM is based on the expression proposed by Cheng *et al.* (2009) where several assumption have been made. For example: plug flow, geometrical size bin distributions, perfect mixing, immediate nucleation and breakage of particle k into $k - 1$ and $k - 2$ particles. The boundaries of in the application of the PBM are given by the validity of this assumption which are going to be broken down and analysed later in this chapter, see Section 7.8.

The fitting of the model will be computed using gPROMS, a flexible modelling tool capable of solving multiple differential equations. Four parameters will be estimated, two belonging to aggregation, (collision rate and collision efficiency) and two corresponding to breakage (shear exponent and particle size exponent).

Finally, a sensitivity analysis will be performed in which guidances for particle reduction will be given based on the PBM results in Section 7.7.1.

7.5 Population Balance formulation and Solution

Since first introduced, the PBM equation by Cheng *et al.* (2009) presents major difficulties for its integration (e.g. ignorance of the real exact value of α , the daughter particle size distribution, etc.). For this reason four major assumptions will be made. Similar assumptions were made by other authors such as Serra & Casamitjana (1998). The first one involves the breakage and aggregation modes:

7.5 Population Balance formulation and Solution

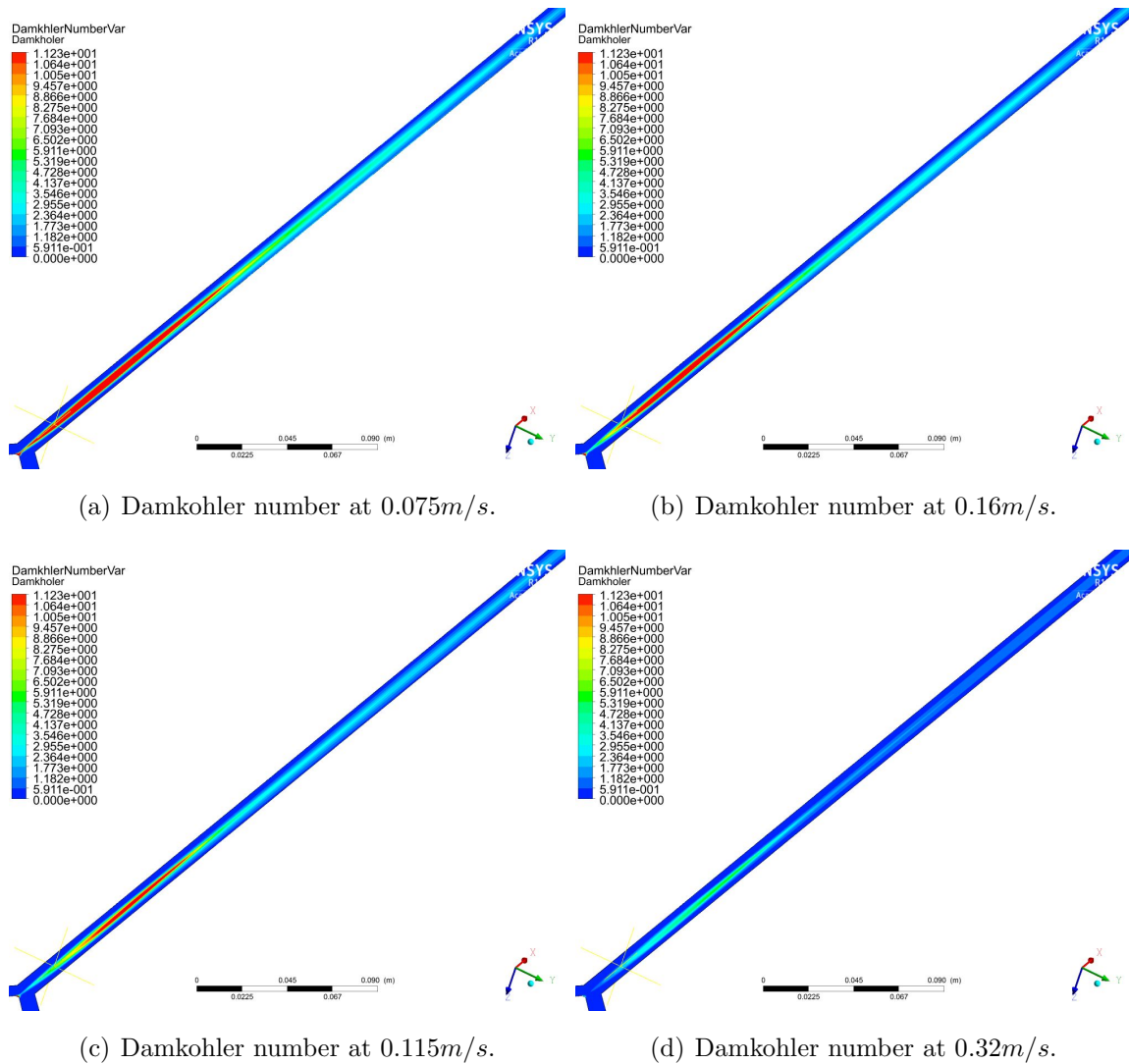


Figure 7.7: Damkohler number at various velocities. Warmer colours shows where reaction is limited by mixing. Reaction occurs mainly in the central section of the pipe for around 5 to 20 cm. The largest flow rates show the less mixing limiting reaction.

7.5 Population Balance formulation and Solution

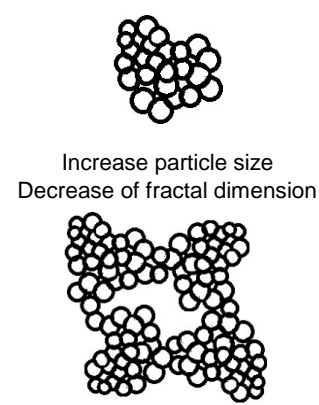
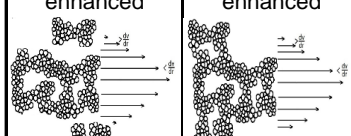
		Experimental conditions	
		High pH (9.5)	
Driving force	Phenomena	High flow (200ml/min)	Low flow (140ml/min)
Chemical Potential	Reaction	ZnNO ₃ (0.2M) NaCO ₃ (0.4M)	
		Reaction Limited (Fast Reaction & Fast mixing)	
Supersaturation	Nucleation	Homogeneous	
Surface energy	Aggregation	Weak surface repulsive forces Reaction limited aggregation	
		 <p style="text-align: center;">Increase particle size Decrease of fractal dimension</p>	
Surface energy Shear stresses	Restructuring	Breakage enhanced	Aggregation enhanced
			

Figure 7.8: Descriptive model of the aggregation phenomena contemplated for the formulation of the population balance model. Contains reaction, nucleation, aggregation and breakage.

7.5 Population Balance formulation and Solution

1. It will be assumed that aggregation of particle k only occurs by collision of particles i and j in such a way that $k = i + j$. Therefore summations are simplified to two terms. Similarly, breakage of one particle m is assumed to yield two particles of size $m - 1$ and $m - 2$. Therefore the daughter breakage function is equal to 1 since only one breakage mode is allowed. These assumptions are justified since particles are mainly affected by particles of a similar size. For example a particle of size k is composed mainly of particles of $k - 1$ and $k - 2$, as consequence smaller particles account for a smaller fraction of the particle.
2. The second major simplification is the plug flow assumption. Under turbulent conditions axial convective dispersion increases yielding a nearly flat velocity profile. Under these conditions the accumulation term can be neglected and convective transport is simplified to the reactor length or residence time, this being the external coordinate. This simplification is to be discussed further in later Sections (7.8)
3. The third simplification assumes thermal motion is negligible. Preliminary studies showed particle size around $10\mu m$ which yields a Peclet number around 100 for shear rates of $100s^{-1}$, see Section 6.2(a). This suggests kinetic forces prevailing over thermal. Hence, thermal terms are neglected and collision frequency is computed as a function of shear only.
4. Finally, as consequence of the fast precipitation kinetics nucleation is to be considered as an impulse function. This means that crystals are created in one single event opposite to as step function, where nucleation occurs along the length of the reactor. Let us justify this assumption referring to Bucca *et al.* (2009) who found an induction time of hydrozincite to be the lowest of several other sparingly soluble compounds indicating the fast character of this precipitation. CFD simulation has been used to further justify this assumption which is discussed in Section 7.8

Under these assumptions, the expression from Cheng *et al.* (2009) becomes:

7.5 Population Balance formulation and Solution

$$\begin{aligned} \frac{u}{X} \frac{\partial n_k}{\partial \tau} = & \frac{1}{2} \sum_{j=k-i}^{j=\infty} \alpha_{eff}(i, j) K_{i,j}^a (AggFac) n_i(\tau) n_j(\tau) - n_k \sum_{i=1}^{\infty} K_{i,j}^a n_i(\tau) + \\ & + \sum_{m=k+1}^{m=\infty} K_m^b n_m(\tau) \Gamma_{m,k}^b - K_m^b (P_1, P_2) n_k(\tau) \end{aligned} \quad (7.4)$$

where $\dot{\gamma}$ is the shear stress expressed in s^{-1} calculated as shown in Section 3.10

Tracking $D[4,3]$ along the aggregation process allows good understanding of the dynamics and is a tool to compare results across experiments and simulations. $D[4,3]$ can be derived from the momentums of the size distributions as described by Equation 7.5.

$$D[4, 3] = \frac{\sum_{i=0}^{\infty} n_i L_i^4}{\sum_{i=0}^{\infty} n_i L_i^3} \quad (7.5)$$

In order to improve the convergence of the models, scale factors have been introduced in the aggregation and breakage rates ($K_{i,j}^a(\dot{\gamma}, AggFac)$ and $K_m^b(\dot{\gamma}, P_1, P_2)$). The scale factors are a kind of transformation of certain variables which allows the domain of the solution to be scaled down from a large space to a smaller one. Exponentials are a common choice as scaling factors. In this case the term of breakage and aggregation will read as:

$$K_{i,j}^a = \dot{\gamma}^{Aggfac} (L_i + L_j)^3 \quad (7.6)$$

whereas for breakage:

$$K_{i,j}^b = \dot{\gamma}^{P_1} \left(\frac{L_i}{L_0} \right)^{P_2} \quad (7.7)$$

In this expression $\dot{\gamma}$ stands for shear rate, L_n is the size of the aggregate in metres. and L_0 is the initial size of the aggregate set as $20nm$.

Collision efficiency α was computed assuming there are no repulsive forces between particles. Thus, only the ratio between attractive forces (Hamaker constant H) and

7.6 Data collection and optimization procedure.

shear forces $6\pi\mu\dot{\gamma}(R_i + R_j)^3$ were considered important (Berre *et al.*, 1998). The expression chosen for computing the value of aggregation is as follows:

$$\alpha = K_\alpha \left(\frac{6\pi\mu\dot{\gamma}(R_i + R_j)^3}{8H} \right)^{-0.18} \quad (7.8)$$

Where μ is the kinematic viscosity, $\dot{\gamma}$ is the shear stress R_i and R_j are the radius of the two colliding particles.

The solution of Equation 7.4 was computed using gPROMS. This equation-based modelling tool allows input of the equation directly yielding the solution as a number density function. For the external variable and 1-dimensional formulation, the reactor length was selected, and appropriate transformations where applied. The software utilizes its own discretization scheme of the external variable base on Runge Kutta method with scaling factors. For the discretization of sizes (internal variable), 26 bins were selected in the range of 0.02 to 2500 μm following a geometrical low. Thus, one size bin results of the summation of the two previous ones which benefits the solution of the aggregation terms.

Regarding the choice of optimization parameters in Equation ??, we utilized four AggFac , k_α , P_1 and P_2 . The selection of these factors was not arbitrary but each one accounts for the degree of influence of one specific variable. It will allow us to study individual influences, shear size or surface forces on the aggregation process. Aggfac can be read as the degree of implication of shear in the aggregation. k_α accounts for the efficiency of the collisions. P_1 and P_2 account for the influence of shear and size on the breakage equations.

7.6 Data collection and optimization procedure.

The set of data commented on Section 6.2.1 was used for model fitting. The PSD of aggregating hydrozincite was measured as a function of flow rate and reactor length. A range of flow rates was selected using a Marlow Watson peristaltic pump 520s. The Malvern Mastersizer light scattering device was attached to the outlet of a tubular reactor to which different silicon tube lengths were attached to control reactor length. Further details of the experimental set-up can be found in Section 3.3.

Optimization required the experimental bin distribution data to be adapted to match with the selected geometric discretization scheme in the simulation. For this purpose, the volume percentage yielded by the Mastersizer, which came in 100 exponential bins, was scaled down to 26 bins in geometrical progression. Together with the size distribution, the $D[4,3]$ has been measured through light scattering. It provides guidance on the goodness of fit and on the general trend of the size.

After bin resizing, the experimental data was uploaded into gPROMS. An optimization routine was then carried out which minimized the difference between experimental and simulated size distributions.

7.7 Results and Discussion

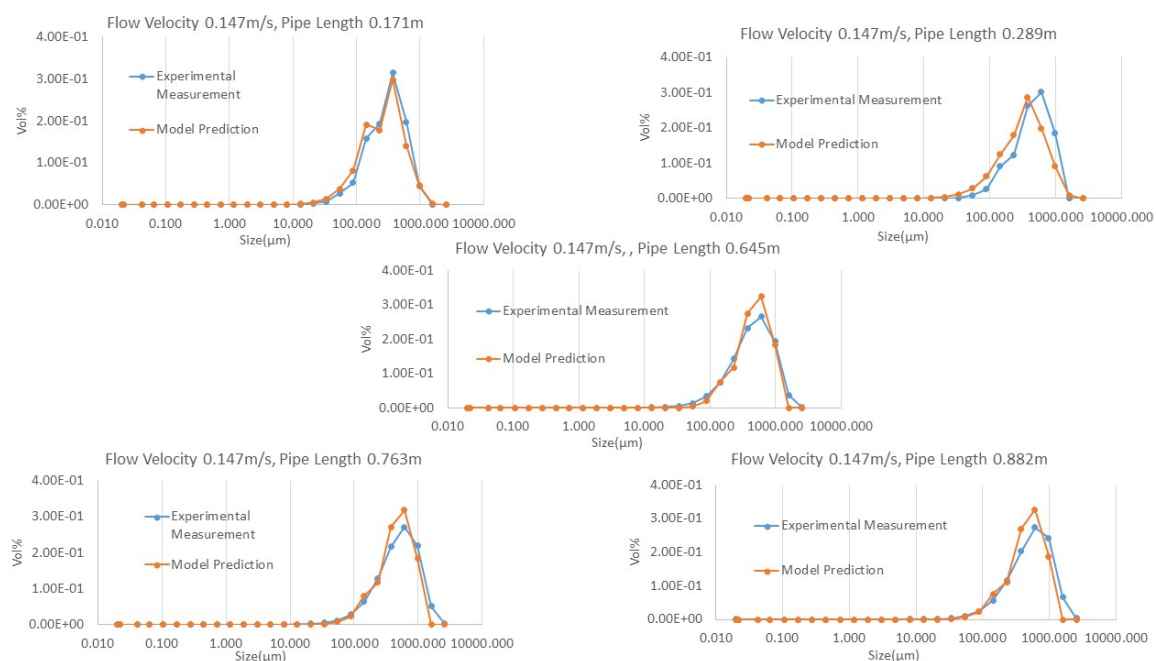


Figure 7.9: Experimental particle size distribution vs. model prediction for various reactor positions 0.17, 0.29, 0.64, 0.76 and 0.88m from the Y-junction for 0.147m/s.

Figures 7.9, 7.10, 7.11, 7.12 and 7.13 shows the fit of the particle size distribution as estimated by gPROMS with experimental reading. Features such as elbows and bimodal distribution are described by the model although divergences were found in

7.7 Results and Discussion

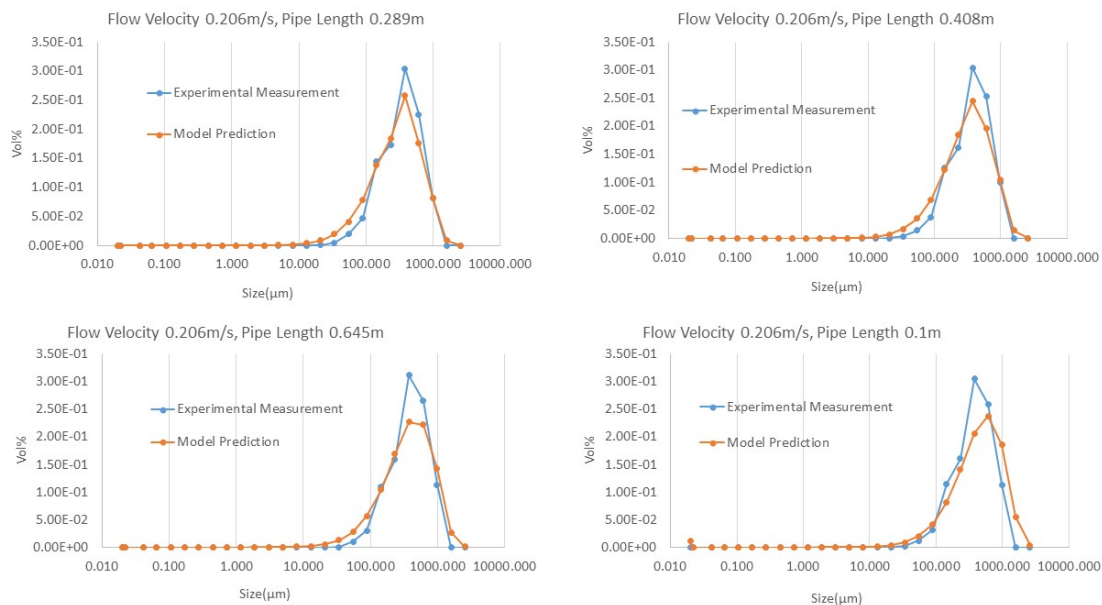


Figure 7.10: Experimental particle size distribution vs. model prediction for various reactor positions 0.29, 0.41, 0.64 and 1m from the Y-junction for 0.206m/s .

some cases. The estimated parameters are shown in Table 7.2 together with their 95% confidence intervals. Voids in the data corresponds to parameters which were set based on educated guesses as problems with convergence of the optimization routine were found. Additionally to the 95% intervals, the accuracy of the model was judged by following the variable $D[4,3]$ along the experiments (shown in Figure 7.14).

Figure 7.14 show the evolution of $D[4,3]$ as measured by SLS as well as the one obtained from simulation using Equation 7.5 after parameter estimation.

The model seems to systematically over-predict the size as well as yielding different trends when compared with the experimental data. The larger $D[4,3]$ is believed to be caused by the weight of larger particles on the size distribution. The tail of the model prediction of the PDS observed in Figures 7.9, 7.10, 7.11, 7.12 and 7.13 largely contributes to increasing the value of the $D[4,3]$ when compared with experimental values. The divergences on the trend of the smaller flow rates (which show increasing trend despite they were expected to be flat) for the model predictions is probably due to the incapability of the model to handle laminar flows. Improvements in this area

7.7 Results and Discussion

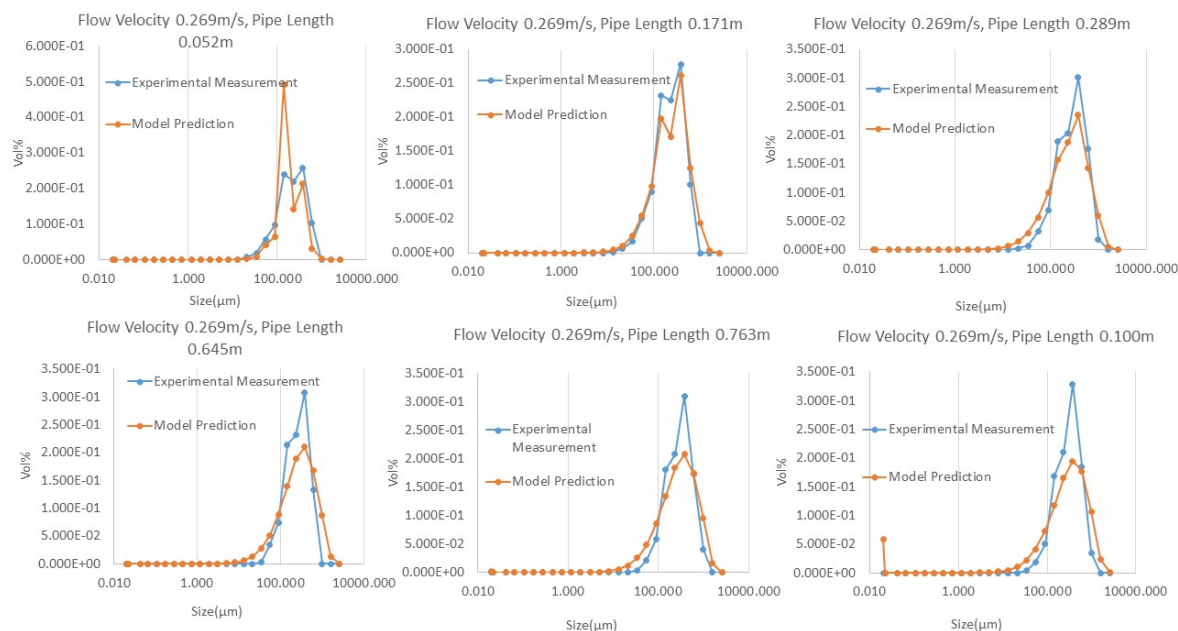


Figure 7.11: Experimental particle size distribution vs. model prediction for various reactor positions 0.05, 0.17, 0.29, 0.64, 0.76 and 1m from the Y-junction for 0.296m/s .

are to be addressed in future work.

Another discrepancy of the model with the experimental data is the location of the aggregation event. Based on experimental data, the event is located around a length of 0.2m whereas it is closer to the origin in the case of the simulation. It is believed that kinetics of aggregation are slower in reality as compared with the model. Whereas the simulation predicts that aggregation is instantaneous, commencing from the injunction point, based on CFD simulation, we know that mixing is a limiting step. In reality, aggregation may commence further along the pipe rather than at the very entrance to the reactor.

The simulated final value of the $D[4,3]$ also differs significantly from the experimental one. Reasons for this can be listed as: small discrepancies in the PSD fitting of large particles can yield a large difference in the $D[4,3]$ due to the way it weighs in the formula, possible saturation of the SLS detector with larger particles and insufficient resolution of the particle size bins for larger sizes, which coupled to the sensitivity of the $D[4,3]$ upon size, makes it important.

7.7 Results and Discussion

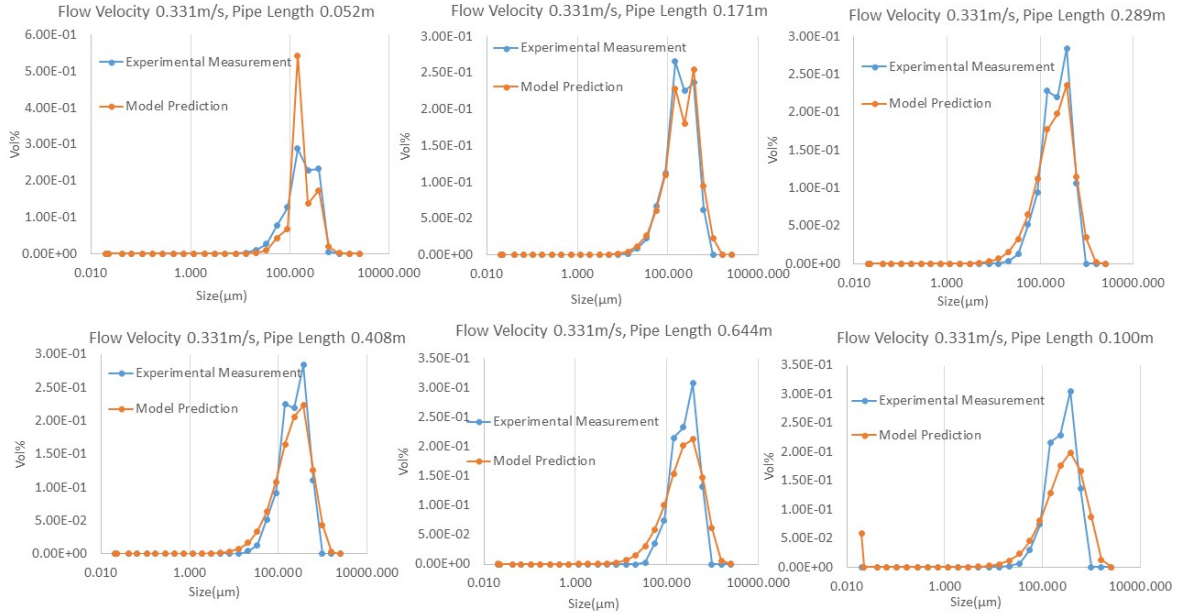


Figure 7.12: Experimental particle size distribution vs. model prediction for various reactor positions 0.05, 0.17, 0.29, 0.64, 0.76 and 1m from the Y-junction for 0.331m/s.

Table 7.2 shows the results of the parameter estimation together with its 95% confidence intervals from gPROMS. The divergence of the optimization routine forced the procedure to fix k_α in order to decrease one degree of freedom. As a consequence, the confidence interval is not applicable on these cases. Additional to the table, values of the fitting parameters for the five different shear rates have been plotted as a function of flow velocity intending to observe trends in the process behaviour. In this manner, Figures 7.15(a), 7.15(b), 7.15(c) and 7.15(d) belong to the trends of $AggFac$, K_α , P_1 and P_2 respectively.

$AggFac$ takes part of the collision frequency following the equation $K_{i,j}^a = \dot{\gamma}^{AggFac} (L_i + L_j)^3$ hence indicating the influence of shear on the collision frequency. K_α is part of the expression for the collision frequency $\alpha = K_\alpha \left(\frac{6\pi\mu\dot{\gamma}(R_i+R_j)^3}{8H} \right)^{-0.18}$ therefore it is a proportional factor of the flow number. (Ratio between kinetic and surface forces). On the side of breakage, P_1 and P_2 are exponential factors showing the degree of influence of shear stress and size respectively following the equation: $K_{i,j}^b = \dot{\gamma}^{P_1} \left(\frac{L_i}{L_0} \right)^{P_2}$

Figure 7.15(a) shows the trend of aggregation factor with velocity. Although the

7.7 Results and Discussion

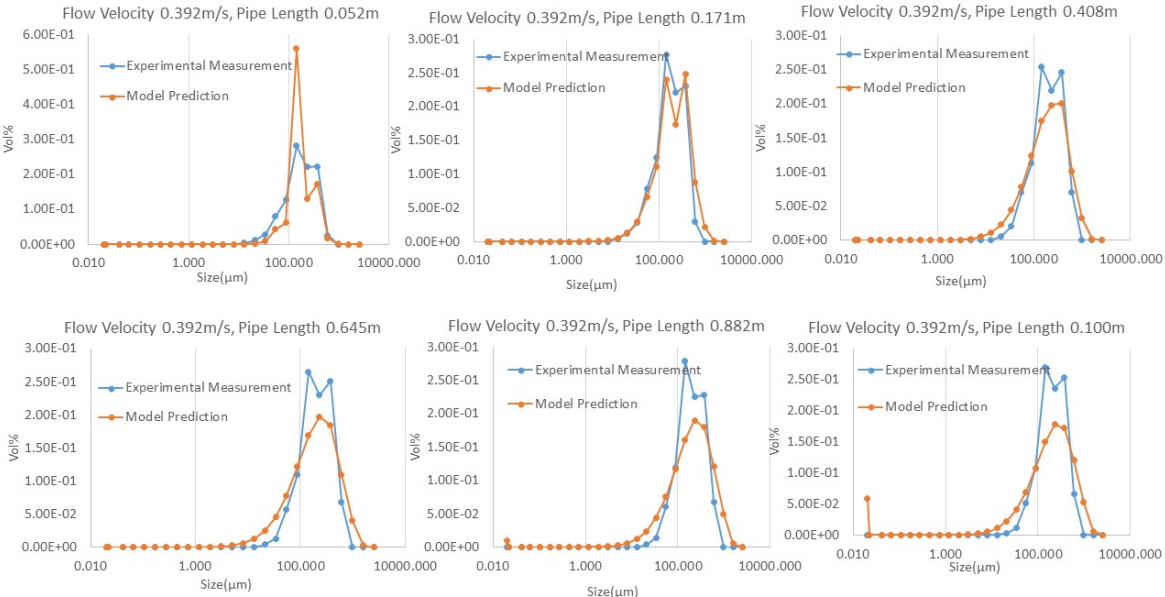


Figure 7.13: Experimental particle size distribution vs. model prediction for various reactor position 0.05, 0.17, 0.29, 0.64, 0.76 and 1m from the Y-junction for 0.392m/s.

overall trend is decreasing the R^2 does not indicate a good fit. This tendency suggest that dependence of collision rate on shear deceases with flow rate. This means that although the aggregation rate increases, as a consequence of the increased shear rate, its dependence on shear will be smaller.

Figure 7.15(b) shows that aggregation efficiency, k_α , decreases with flow rate. It is believed that this prediction is accurate as greater shear would imply a larger particle velocity. Eventually, this velocity would reduce the efficiency of aggregation.

The simultaneous decrease of k_α and $AggFac$ in Figures 7.15(a), 7.15(b) indicates an overall decrease of the aggregation rate. Therefore, based on this analysis we can conclude that the overall aggregation rate decreases with flow rate.

Figure 7.15(c) presents a linear decrease of P_1 with flow velocity. Similar to previous $AggFac$, the present work predicts a decreased dependence of breakage rate with shear. The linear decrease of value P_1 as the flow velocity increases can be explained taking into account the size of the aggregates. As pointed out in a previous section (Section 2.4.3), the effect of shear on smaller particles is not as intense as in larger

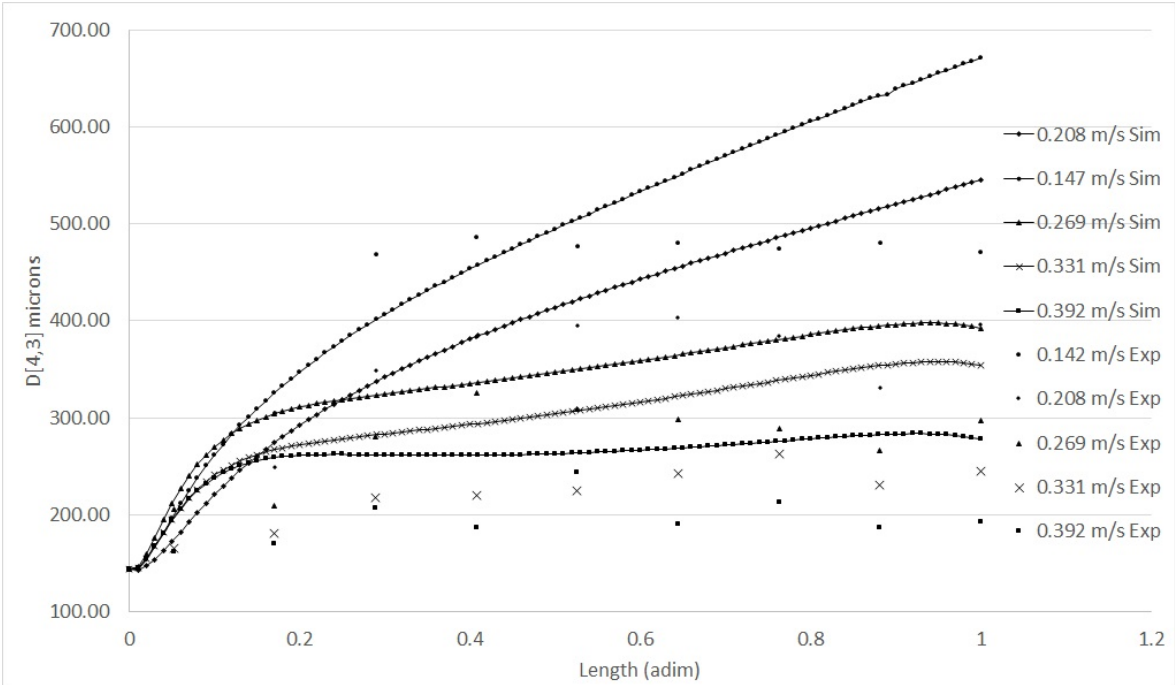
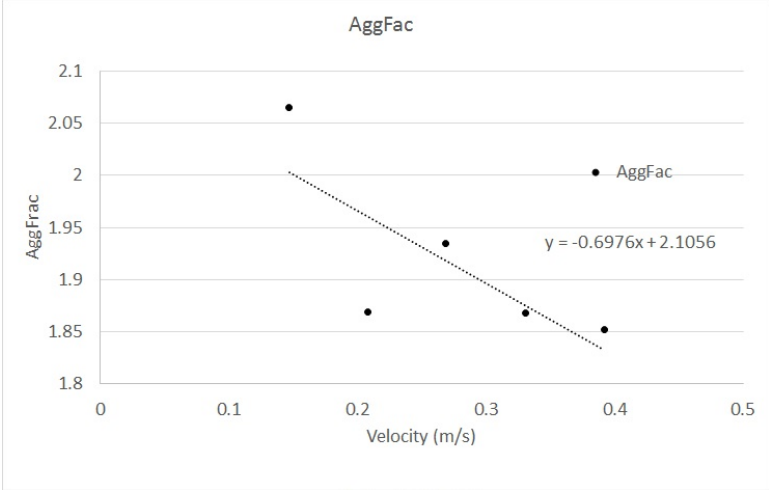


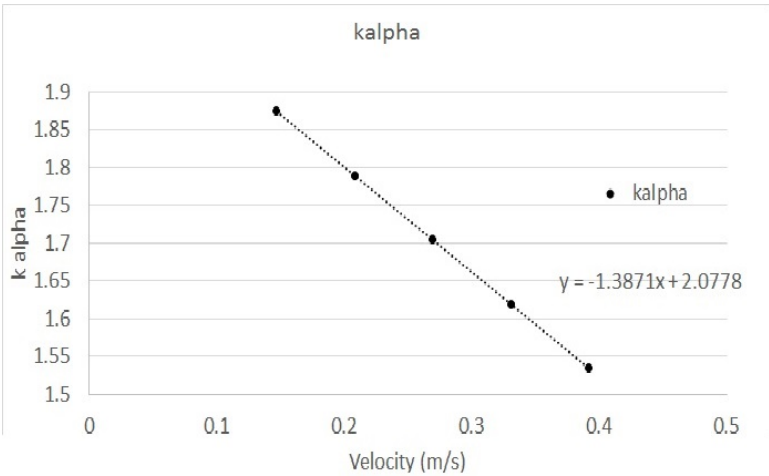
Figure 7.14: Simulated and experimental D[4,3]. Discrepancy between simulated and experiment is appreciated. This different is believed to be caused by the larger weight that large particles has in the D[4,3]. A steady state is found for high flow rates, whereas unfeasible increasing particle size is found at low flow rates.

ones. Therefore it is understandable that P_1 , the scaling factor of shear decreases. P_2 on the other hand, presents an increasing trend with velocity. This means that the major contribution to the increase in breakage rate is on the side of the size. It was pointed out in Section 2.4.3 that larger flocs are more sensitive to shear. This is backed up by the present data.

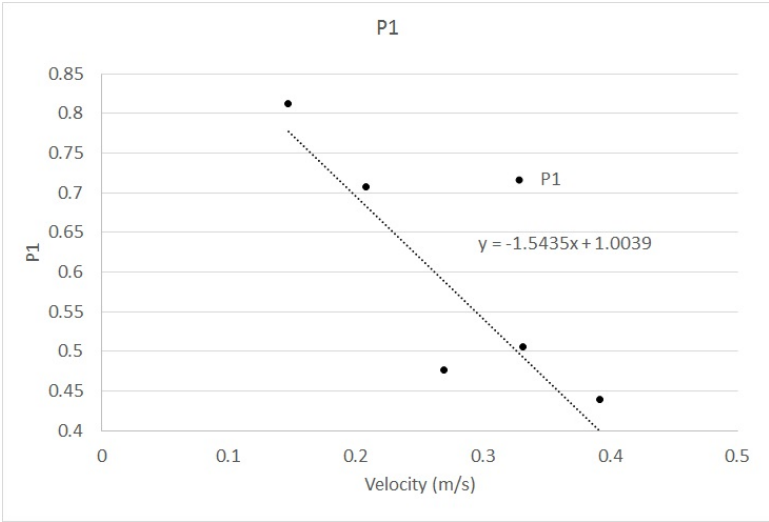
Due to problems in the parameter estimation routine, one of the variables, k_α , was kept constant following a decreasing linear relation based on an educated guess. The selection of the line involved results from previous failure simulations and tentative values of k_α .



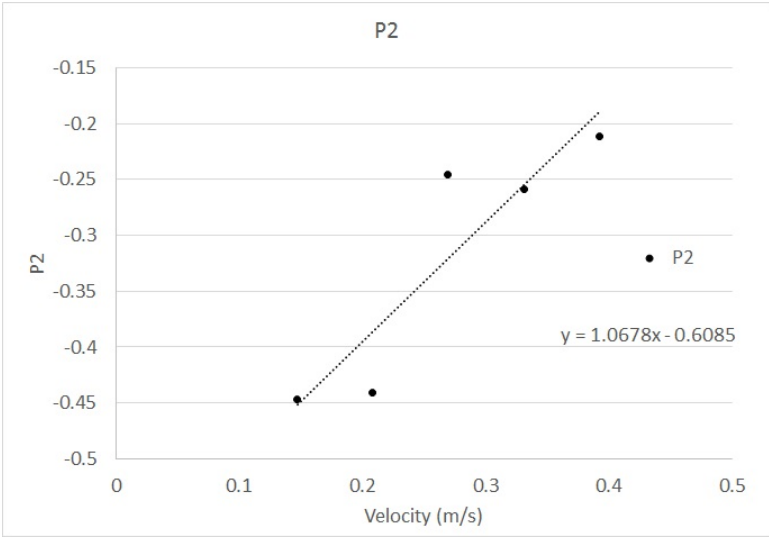
(a) Parameter estimation results for the aggregation factor, $Aggfac$, of the collision frequency $K_{i,j}^a = \dot{\gamma}^{Aggfac}(L_i + L_j)^3$. The decreasing trend of $Aggfac$ with velocity indicates a reduction in the influence of shear as flow rate increases.



(b) Parameter estimation results for the collision efficiency factor, k_α , as a function of velocity. Where collision frequency reads as follows: $\alpha = K_\alpha \left(\frac{6\pi\mu\dot{\gamma}(R_i+R_j)^3}{8H} \right)^{-0.18}$. Due to problems in the optimization routine, k_α was estimated based on trial and error and educated guess based on previous parameter estimation. The decrease of k_α with flow rate indicates that collision are less efficient as velocity increases.



(c) Parameter estimation results for the P_1 factor in the breakage kernel, $K_{i,j}^b = \dot{\gamma}^{P_1} \left(\frac{L_i}{L_0}\right)^{P_2}$. The decreasing trend of P_1 indicates a decreasing relation between breakage rate and shear rate.



(d) Parameter estimation results for the P_2 factor in the breakage kernel, $K_{i,j}^b = \dot{\gamma}^{P_1} \left(\frac{L_i}{L_0}\right)^{P_2}$. The increase of P_2 indicates the increasing dependence of breakage rate on particle size.

Figure 7.15: Graph showing the optimized parameters from the population balance model. The parameter k_α was chosen to be constant in the optimization due to indetermination in the parameter estimation. The rest of parameters correlate quite well.

Table 7.2: Results for parameter estimation for particle size distribution to the PBM (Parameters: $AggFac$, k_α , P_1 and P_2) and its 95% confidence interval

	95% confidence interval				
	0.147m/s	0.208m/s	0.269m/s	0.331m/s	0.392m/s
$AggFac$	2.065±0.99	1.869±–	1.935±0.05	1.868±0.05	1.852±0.054
k_α	1.874±5.66	1.789±–	1.705±–	1.618±–	1.534±–
P_1	0.812±0.27	0.707±0.21	0.477±0.12	0.505±0.125	0.439±0.093
P_2	-0.447±0.17	-0.441±0.086	-0.246±0.065	-0.258±0.074	-0.212±0.057

7.7.1 Sensitivity analysis

The dependence of the size distribution as a function of equation parameters is to be assessed in the present section. For this purpose a sensitivity analysis has been performed consisting of changing the model variables, velocity and reactor length. For analysis purposes, a chemometric model will be used to fit average $D[4,3]$ thus obtaining a simplified version of the PBM less accurate but easier to analyse.

The question to be answered in this section is to identify the conditions at which the aggregation process provides the smallest particle size. For answering this question, a face centered experimental design is to be used. The matrix of experiments to be performed can be read in Table 7.3. It will test the influence of each variable individually for latter explore the non linear relation between the variables.

Results from face centred simulations are shown in Figure 7.16. A maximum in the size can be observed around length 1.5m and velocity 0.211m/s although the trend indicates that larger particles can be obtained if the velocity is reduced further. Similarly the minimum size was found to be 0.5m and 0.40m/s however the trend indicates that minimum residence time and maximum velocity should be effective in decreasing the particle size. Although the effect would not be as dramatic, the single effect of large velocity values should be enough to decrease the particle as the single most important factor was found when fitting the results of the analysis to a polynomial distribution Equation 7.9. In this equation the highest coefficients correspond to the velocity u .

$$P(X, u) = 614.5 + 93.93X - 1852u - 95.99Xu - 16.14X^2 + 1863u^2 \quad (7.9)$$

Table 7.3: Matrix of variables for the sensitivity analysis of velocity, u , and reactor length, X .

		X (m)	u (m/s)	D[4,3] μ m
0	0	1.5	0.27	320.62
0	1	1.5	0.394	226.82
0	-1	1.5	0.211	398.96
1	0	2.5	0.27	314.93
-1	0	0.5	0.27	302.36
-1	1	0.5	0.394	214.84
-1	-1	0.5	0.211	328.27
1	-1	2.5	0.211	396.77
1	1	2.5	0.294	238.76

7.8 Limitations of the Model

Instantaneous reaction assumption. The assumption of instantaneous reaction has been assessed using computational fluid dynamics. It is believed, that although the reaction is fast, it may be limited by species transport. In order to assess the importance of reaction kinetics against mixing kinetics, the Damkohler number has been obtained using the methodology described in Section 3.11.

The localization and the variable length of the plume are dependent on velocity indicating that the PBM used in the section had limitations. For example, based on the CFD results, the assumption of immediate nucleation in this model seems to only be valid for the case of high flow rates. In this case, mixing is not a limiting step and the reaction is accomplished in a short length (0.2m) see Figure 7.7(d). On the other hand, small flow rates seem to yield a longer plumes which extend for longer lengths, in the order of magnitude of the PSD measurements (0.5m). Under these circumstances we cannot be certain that reaction is not influencing the readings.

Plug flow assumption. The assumption of plug flow was experimentally tested by a tracer method. A residence time distribution was obtained from a pulsed input of NaOH as described in Section 3.12 which was fitted to the two models: tanks in series

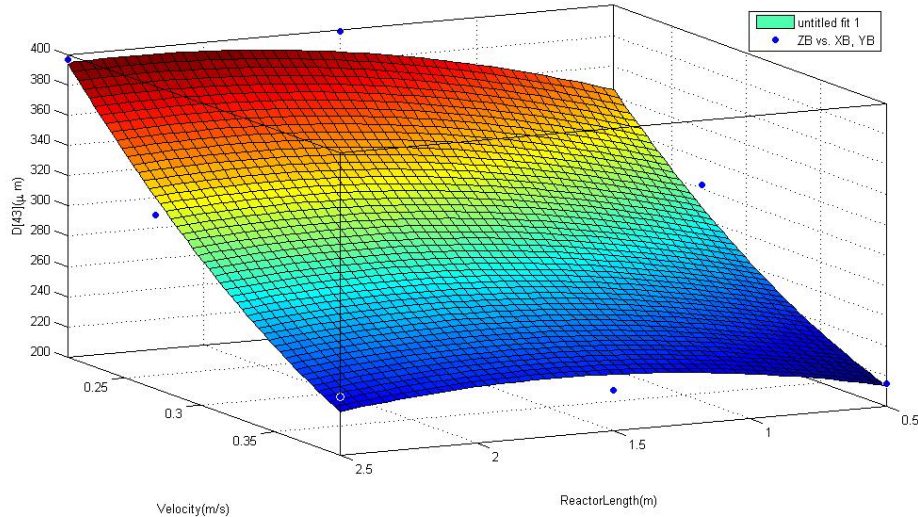


Figure 7.16: Sensitivity analysis for variables reactor length (X) and velocity (u). The minimum particle size can be found at largest flow rate and the shortest residence time. Whereas lower flow rates promote larger particle sizes

and dispersion model.

Tracer experiments have been used as a method to characterize the mesoscale of mixing of the tubular reactor. The results of this study will reveal the similarities or differences between the reactor and the ideal plug flow. The concentration of OH ions was computed from the pH to be normalized later using Equation 3.13. Also the time was normalized with the mean time (t_m). In this fashion, the one parameter model, tanks in series and dispersion, can be used as in Equations 3.11 and 3.12 (Fogler, 2006a). Notice that the experiment could only be carried out at low flow rate (29ml/min) since the pH meter did not provide sufficient time resolution.

The fit of the models is shown in Figure 7.17 together with the experimental data. There are small experimental features uncovered by the model. i.e. the exact position of the maximum of the slightly larger tail around 1.3 dimensionless time. Regardless of these features, the model provides a decent approximation of the experimental data.

The fits of this model suggest behaviour close to that expected from a plug flow reactor. On one hand, the tanks-in-series model predicts 125 batch reactors which suggest a rather ideal reactor. On the other hand, the small Peclet number calculated from the dispersion model (0.004) suggests a small diffusive transport compared with

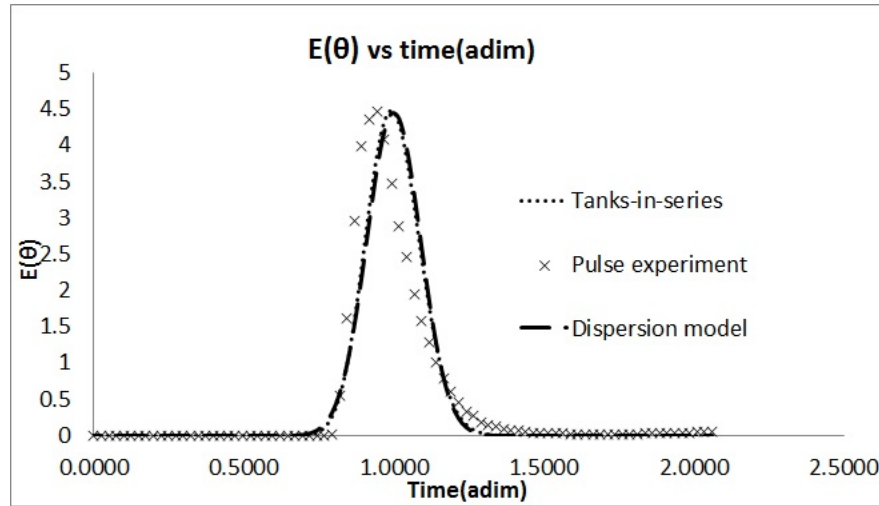


Figure 7.17: Fitting of CSTR and PF models to the experimental tracer experiment. The number of 125 reactor was approximated and a Peclet number of 0.004. Both models support the assumption of plug flow like behaviour

convection.

In light to these results, the assumption of a plug flow like behaviour is proved and will be used to further the present and future studies.

7.9 Conclusions

In this section a general model has been derived for explaining the experimental results obtained in the previous section which covered mixing, nucleation, aggregation, breakage and ripening. Initially CFD simulations were carried out from where information about mixing and reaction was obtained. Then a mathematical model (PBM) has been applied to some of the size distribution data described in Section 6.2.1. The results of this parameter estimation were then evaluated on a sensitivity analysis which provided guidance on which conditions to choose for the lowest particle size. Finally the model assumptions have been critically revised.

In this section it has been learned that:

- Reaction is slightly limited by mixing as deduced by the Damkoholer number greater than unity. Initially, a reaction front is created in the collision zone

between the streams. Then mixing homogenizes the reactants across the reactor section. Finally, they are consumed rapidly as the mixture exits the reactor.

- pH and flow rate are the two most important contribution which defines the final particle size. The pH would affect reaction kinetics and surface chemistry whereas flow rate affects mixing kinetics and aggregation-breakage equilibrium.
- Although the model fit to the PSD seems to diverge when looking at the position of the final particles size and aggregation event, other features such as correct size values and the right model of the aggregation phenomena, leads to the conclusion that this model could be valid as a rough estimation of the aggregation of hydrozincite in tubular reactors.
- It is been observed that large flow rates and small residence times are the best conditions to obtain the smallest particle size, although, flow rate is the single most important contribution.
- The plug flow assumption of the model seems to be validated from the tracer experiments. On the other hand, the single nucleation event assumption seems to only be valid for large flow rates as the CFD simulation shows.

Chapter 8

Magnesium Doped Hydrozincite Precipitation: Segregation Coefficient and XRD Study

8.1 Introduction

In order for an API to be effective it needs to be available at the site of absorption. Solubility of a solid material defines the availability and hence needs to be controlled. Among the methods for solubility control are: polymorph selection, particle size control or encapsulation (Savjani *et al.*, 2012b). Material doping presents itself as an affordable and effective way of tuning the crystal solubility. It relies on the principle that a crystalline material with a large concentration of imperfections, such as kinks and dislocations, is more soluble than that with more perfect crystal structure where molecules have found their minimum energy location in the crystal lattice.

The use of sparingly soluble materials for the controlled release of API has interest for the cosmetics (Schwartz & Johnson, 2004) and pharmaceuticals industries (Hasan *et al.*, 2012). The present study assesses the incorporation of Mg^{2+} ions in zinc carbonate crystalline structure. It quantifies its presence and tries to explain the mechanism of incorporation based on the concepts of solid solution, ions trapping and ion substitution. Based on the uniqueness of the crystal phase and the independence of crystal distortion with Mg^{2+} incorporation, we conclude that for the range of Mg^{2+}

concentration used in this study the most likely manner of Mg incorporation is ion substitution. This means that due to the similarity in the properties of Mg and Zn ions, similar radius, bond distances, charge, etc. Mg takes the place of Zn in the crystal structure with no effect on the XRD pattern. This is only limited by the difference in electronegativity between the two metals which is too large for Mg to freely substitute Zn in the crystal structure.

Due to its low solubility, the efficiency of hydrozincite is limited. However, its bilayer structure and biocompatibility makes it a good candidate for drug delivery processes.

Magnesium was chosen in this study as dopant. Mg^{2+} ion was found to alter the crystal growth of other sparingly soluble compounds similar to hydrozincite, such as calcite through the impurity incorporation mechanism (Davis, 2000). Also, the crystallographic plane distance of calcite was shown to change along the plane (112) as Mg^{2+} concentration increased (Goldsmith *et al.*, 1956). Additionally, similarities between Zn^{2+} and Mg^{2+} such as ionic radius ($(Zn^{2+} 0.72\text{\AA}$ and $Mg^{2+} 0.74\text{\AA})$) or charge (+2), makes it a good candidate to fulfil Goldsmith rules (Section 2.2.4) and hence undergo substitution easily. Studies by Sarma & Sarma (2016) found that Mg^{2+} plays an important role in nucleation and growth of calcium phosphate. At low concentration Mg^{2+} increases the crystallinity of the material, whereas at high concentrations the opposite occurs and amorphous calcium carbonate was found.

The system ZnO+MgO has been well studied for its importance to the semiconductor industries (Segnit & Holland, 1964). It is observed from the studies of Segnit that a limited amount of MgO can be mixed with ZnO (only 2%), as a consequence of the disparity in the crystal structures, cubic for MgO and hexagonal for ZnO. In other words they cannot form solid solutions.

More recently, precipitation models have been developed for the system zinc acetate-sodium hydroxide in the presence of various concentrations of magnesium ions. (Elangovan *et al.*, 2015). Results showed the crystalline size increased with Mg^{2+} composition up to 5%. An increasing crystal volume was also found by Qiu *et al.* (2008) when studying the photocatalytic properties of ZnO. Hydrozincite as precursor of ZnO is believed to behave similarly although it is to be proven in this study. On the other hand, the system of interest to us, Mg+Zn+CO₃, is relatively unknown. There have been previous studies where Mg^{2+} doped hydrozincite from three different manufacturers was tested

for solubility Schwartz & Johnson (2004). Although a relationship was found between crystallite size and the amount of Mg^{2+} in the structure and solubility, the study has not been reproduced. Therefore, in the present study Mg^{2+} doped hydrozincite will be studied.

For this purpose, this study will use the precipitation method described in Section 3.7 for the production of doped hydrozincite. Then the amount of Mg^{2+} trapped in the structure will be analyzed and a mechanism of absorption will be suggested. Also the crystal structure is to be analyzed by XRD noting the changes in the cell parameters and crystalline size. Finally, the maturity of the adsorption is to be studied using a crystal structure software.

8.2 Results and discussion

A number of physical and chemical mechanisms can explain the incorporation of Mg^{2+} into hydrozincite structure. Some involve the formation of solid solution, incorporation of individual ions, co-precipitation, etc. With the purpose of elucidating the nature of this incorporation, various analytical techniques were carried out over a set of experiments designed to have an influence on Mg^{2+} concentration in the crystal structure. The amount of Mg^{2+} in the solid was captured by AAS, morphology by SEM and STEM finally X-ray powder diffraction revealed changes in the crystal structure.

8.2.1 SEM

SEM revealed surface features such as surface roughness. In this section we will study the influence of Mg^{2+} on the morphology of hydrozincite.

Previous studies have used dopant (including acetic acid, PVP or SDS) to change the morphology of hydrozincite thus obtaining a variety of particle shapes such as chrysanthemum, round or plate (Bitenc *et al.*, 2008). In this section, magnesium is tested as dopant to find unimportant changes in its appearance.

Figures 8.1(a), 8.1(b) and 8.1(c) shows SEM images captured at different scales of hydrozincite crystals obtained at equal supersaturation (0.1M of Zn) in which the presence of Mg^{2+} has been varied for values 3, 6 and 10%. Captures vary in scale therefore, details of surface features can be observed in detail. All of the particles



(a) SEM image of Mg^{2+} doped hydrozincite. 0.1M Zn^{2+} and 3% Mg^{2+} over zinc. (b) SEM image of Mg^{2+} doped hydrozincite. 0.1M Zn^{2+} and 6% Mg^{2+} over zinc. (c) SEM image of Mg^{2+} doped hydrozincite. 0.1M Zn^{2+} and 10% Mg^{2+} over zinc.

Figure 8.1: SEM images of hydrozincite synthesized at various concentrations and various impurity ratios. The morphology is not altered by the amount of impurity ratio.

share crystalline features such as sharp edges and defined angles. It can be observed that the degree of aggregation differs from sample to sample. This is probably due variation in the sample preparation procedure. Only Figure 8.1(c) seems to differ from its neighbors in the aggregated appearance. However, the sharp edges still remain sharp.

The mechanism for morphology modification by dopants or supersaturation are well known among scientists (Meldrum & Cölfen, 2008; Wu *et al.*, 2011; Zhang, 2002). Dopant can interact with the primary material, in number of ways. For example, surface tension may be affected by surfactants, directly modifying structure while crystallizing. Dopant can also form co-crystals or be incorporated in the structure which yields different crystal structures and hence, a completely different morphology. In the present case, the relative low concentration and inactivity of Mg^{2+} yield products with negligible changes in structure. Therefore morphology would be independent of Mg^{2+} concentration.

MgCl used in this study as dopant for hydrozincite has negligible influence on particle morphology. The following sections will assess the presence of the ions in the crystal structure and their changes as a function of concentration and Mg^{2+} concentration.

8.2.2 Dopant adsorption

Light absorption of the ionized sample data was acquired by means of AAS, as described in Section 3.7.1. The mass ratio of Mg^{2+} to mass of Zn^{2+} in solid sample was calculated as well as the Mg^{2+} % in the initial solution. The presentation of data in this format is useful for the reader as well as being representative of the physics. Additionally, the segregation coefficient was calculated which refers to the amount of moles of Mg^{2+} in solution over the amount of moles of Mg^{2+} in the final sample. It accounts for the amount trapped in the sample compared with the initial one in the solution. In other words, the efficiency of the adsorption.

When plotting the mass percentage of Mg^{2+} in the sample against the Mg over Zn ratio, shown in Figure 8.2, we observe a trend close to a linear increase. For various concentrations of Zn^{2+} the amount of dopant adsorbed seems to differ slightly from the linear trend, probably indicating a more complex mechanism rather than simple linear adsorption.

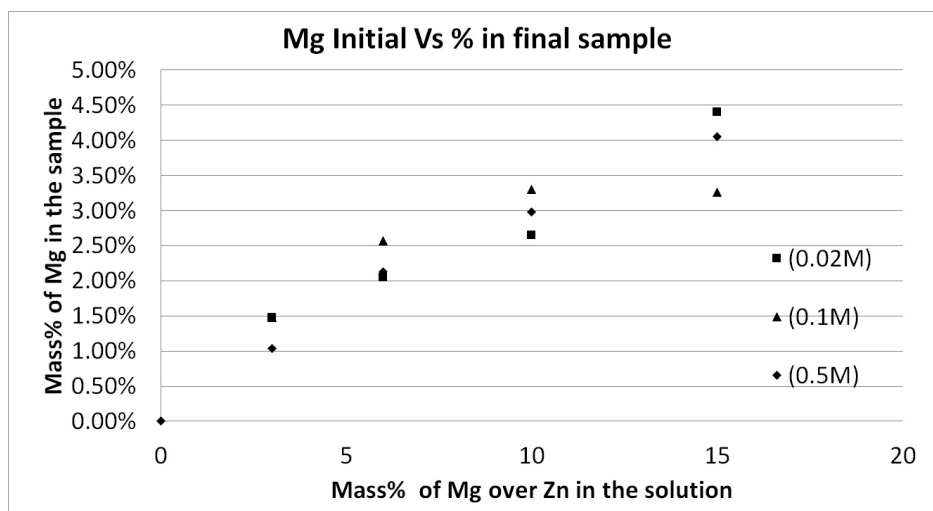


Figure 8.2: Mass percentage of Mg^{2+} in the sample as a function of the percentage of Mg^{2+} over Zn^{2+} in solution at three different zinc concentrations (0.002, 0.1 and 0.5M). Increasing Mg^{2+} is found in the solid sample as the amount of Mg^{2+} increases in the solution. The relationship is almost linear with increasing slope as the supersaturation decreases.

A common adsorption model is the Langmuir isotherm which is normally used to fit

the adsorption process, (Langmuir, 1918). Although initially used for gas adsorption on solid surfaces, it has also been used for ions in solution, (Davis, 2000; Nielsen *et al.*, 2013). It assumes a limited number of adsorption site which can be filled or not based on the kinetic driving the processes of absorption and desorption.

$$\frac{Mg_{solid}^{+2}}{Zn_{solid}^{+2}} = K_1 \frac{K_{eq}[Mg^{+2}]_{liq}}{1 + K_{eq}[Mg^{+2}]_{liq}} \quad (8.1)$$

where Mg_{solid}^{+2} and Zn_{solid}^{+2} are the mass of magnesium and zinc in the solid particles. $[Mg^{+2}]_{liq}$ is the concentration of magnesium in the liquid before precipitation. K_1 accounts for the extent of the adsorption. K_{eq} is a constant accounting for the velocity towards equilibrium.

Figure 8.3 represents the mass fraction of Mg^{2+} over Zn^{2+} in the y-axis and the molar concentration of Mg^{2+} in solution in the x-axis. It can be observed that regardless of the change in the change of the Zn^{2+} concentration, the ratio of Mg^{2+} over Zn^{2+} is in the same range. This indicates the independence of the absorption ratio from the zinc concentration.

The quality of the fit of the Langmuir model to the experimental data suggest that an absorption model is a valid approach for modelling the incorporation of Mg^{2+} . Table 8.1 shows the parameters fitted by Equation 8.1. The driving force of the adsorption is therefore the concentration of Mg ions. Langmuir type behaviour is characteristic of a process in which there is an equilibrium between absorption and desorption on a surface. We will consider this mechanism for explaining the nature of Mg doping.

The lack of a constant ratio between Mg^{2+} and Zn^{2+} make us dismiss the hypothesis of co-crystal formation where constant ratios between the ions are expected. Instead, this is characteristic of a different mechanism such as substitution of atoms or ions trapped on the crystal structure (step pinning). The viability of both hypotheses is to be assessed in Section 8.2.3.

Also in the zinc concentration, the supersaturation, seems to influence the absorption of magnesium. For the same concentration of Mg^{2+} in solution, the absorption decreased as concentration increased. However, the influence of supersaturation is secondary when compared with the effect of Mg^{2+} concentration.

It is believed that the equilibrium stage of the adsorption is intensified due to the lowered kinetics of the precipitation. As shown by the trend of the equilibrium constant,

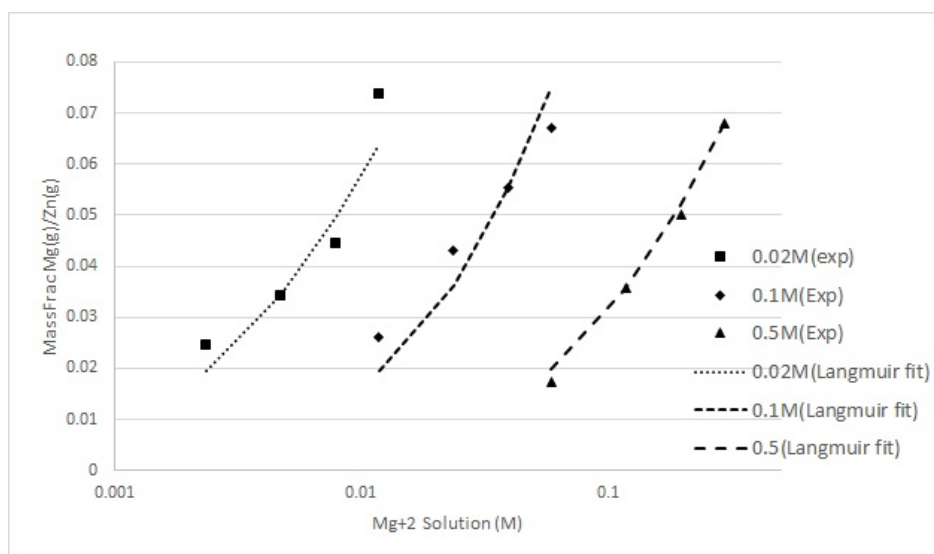


Figure 8.3: Mass fraction of Mg^{2+} over Zn^{2+} in solid against Mg concentration in solution at three zinc concentrations (0.002, 0.1 and 0.5M). Dashed lines represent the Langmuir fitting using Equation 8.1. A Langmuir like model is valid for model the absorption of Mg^{2+} in hydrozincite

K_{eq} represents the velocity of approximation to the equilibrium which is larger in the case of the lowest concentration. We can then conclude that lower precipitation kinetics increases the velocity of absorption.

Figure 8.4 shows the segregation coefficient against Mg^{2+} percentage over zinc in solution. The segregation coefficient is a ratio between the mass of Mg^{2+} in the sample and mass of Mg^{2+} in the solution being a measure of the adsorption efficiency.

AAS data indicates that the hydrozincite the synthesized at high concentrations of reactant has the capability of absorbing a smaller amount of Mg^{2+} when compared the with sample synthesized at low concentration. On the other hand, low concentration are capable of trapping more Mg^{2+} from the initial solution up to 40% in the case of low Mg^{2+} content. Additionally, the intermediate concentration seems to have greater flexibility in the efficiency of Mg^{2+} absorption. It ranges 40% for low concentration of Mg^{2+} and decreases to 0.8% for 15% of Mg^{2+} in solution.

It is observed that smaller concentrations of Zn^{2+} and Mg^{2+} allows, in proportion, larger amounts of Mg^{2+} in hydrozincite structure. In other words, Mg^{2+} absorption is

Table 8.1: Langmuir model fitting parameters. K_{eq} equilibrium constant and K_1 extension of the adsorption. Fitting for the three Zn^{2+} concentrations.

Fitting Parameter of the Langmuir model. Equation 8.1.		
	K_{eq}	K_1
0.02M	64.69	0.147
0.1M	6.98	0.257
0.5M	2.19	0.174

improved as supersaturation decreases. Similar results were obtained from Langmuir curves where the fitting parameter K_{eq} had a larger value for the lowest concentration. In addition a minimum in the segregation coefficient for 0.02M zinc can be found at 10%Mg.

The Langmuir like trend observed in both, Figures 8.3 and 8.4 suggests the existence of a limiting amount of Mg^{2+} allowed in the hydrozincite structure. This short of phenomena is characteristic of Langmuir systems where adsorption kinetics decreased as the systems reaches the equilibrium. Based on these results we can conclude that there is some kind of limiting factor in the absorption of Mg^{2+} and that the ions can not be freely substituted. It can, therefore, be hypothesized that the number of locations at which Mg can be incorporated is limited, similarly to a Langmuir adsorption phenomena.

Let us comment on the solubility products of Mg^{2+} and Zn^{2+} salts. Solubility products of both, magnesium and zinc carbonate differed significantly. Bénézeth *et al.* (2011) reported concentrations of $1.810^{-4}M$ for $MgCO_3$, whereas Schindler *et al.* (1969) reported 2.4110^{-6} . Assuming that equilibrium of formation of hydrozincite does not affect the one from Mg, a solid solution of $MgCO_3$ in hydrozincite would, theoretically, have a ratio around 1:100 of Mg^{2+} to Zn^{2+} ratio. From AAS we observe that the actual range goes from 14 to 50 times. This is much higher than expected when assuming simple solid solution.

Based on the solubility difference between magnesium carbonate and hydrozincite we can expect hydrozincite to be much more likely to precipitate than magnesium carbonate. Therefore the presence of Mg in the form of magnesium carbonate is very

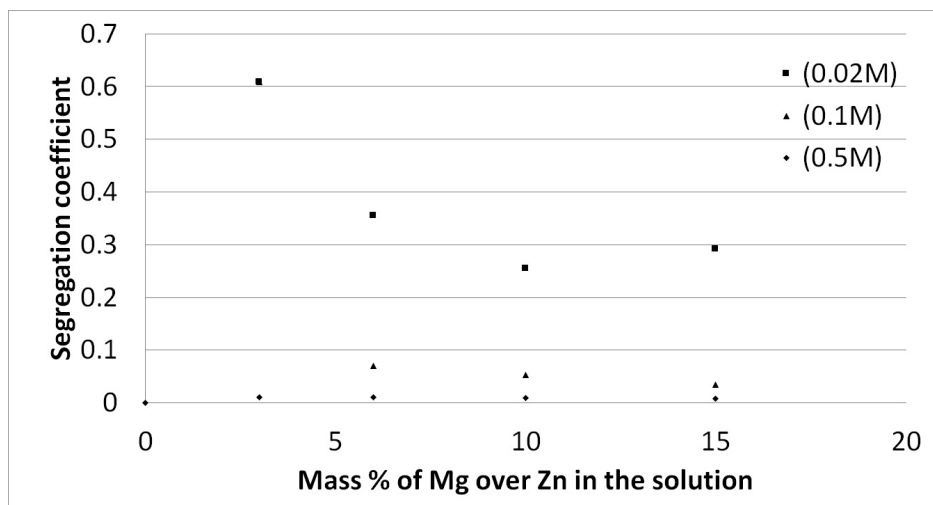


Figure 8.4: Segregation coefficient vs. percentage of magnesium over zinc in solution at three zinc concentrations (0.02M 0.1M and 0.5M). Larger segregation was found at the lowest concentration of zinc indicating better absorption as supersaturation decreases.

unlikely. Additionally, the difference between the theoretical and the experimental Mg to Zn ratio is too large for solid solution to be considered. This will be supported by the XRD spectrum reported in the next section.

8.2.3 XRD analysis

Figures 8.5, 8.6 and 8.7 show the XRD patterns for product synthesized at different concentration of Zn^{2+} and Mg^{2+} grouped by zinc concentrations. A peak match by HighScorePlus found that all the samples corresponded to hydrozincite. In spite of the noticeable difference in peak ratios of the product synthesized at 0.5M, the XRD pattern still matches the Reference pattern for hydrozincite. The changes in synthesis conditions caused the product to alter its crystalline structure and hence its XRD spectrum. Alteration in the spectrum present themselves as changes in background, peak position or peak intensity.

The change in crystal structure observed when product is synthesized at high concentration (Figure 8.7) is believed to be a consequence of fast precipitation. Different arrangements of zinc carbonate were found. Pawley analysis revealed an increment on all unit cell parameters for high concentrations, compared with product synthesized

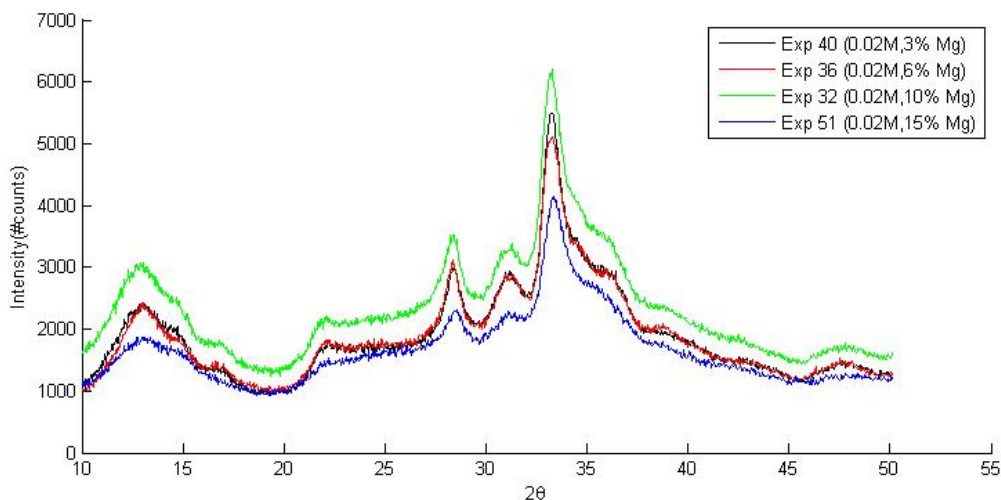


Figure 8.5: XRD spectrum of doped hydrozincite synthesized at 0.02M at various Mg^{2+} concentrations in solution (3, 6, 10, 15% of Mg^{2+} over Zn^{2+} in solution).

at lower zinc concentration. Additionally, the disappearance of the peak located at 12° is an interesting feature indicating the loss of the preferred orientation along the plane 001. In other words, the bilayer structure disappears at high supersaturations. It is believed that fast crystallization prevents the product from arranging its bilayer structure.

A broadening in peak 001 at 12° was observed in all the samples. Its relative intensity against other peaks noticeably decreases when compared with the reference spectrum. This indicates the distortion of the distance between zinc hydroxide layers. Table 8.5 shows the crystalline radius as calculated by the Scherrer equation from peak 36° . A lack of correlation between Mg^{2+} and size is observed, implying the independence of crystal structure from Mg^{2+} concentration. Similar results were obtained from other peaks but are not shown here for clarity.

The existence of solid solution between $MgCO_3$ and hydrozincite was assessed in the previous section based on the solubility of the solids and the Mg^{2+} over Zn^{2+} ratio. In this section, the named mechanism will be assessed based on the XRD patterns. Solid solutions are characterized by a mixture of different phases, both preserving their crystal structure. It is common to find that both structures match space groups which make them more compatible. In the present case, an analysis using HighScorePlus

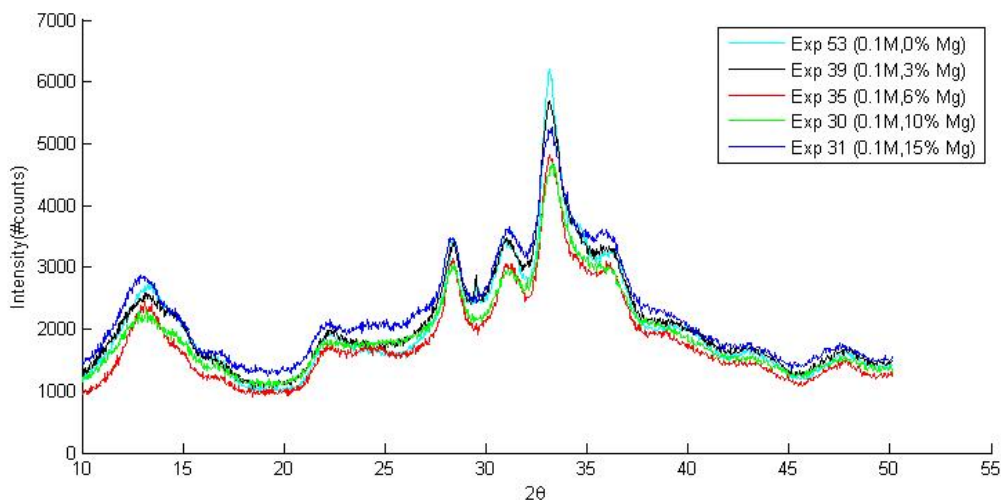


Figure 8.6: XRD spectrum of doped hydrozincite synthesized at 0.1M at various Mg^{2+} concentrations in solution (0, 3, 6, 10, 15% of Mg^{2+} over Zn^{2+} in solution).

showed one single crystallographic phase. Therefore the presence of a solid solution between Mg and Zn products is discarded.

As an alternative to the hypothesis of the solid solution or free ions incorporation within the crystal structure, ion substitution is an alternative mode of interaction between crystal structure and foreign ion. Studies done on calcite doped with Mg^{2+} Goldsmith *et al.* (1956) and more recently with SO_4^{-4} Kontrec *et al.* (2004) indicates doped ions disrupt the crystal structure increasing the unit cell volume proportionally to the amount of Mg incorporated. Sarma & Sarma (2016) on the other hand, reported a sudden change in unit cell volume as Mg^{2+} was incorporated in calcium phosphate.

In order to assess the changes in crystal lattice parameters a Pawley analysis was carried out on the spectrum presented in Figures 8.5, 8.6 and 8.7 yielding the unit cell parameters reported in Tables 8.2, 8.3 and 8.4.

This study intended to observe the disruption of the structure caused by foreign atoms incorporated in the lattice as reported in the literature. Results show no clear correlation between the amount of Mg^{2+} in the sample and the crystal unit cell volume. This can be observed in Figure 8.8 where the cell volume value, in cubic angstroms, is scattered around the reference unit cell value. This could be explained by the low absorption of Mg^{2+} in hydrozincite, the similarities in atomic radius between Zn^{2+}

8.2 Results and discussion

Table 8.2: Results from Pawley refinement (unit cell parameters $a, b, c, \alpha, \beta, \gamma$ and cell volume) for samples synthesized at 0.02M Zn^{2+} concentration at various Mg^{2+} concentrations. (0, 3, 6, 10, 15% of Mg^{2+} over Zn^{2+} in solution).

	0.02M				σ
	3%	6%	10%	15%	
a	13.292	13.712	13.672	13.281	
b	6.341	6.358	6.420	6.318	
c	5.126	5.316	5.408	5.129	
α	90	90	90	90	
β	96.04	97.42	94.33	96.22	
γ	90	90	90	90	
Cell Vol.	429.61	459.52	473.29	427.87	

Table 8.3: Results from Pawley refinement (unit cell parameters $a, b, c, \alpha, \beta, \gamma$ and cell volume) for samples synthesised at 0.1M Zn^{2+} concentration at various Mg^{2+} concentrations. (0, 3, 6, 10, 15% of Mg^{2+} over Zn^{2+} in solution).

	0.1M				σ
	3%	6%	10%	15%	
a	13.381	13.765	13.903	13.88	
b	6.399	6.386	6.482	6.471	
c	5.1747	5.385	5.476	5.477	
α	90	90	90	90	
β	95.938	97.268	94.215	94.226	
γ	90	90	90	90	
Cell Vol.	440.67	469.57	492.10	490.57	

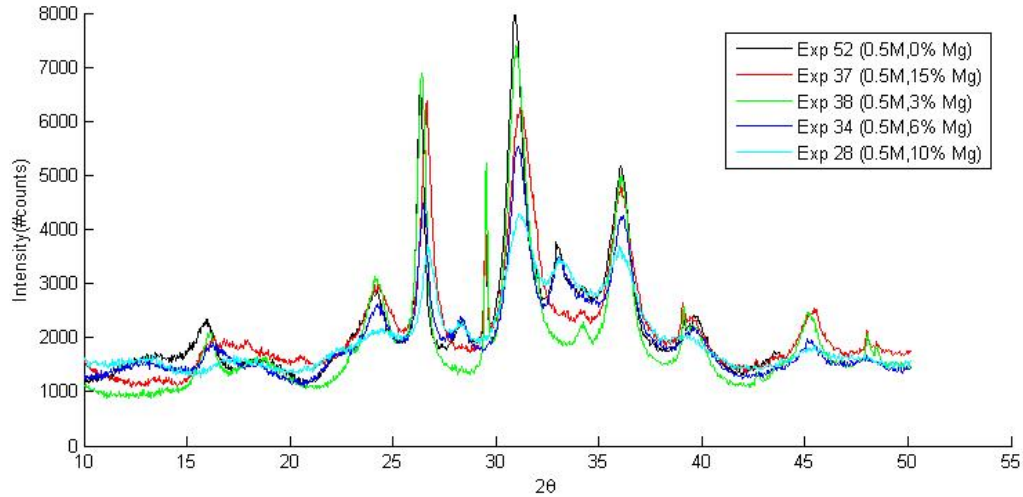


Figure 8.7: XRD spectrum of doped hydrozincite synthesized at 0.5M at various Mg^{2+} concentrations in solution. (0, 3, 6, 10, 15% of Mg^{2+} over Zn^{2+} in solution)

and Mg^{2+} .

Lattice cell parameters change evenly in all directions as observed in Tables 8.2, 8.3 and 8.4 which confirms that disruption of the lattice structure occurs homogeneously across the whole volume.

The crystalline size, r_c , has been computed using the Debye-Scherrer's expression introduced in Section 2.7.4:

$$r_c = \frac{K\lambda}{\beta \cos\theta} \quad (8.2)$$

In this expression γ is the X-ray wavelength ($=0.15405\text{nm}$), β is the peak's full width at half maximum (FWHM), K is constant normally 0.9 and θ is the Bragg diffraction angle.

Comparing crystal structure of magnesite and hydrozincite. In order to further support the theory of Mg^{2+} incorporation by substitution of Zn^{2+} in the crystal structure, it is important to assess the compatibility both chemically and physically. Goldschmidt's Rules state that for atom substitution to occur freely a certain change and radii criteria must be met. Charge criteria is met since Zn^{2+} and Mg^{2+} both hold charge 2, also size criteria (Mg^{2+} 0.72\AA and Zn^{2+} 0.74\AA) Shannon (1976). Based on these rules free substitution should occur between Zn^{2+} and Mg^{2+} although, as

8.2 Results and discussion

Table 8.4: Results from Pawley refinement (unit cell parameters $a, b, c, \alpha, \beta, \gamma$ and cell volume) for samples synthesized at 0.5M Zn^{2+} concentration at various Mg^{2+} concentrations. (0, 3, 6, 10, 15% of Mg^{2+} over Zn^{2+} in solution).

	0.5M					σ
	0%	3%	6%	10%	15%	
a	13.94	14.14	14.34	13.74	13.46	
b	6.40	6.59	6.69	6.38	6.24	
c	5.50	5.38	5.39	5.41	5.47	
α	90	90	90	90	90	
β	97.41	98.69	97.84	97.15	97.18	
γ		90	90	90	90	
Cell Vol.	486.4	495.4	512.8	470.5	455.5	

Table 8.5: Sheerer radii calculated from peak 36. For three zinc concentrations and various Mg^{2+} percentages (0, 3, 6, 10, 15% of Mg^{2+} over Zn^{2+} in solution).

Conc.	0.1M				
	0%	3%	6%	10%	15%
0.02M	49.022	39.253	—	—	—
0.1M	51.711	32.793	39.946	34.062	30.097
0.5M	303.74	61.67	44.37	29.61	68.78

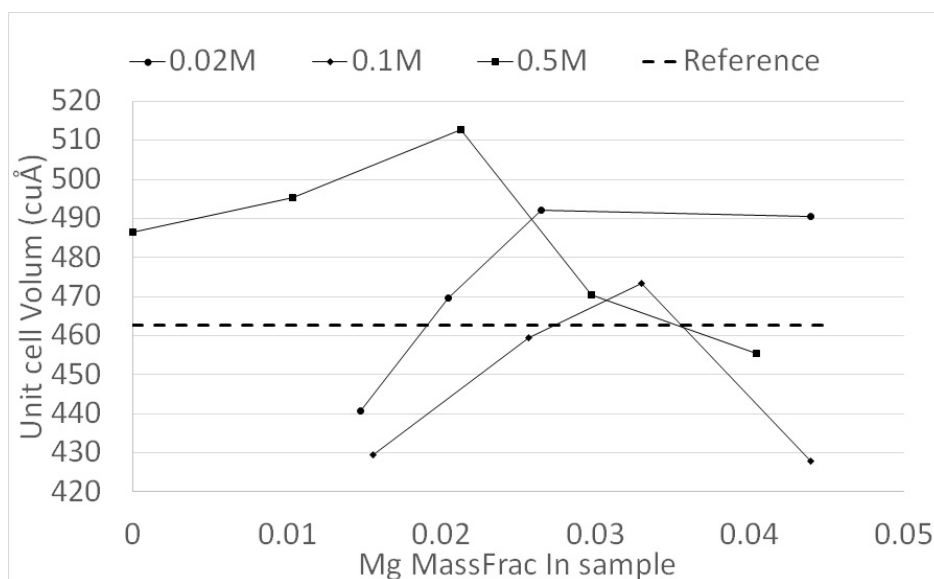


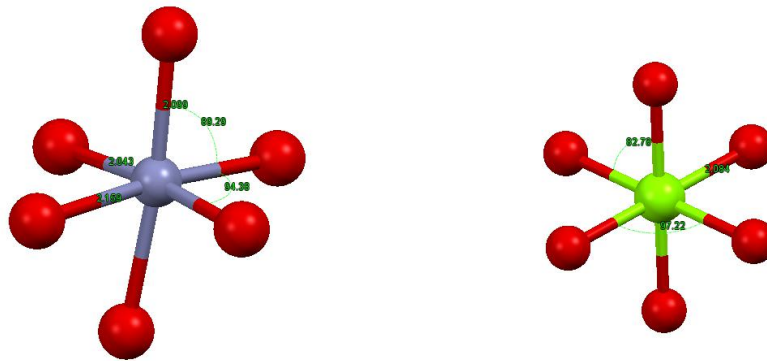
Figure 8.8: Unit cell volume as a function of Mg^{2+} mass fraction in sample for three concentrations. Dashed line corresponds to reference unit cell volume (Ghose, 1964). There was no significant relation between the unit cell volume and the mass fraction of Mg^{2+} in the sample.

observed in the AAS data, a Langmuir kind of adsorption occurs instead indicating a limiting Mg^{2+} in the solid.

Ringwood's modification to Goldsmith's rules introduced the concept of electronegativity when evaluating the affinity of the atoms to the crystal structure. When comparing the electronegativity of both Zn^{2+} and Mg^{2+} we observe values of 1.65 and 1.31 respectively. This difference could explain the Langmuir type of behaviour towards a limiting amount of Mg^{2+} in the structure. However, it is to be pointed out that the Langmuir tendency is gentle, almost lineal, which indicates that the effect of electronegativity is small.

Finally, the study of the co-ordination sphere of Zn^{2+} and Mg^{2+} allows deeper understanding of the source of compatibility between Mg^{2+} and hydrozincite. Both Mg^{2+} and Zn^{2+} form complex with hydroxide molecules in water. Looking at the crystal structures of Magnesium carbonate (Graf, 1961) and hydrozincite (Ghose, 1964), Figures 8.9(a) and 8.9(b), similarity between the octahedral structures arise. The distance between Mg^{2+} and OH^- in magnesium hydroxide is 2.084 Å where is 2.043 or

2.159Å in zinc. Also the angles between metal and OH^- bounds resemble significantly, being 82.79 and 97.22 for magnesium carbonate and 89.29 and 94.28 for hydrozincite. Although there is a tetrahedral zinc in hydrozincite, there were no reports of tetrahedral magnesium which could match the site. As a consequence of these similarities, the steric forces on the octahedral Mg^{2+} structure are small and hence more likely to be compatible with the hydrozincite structure.



(a) Distances and angles of the octahedral zinc in hydrozincite.

(b) Distances and angles of the octahedral magnesium in magnesium carbonate

Figure 8.9: Geometry of Metal ions Zn^{2+} and Mg^{2+} in the crystal structure of hydrozincite and Magnesite respectively. Similarities between the two structures allow substitution without disruption of crystal structure.

Based the results of these studies, guidance can be provided for altering hydrozincite crystal structure via doping. For example, since Mg^{2+} and Zn^{2+} differs sparingly, the use of ions such as Ca or Ba are suggested. The radius of these ions (Ca^{2+} 1.00Å and Ba^{2+} 1.35Å)(Shannon, 1976) and the electronegativity (1.00 for Ca and 0.89 for Ba) is expected to significantly disrupt the structure as well as avoiding solid solution. (N’Konou *et al.*, 2016)

8.3 Conclusions

The influence of Mg^{2+} ions in hydrozincite crystal structure and morphology will be assessed in this section. AAS provided the amount of foreign ion is the solid sample

to which segregation coefficients and Langmuir models were applied. XRD reveal that crystal structure remains unchanged in the presence of magnesium ions.

- From SEM images it is concluded that morphology remained unchanged for the range of Mg^{2+} studied.
- Magnesium ions were found to be incorporated in the samples when analyzed by AAS. The Langmuir absorption model indicates that Mg^{2+} is present in the solid. It has been found that lower supersaturation is more efficient in absorbing the foreign ion. For the same concentration, the incorporation follows an absorption isotherm indicating a limiting value of Mg^{2+} which can be incorporated in the sample.
- The mechanism of incorporation is believed to be ion substitution. However, the XRD spectra does not indicate the presence of additional phases due to low concentration and similarity of the zinc and magnesium ions. The electronegativity difference between the two ions is believed to limit the absorption of Mg^{2+} .

Chapter 9

Conclusions and Future Work

9.1 Introduction

The aim of this chapter is to summarize the outcomes of this work, compare the results with its objectives, provide guidelines for process development and suggest the future direction of the research.

9.2 Conclusions

The continuous synthesis of hydrozincite has been investigated in this work emphasizing the study of parameters affecting solubility such as aggregate size and primary particle size. A continuous T-mixer was chosen as it provides the appropriate mixing conditions for the crystallization of fast reactive materials being more efficient at large flow rates.

9.2.1 Characterization of hydrozincite produced by continuous precipitation

The material's essential properties have been characterized with emphasis on its crystallization properties. For example, studies on induction time revealed a small nucleation barrier with an activation energy around 0.051 J/m^2 . When compared to similar values in the literature, this was found to be a small barrier which allows nucleation to occur almost instantaneously. The carbonate equilibrium chemistry was found to govern the hydrozincite solubility together with the influence of other soluble zinc hydroxide salts.

When studying the process conditions influencing size, pH and concentration were identified as major factors for solution stabilization. Surface potential was found to have a maximum attraction around a pH of 7, (the isoelectric point) whereas concentration was found to increase the particle collision frequency. Other factors such as shear or surfactant concentration had less influence although its usefulness must not be neglected.

9.2.2 Model development for the precipitation of hydrozincite in tubular reactors

Based on the information gathered in this work, a model for the precipitation of hydrozincite has been created which includes, nucleation, aggregation, breakage and ripening. Properties such as flow rate and pH play a major role in controlling the precipitation reaction as well as the particle surface force and its relation to flow dynamic. Also concentration is an important factor which affects the aggregation process decreasing the overall kinetics.

A population balance model (PBM) has been put together aiming to characterize the particle size distribution along the plug flow reactor. It is been observed that residence time is the single most important parameter controlling the particle size followed by pH. Assumptions in this model have been assessed where it was found that instantaneous reaction assumption is only valid for high flow rates. It was also found that it is correct to assume plug flow conditions. This was achieved using CFD and tracer experiments.

9.2.3 Magnesium incorporation on hydrozincite crystal structure

Analysis of the morphology, ions incorporation and crystal unit cell parameters, revealed that hydrozincite remains unchanged in morphology and crystal structure despite being capable of adsorbing ions within its crystal structure. It is believed that this incorporation entails the substitution of zinc ions by magnesium ions based on its similarity in ionic radius and charge. However, the Langmuir model assumes that there

is a limit to the amount of magnesium substituted which is believed to be caused by the difference in electro/negativity of the two ions, Mg and Zn.

Other ions such as calcium or barium are suggested for alteration of the crystal since they have a similar charge and electro/negativity but with a greater difference in ionic radius.

9.3 Review of Aims and Objectives

Let us recall the objectives of this project and compare them with the outcome of the project. The objectives were listed in Section 1.2:

This project has aimed to firstly, elucidate the mechanisms involved in the precipitation phenomena and the relations between them and secondly, to elucidate control parameters which allows the control of particle size in certain ranges as well as meeting the restrictions placed by the industrial process. Regarding the first point, the lack of an integrated approach to the precipitation phenomena was observed in the literature. It was found in the process of the literature search that only practical approaches for targeting certain particle sizes, or study of individual phenomena were carried out.

Therefore an approach which covers individual phenomena as well as the overall context was needed. In this context, the processes of mixing, nucleation, aggregation, breakage and Ostwald ripening have been studied individually. Additionally, the processes of mixing and nucleation have been studied in combination with each other as well as the aggregation and breakage phenomena. Finally, the influence of pH, concentration, shear and Ostwald ripening have been studied in relation to the final particle size and morphology.

Let us recall the objectives regarding the second aspect of the project, which covered the evaluation of particle size as a function of process parameters and material properties.

- Develop the understanding and propose methodologies for the size control of zinc carbonate around the $1\mu m$ particle size.
 - Particle size tuneable between 0.8 and $1.8\mu m$ via process levers.
 - 90% of the mass in particles was less than $3\mu m$.

- Continuous or batch scalable processes to 1000 to 10000 tonnes per year.
- Remove the grinding step.
- 2% of solid material in the suspension prior to separation steps.
- pH in the range 2 to 12 in production and 6 to 9 in the final product.
- Primary particle size control of magnesium doped hydrozincite by varying the doping level with the process condition.
 - Doping 0.1 to 3%w Mg/Zn.
 - Avoidance of common dispersant as they interfere with zinc liability

9.3.1 Study of individual phenomena involved in the precipitation phenomena

As introduced earlier the individual studies of the precipitation phenomena of hydrozincite revealed a solid material with a very low crystallization energy barrier and low solubility. The supersaturation, and therefore the rate of nucleation, are very large. It has been observed that also as a consequence of the large supersaturation the size of the resulting crystals was small, yielding a system with significant surface area. This causes the system to enter the colloidal domain where phenomena such as aggregation and breakage of aggregate are of great importance: a consequence also of the large surface area in the increased importance of surface chemistry and its dependence with on pH. The surface of the carbonate transforms into bicarbonate as pH decreases which increases sensitivity which also increases the surface potential. The extent of aggregation is therefore decreased so the lowest particle size at a pH value of around 6.5.

Residence time is a major factor influencing a variety of phenomena. Reaction rate, for example, is initially limited by poor mixing: however, as the fluid moves forwards in the reactor the mixing progresses and the reaction can reach completion. Similarly, aggregation occurs at a very low extent near the mixing area, however, as residence time progresses, the kinetics of aggregation increases greatly as well as the break kinetics. Aggregation and breakage would eventually find a dynamic equilibrium

after some residence time, depending on flow rate, after which they become independent of residence time.

Reactant concentration was found to direct the supersaturation and hence the nucleation rate but also was found to influence the aggregation and breakage kinetics. Lower concentration implies less solid material concentration which decreases aggregation and breakage rates. Studies in this regard showed a decrease in particle size as concentration was decreased.

Finally the flow rate directly affected mixing as can be observed in the CFD simulation, which had an effect on reaction. It was also found to increase the effect of particle breakage through its influence on shear rate.

9.3.2 Holistic view of the precipitation phenomena.

Process parameters (pH, flow rate, concentration and residence time), process variables, (supersaturation, surface potential and shear rate), phenomena (mixing, reaction, aggregation and breakage) and process product present a complex interconnection which this work has attempted to clarify. Some aspects of the complexity of the precipitation process have been elucidated. Figure 9.1 shows the interactions studied on this work.

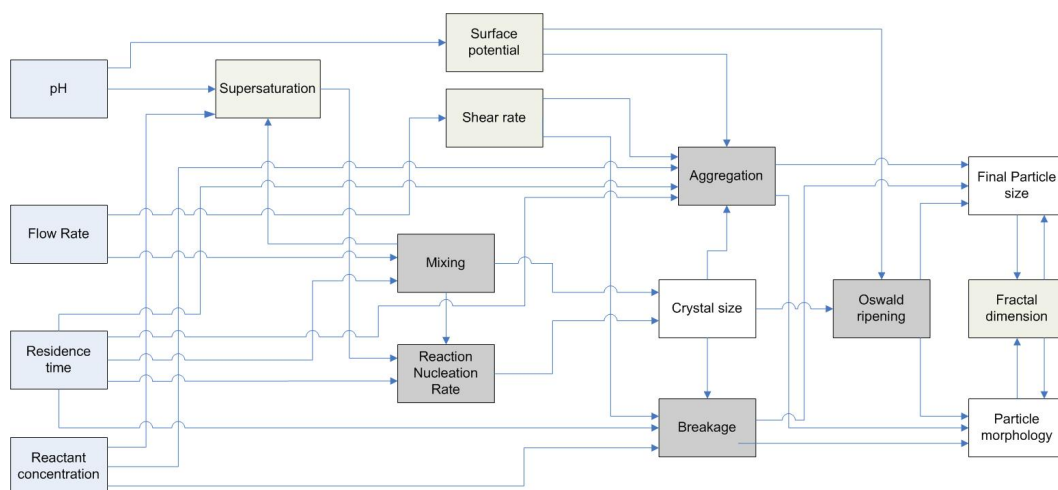


Figure 9.1: Diagram showing the process parameters (blue), the process variables (beige), the process phenomena (grey), and the features of the final product (white). The arrows show the influences between the parameter variable phenomena and the product features observed in this work.

9.3.3 Particle size and morphology control in a precipitation process

Regarding the development of methodologies for particle control, this study has identified flow rate, pH and concentration as the main process factors. In Section 5.2.3 it was found that pH and concentration can be used for tuning the particle size from $d(0.9) = 50$ to $7.06\mu m$. Further decrease was obtained when residence time was decreased down to $D[4,3] = 3\mu m$ in the tubular reactor (see Section 6.2.4). In the process of decreasing the particle size it was found that the aggregation phenomena had played a major influence on the particle size thus making the process difficult to control around the fine sizes. For instance, the large aggregate kinetics, promoted by the large number of nuclei after crystallization and its small surface potential, enhanced larger particle sizes.

Among the physical processes studied in this work, shear and ripening, ripped material under high shear and low concentrations was found to yield the lowest particle size. In general, particle size was reduced by 60% under the highest shear conditions and the lowest particle size was found when ripped material was placed in the wet mill at low concentrations.

When studying the chemical factors influencing size we found that decreasing pH was an efficient way of decreasing the particle size. After a certain residence time in a tubular reactor particles aggregated and increased in size. Therefore, a short residence time and a low pH are the most efficient parameters to play with for controlling particle size.

9.3.4 Scale-up potential

The current process as designed for laboratory scale, is capable of producing around 2 tonnes of solid hydrozincite with a mean particle size of $20\mu m$ with a 5% solid material per weight per year or $400Kg/year$ in case the required particle size is $3\mu m$ with a 2%w of solid.

In order to scale-up this process for the required 10000 to 1000 tonnes per annum, three different approaches are going to be developed: increasing the size of the current equipment, utilizing impinging jet reactors or changing the set-up for one with better capabilities such as a multi-inlet vortex mixer. The scale-up such as Reynolds number

and micro-mixing time were chosen to ensure the flow conditions provided rapid mixing compared with reaction, therefore avoiding heterogeneous precipitation. The design is going to be limited by the pumping energy, the Reynolds number and velocity inside the pipe number as there are common design constrictions. For the calculations it has been assumed 365/24 continuous operation and a conversion of 99% to the final product.

Scale-up of the current set-up in order to generate 1000 tonnes per year of solid hydrozincite a flow rate of 15000L/h of solution is required. Assuming a flow rate of 1.25m/s, common in design, a pipe diameter of 6.4cm is required. This yielded a Reynolds number around the 10^5 and required 0.007atm of pressure gradient with 3.14W of work to pump the fluid.

Although all design parameters are in the range of normal operating condition, the diameter of the pipe is believed to be too large to achieve the desired homogeneous micromixing. Heterogeneous conditions are likely to precipitate material with larger and inhomogeneous particle size.

Impinging jet reactors in order to solve the micromixing problem impinging jet reactors are commonly used in industry. After the appropriate calculations it was found that 500 impinging jet reactors were needed to work in parallel to produce 1000 tonnes per year of product. Each of them with a diameter of 1mm operating at 0.5atm pressure difference and consuming 0.39 W of pumping power. The jet velocity in this case would be around 10m/s and the Reynolds 10^5 .

This option seems to be unfeasible from the industrial point of view due to the cost of operation and maintenance of 500 small reactors with a tendency for blockage.

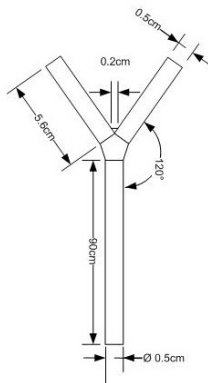
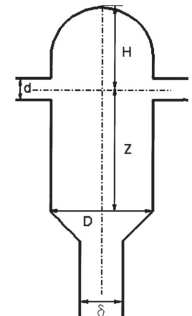
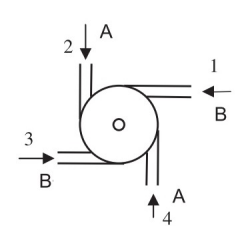
Multi inlet vortex mixer is especially design for reaction which required small micromixing time. The multi-inlet vortex relies on the creation of a turbulent vortex by four tangential flows (Liu *et al.*, 2008). For the production of 1000 tonnes per year, 35 individual setups are required operating at 0.008 atm and consuming 0.1 W of power. The diameter of the pipe was selected from the designs by Liu *et al.* (2008) and equals to 10mm which yielded a velocity of 1.25m/s and a $1.3 \cdot 10^5$ Reynolds number.

Although the operating conditions in this set are within the normal operating conditions, the number of reactors needed to achieve the target production would require a considerable amount of maintenance. However, the quality of the product is believed to be within specifications. Therefore, this equipment would be recommended as a

9.4 Suggestions for Future Work

feasible solution for the design problem. Table 9.1 summarizes the results from this study.

Table 9.1: Summary of the operating conditions for the operation of the alternative reaction set-ups

	Current	Impinging Jet	Multi-inlet reactor
			
Outlet Dia	6cm	1mm	1.1cm
%w Zn	5%	5%	5%
Flow Rate	15000L/h	28L/h	430L/h
Velocity	1.25m/s	10m/s	1.25m/s
Reynolds	10^5	10^4	$1.5 \cdot 10^4$
h_p	0.1m	5m	0.1m
Power	3500mW	400mW	9mW
N Units	1	500	35

9.4 Suggestions for Future Work

The ultimate goal of this work was to further improve the understanding of the precipitation of hydrozincite in order to control its particle size. Although considerable work has been carried out in completing the knowledge gap around this material, much more work is needed to complete the development of the industrial process to achieve the particle size target in a consistent way.

Firstly, the studies on process development for obtaining the targeted particle size must be carried out. This would involve further experimental work on the use of surfactant at low pH as well as examination of alternative geometries such as the multi-inlet vortex reactor. In this same vein, a development of a surface chemistry model to predict the ζ -potential would be of great use as this property has been demonstrated to greatly affect the particle size distribution. This would likely involve the gathering of ζ -potential at different pH and surfactant concentrations. Regarding the use of alternative geometries, the multi-inlet vortex reactor seems a strong candidate for providing small residence and micromixing times. This would involve the construction of a new set-up and further experimental work using the most successful process conditions found in this work, i.e. low concentration and low pH minimizing residence time and strong micro-mixing conditions.

The studies carried out using the inline light scattering apparatus show promising results for the study of reactive crystallization processes. However, the equipment has a lot of potential for improvement. For example, a peristaltic pump with a higher number of lobes would improve the homogeneity of the flow. Also a thinner tubular pipe would allow sudden flow changes from entering the flow cell. Improvements of such a kind would allow more reliable reading. Additionally, the in-line light scattering presents great potential in the study of new mixing systems such as impinging jets and multi-inlet vortex reactors.

Regarding magnesium incorporation, the studies carried out in this thesis suggest the potential of other elements such as calcium or boron on modifying the crystal structure of hydrozincite. Experiments in this regard, would use the same methodology developed for Mg doping substituting $MgCl_2$ for water soluble salts of calcium or boron such as $CaCl_2$ or borax salt ($Na_2B_4O_7$). It is expected that hydrozincite crystal structures would be significantly disrupted and solubility enhanced as a consequence when larger ions become part of the structure.

Additional improvements to the population balance model would improve the reliability of the predictions of the particle size as well as expanding the scope of its application for lower pH and lower reaction kinetics. This would involve the incorporation of a surface chemistry model for predicting the repulsive interaction between particles, a nucleation rate model for the initial boundary condition, and a micromixing model for predicting the relative importance of reaction and mixing as well as the

9.4 Suggestions for Future Work

size of the turbulent eddies. The complete development of such a model would be of great use for industry and academia for the complete understanding of the precipitation process.

Appendix A

Code samples

A.1 PHREEQC

The generation of solubility data

```
Input file: C:\Users\pm12pmm\OneDrive\Dropbox\Backed
up PhD\PHREEQS\Hydrozincite Ionic Strenght.pqi
Output file: C:\Users\pm12pmm\OneDrive\Dropbox\Backed
up PhD\PHREEQS\Hydrozincite Ionic Strenght.pqi
Database file: C:\Program Files (x86)\USGS\Phreeqc
Interactive 3.1.7-9213\database\minteq.v4(2).dat
```

```
-----
Reading data base.
-----
```

```
SOLUTION_MASTER_SPECIES
SOLUTION_SPECIES
SOLUTION_SPECIES
PHASES
PHASES
SURFACE_MASTER_SPECIES
SURFACE_SPECIES
END
```

```
-----  
Reading input data for simulation 1.  
-----
```

```
DATABASE C:\Program Files (x86)\USGS\Phreeqc  
Interactive 3.1.7-9213\database\minteq.v4(2).dat
```

```
TITLE De-ionized water
```

```
SOLUTION 2
```

```
temp      20  
pH        8.6233  
pe        4  
redox     pe  
units     ppm  
density   1  
water     0.01 # kg
```

```
EQUILIBRIUM_PHASES 1
```

```
Hydrozincite 0 0.01
```

```
TITLE De-ionized water
```

```
SOLUTION 2
```

```
temp      20  
pH        8.6233  
pe        4  
redox     pe  
units     ppm  
density   1  
water     0.01 # kg
```

```
EQUILIBRIUM_PHASES 1
```

```
Hydrozincite 0 0.01
```

```
END
```

```
-----
```

```
TITLE
```

```
-----
```

```
De-ionized water
```

A.1 PHREEQC

 Beginning of initial solution calculations.

Initial solution 2.

-----Solution composition-----

Elements	Molality	Moles
----------	----------	-------

Pure water

-----Description of solution-----

pH	=	8.623
pe	=	4.000
Activity of water	=	1.000
Ionic strength	=	1.445e-06
Mass of water (kg)	=	1.000e-02
Total alkalinity (eq/kg)	=	2.885e-06
Total carbon (mol/kg)	=	0.000e+00
Total CO2 (mol/kg)	=	0.000e+00
Temperature (C)	=	20.00
Electrical balance (eq)	=	-2.885e-08
Percent error, 100*(Cat- An)/(Cat+ An)	=	-99.83
Iterations	=	0
Total H	=	1.110137e+00
Total O	=	5.550684e-01

-----Distribution of species-----

Species	Molality	Activity	Log Molality	Log Activity	Log Gamma	mole V cm/mol
---------	----------	----------	-----------------	-----------------	--------------	------------------

A.1 PHREEQC

OH-	2.888e-06	2.884e-06	-5.539	-5.540	-0.001	(0)
H+	2.386e-09	2.383e-09	-8.622	-8.623	-0.001	0.00
H2O	5.551e+01	1.000e+00	1.744	0.000	0.000	18.05
H(0)	8.442e-29					
H2	4.221e-29	4.221e-29	-28.375	-28.375	0.000	(0)
O(0)	2.296e-37					
O2	1.148e-37	1.148e-37	-36.940	-36.940	0.000	(0)

-----Saturation indices-----

Phase	SI**	log IAP	log K(293 K,	1 atm)
O2(g)	-34.31	50.49	84.80	O2

**For a gas, SI = log10(fugacity). Fugacity = pressure * phi / 1 atm.
 For ideal gases, phi = 1.

 Beginning of batch-reaction calculations.

Reaction step 1.

Using solution 2.

Using pure phase assemblage 1.

-----Phase assemblage-----

Phase	SI	log IAP	log K(T, P)	Moles in assemblage		
				Initial	Final	Delta
Hydrozincite	-0.00	-14.85	-14.85	1.000e-02	1.000e-02	-5.443e-08

A.1 PHREEQC

-----Solution composition-----

Elements	Molality	Moles
C	2.177e-06	2.177e-08
Zn	5.443e-06	5.443e-08

-----Description of solution-----

pH	= 8.919	Charge balance
pe	= -3.440	Adjusted to redox equilib
Activity of water	= 1.000	
Ionic strength	= 8.686e-06	
Mass of water (kg)	= 1.000e-02	
Total alkalinity (eq/kg)	= 1.377e-05	
Total CO2 (mol/kg)	= 2.177e-06	
Temperature (C)	= 20.00	
Electrical balance (eq)	= -2.885e-08	
Percent error, 100*(Cat- An)/(Cat+ An)	= -21.86	
Iterations	= 16	
Total H	= 1.110137e+00	
Total O	= 5.550685e-01	

-----Distribution of species-----

Species	Molality	Activity	Log Molality	Log Activity	Log Gamma	mole V cm/mol
OH-	5.714e-06	5.694e-06	-5.243	-5.245	-0.001	(0)
H+	1.209e-09	1.205e-09	-8.918	-8.919	-0.001	0.00
H2O	5.551e+01	1.000e+00	1.744	-0.000	0.000	18.05
C(4)	2.177e-06					
HC03-	2.088e-06	2.081e-06	-5.680	-5.682	-0.001	(0)
C03-2	7.427e-08	7.327e-08	-7.129	-7.135	-0.006	(0)

A.1 PHREEQC

ZnCO3	8.364e-09	8.364e-09	-8.078	-8.078	0.000	(0)
H2CO3	6.005e-09	6.005e-09	-8.221	-8.221	0.000	(0)
ZnHCO3+	1.185e-10	1.181e-10	-9.926	-9.928	-0.001	(0)
H(0)	1.643e-14					
H2	8.215e-15	8.215e-15	-14.085	-14.085	0.000	(0)
O(0)	0.000e+00					
O2	0.000e+00	0.000e+00	-65.518	-65.518	0.000	(0)
Zn	5.443e-06					
Zn(OH)2	2.197e-06	2.197e-06	-5.658	-5.658	0.000	(0)
Zn+2	2.011e-06	1.984e-06	-5.697	-5.702	-0.006	(0)
ZnOH+	1.134e-06	1.130e-06	-5.946	-5.947	-0.001	(0)
Zn(OH)3-	9.238e-08	9.206e-08	-7.034	-7.036	-0.001	(0)
ZnCO3	8.364e-09	8.364e-09	-8.078	-8.078	0.000	(0)
ZnHCO3+	1.185e-10	1.181e-10	-9.926	-9.928	-0.001	(0)
Zn(OH)4-2	3.106e-11	3.064e-11	-10.508	-10.514	-0.006	(0)

-----Saturation indices-----

Phase	SI**	log IAP	log K(293 K,	1 atm)	
CH4(g)	-26.99	-68.80	-41.81	CH4	
CO2(g)	-6.81	-24.97	-18.16	CO2	
Hydrozincite	-0.00	-14.85	-14.85	Zn(OH)1.2(CO3)0.4	
O2(g)	-62.88	21.91	84.80	O2	
Smithsonite	-2.88	-12.84	-9.95	ZnCO3	
Zincite	0.53	12.14	11.60	ZnO	
Zn(OH)2	-0.06	12.14	12.20	Zn(OH)2	
Zn(OH)2(am)	-0.58	12.14	12.71	Zn(OH)2	
Zn(OH)2(beta)	0.13	12.14	12.00	Zn(OH)2	
Zn(OH)2(epsilon)	0.36	12.14	11.78	Zn(OH)2	
Zn(OH)2(gamma)	0.40	12.14	11.73	Zn(OH)2	
ZnCO3:1H2O	-2.58	-12.84	-10.26	ZnCO3:1H2O	
Znmetal	-25.07	1.18	26.25	Zn	
ZnO(active)	0.68	12.14	11.45	ZnO	

**For a gas, $SI = \log_{10}(\text{fugacity})$. Fugacity = pressure * phi / 1 atm.
For ideal gases, phi = 1.

End of simulation.

Reading input data for simulation 2.

END

End of simulation.

Reading input data for simulation 3.

TITLE Distilled water

SOLUTION 2

temp 20
pH 7.23
pe 4
redox pe
units mmol/kgw
density 1
water 1 # kg

EQUILIBRIUM_PHASES 1

Hydrozincite 0 10

END

TITLE

Distilled water

Beginning of initial solution calculations.

Initial solution 2.

-----Solution composition-----

Elements	Molality	Moles
----------	----------	-------

Pure water

-----Description of solution-----

pH	=	7.230
pe	=	4.000
Activity of water	=	1.000
Ionic strength	=	8.773e-08
Mass of water (kg)	=	1.000e+00
Total alkalinity (eq/kg)	=	5.762e-08
Total carbon (mol/kg)	=	0.000e+00
Total CO2 (mol/kg)	=	0.000e+00
Temperature (C)	=	20.00
Electrical balance (eq)	=	-5.762e-08
Percent error, $100 * (\text{Cat} - \text{An}) / (\text{Cat} + \text{An})$	=	-32.84
Iterations	=	0
Total H	=	1.110137e+02
Total O	=	5.550683e+01

A.1 PHREEQC

-----Distribution of species-----

Species	Molality	Activity	Log Molality	Log Activity	Log Gamma	mole V cm/mol
OH-	1.165e-07	1.165e-07	-6.934	-6.934	-0.000	(0)
H+	5.892e-08	5.890e-08	-7.230	-7.230	-0.000	0.00
H2O	5.551e+01	1.000e+00	1.744	0.000	0.000	18.05
H(0)	5.164e-26					
H2	2.582e-26	2.582e-26	-25.588	-25.588	0.000	(0)
O(0)	0.000e+00					
O2	0.000e+00	0.000e+00	-42.513	-42.513	0.000	(0)

-----Saturation indices-----

Phase	SI**	log IAP	log K(293 K,	1 atm)
O2(g)	-39.88	44.92	84.80	O2

**For a gas, SI = log₁₀(fugacity). Fugacity = pressure * phi / 1 atm.
For ideal gases, phi = 1.

Beginning of batch-reaction calculations.

Reaction step 1.

Using solution 2.

Using pure phase assemblage 1.

-----Phase assemblage-----

Moles in assemblage

A.1 PHREEQC

Phase	SI	log IAP	log K(T, P)	Initial	Final	Delta
Hydrozincite	0.00	-14.85	-14.85	1.000e+01	1.000e+01	-6.076e-06

-----Solution composition-----

Elements	Molality	Moles
C	2.431e-06	2.431e-06
Zn	6.076e-06	6.076e-06

-----Description of solution-----

pH = 8.812 Charge balance

pe = -3.411 Adjusted to redox equilib

Activity of water = 1.000

Ionic strength = 9.893e-06

Mass of water (kg) = 1.000e+00

Total alkalinity (eq/kg) = 1.221e-05

Total CO2 (mol/kg) = 2.431e-06

Temperature (C) = 20.00

Electrical balance (eq) = -5.762e-08

Percent error, 100*(Cat-|An|)/(Cat+|An|) = -0.41

Iterations = 17

Total H = 1.110137e+02

Total O = 5.550685e+01

-----Distribution of species-----

Species	Molality	Activity	Molality	Log Activity	Log Gamma	Log cm/mol	mole V
OH-	4.470e-06	4.453e-06	-5.350	-5.351	-0.002	(0)	
H+	1.546e-09	1.540e-09	-8.811	-8.812	-0.002	0.00	

A.1 PHREEQC

H2O	5.551e+01	1.000e+00	1.744	-0.000	0.000	18.05
C(4)	2.431e-06					
HCO3-	2.346e-06	2.337e-06	-5.630	-5.631	-0.002	(0)
CO3-2	6.530e-08	6.435e-08	-7.185	-7.191	-0.006	(0)
ZnCO3	1.039e-08	1.039e-08	-7.983	-7.983	0.000	(0)
H2CO3	8.623e-09	8.623e-09	-8.064	-8.064	0.000	(0)
ZnHCO3+	1.883e-10	1.876e-10	-9.725	-9.727	-0.002	(0)
H(0)	2.347e-14					
H2	1.173e-14	1.173e-14	-13.931	-13.931	0.000	(0)
O(0)	0.000e+00					
O2	0.000e+00	0.000e+00	-65.828	-65.828	0.000	(0)
Zn	6.076e-06					
Zn+2	2.848e-06	2.806e-06	-5.546	-5.552	-0.006	(0)
Zn(OH)2	1.901e-06	1.901e-06	-5.721	-5.721	0.000	(0)
ZnOH+	1.254e-06	1.250e-06	-5.902	-5.903	-0.002	(0)
Zn(OH)3-	6.253e-08	6.230e-08	-7.204	-7.206	-0.002	(0)
ZnCO3	1.039e-08	1.039e-08	-7.983	-7.983	0.000	(0)
ZnHCO3+	1.883e-10	1.876e-10	-9.725	-9.727	-0.002	(0)
Zn(OH)4-2	1.646e-11	1.622e-11	-10.784	-10.790	-0.006	(0)

-----Saturation indices-----

Phase	SI**	log IAP	log K(293 K,	1 atm)	
CH4(g)	-26.21	-68.03	-41.81	CH4	
CO2(g)	-6.66	-24.82	-18.16	CO2	
Hydrozincite	0.00	-14.85	-14.85	Zn(OH)1.2(CO3)0.4	
O2(g)	-63.19	21.61	84.80	O2	
Smithsonite	-2.79	-12.74	-9.95	ZnCO3	
Zincite	0.47	12.07	11.60	ZnO	
Zn(OH)2	-0.13	12.07	12.20	Zn(OH)2	
Zn(OH)2(am)	-0.64	12.07	12.71	Zn(OH)2	
Zn(OH)2(beta)	0.07	12.07	12.00	Zn(OH)2	
Zn(OH)2(epsilon)	0.29	12.07	11.78	Zn(OH)2	

A.1 PHREEQC

Zn(OH)2(gamma)	0.34	12.07	11.73	Zn(OH)2
ZnCO3:1H2O	-2.48	-12.74	-10.26	ZnCO3:1H2O
Znmetal	-24.98	1.27	26.25	Zn
ZnO(active)	0.62	12.07	11.45	ZnO

**For a gas, SI = log10(fugacity). Fugacity = pressure * phi / 1 atm.
For ideal gases, phi = 1.

End of simulation.

Appendix B

Code samples

B.1 Topas Pawley Refinement

```
'-----  
'Input File for simple Rietveld Refinement  
'Use save/set current button then run with F6 in topas  
'Replace $ and # symbols with text/numbers as needed  
'-----  
  
r_wp 4.12946266 r_exp 2.18197527 r_p 2.75572863 r_wp_dash 7.96472968 r_p_dash  
5.86030951 r_exp_dash 4.2084999 weighted_Durbin_Watson 0.286849822 gof 1.8925341  
  
'-----  
'General information about refinement here  
'Remove comments as required  
'-----  
  
iters 100000  
chi2_convergence_criteria 0.001  
'do_errors  
  
'-----
```

B.1 Topas Pawley Refinement

```
'Information on datafile etc here
'Check that default weighting is appropriate for your data
'-----
xdd Exp28.xy
x_calculation_step = Yobs_dx_at(Xo); convolution_step 4
bkg    1000.08598 -494.494826 -180.043952 -58.5244432

'd8 Ge(111) monochromator Vantec Cu Ka1
LP_Factor(!th2_monochromator, 27.26)
CuKa1(0.0001)

Specimen_Displacement(@,-0.17593')
Zero_Error(@, 0.17053')

hkl_Is
TCHZ_Peak_Type(pku, 1.90547'_LIMIT_MAX_2,pkv, 1.15000',pkw,
0.06033',!pkz, 0.0000,pky, 2.00000'_LIMIT_MAX_2,!pkxz, 0.0000)
Simple_Axial_Model(axial, 43.30206')
phase_name 1964
a @ 13.462162'
b @ 6.238057'
c @ 5.466418'
al 90
be @ 97.18132'
ga 90
volume 455.456'

space_group "C2/m"
load hkl_m_d_th2 I
{
```

B.1 Topas Pawley Refinement

2	0	0	2	6.678279	13.24691	@	4.95201'
1	1	0	4	5.652012	15.66614	@	0.00000' _LIMIT_MIN_1e-015
0	0	1	2	5.423537	16.33051	@	4.10012'
2	0	-1	2	4.493960	19.73932	@	4.36037'
1	-1	-1	4	4.021006	22.08867	@	7.64751'
2	0	1	2	3.973978	22.35341	@	0.45915' _LIMIT_MIN_1e-015
1	1	1	4	3.813808	23.30508	@	18.78628'
3	1	0	4	3.623873	24.54508	@	29.42217'
4	0	0	2	3.339140	26.67511	@	105.53380'
3	-1	-1	4	3.165611	28.16670	@	41.17718'
0	2	0	2	3.119029	28.59625	@	10.89976'
4	0	-1	2	3.016784	29.58716	@	0.00008' _LIMIT_MIN_1e-015
3	1	1	4	2.880780	31.01829	@	188.50623'
2	2	0	4	2.826006	31.63508	@	75.78888'
0	2	1	4	2.711769	33.00503	@	3.73172' _LIMIT_MIN_1e-015
4	0	1	2	2.703799	33.10511	@	5.00477' _LIMIT_MIN_1e-015
0	0	2	2	2.696903	33.19221	@	150.02254'
2	0	-2	2	2.629737	34.06550	@	98.79066'
2	-2	-1	4	2.562351	34.98988	@	45.17827'
1	-1	-2	4	2.496983	35.93669	@	218.03066'
5	1	0	4	2.455628	36.56311	@	30.42215'
2	2	1	4	2.453564	36.59496	@	28.96813'
2	0	2	2	2.409718	37.28511	@	70.32194'
1	1	2	4	2.395991	37.50666	@	0.00003' _LIMIT_MIN_1e-015
5	-1	-1	4	2.340349	38.43294	@	61.89331'
4	2	0	4	2.285603	39.39106	@	0.00000' _LIMIT_MIN_1e-015
3	-1	-2	4	2.279332	39.50394	@	92.02027'
4	0	-2	2	2.246980	40.09692	@	0.00000' _LIMIT_MIN_1e-015
6	0	0	2	2.226093	40.48953	@	74.98535'
4	-2	-1	4	2.168434	41.61537	@	10.61327' _LIMIT_MIN_1e-015
6	0	-1	2	2.156232	41.86191	@	0.00005' _LIMIT_MIN_1e-015
5	1	1	4	2.146258	42.06565	@	63.27210'
1	3	0	4	2.072380	43.64065	@	0.00000' _LIMIT_MIN_1e-015
3	1	2	4	2.054604	44.03790	@	100.98503'

B.1 Topas Pawley Refinement

4	2	1	4	2.046455	44.22247	@	0.00006' _LIMIT_MIN_1e-015
0	2	2	4	2.040044	44.36884	@	0.00000' _LIMIT_MIN_1e-015
2	-2	-2	4	2.010503	45.05626	@	152.50259'
6	0	1	2	1.986989	45.61932	@	94.93366'
4	0	2	2	1.974491	45.92454	@	0.00000' _LIMIT_MIN_1e-015
5	-1	-2	4	1.934172	46.93854	@	121.99945'
1	-3	-1	4	1.933713	46.95036	@	11.71067' _LIMIT_MIN_1e-015
1	3	1	4	1.909230	47.58932	@	22.30257' _LIMIT_MIN_1e-015
2	2	2	4	1.906904	47.65096	@	7.83627' _LIMIT_MIN_1e-015
3	3	0	4	1.884004	48.26676	@	185.75771'
6	0	-2	2	1.836902	49.58663	@	62.31574'
7	1	0	4	1.824631	49.94288	@	69.84515'
4	-2	-2	4	1.823147	49.98633	@	185.13944'

}

Appendix C

Code samples

C.1 gPROMS code

Models

```
PARAMETER
NoGrid          as INTEGER      # sizes
VARIABLE

n              AS ARRAY(Nogrid)  OF NumberParticles
# number of crystals[#]
m3            AS ThirdMomentum
              # Third Momentum of the size distribution [#m3]
m3Vol         As ThirdMomentum
              # Third Momentum of the size distribution [#m3]
m4            AS FourthMomentum
              # Third Momentum of the size distribution [#m4]
m4Vol         As FourthMomentum
              # Third Momentum of the size distribution [#m4]
nt            AS NumberParticles
              # Total number of particels [#]
lnnt          AS Dimensionalless
              # Natural logaritm of the total number of particles.
```

```

df                AS Dimensionalless
# Fractal dimension.
d43               AS Dimensionalless
# D[4,3] of the size distribution based on number[adim]
d43Vol           AS Dimensionalless
# D[4,3] of the size distribution based on volum fraction[adim]
BirthA           AS ARRAY(Nogrid)    OF NucleationRate
# BirthA rate of particles [#m3/s]
DeathA           AS ARRAY(Nogrid)    OF NucleationRate
# DeathA rate of particles [#m3/s]
BirthB           AS ARRAY(Nogrid)    OF NucleationRate
# Birth rate of particles by breakage of bigger ones [#m3/s]
DeathB           AS ARRAY(Nogrid)    OF NucleationRate
# Death rate of particles by breakage into smaller ones on

Volumne_Fraction AS ARRAY(Nogrid)    OF Fraction          # Volumne fraction []
Phi              AS Fraction
# Initial Volumn Fraction of solids

AggFac           AS Dimensionalless
#Fitting parameter for aggregation (includes Shear Rate)
Kr               AS ARRAY(Nogrid,Nogrid)    OF Colliscion_frequency
# agglomeration kernel [collicions/s]
alpha            AS ARRAY(Nogrid,Nogrid)    OF Dimensionalless
# Efficiency of collisions []
kalpha           AS Dimensionalless
# Proportional factor

Kb               AS ARRAY(Nogrid)          OF Colliscion_frequency
# brekage kernel [collicions/s]
P1               AS Dimensionalless
#Fittingparameters for breakage kernel (includes Shear Rate)
P2               AS Dimensionalless
#Fittingparameters for breakage kernel

```

```
L          AS  ARRAY(Nogrid)          OF length
# size of the crystal [m]

d          AS  length
# diameter of the tube
X          AS  length
# length of the reactor [m]
xl        AS  length
# Position in the reactor []

u          AS  velocity
# average velocity of fluid [m/s]
G          As  shear_rate
# Shear Rate for turbulent flows.

#maxL      OF  length
# larger crystal size [m]
minL      AS  length
# initial crystal size [m]
#n_log     OF  dimensionless
# power law index
DeltaL    AS  length
# Length step [m]
H          As  energy
# Hamaker constant [J]
EQUATION
#Variable trasphormation, Time into adimesnional length
$xl=X;

#####Shear rate#####
G=u*1190.2-76.402;
#AggFac=u*0.6809+1.9558;
#kalpha=-u*15.242+11.159;
```



```

#P1=1.3867*log(u)+0.9414;
#P2=-1.850*u+2.8524;

#####bins#####
#Define bin size Fibonacci space
1e6*L(1)=1e6*minL;
1e6*L(2)=1e6*(minL+DeltaL);
FOR i:=3 TO NoGrid DO
    1e6*L(i)=1e6*(L(i-1)+L(i-2));
END

#####aggreagtion efficiency#####
#Flow number###Wang2005b
FOR i:= 1 TO Nogrid DO
    FOR j:= 1 TO Nogrid DO
        alpha(i,j)=kalpha*(3.14159*0.001*G*(L(i)+L(j))^3/8/H)^(-0.18);
    END
END

#####Aggregation frequency#####
#Define kernel of aggregation (It is a matrix Nogrid*Nogrid)
FOR i:= 1 TO Nogrid DO
    FOR j:= 1 TO Nogrid DO
        Kr(i,j)/L(i)^4=(G^AggFac*(L(i)+L(j))^3)/L(i)^4;
    END
END

#BirthA Term Base on Fibonacci
BirthA(1)=0;
BirthA(2)/L(2)^3=(alpha(1,1)*Kr(1,1)*n(1)*n(1))/L(2)^3;
FOR i:= 3 TO Nogrid DO
    BirthA(i)/L(i)^4=(alpha(i-1,i-2)*Kr(i-1,i-2)*n(i-2)*n(i-1))/L(i)^4;
END

#DeathA Term Fibonacci

```

```

DeathA(1)/L(1)^3=(Kr(1,1)*n(1)*n(1)+Kr(1,2)*n(2)*n(1))/L(1)^3;
FOR i:= 2 TO Nogrid-2 DO
    DeathA(i)/L(i)^4=(Kr(i,i+1)*n(i+1)*n(i))/L(i)^4;
END
DeathA(Nogrid)=0;
DeathA(Nogrid-1)=0;

#####BreKage#####

Kb(1)=0;
FOR i:=2 TO Nogrid DO
    Kb(i)=G^P1*(L(i)/minL)^P2;
End

#Birth By breakage of particles one size bigger
FOR i:=1 TO Nogrid-2 DO
    #BirthB(i)=Kb(i+1)*n(i+1)*1;
    #Ones stands for the breakage distribution function
    BirthB(i)=Kb(i+1)*n(i+1)+Kb(i+2)*n(i+2);
End
BirthB(Nogrid-1)=0;
BirthB(Nogrid)=0;

DeathB(1)=0;
FOR i:=2 TO Nogrid DO
    DeathB(i)=Kb(i)*n(i);
END
#####Population balance#####

FOR i:= 1 TO Nogrid DO
    ((u/X*$n(i))*L(i)^3)=((BirthA(i)-DeathA(i)+BirthB(i)-DeathB(i))*L(i)^3);
END
#####Mass balance calcualtion#####
#Third Momuntun of the population balance

```

```
m3=sigma(n*L^3);
m3Vol=sigma(Volumne_Fraction*L^3);
m4=sigma(n*L^4);
m4Vol=sigma(Volumne_Fraction*L^4);
d43=m4/m3;
d43Vol=m4Vol/m3Vol;
nt=sigma(n);
lnnt=(nt)/1e14;
#Calculation of the volumne fraction
FOR i:=1 TO Nogrid DO
(Volumne_Fraction(i))=(n(i)*L(i)^df/m3);
END

#####Initial conditions#####
INITIAL
FOR i:=1 TO 19 DO
n(i)=0;
END
n(20)=(Phi/(4/3*3.14159*(1.43662E-4)^df)); ##chnaged from minL
FOR i:=21 TO Nogrid DO
n(i)=0;
END
xl=0;
```

Processes

UNIT

Flowsheet AS Test

SET

Start Unit Specifications

 WITHIN Flowsheet DO

```
        WITHIN AggregationModel001 DO
            NoGrid := 26 ; # 26 #
        END # WITHIN AggregationModel001
    END # WITHIN Flowsheet
# End Unit Specifications
```

```
ASSIGN
```

```
# Start Unit Specifications
    WITHIN Flowsheet DO
        WITHIN AggregationModel001 DO
            AggFac := 0.43 ; # 0.43 adim
            d := 0.008 ; # 0.008 m
            DeltaL := 2e-9 ; # 2e-9 m
            df := 3 ; # 3 adim
            H := 3.5e-20 ; # 3.5e-20 J
            kalpha := 1.8 ; # 1.8 adim
            minL := 2e-8 ; # 2e-8 m
            P1 := 0.8 ; # 0.8 adim
            P2 := -0.6 ; # -0.6 adim
            Phi := 2e-4 ; # 2e-4 adim
            u := 0.141 ; # 0.141 m/s
            X := 4.22 ; # 4.22 m
        END # WITHIN AggregationModel001
    END # WITHIN Flowsheet
# End Unit Specifications
```

```
INITIALISATION_PROCEDURE
```

```
# Start Default Initialisation Procedure
    USE
        : DEFAULT;
    END
    SAVE "Test_InitialGuess";
# End Default Initialisation Procedure
```

SOLUTIONPARAMETERS

```
ReportingInterval := 0.01
IndexReduction := ON
PerformStrictDAEStructuralChecks := ON
IntrinsicTasks := OFF
```

SCHEDULE

SEQUENCE

```
CONTINUE FOR 1
END # SEQUENCE
```

References

- ABLER, M.M. & COMPANY), M. (1995). United States Patent [19] [11] Patent Number : [45] Date of Patent :. 3-6. 59
- AHMED, F. (1995). Simulation of flocculation process through coarse media bed. *Journal of the civil engineering division*, **23**. 51
- ALHAWI, T., REHAN, M., YORK, D. & LAI, X. (2015). Synthesis of zinc carbonate hydroxide nanoparticles using microemulsion process. *Procedia Engineering*, **102**, 346–355. 8, 62, 67
- ALWAN, A.K. & WILLIAMS, P.A. (1979). Mineral formation from aqueous solution. Part I. The deposition of hydrozincite, $Zn_5(OH)_6(CO_3)_2$, from natural waters. *Transition Metal Chemistry*, **4**, 128–132. 59
- AUBERT, C. & CANNELL, D.S. (1986). Restructuring of colloidal silica aggregates. *Physical Review Letters*, **56**, 738–741. 56, 127, 163
- BADYGA, J. & BOURNE, J.R. (1999). *Turbulent mixing and chemical reactions*. 4, 37, 43, 174, 176
- BADYGA, J. & POHORECKI, R. (1995). Turbulent micromixing in Chemical Reactors - a Review. *Chemical Engineering Journal*, **58**, 183. xiii, 38, 39, 40, 41, 43
- BALAKIN, B., HOFFMANN, A.C. & KOSINSKI, P. (2012). The collision efficiency in a shear flow. *Chemical Engineering Science*, **68**, 305–312. 57
- BELL, R.P. (1969). *Acids and Bases Their quantitative behaviour*. 15

REFERENCES

- BEMS, B., SCHUR, M., DASSENOY, A., JUNKES, H., HEREIN, D. & SCHLÖGL, R. (2003). Relations between synthesis and microstructural properties of copper/zinc hydroxycarbonates. *Chemistry (Weinheim an der Bergstrasse, Germany)*, **9**, 2039–52. 60
- BÉNÉZETH, P., SALDI, G.D., DANDURAND, J.L. & SCHOTT, J. (2011). Experimental determination of the solubility product of magnesite at 50 to 200C. *Chemical Geology*, **286**, 21–31. 213
- BENJAMIN, M.M. (2002). *Water Chemistry*. McGraw-Hill series in water resources and environmental engineering, Waveland Press, Incorporated. 120
- BERRE, F.L., CHAUVETEAU, G. & PEFFERKORN, E. (1998). Perikinetic and Orthokinetic Aggregation of Hydrated Colloids. *Journal of Colloid and Interface Science*, **199**, 1–12. 192
- BHUIYAN, M.I.H., MAVINIC, D.S. & BECKIE, R.D. (2007). a Solubility and Thermodynamic Study of Struvite. *Environmental Technology*, **28**, 1015–1026. 120
- BIRD, R.B., STEWART, W.E. & LIGHTFOOT, E.N. (2007). *Transport Phenomena*. Wiley International edition, Wiley. 37
- BITENC, M., MARINŠEK, M. & CRNJAK OREL, Z. (2008). Preparation and characterization of zinc hydroxide carbonate and porous zinc oxide particles. *Journal of the European Ceramic Society*, **28**, 2915–2921. 62, 143, 208
- BRAGG, L.W. (1913). The Diffraction of Short Electromagnetic Waves by a Crystal. 74
- BRANDEL, C. & TER HORST, J.H. (2015). Measuring induction times and crystal nucleation rates. *Faraday Discuss.*, **179**, 199–214. 20, 118
- BRECEVIC, L. & KRALJ, D. (2007). On Calcium Carbonates : from Fundamental Research to Application. *Croatica Chemica Acta*, **80**, 467–484. xiii, 34, 35, 79
- BUCCA, M., DIETZEL, M., TANG, J., LEIS, A. & KÖHLER, S.J. (2009). Nucleation and crystallization of otavite, witherite, calcite, strontianite, hydrozincite, and

REFERENCES

- hydrocerussite by CO₂ membrane diffusion technique. *Chemical Geology*, **266**, 152–165. 119, 190
- BUSENBERG, E. & PLUMMER, L.N. (1986). The solubility of BaCO₃(cr) (witherite) in CO₂-H₂O solutions between 0 and 90C, evaluation of the association constants of BaHCO₃⁺(aq) and BaCO₃(aq) between 5 and 80C, and a preliminary evaluation of the thermodynamic properties of Ba²⁺(aq). *Geochimica et Cosmochimica Acta*, **50**, 2225–2233. 120
- CAMACHO CORZO, D.M., BORISSOVA, A., HAMMOND, R.B., KASHCHIEV, D., ROBERTS, K.J., LEWTAS, K. & MORE, I. (2014). Nucleation mechanism and kinetics from the analysis of polythermal crystallisation data: methyl stearate from kerosene solutions. *CrystEngComm*, **16**, 974–991. xi, 20, 23
- CAMP, T.R. & STEIN, P.C. (1943). *Velocity Gradients and Internal Work in Fluid Motion*. Boston, Massachusetts. 50
- CARDIN, C., DAVIS, J., HART, J. & SCHMIDT, D. (1992). Antidandruff shampoo compositions. 60
- CASSON, L.W. & LAWLER, D.F. (1990). Flocculation in turbulent flow measurement and modeling of particle size distributions. *Journal AWWA*, 54–68. 159
- CHAKRABORTI, R.K., GARDNER, K.H., ATKINSON, J.F. & VAN BENSCHOTEN, J.E. (2003). Changes in fractal dimension during aggregation. *Water Research*, **37**, 873–883. 55, 163
- CHEN, C., LIU, P. & LU, C. (2008). Synthesis and characterization of nano-sized ZnO powders by direct precipitation method. *Journal of Ceramic Processing Research*, **144**, 509–513. 62, 83
- CHEN, C., YU, B., LIU, P., LIU, J.F. & WANG, L. (2011). Investigation of nano-sized ZnO particles fabricated by various synthesis routes. *Journal of Ceramic Processing Research*, **12**, 420–425. 60

REFERENCES

- CHENG, J., YANG, C., MAO, Z.S. & ZHAO, C. (2009). CFD modeling of nucleation, growth, aggregation, and breakage in continuous precipitation of barium sulfate in a stirred tank. *Industrial and Engineering Chemistry Research*, **48**, 6992–7003. 3, 95, 187, 190
- CHERNOV, A.A. (1961). Spiral Growth of Crystals,. *Sov Phys Uspekhi*, **73**, 277–331. 30
- CHUN ZENG, H. (2007). Ostwald Ripening: A Synthetic Approach for Hollow Nanomaterials. *Current Nanoscience*, **3**, 177–181. 74
- CLEVER, H.L., JOHNSON, S.A. & DERRICK, M.E. (1985). The solubility of some sparingly soluble mercury salts in water and aqueous electrolyte solutions. *Journal of Physical and Chemical Reference Data*, **14**, 631–680. 59
- CUBILLAS, P. & ANDERSON, M.W. (2010). *SynthesisMechanism: Crystal Growth and Nucleation*. xii, 28, 30
- CUI, Y. & MYERSON, A.S. (2014). Experimental evaluation of contact secondary nucleation mechanisms. *Crystal Growth and Design*, **14**, 5152–5157. 22
- DAVIS, K.J. (2000). The Role of Mg²⁺ as an Impurity in Calcite Growth. *Science*, **290**, 1134–1137. 207, 211
- DEBYE, P. & HUCKEL, E. (1954). On the theory of electrolytes. I. Freezing point depression and related phenomena. *The Collected Papers of Peter JW ...*, 1–6. 15, 16
- DERJAGUIN, B. & LANDAU, L. (1941). Theory of the stability of strongly charged lyophobic sols and of the adhesion of strongly charged particles in solutions of electrolytes. *Acta Physico Chemica URSS*, **14**, 633. 45
- DINNEBIER, R.E. & BILLINGE, S.J.L., eds. (2008). *Powder Diffraction*. Royal Society of Chemistry, Cambridge. xiv, 75, 77, 78
- DIRKSEN, J.A. & RING, T.A. (1991). Fundamentals of Crystallization: Kinetic Effects on Particle Size Distributions and Morphology. *Chem. Eng. Sci.*, **46**, 2389–2427. 2

REFERENCES

- DOSCH, R., TUTTLE, B. & BROOKS, R. (1986). Chemical preparation and properties of high-field zinc oxide varistors. *J. Mater. Res*, **87185**. 79
- DUKHIN, A.S. & GOETZ, P.J. (1996). Acoustic and Electroacoustic Spectroscopy. *Langmuir*, **12**, 4336–4344. 93
- EATON, J.K. & FESSLER, J.R. (1994). Preferential concentration of particles by turbulence. *Int. J. Multiphase flow*, **20**, 169–209. xiv, 56, 57
- EESA, M. (2009). *CFD studies of complex fluid flows in pipes*. Ph.D. thesis. xv, 98, 99, 104
- EINSTEIN, A. (1965). Concerning an heuristic point of view toward the emission and transformation of light (English translation). *American Journal of Physics*, **33**, 367. 75
- ELANGOVA, S.V., SIVAKUMAR, N. & CHANDRAMOHAN, V. (2015). Magnesium doped zinc oxide nanocrystals for photo-catalytic applications. *Journal of Materials Science: Materials in Electronics*, **26**, 8753–8759. 207
- FANI, A., CAMARRI, S. & SALVETTI, M.V. (2013). Investigation of the steady engulfment regime in a three-dimensional T-mixer. *Physics of Fluids*, **25**. 99
- FLESCH, J.C., SPICER, P. & PRATSINIS, S.E. (1999). Laminar and Turbulent Shear-Induced Flocculation of Fractal Aggregates. *AIChE Journal*, **45**, 1114–1124. 55, 157, 171
- FOGLER, H.S. (2006a). Distributions of residence times for chemical reactors. *Elements of Chemical Reaction Engineering*, 867–944. 203
- FOGLER, S. (2006b). *Elements of Chemical Reaction Engineering*. Upper Saddle River, NJ, 4th edn. xiii, 42, 43, 44, 102
- FORSYTH, C., MULHERAN, P.A., FORSYTH, C., HAW, M.D., BURNS, I.S. & SEFCIK, J. (2015). Influence of Controlled Fluid Shear on Nucleation Rates in Glycine Aqueous Solutions. *Crystal growth and Design*, **15**, 94–102. 22, 23

REFERENCES

- FOURNIER, M.C., FALK, L. & VILLERMAUX, J. (1996). A new parallel competing reaction system for assessing micromixing efficiency Determination of micromixing time by a simple mixing model. *Chemical Engineering Science*, **51**, 5187–5192. 179
- FRANK, F.C. & VAN DER MERWE, J.H. (1949). One-Dimensional Dislocations. I. Static Theory. *Proceedings of the Royal Society of London A: Mathematical, Physical and Engineering Sciences*, **198**, 205–216. 28
- FUJITA, S.I., SATRIYO, A.M., SHEN, G.C. & TAKEZAWA, N. (1995). Mechanism of the formation of precursors for the Cu/ZnO methanol synthesis catalysts by a coprecipitation method. *Catalysis Letters*, **34**, 85–92. 60, 62, 67, 108
- GHOSE, S. (1964). The crystal structure of hydrozincite, $Zn_5(OH)_6(CO_3)_2$. *Acta Crystallographica*, **17**, 1051–1057. xxii, 66, 150, 220
- GIANGUZZA, A., PELIZZETTI, E. & SAMMARTANO, S. (2002). *Chemistry of Marine Water and Sediments*. Environmental Science and Engineering / Environmental Science, Springer. 16
- GILLIAN, J.M. & KIRWAN, D.J. (2008). Identification and Correlation of Mixing Times in Opposed-Jet Mixers. *Chemical Engineering Communications*, **195**, 1553–1574. 44
- GOLDSMITH, J., GRAF, D.L. & JOENSUU, O.I. (1956). The occurrence of magnesian calcite in nature. **7**, 212–230. 26, 207, 216
- GOTO, S. & VASSILICOS, J.C. (2006). Self-similar clustering of inertial particles and zero-acceleration points in fully developed two-dimensional turbulence. *Physics of Fluids*, **18**, 1–21. 57
- GRAF, D.L. (1961). Crystallographic tables for the rhombohedral carbonates. *American Mineralogist*, **46**, 1283–1316. 220
- GRAHAME, D.C. (1947). The Electrical Double Layer and the Theory of Electrocapillarity. *Chemical Reviews*, **41**, 441–501. 46
- GRAUER, R. & FEITKNECHT, W. (1967). THERMODYNAMISCHE ZINKKORROSION IN CARBONATHALTIGEN LÖSUNGEN. *Corrosion Science*, **7**. 61

REFERENCES

- GREGORY, J. (1981). Flocculation in laminar tube flow. *Chemical Engineering Science*, **36**, 1789–1794. 51, 174, 177
- HAMAKER, H. (1937). The Londonvan der Waals attraction between spherical particles. *Physica*, **4**, 1058–1072. 47
- HANHOUN, M., MONTASTRUC, L., AZZARO-PANTEL, C., BISCANS, B., FRÈCHE, M. & PIBOULEAU, L. (2013). Simultaneous determination of nucleation and crystal growth kinetics of struvite using a thermodynamic modeling approach. *Chemical Engineering Journal*, **215-216**, 903–912. 3, 120, 121
- HARBOTTLE, D. (2008). *Physical Modelling of Colloidal Flows*. Ph.D. thesis, Leeds University. 174
- HARGITTAI, I. (2009). Christopher Hammond: The basics of crystallography and diffraction. Third edition. *Structural Chemistry*, **20**, 751–751. xii, 25
- HASAN, S., ALI, H.A., AL-QUBAISI, M., HUSSEIN, M.Z., ISMAIL, M., ZAINAL, Z. & HAKIM, M.N. (2012). Controlled-release formulation of antihistamine based on cetirizine zinc-layered hydroxide nanocomposites and its effect on histamine release from basophilic leukemia (RBL-2H3) cells. *International Journal of Nanomedicine*, **7**, 3351–3363. 59, 206
- HELMHOLTZ, H. (1853). Ueber einige Gesetze der Vertheilung elektrischer Strome in körperlichen Leitern mit Anwendung auf die thierisch-elektrischen Versuche. *Annalen der Physik*, **165**, 211–233. 46
- HOGG, R., HEALY, T.W. & FUERSTENAU, D.W. (1966). Mutual coagulation of colloidal dispersions. *Trans. Faraday Soc.*, **62**, 1638–1651. 47
- HU, S.H., CHEN, Y.C., HWANG, C.C., PENG, C.H. & GONG, D.C. (2010). Analysis of growth parameters for hydrothermal synthesis of ZnO nanoparticles through a statistical experimental design method. *Journal of Materials Science*, **45**, 5309–5317. 8, 60, 62, 67, 108
- IBASETA, N. & BISCANS, B. (2010). Fractal dimension of fumed silica: Comparison of light scattering and electron microscope methods. *Powder Technology*, **203**, 206–210. 3, 72, 74, 82

REFERENCES

- JIANG, S. & TER HORST, J.H. (2011). Crystal nucleation rates from probability distributions of induction times. *Crystal Growth and Design*, **11**, 256–261. 4, 22
- JOHNSON, B.K. & PRUD’HOMME, R.K. (2003). Chemical processing and micromixing in confined impinging jets. *AIChE Journal*, **49**, 2264–2282. xiii, 4, 38
- JONES, A.G., HOSTOMSKÝ, J. & WACH, S. (1996). Modelling and Analysis of Particle Formation During Agglomerative Crystal Precipitation Processes. *Chemical Engineering Communications*, **146**, 105–130. 53
- K.A. KUSTERS (1991). *The influence of turbulence on aggregation of small particles in agitated vessels*. Ph.D. thesis. 54
- KAHLWEIT, M. (1975). Ostwald ripening of precipitates. *Advances in Colloid and Interface Science*, **5**, 1–35. xiii, 34, 36, 139
- KAKIUCHI, K., SAITO, M. & FUJIHARA, S. (2008). Fabrication of ZnO films consisting of densely accumulated mesoporous nanosheets and their dye-sensitized solar cell performance. *Thin Solid Films*, **516**, 2026–2030. 62
- KALUZA, S., SCHRÖTER, M.K., NAUMANN D’ALNONCOURT, R., REINECKE, T. & MUHLER, M. (2008). High Surface Area ZnO Nanoparticles via a Novel Continuous Precipitation Route. *Advanced Functional Materials*, **18**, 3670–3677. 62
- KICKELBICK, G., FALK, G. & QUINTEN, D. (2012). Continuous Processing of Nano-sized Zinc Oxide Powders in Impinging jet Micro-reactors for Opto-electronic Applications. *Cfi-Ceramic Forum International*, **89**, E37–E42. 8, 60, 62
- KLEIN, R. & MEAKIN, P. (1989). Universality in colloid aggregation. *Nature*. 2, 150
- KONTREC, J., KRALJ, D., BREČEVIĆ, L., FALINI, G., FERMANI, S., NOETHIG-LASLO, V. & MIROSAVLJEVIĆ, K. (2004). Incorporation of inorganic anions in calcite. *European Journal of Inorganic Chemistry*, 4579–4585. 3, 26, 216
- KOSTOGLU, M. & KARABELAS, A. (1998). Comprehensive Modeling of Precipitation and Fouling in Turbulent Pipe Flow. *Industrial and Engineering Chemistry Research*, **37**, 1536–1550. 2

REFERENCES

- KUSTERS, K.A. (1991). *The influence of turbulence on aggregation of small particles in agitated vessels*. Ph.D. thesis, Eindhoven University of technology. 56, 159
- LANGMUIR, I. (1918). The Adsorption of Gases on Plane Surfaces of Glass, Mica and Platinum. *Journal of the American Chemical Society*, **40**, 1361–1403. 211
- LASHERAS, J., EASTWOOD, C., MARTÍNEZ-BAZAN, C. & MONTANES, J. (2002). A review of statistical models for the break-up of an immiscible fluid immersed into a fully developed turbulent flow. **28**, 247–278. 53
- LEE, J.W., CHOI, W.C. & KIM, J.D. (2010). Size-controlled layered zinc hydroxide intercalated with dodecyl sulfate: effect of alcohol type on dodecyl sulfate template. *CrystEngComm*, **12**, 3249. 59
- LI, J., FAN, H. & JIA, X. (2010). Multilayered ZnO Nanosheets with 3D Porous Architectures Synthesis and Gas Sensing Application support. 14684–14691. 62
- LI, S., GROSS, G., GÜNTHER, P. & KÖHLER, J. (2011). Hydrothermal micro continuous-flow synthesis of spherical, cylinder-, star- and flower-like ZnO microparticles. *Chemical Engineering Journal*, **167**, 681–687. 62
- LI, Z., SHEN, X., FENG, X., WANG, P. & WU, Z. (2005). Non-isothermal kinetics studies on the thermal decomposition of zinc hydroxide carbonate. *Thermochimica Acta*, **438**, 102–106. 7, 62
- LIANG, K., WHITE, G., AND DEREK WILKINSON, FORD, L.J., ROBERTS, K.J. & WOOD, W.M.L. (2004). An Examination into the Effect of Stirrer Material and Agitation Rate on the Nucleation of L-Glutamic Acid Batch Crystallized from Supersaturated Aqueous Solutions. *Crystal Growth and Design*, **4**, 1039–1044. 116
- LIN, M., KLEIN, R., LINDSAY, H., WEITZ, D., BALL, R. & MEAKIN, P. (1990). The Structure of Fractal Aggregates of Finite Extent. 3, 55, 163, 169, 174, 176
- LIU, J. & RASMUSON, A.C. (2013). Influence of agitation and fluid shear on primary nucleation in solution. *Crystal Growth and Design*, **13**, 4385–4394. 22, 115

REFERENCES

- LIU, Y., JIAN-ER, Z., LARBOT, A. & PERSIN, M. (2007). Preparation and characterization of nano-zinc oxide. *Journal of Materials Processing Technology*, **189**, 379–383. 62, 67, 108
- LIU, Y., CHENG, C., LIU, Y., PRUD'HOMME, R.K. & FOX, R.O. (2008). Mixing in a multi-inlet vortex mixer (MIVM) for flash nano-precipitation. *Chemical Engineering Science*, **63**, 2829–2842. 229
- MANDELBROT, B. (1967). How long is the coast of britain? Statistical self-similarity and fractional dimension. *Science (New York, N.Y.)*, **156**, 636–638. 73
- MANN, S., HEYWOOD, B.R., RAJAM, S. & WADE, V.J. (1991). Molecular Recognition in Biomineralization. *Mechanisms and Phylogeny of Mineralization in Biological Systems*, 47–55. 2
- MEAKIN, P. (1992). Aggregation kinetics. *Physica Scripta*, **46**, 295–331. 73
- MEAKIN, P. & FAMILY, F. (1988). Structure and kinetics of reaction-limited aggregation. *Physical Review A*, **38**, 2110–2123. 55, 169, 174, 176
- MEDAS, D., DE GIUDICI, G., PODDA, F., MENEGHINI, C. & LATTANZI, P. (2014). Apparent energy of hydrated biomineral surface and apparent solubility constant: An investigation of hydrozincite. *Geochimica et Cosmochimica Acta*, **140**, 349–364. 109, 120
- MELDRUM, F.C. & CÖLFEN, H. (2008). Controlling mineral morphologies and structures in biological and synthetic systems. *Chemical Reviews*, **108**, 4332–4432. 209
- MIAO, J., XUE, M. & FENG, Q. (2006). Hydrothermal synthesis of layered hydroxide zinc benzoate compounds and their exfoliation reactions. 474–480. 59
- MIE, G. (1908). Beiträge zur Optik trüber Medien, speziell kolloidaler Metallösungen. *Annalen der Physik*. 72
- MULLIN (2001). *Crystallization*. xi, xii, 19, 22, 26, 29, 100, 115, 120, 121, 152, 174

REFERENCES

- MUSIĆ, S., POPOVIĆ, S., MALJKOVIĆ, M. & DRAGČEVIĆ, . (2002). Influence of synthesis procedure on the formation and properties of zinc oxide. *Journal of Alloys and Compounds*, **347**, 324–332. 60
- MYERSON, A. (2002). *Handbook of industrial crystallization*. October. xii, 1, 32, 33, 45
- NIELSEN, A. & SÖHNEL, O. (1971). INTERFACIAL TENSIONS ELECTROLYTE CRYSTAL-AQUEOUS SOLUTION, FROM NUCLEATION DATA. *Journal of Crystal Growth*, **11**, 233–242. 21, 120
- NIELSEN, L.C., DE YOREO, J.J. & DEPAOLO, D.J. (2013). General model for calcite growth kinetics in the presence of impurity ions. *Geochimica et Cosmochimica Acta*, **115**, 100–114. 211
- N'KONOU, K., HARIS, M., LARE, Y., BANETO, M., NAPO, K. & TORCHIO, P. (2016). Effect of barium doping on structural and optical properties of zinc oxide nanoparticles synthesized by microwave hydrothermal method. *Physica Status Solidi (B)*, **253**, 260–266. 221
- NYVLT, J., RYCHLY, R., GOTTFRIED, J. & WURZELOVA, J. (1970). Metastable zone-width of some aqueous solutions. *Journal of Crystal Growth*, **6**, 151–162. 23
- OLES, V. (1992). Shear-induced aggregation and breakup of polystyrene latex particles. *Journal of Colloid And Interface Science*, **154**, 351–358. xiv, 58, 157, 161, 162, 163, 174
- PANDYA, J. & SPIELMAN, L. (1983). Floc breakage in agitated suspensions: Effect of agitation rate. *Chemical Engineering Science*, **38**, 1983–1992. 53, 54
- PARKHURST, D. & APPELO, C. (2013). Description of Input and Examples for PHREEQC Version 3A Computer Program for Speciation, Batch-Reaction, One-Dimensional Transport, and Inverse Geochemical Calculations. 91
- PATRUNO, L.E., DORAO, C.A., SVENDSEN, H.F. & JAKOBSEN, H.A. (2009). Analysis of breakage kernels for population balance modelling. *Chemical Engineering Science*, **64**, 501–508. 54

REFERENCES

- PICCA, R.A., SPORTELLI, M.C., LOPETUSO, R. & CIOFFI, N. (2017). Electrosynthesis of ZnO nanomaterials in aqueous medium with CTAB cationic stabilizer. *Journal of Sol-Gel Science and Technology*, **81**, 338–345. 62
- POHORECKI, R. (1982). THE USE OF A NEW MODEL OF MICROMIXING FOR DETERMINATION CRYSTAL SIZE IN PRECIPITATION. 1, 2
- POURMORTAZAVI, S.M., MARASHIANPOUR, Z., KARIMI, M.S. & MOHAMMAD-ZADEH, M. (2015). Electrochemical synthesis and characterization of zinc carbonate and zinc oxide nanoparticles. *Journal of Molecular Structure*, **1099**, 232–238. 62
- PREIS, W. & GAMSJÄGER, H. (2001). (Solid + solute) phase equilibria in aqueous solution. XIII. Thermodynamic properties of hydrozincite and predominance diagrams for (Zn²⁺ + H₂O + CO₂). *The Journal of Chemical Thermodynamics*, **33**, 803–819. 65, 114
- PUDUKUDY, M. & YAAKOB, Z. (2014). Simple chemical synthesis of novel ZnO nanostructures: Role of counter ions. *Solid State Sciences*, **30**, 78–88. 62, 67
- QIU, X., LI, L., ZHENG, J., LIU, J., SUN, X. & LI, G. (2008). Origin of the enhanced photocatalytic activities of semiconductors: A case study of ZnO doped with Mg²⁺. *Journal of Physical Chemistry C*, **112**, 12242–12248. 3, 4, 207
- RAHIMI, H. & SOLAIMANY NAZAR, A.R. (2010). Asphaltene aggregates fractal restructuring model, a population balance approach. *Energy and Fuels*, **24**, 1088–1093. 55
- REINERT (1965). *Dissertation*. Ph.D. thesis, Bern. 64
- ROELANDS, C.P.M., ROESTENBERG, R.R.W., TER HORST, J.H., KRAMER, H.J.M. & JANSSENS, P.J. (2004). Development of an experimental method to measure nucleation rates in reactive precipitation. In *Crystal Growth and Design*. 4
- ROELANDS, M., DERKSEN, J., TER HORST, J., KRAMER, H. & JANSSENS, P. (2003). An analysis of mixing in a typical experimental setup to measure nucleation rates of precipitation processes. *Chemical Engineering and Technology*, **26**, 296–303. 4, 98, 101

REFERENCES

- SARKAR, D. & KHILAR, K.C. (2009). Microemulsion Mediated Synthesis of Nanoparticles for Nanoparticles Synthesis. *Recent Advances in Nanoscience and Technology*, **28**, 25–37. 62
- SARMA, B.K. & SARMA, B. (2016). Role of magnesium on the biomimetic deposition of calcium phosphate. *Journal of Physics: Conference Series*, **765**, 012025. 3, 4, 26, 207, 216
- SAVJANI, K.T., GAJJAR, A.K. & SAVJANI, J.K. (2012a). Drug solubility: importance and enhancement techniques. *ISRN pharmaceuticals*, **2012**, 195727. 24
- SAVJANI, K.T., GAJJAR, A.K. & SAVJANI, J.K. (2012b). Drug solubility: importance and enhancement techniques. *ISRN pharmaceuticals*, **2012**, 195727. 206
- SCHIKARSKI, T., PEUKERT, W. & AVILA, M. (2016). Direct numerical simulation of water-ethanol flows in a T-mixer. 99
- SCHINDLER, P., REINERT, M. & GAMSJAGER, H. (1969). Löslichkeitskonstanten und Freie Bildungsenthalpien von $ZnCO_3$ und $Zn_5(OH)_6(CO_3)_2$ bei 25. **52**, 3–8. xxiv, 59, 61, 63, 64, 65, 91, 100, 120, 213
- SCHWARTZ, J. & JOHNSON, E. (2004). Composition comprising particulate zinc materials having a defined crystallite size. xi, 6, 60, 206, 208
- SEGNIT, E. & HOLLAND, A. (1964). The System $MgO-ZnO-SiO_2$. *Journal of the american ceramic society*, **48**, 409. 207
- SELOMULYA, C., BUSHELL, G., AMAL, R. & WAITE, T.D. (2003). Understanding the role of restructuring in flocculation: The application of a population balance model. *Chemical Engineering Science*, **58**, 327–338. 55, 158, 163
- SERRA, T. & CASAMITJANA, X. (1998). Modelling the Aggregation and Break-up of Fractal Aggregates in a Shear Flow. *Applied Scientific Research*, **59**, 255–268. 2, 3, 8, 54, 187
- SERRA, T., COLOMER, J. & CASAMITJANA, X. (1997). Aggregation and Breakup of Particles in a Shear Flow. *Journal of colloid and interface science*, **187**, 466–73. 3, 56, 58, 158, 159, 161, 174, 176

REFERENCES

- SHAMSIPUR, M., POURMORTAZAVI, S.M., HAJIMIRSADEGHI, S.S. & ROUSHANI, M. (2013a). Applying Taguchi robust design to the optimization of synthesis of barium carbonate nanorods via direct precipitation. *Colloids and Surfaces A: Physicochemical and Engineering Aspects*, **423**, 35–41. 60
- SHAMSIPUR, M., POURMORTAZAVI, S.M., HAJIMIRSADEGHI, S.S., ZAHEDI, M.M. & RAHIMI-NASRABADI, M. (2013b). Facile synthesis of zinc carbonate and zinc oxide nanoparticles via direct carbonation and thermal decomposition. *Ceramics International*, **39**, 819–827. 7, 8, 62
- SHANNON, R.D. (1976). Revised effective ionic radii and systematic studies of interatomic distances in halides and chalcogenides. *Acta Crystallographica Section A*, **32**, 751–767. 218, 221
- SMOLUCHOWSKI, M. (1917). Versuch einer mathematischen Theorie der Koagulationskinetik kolloider Lösungen. *Zeitschrift f. Physik. Chemie.*, **1210**. 2, 3, 8, 49, 95, 174, 177
- SÖHNEL, O. & GARSIDE, J. (1992). *Precipitation: basic principles and industrial applications*. 32
- SÖHNEL, O. & MULLIN, J. (1978). A method for the determination of precipitation induction periods. *Journal of Crystal Growth*, **44**, 377–382. 119, 120, 121
- SOOS, M., MARCHISIO, D., SEFCIK, J. & MORBIDELLI, M. (2005). Aggregation and Breakage of Nanoparticle Dispersions in Heterogeneous Turbulent Flows. *CFD in Chemical Reaction Engineering*. 2, 3
- SOOS, M., WANG, L., FOX, R.O., SEFCIK, J. & MORBIDELLI, M. (2007). Population balance modeling of aggregation and breakage in turbulent Taylor-Couette flow. *Journal of Colloid and Interface Science*, **307**, 433–446. 3, 8, 54, 58, 174, 177
- STERN, O. (1924). ZUR THEORIE DER ELEKTROLYTISCHEN DOPPELSCHICHT. *Zeitschrift fr Elektrochemie und angewandte physikalische Chemie*, **30**, 508–516. 46

REFERENCES

- STOJANOVIĆ, Z., MARKOVIĆ, S. & USKOKOVIĆ, D. (2010). Measurement of particle size distribution using laser light diffraction. 71
- SUN, Y. (2016). A Series of Unique Architecture Building of Layered Zinc Hydroxides: Self-Assembling Stepwise Growth of Layered Zinc Hydroxide Carbonate and Conversion into Three-Dimensional ZnO. 59, 79
- TAMBO, N. & WATANABE, Y. (1979). Physical aspect of flocculation process-I: Fundamental treatise. *Water Research*, **13**, 429–439. 54
- TAVARE, N.S. (1986). Mixing in continuous crystallizers. *AIChE Journal*, **32**, 705–732. 4
- TAVARE, N.S. (1995). Mixing, reaction, and precipitation: Interaction by exchange with mean micromixing models. *AIChE Journal*, **41**, 2537–2548. 43
- TSENG, C.C., CHOU, Y.H., LIU, C.M., LIU, Y.M., GER, M.D. & SHU, Y.Y. (2012). Microwave-assisted hydrothermal synthesis of zinc oxide particles starting from chloride precursor. *Materials Research Bulletin*, **47**, 96–100. 62
- TURIANICOVA, E., KANUCHOVA, M., ZORKOVSKA, A., HOLUB, M., BUJNAKOVA, Z., DUTKOV??, E., BALAZ, M., FINDORAKOVA, L., BALINTOVA, M. & OBUT, A. (2016). CO₂ utilization for fast preparation of nanocrystalline hydrozincite. *Journal of CO₂ Utilization*, **16**, 328–335. 59, 62
- VALIOULIS, I.A. & LIST, E.J. (1984). Collision Efficiencies of Diffusing Spherical Particle. *Advanced Functional Materials*, **20**, 1–20. 53
- VAN CAPPELLEN, P., CHARLET, L., STUMM, W. & WERSIN, P. (1993). A surface complexation model of the carbonate mineral-aqueous solution interface. *Geochimica et Cosmochimica Acta*, **57**, 3505–3518. xxiv, 69, 70, 149
- VAN DE VEN, T. & MASON, S. (1977). The microrheology of colloidal dispersions V I I . Orthokinetic doublet formation of spheres. **479**, 468–479. 52
- VAN DER EERDEN, J.P., BENNEMA, P. & CHEREPANOVA, T.A. (1978). Survey of Monte Carlo Simulations of Crystal Surfaces and Crystal Growth. *Prog. Crystal Growth Charact.*, **1**, 219–254. 29

- VERWEY, E. & OVERBEEK, J. (1948). *Theory of the stability of lyophobic colloids*. 45
- VILLERMAUX, J. (1994). A generalised mixing model for initial contacting of reactive fluids. *Chemical Engineering Science*, **49**, 5127–5140. 41, 42, 44
- VOLMER, M. (1939). *Kinetics of Phase Formation*. Chemische Reaktion, T. Steikopff. 20
- VON LAUE, M. (1915). Concerning the detection of X-ray interferences. *Nobel lecture*. 74
- WANG, L. & MUHAMMED, M. (1999). Synthesis of zinc oxide nanoparticles with controlled morphology. *Journal of Materials Chemistry*, **9**, 2871–2878. 62, 111
- WANG, L., MARCHISIO, D.L., VIGIL, R.D. & FOX, R.O. (2005a). CFD simulation of aggregation and breakage processes in laminar Taylor-Couette flow. *Journal of Colloid and Interface Science*, **282**, 380–396. 8
- WANG, L., VIGIL, R.D. & FOX, R.O. (2005b). CFD simulation of shear-induced aggregation and breakage in turbulent Taylor-Couette flow. *Journal of Colloid and Interface Science*, **285**, 167–178. 4
- WANG, Y., LI, J. & HONG, R. (2012). Large scale synthesis of ZnO nanoparticles via homogeneous precipitation. *Journal of Central South University*, 863–868. 60
- WATSON, J.D. & CRICK, F.H.C. (1953). Molecular structure of nucleic acids. 74
- WEI, H. & GARSIDE, J. (1997). Application of CFD Modelling to Precipitation Systems. *Chemical Engineering Research and Design*, **75**, 219–227. 4
- WINTSCH, R.P. & DUNNING, J. (1985). The effect of dislocation density on the aqueous solubility of quartz and some geologic implications: A theoretical approach. *Journal of Geophysical Research*, **90**, 3649–3657. 24
- WOLTERS, M., CHARLET, L. & VAN CAPPELLEN, P. (2008). The surface chemistry of divalent metal carbonate minerals: A critical assessment of surface charge and potential data using the charge distribution multi-site ion complexation model. *American Journal of Science*, **308**, 905–941. 69, 70, 167, 168

REFERENCES

- WU, L., WU, Y. & LÜ, Y. (2006). Self-assembly of small ZnO nanoparticles toward flake-like single crystals. *Materials Research Bulletin*, **41**, 128–133. 62
- WU, W. & JIANG, Q. (2006). Preparation of nanocrystalline zinc carbonate and zinc oxide via solid-state reaction at room temperature. *Materials Letters*, **60**, 2791–2794. 62
- WU, W.Y., KUNG, W.Y. & TING, J.M. (2011). Effect of pH Values on the Morphology of Zinc Oxide Nanostructures and their Photoluminescence Spectra. *Journal of the American Ceramic Society*, **94**, 699–703. 62, 209
- WULFF, G. (1901). Zur Frage der Geschwindigkeit des Wachstums und der Auflösung der Krystallflagen. *Zeitschrift für Krystallographie und Mineralogie*, **34**, 449–530. 27
- XIAO, Y., TANG, S.K., HAO, H., DAVEY, R.J. & VETTER, T. (2017). Quantifying the Inherent Uncertainty Associated with Nucleation Rates Estimated from Induction Time Data Measured in Small Volumes. *Crystal Growth and Design*, **17**, 2852–2863. 23
- YANG, H. (2013a). Nucleation of Butyl Paraben in Different Solvents. 23
- YANG, H.Å.C.R. (2013b). Nucleation of butyl paraben in different solvents. *Crystal Growth and Design*, **13**, 4226–4238. 3, 82
- YOU, J.B., KANG, K., TRAN, T.T., PARK, H., HWANG, W.R., KIM, J.M. & IM, S.G. (2015). PDMS-based turbulent microfluidic mixer. *Lab Chip*, **15**, 1727–1735. 101
- ZEMAITIS, J.F. (1986). *Handbook of aqueous electrolytes thermodynamics*. 15, 16
- ZHANG, J. (2002). Control of ZnO Morphology via a Simple Solution Route. *Chemistry of Materials*, **14**, 4172–4177. 209
- ZHANG, S., FORTIER, H. & DAHN, J. (2004a). Characterization of zinc carbonate hydroxides synthesized by precipitation from zinc acetate and potassium carbonate solutions. *Materials Research Bulletin*, **39**, 1939–1948. 60

REFERENCES

- ZHANG, S., FORTIER, H. & DAHN, J. (2004b). Characterization of zinc carbonate hydroxides synthesized by precipitation from zinc acetate and potassium carbonate solutions. *Materials Research Bulletin*, **39**, 1939–1948. 62, 67
- ZHANG, S., YANG, H. & SINGH, L. (2014). Increased information leakage from text. *CEUR Workshop Proceedings*, **1225**, 41–42. 45, 48
- ZIRINO, A. & YAMAMOTO, S. (1972). A pH-dependent model for the chemical speciation of copper, zinc, cadmium and lead in seawater. *Limnol. Oceanogr.*, **17**. 61, 64